UNIVERSITÀ DEGLI STUDI DI MILANO

PHD SCHOOL IN PHYSICS, ASTROPHYSICS AND APPLIED PHYSICS
DEPARTMENT OF PHYSICS

CYCLE XXXII

On Neutron Stars' Crusts Breaking and Gravitational Waves Emission

Disciplinary Scientific Sector FIS/05

Director of the School: Professor Matteo Paris

Supervisor of the Thesis: Professor Matteo PARIS

Co-Supervisor of the Thesis: Dottor Gabriele CAMBIOTTI

PhD Thesis of
Elia Giliberti

Academic Year 2019/2020

Commission of the final examination:

External Member:
Professor Karwasz Grzegorz, Nicolaus Copernicus University

External Member:
Professor Giacomazzo Bruno, Università degli Studi di Milano Bicocca

Internal Member:
Professor Sabadini Roberto, Università degli Studi di Milano

Final examination:

Monday, 20 January 2020

Università degli Studi di Milano, Dipartimento di Fisica, Milano, Italy

To my family and my darling Cionau

Cover illustration:

Detailed image of the Crab Nebula. Credits: NASA, ESA, NRAO/AUI/NSF and G. Dubner (University of Buenos Aires)

MIUR subjects:

FIS/05 -Astronomia e Astrofisica

PACS:

97.60.Jd Neutron Stars
97.60.Gb Pulsars
04.30.w Gravitational waves

Contents

Introduction

Motivation

The vision of the sky has been inspiring and fascinating mankind for millennia: the vastness and the incredible beauty of the cosmos has led to the growth of deep and fruitful questions about Nature. But modern physics, in fact, born only when Galileo looked at the Moon with its *cannochiale*, discovering mountains and valleys as the ones in the Padua surroundings, and when Newton unified in a single coherent framework the reasons for the fall of bodies on Earth and those for the motion of planets around the sun. The vision of the sky expands the human mind, and it is precisely the study of objects more and more distant and different from those we can see every day that pushes to new knowledge and allows us to shed some new light on fundamental physics back on the Earth. This incredible bond between more and more exotic conditions and everyday physics is even stronger when we talk about neutron stars. These are among the most extreme objects in the Universe, since a mass of the order of that of the Sun is squeezed within a sphere of radius 10 km, with a typical magnetic field of even 10^{12}G.

The compactness of a star like this gives rise to incredible properties of matter: large part of the star is in a superfluid or in a superconductive phase and, despite its very high temperature, typycally 10^8K, the outer layer (the crust) remains solid. Since nearly all the features of these mysterious objects are extreme, they represent an unique opportunity to test and study Nature.

After 50 year of research, we still have a poor understanding of neutron stars' physics. For example, at the present time we still do not know the equation of state for such objects, i.e. how matter behaves in such exotic conditions, and this fact is principally due to our uncertainties on nuclear physics at extreme densities. Some theories even suggest that, in some peculiar cases, neutron stars' matter could be composed of quarks, and that thus there could exist macroscopically extended stars bounded not by gravity but by the attraction due to the strong interaction. Moreover, these stars show quantum features on macroscopic scales: most of their interior is in a superfluid state, completely filled by quantum vortices that can extend throughout almost the whole star. Even further, neutron stars are the strongest magnets in the Universe, and their study can teach us a lot also about extreme magnetic fields. Finally, neutron stars can be used to test General Relativity and our model about the Universe in at least two ways. The first is the direct detections of gravitational waves from neutrons star/neutron star mergers; the other is based on another incredible feature of pulsars[1], their outstanding rotational stability. In

[1]Pulsars (i.e. pulsating stars) are rotating neutron stars, emitting electromagnetic waves observed in the form of periodic pulse.

fact, it has been shown that some millisecond pulsars have a timing stability comparable to the most precise atomic clocks (Matsakis et al. 1997). The idea (Sazhin 1978) is then that the observation of the emission of different millisecond pulsars and the correlation of their timing residuals can be used to detect a stochastic gravitational-waves background from binary black holes in the cores of galaxies. In summary, neutron stars are, at least at the present time, the only possibility to test our theoretical predictions on nuclear and fundamental physics in those conditions.Since their study links, in a complicated but fascinating way, completely different physics fields, neutron stars are among the most exciting objects in the Universe.

In the neutron star literature one of the almost ubiquitous studied effect is the crust breaking. This process is known as *starquake* (or crustquake) and its relation to glitches in pulsars (Baym et al. 1969; Ruderman 1991) and to bursts[2] in magnetars (Thompson & Duncan 1995; Lander et al. 2015; Keer & Jones 2015) is supported by different studies, underlining that the glitch sizes (Melatos et al. 2008a; Howitt et al. 2018) and the burst-energy distribution seems to follow a power law (Cheng et al. 1996; Göğüş et al. 2000), as do earthquakes on Earth. The quakes may also drive NSs precession, as explored by Ushomirsky et al. (2000), as well as the evolution of the magnetic field (Link et al. 1998; Lander & Gourgouliatos 2019). On the other hand, the rigid crust can sustain triaxial deformations (referred to as *mountains* in the literature), whose size may be enough to emit gravitational waves detectable in the near future (Abbott et al. 2017).

Despite the importance of starquakes for a variety of astrophysical phenomena, there is still a lack of "realistic" and quantitative models for the study of crust deformations under different types of loading forces. To date, in fact, most of the studies rely on different approximations, either in the neutron star structure description, where the star is idealized as a uniform elastic sphere (see e.g. Baym et al. 1969; Franco et al. 2000; Fattoyev et al. 2018) or as a two-layers sphere (Giliberti et al. 2018) or the Cowling approximation is used (as in Ushomirsky et al. 2000), which is expected to have a considerable impact on the estimates of the deformations and on the related quadrupole moment (Haskell et al. 2006). As far as I know there is only one complete solution for a stratified neutron star: the one obtained by Cutler et al. (2003). However, also in this case, the approach is not general enough, since the solution is found only in the case of uniform rotation.

The aim of this PhD work is to introduce and study a consistent model useful to describe, in Newtonian Gravity, the deformation of a stratified, self-gravitating, compressible neutron star under the effect of a general chosen loading. Neutron stars are clearly relativistic objects since the dimensionless potential, defined as a proper combination of the stellar mass M, radius R, the speed of light c and the gravitational constants G,

$$\tilde{\phi} = \frac{GM}{Rc^2},$$

that gives us a rough estimate of how large are the discrepancies between the Newtonian and the Relativistic regimes, reaches the value $\tilde{\phi} \simeq 0.2 \div 0.3$ (remember that for the Sun $\tilde{\phi} \simeq 10^{-5}$ and for a black hole $\tilde{\phi} = 0.5$). However, the Newtonian approximation is excellent at the low densities of the crust (Haskell et al. 2006) and thus it is largely used in the neutron stars crust literature (Ushomirsky et al. 2000; Cutler et al. 2003; Haskell et al. 2008; Fattoyev et al. 2018), as a reasonable first order approximation. In this sense, the present formalism, based on the purely Newtonian framework, remains highly valuable since it is easier to use and can give also analytical solutions, shedding light on the main parameters that govern the elastic response of neutron stars to various kinds of loads.

[2]Glitches are sudden increases of pulsar's spin frequency, while burst are abrupt emission of hard X-ray/soft-γ-rays.

The main idea is to adapt a model, first introduced in the literature by Sabadini et al. (1982) for the study of the Earth and rocky planets, to neutron stars. For this reason I wrote a computer code for the model solving, that takes into account specific different physical characteristics of a neutron star. Within this approach we can describe the most recent models regarding different kind of forces; I decided to study the effect of three different loads: uniform rotation, differential rotation and pinning force due to superfluid vortices.

These three loads are related to pulsars glitches. In fact, the idea is that all the previously cited forces could stress the crust until it breaks, causing a starquake. The rupture of the crust, in turn, might trigger a sudden release of angular momentum between the superfluid interior of the star and the normal component. For this reason in all the three cases of uniform rotation, differential rotation and pinning force I calculated the stellar deformation, focusing on the following three main aspects:

1. the crust breaking threshold between two glitches, i.e. the possibility that the crust fails, causing a starquake;

2. the dependence of the deformation on the stellar mass;

3. the effect both of different adiabatic index values and equations of state on the response of the star.

Finally, I focused my attention on fast rotating, accreting pulsars. Their observed spin frequency distribution seems to indicate that they emit gravitational waves, but the origin of their quadrupolar deformation is still debated in the literature. In this dissertation I studied to the best of my knowledge, for the first time in the literature, the effect of a sequence of starquakes and I estimated the maximum quadrupolar deformation that they can induce on rotating neutron stars.

Thesis overview

This work is organized into 6 chapters, as follows:

• Chapter 1 The state of the art of the knowledge regarding neutron star is summarized. We describe what neutron stars are, how they are classified nowadays, and the most recent theoretical understanding of their inner structure. We also introduce the glitch phenomenon and its trigger mechanism, that will be deeply studied in the following chapters.

• Chapter 2 In this chapter is described in detail the model used, following Sabadini et al. (2016). However, we focus our attention on the peculiar characteristic of pulsars, by discussing the main elastic properties of neutron star matter, stressing the role of the adiabatic index on the star's response and its relation to different astrophysical scenarios.

• Chapter 3 Franco, Link and Epstein (Franco et al. 2000) model was one of the first attempt introduced in the literature to study neutron star deformation due to centrifugal force. In this model the star is described as an homogeneous, incompressible object with a fluid core and an elastic crust. This chapter shows that this approach can be seen as the incompressible limit case of our model. Furthermore, I demonstrate that our model can easily be used to generalized Franco, Link and Epstein results to the case of a star with a fluid core and an elastic crust with different density, or to test the Cowling approximation. Finally we use the incompressible model to calculate the strain developed between two glitches and to verify whether a starquake can trigger a glitch. This part is based on the work already published in Giliberti et al. (2019).

• Chapter 4 We apply the general model to study the deformation of a compressible neutron star, described with a polytropic $n = 1$ equation of state, under the effect of uniform rotation. We compare our results to the case of an incompressible star obtained in the previous chapter, focusing in particular on the glitch analysis. This part is a presentation of an actually submitted work (Giliberti et al. 2019).

• Chapter 5 We extend the analysis of compressible neutron star by introducing two other loads, the pinning of superfluid vortices and the differential rotation between the superfluid and the normal component that this pinning induces. We study the deformation and the maximum strained caused by both these forces, and apply our model to the case of pulsar glitches. This chapter ends the second part of the work.

• Chapter 6 All the Low Mass X-Ray Binaries pulsars have a frequency well below the breakup frequency threshold of about 1 kHz; recent theoretical models for such systems thus invoke the emission of gravitational waves as a mechanism that keep the rotation frequency of this star below the breakup limit. By using our model we explore this statement in this chapter, estimating the maximum ellipticity due to a sequence of starquakes on a very fast rotating neutron star, calculate the corresponding gravitational waves emission and the equilibrium frequency. This part of work is contained in a paper now in writing.

Finally we draw some general conclusion on the work presented: further loads can be included into this general model, such as magnetic field forces or mountains due to accretion, giving the opportunity of a realistic study of many different astrophysical scenarios. The main problems underlying crust breaking modeling are then reviewed and the future directions are summarized.

Part I
State of the Art

CHAPTER 1

Pulsars

1.1 Neutron star: a historical introduction

Neutron stars firstly appear on the stage of physics thanks to Landau (Landau 1932), who wrote a paper on the possible existence of a star containing matter of nuclear density. In particular, Landau speculated that in this object "the density of matter becomes so great that atomic nuclei come in close contact, forming one gigantic nucleus". Two years later Baade & Zwicky (1934a,b) proposed the idea that supernovas explosion were powered by the gravitational binding energy released in the transition between an ordinary star into a very compact object, consisting of extremely closed packed neutrons.

The next step was achieved by Tolmann (Caltech), Oppenheimer and Volkoff (Berkeley), (Tolman 1939; Oppenheimer & Volkoff 1939) who presented the equation of hydrostatical equilibrium for a spherically symmetric star in the framework of General Relativity (GR). The interesting thing is that both these works were received and published the same day: Tolmann, Oppenheimer and Volkoff discussed their results together, although the derivation of the equations was made independently. The Tolmann-Oppenheimer-Volkoff (TOV) equations are the basic equations for building neutron star models. Incredibly enough also von Neumann and Chandrasekhar obtained the same equation of hydrostatic equilibrium several years earlier (1934), but they decided not to publish their results (Baym, 1982). Oppenheimer and Volkoff, however, using the equation of state of a degenerate relativistic gas of non-interacting neutrons, found that neutron stars should have a maximum gravitational mass of $M_{max} \simeq 0.7 M_{\odot}$. This value is smaller than the Chandrasekhar mass limit of white dwarfs of $M_{max} \simeq 1.44 M_{\odot}$, preventing the formation of neutron stars from ordinary stars. Relying on the limited knowledge of strong interactions and nuclear matter of that time they concluded "*It seems likely that our limit of* $\simeq 0.7 M_{\odot}$ *is near the truth*". With the outbreak of WWII, neutron stars went into oblivion and were largely ignored by the scientific community for 30 years.

In the early 60's the dawn of the X-Ray astronomy focused again the attention on compact object. In fact, isolated neutron star, with a temperature of about a million kelvin would emit thermal radiation in the soft X-Rays. Such emission, however, cannot be detected by ground based facilities, since it is absorbed by the atmosphere. Situation changed when the rocket experiment by Giacconi et al. in 1962 discovered Sco X-1, the first X-ray source of non-solar origin, soon after followed by several other sources. he identification of these sources remain elusive for many years although Shklovsky (Shklovsky 1967) correctly anticipated their origin as accreting neutron stars. The same year Pacini, published in Nature (Pacini 1967) a paper showing that a neutron star rotating rapidly enough and with a strong magnetic field could transform its rotational energy into electromagnetic radiation.

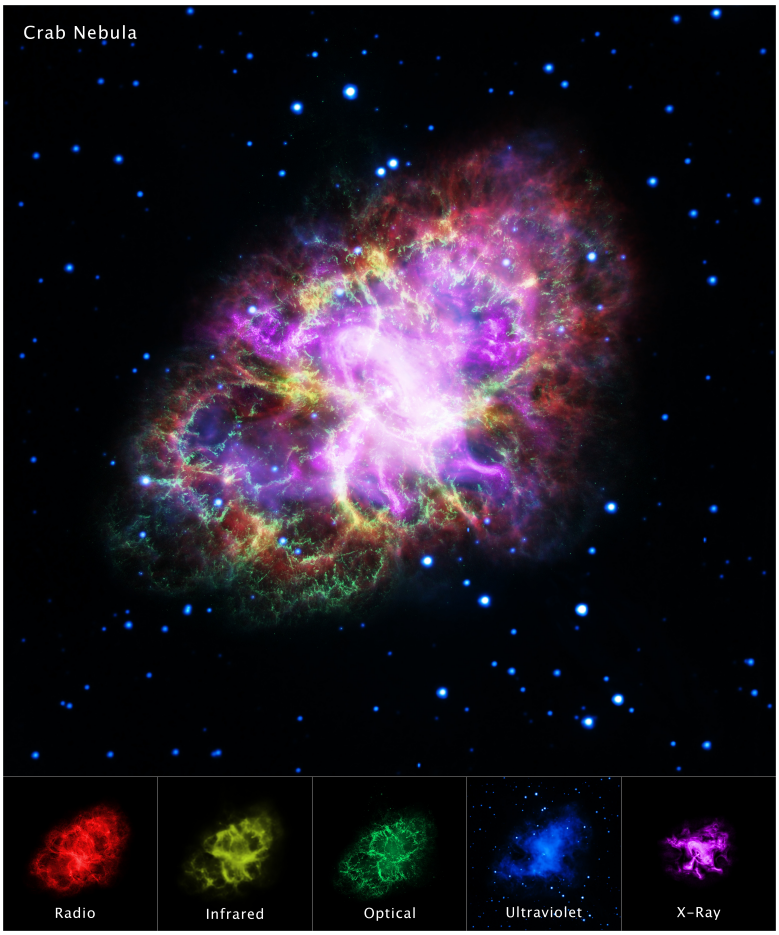

Figure 1.1: Detailed image of the Crab Nebula, the result of a supernova explosion seen by Chinese in the year 1054, which is about 6,500 light-years from Earth. This image was obtained by combining data from five telescopes: The Very Large Array (radio) in red, Spitzer Space Telescope (infrared) in yellow, Hubble Space Telescope (visible) in green, XMM-Newton (ultraviolet) in blue and Chandra X-ray Observatory (X-ray) in purple. The Hubble visible-light image offers a very sharp view of hot filamentary structures that permeate this nebula. The infrared image includes the glow of dust particles absorbing ultraviolet and visible light, and re-radiating at lower energies (longer wavelengths) in the infrared. Ultraviolet radiation and X-rays highlight the energetic cloud of electrons and the core of the pulsar, while the visible-light shows the hot filamentary structure of the nebula. Dust particles absorbing ultraviolet and visible light and re-emitting at lower energies appears in infrared while the neutron star's "wind" of charged emitting at particles energized the surrounding nebula, causing it to emit the radio waves. Credits:NASA, ESA, NRAO/AUI/NSF and G. Dubner (University of Buenos Aires)

In this situation it happened that the first neutron star was detected in a very different, unexpected way. Jocelyn Bell, a graduate student of Antony Hewish, discovered on August 6, 1967, a weak variable radio source. Observations through the months showed that this particular source was incredibly stable; so stable, in effect, that the publication of the discovery was postponed, in order to better understand the origin of this pulse and to exclude a possible artificial origin. Within the beginning of February other three sources were discovered, and it was suggested that they could be oscillating white dwarfs (WDs) or neutron stars. Thomas Gold (Gold 1968) that connected the Bell-Hewish observation with a theory of neutron star lighthouses similar to that of Pacini. The announce of the discovery on Nature (Hewish et al. 1968) starts the pulsars era. The early discover of the Crab pulsar and its period P measurement of $P = 33$ ms (Comella et al. 1969) permits to rule out the WD hypothesis: in fact, at such high spins WDs would be destroyed by centrifugal forces.

1.2 Neutron star formation

Neutron stars are the ultimate stage of stellar evolution of stars starting their life with a mass from 8 to $20 - 30 M_{\odot}$. In fact the entire evolution of a star is determined by its mass: heavier stars will probably produce a stellar black hole, while lighter ones will end their life as white dwarfs: the details of stellar evolution are still developing a research topic, but the main evolutionary aspects are well known, see Fig 1.2. During most of their active life, stars remain in a quasi-equilibrium state, in which their self-gravity is balanced by the pressure of their hot matter. Fusion is the dominant energy source and the thermal and radiation pressure nearly balance gravity for millions to billions of years. The exact timescale depends approximately on the inverse square of the stellar mass (Glendenning 2000). The star evolves through different stages of combustion, from helium to carbon, and then neon, oxygen, magnesium, and silicon: as soon as one element after the other is synthesized, the star forms concentric shells in an onion structure (Fig. 1.3). When each fuel is exhausted, the core contracts further, until the temperature for the next ignition step is reached. Nucleosynthesis stops at Fe, that is the most bound element: beyond this step the fusion is no longer exothermic. In the meantime, the outer layers are still burning, adding mass to the iron core, that contracts under its own gravity. At such density, electrons become relativistic, providing a pressure that grows less rapidly with matter density than in the non-relativistic stage; furthermore, proton-inverse beta decay is energetically favored. The core becomes more and more massive, until it reaches the *Chandrasekhar mass* ($M_{Cha} \simeq 1.44 M_{\odot}$), when the degenerate electrons cannot sustain it anymore against gravity. The core collapses in less than a second, attaining a temperature of about 10^{11}K, and recombining protons and electrons to form neutrons and neutrinos. In these conditions, the neutrinos's cross-section for the interaction with nuclei is sufficiently large to keep them trapped, so that they can escape only by the relatively slow process of diffusion. As the density increases during the collapse, the Fermi energy of the thermalized electrons and neutrinos rises. Their pressure, together with the short-range repulsion between nucleons, stiffens the core, converting the implosion in an explosion. A shock wave originates somewhere in the core interior, traveling outwards, dissipating its energy by photodisintegration of nuclei and neutrino losses, and stalling at a few hundred kilometers from the centre. The outer layers are no longer supported by the core, and starts to fall inward; this material is stopped by the stalled shock, heating the region and turning it into an accretion shock. In this way, a bubble region develops in between the hot core and the shock wave. Here the neutrinos diffused from the core annihilate, giving energy to the expanding bubble. This complex

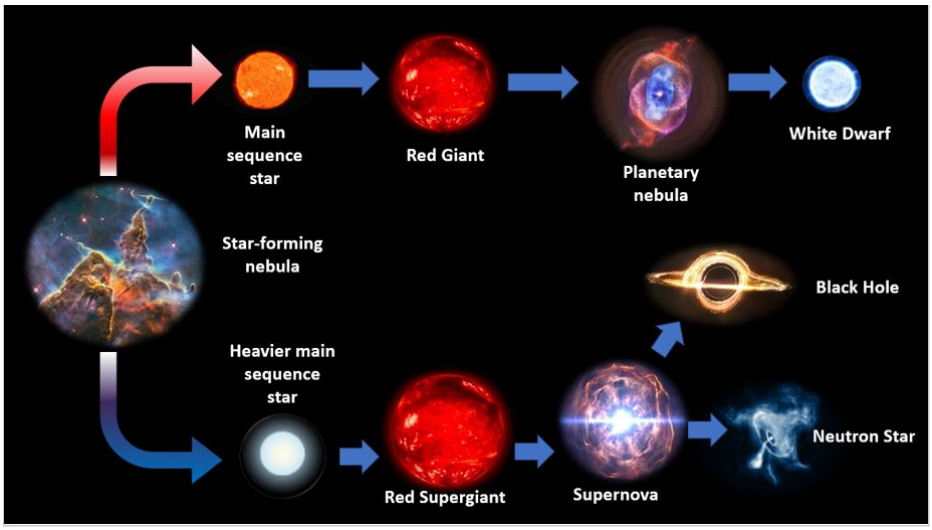

Figure 1.2: Cartoon of stellar evolution: dust and gas collapse in a stellar cloud, forming a protostar, whose fate is determined by its initial mass, composition and the possible presence of a companion. NSs are the ultimate stage of massive stars and are formed in core-collapse supernovae when the massive progenitor sheds its stellar mantle during the explosion O'Connor & Ott (2011). *Upper branch*: Only protostars with about $0.1M_{\odot}$ are hot enough to ignite p-p fusion, while smaller objects become brown dwarfs. The object that has a mass smaller than $8M_{\odot}$ enters in the main sequence, burning hydrogen; when helium starts to be burnt in the core the outer layers expand and the star is a red giant. The following reactions $He + He + He \rightarrow C$ and $C + He \rightarrow O$ can lead to unstable pulsation in the envelope, that is ejected in a filamentary shell surrounding the hot star (planetary nebula). The core cools and contracts, forming a C-O white dwarf. If this object remains isolated simply cools down as a black dwarf; on the contrary, if it accretes matter from a companion it can exceed the Chandrasekhar mass and explodes as a type I-a supernova. *Lower branch*: Protostars with mass in the range $8M_{\odot} \leq 100M_{\odot}$ enter in the main sequence and then reach the Red Supergiant Branch, similarly to lighter stars. Very massive stars ($M \geq 100M_{\odot}$) are thought to produce black holes. Stars with $M \geq 11M_{\odot}$ reach the Fe stage and then explodes as a supernova. The final product of this explosion, depending on mass, can be a black hole or a neutron star. The outcome is thought to depend mainly on the compactness of the core before the collapse, a non monotonic function of the stellar mass parameter, so that the scenario for stars with $15M_{\odot} < M < 50M_{\odot}$ is very uncertain (Sukhbold et al. 2016).

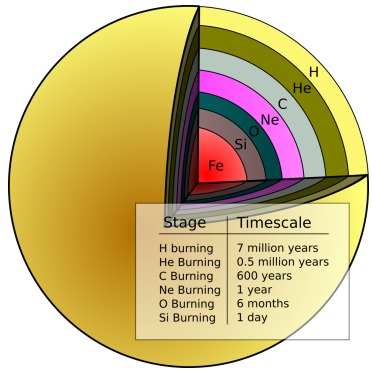

Figure 1.3: Schematic representation (not in scale) of a massive star in its last instants of life. The timescales in the table are calculated for a $25M_{|odot}$ neutron star. Credits to http://large.stanford.edu/courses/2008/ph204/deaconu1/

interplay of neutrino heating and convection revitalized the shock, that blows away the outer part of the star in a *supernova* explosion.

The inner part of the object is the initially opaque proto-neutron star, with a temperature of tens of billions Kelvin. It looses its trapped neutrinos (deleptonization) in seconds and cools to about 1 MeV or less. Finally, the chemical equilibrium is reached and the newly-born neutron star cools down to 10^9K within days. The outer layers of the NS crystallize only after weeks or months, when the temperature is low enough to make important the repulsive Coulomb forces between ions. The star continues to cool essentially through neutrino emission for its first $10^4 - 10^5$ years, since only at about 10^8K the photon emission from the surface becomes the main mechanism for decreasing the star's temperature.

Since the supernova explosion may be not symmetric, many neutron stars are *kicked off* at their birth and this could explain why we have many neutron stars without supernova remnants around them and why their distribution on the galactic plane is more scattered than normal stars one. Supernova explosions rate is estimated to be around 1 per 50 years (Diehl et al. 2006) and thus, supposing that most of these explosions leave a neutron star (instead of a black hole) one expects that our galaxy should contain about $10^8 - 10^9$ neutron stars.

1.3 Neutron star structure

Matter inside NSs can reach extreme conditions, and this is why it is so difficult to describe the innermost interior of these objects. In this first part of our work we focus on isolated NSs, supposed to be made of cold catalyzed matter, i.e. matter in equilibrium with respect to all the possible interactions at zero temperature. Therefore, we expect that the matter is in its ground state with the lowest possible energy. Despite the presence of some differences between the expectations given by the EoSs present in the literature, we can assume that the structure of an ordinary[1] isolated neutron star is the following. Going from the outside inward we find:

[1]Some works explore the hypothesis that there should exist another family of objects, the so called *strange stars*, with radii smaller than those of neutron stars and with very peculiar properties. However, in this thesis we will not discuss the physics of such objects, focusing instead on ordinary neutron stars.

Z	N	A	$\bar{n}_{\rm min}$	$\bar{n}_{\rm max}$
26	30	56	–	4.93×10^{-9}
28	34	62	5.08×10^{-9}	1.63×10^{-7}
28	36	64	1.68×10^{-7}	8.01×10^{-7}
28	38	66	8.28×10^{-7}	8.79×10^{-7}
36	50	86	8.98×10^{-7}	1.87×10^{-6}
34	50	84	1.94×10^{-6}	6.83×10^{-6}
32	50	82	7.09×10^{-6}	1.67×10^{-5}
30	50	80	1.74×10^{-5}	2.97×10^{-5}
28	48	76	3.03×10^{-5}	3.72×10^{-5}
28	50	78	3.82×10^{-5}	4.55×10^{-5}
28	52	80	4.68×10^{-5}	7.79×10^{-5}
42	82	124	8.16×10^{-5}	1.12×10^{-4}
40	82	122	1.16×10^{-4}	1.34×10^{-4}
39	82	121	1.36×10^{-4}	1.59×10^{-4}
38	84	122	1.65×10^{-4}	2.16×10^{-4}
38	86	124	2.20×10^{-4}	2.25×10^{-4}
38	88	126	2.29×10^{-4}	2.59×10^{-4}
38	90	128	2.64×10^{-4}	2.69×10^{-4}

Figure 1.4: Sequence of nuclei in the ground state of the outer crust of neutron star calculated by Pearson et al. (2018) using experimental nuclear data from the 2016 Mass Atomic Evaluation (Wang et al. (2017), upper part), and the theoretical mass table of the HFB-22 model (Goriely et al. (2013), lower part). $\overline{n}_{min}$ and $\overline{n}_{max}$ are the minimum and the maximum density number density at which the corresponding nuclide is present, respectively. The baryon number density are measured in units of fm^{-3} Courtesy of Pearson et al. (2018)

- a very thin plasma *atmosphere*. The thickness of this layer depends on the conditions, ranging from some centimeters for hot NSs to millimeters for the cold ones;

- the *outer crust*, that goes from the lower part of the atmosphere to the neutron drip density ρ_{drip}, that is about $\rho_{drip} = 4 \times 10^{11} \mathrm{g/cm}^3$. This is a **solid layer** coexisting with a gas of degenerate electrons, which gives most of the pressure. Detailed calculations have shown that the most probable crustal equilibrium structure is a body-centered cubic lattice (Chamel & Haensel 2008). Other lattice types (hexagonal closed packed for instance) could also be realized, but only at very small densities (Kohanoff & J.P. 1996). Experimental nuclear data allow us to completely fix the structure of NS crust up to $\rho \sim 6 \times 10^{10} \mathrm{g/cm}^3$, while for higher density the composition of this layer is model dependent. At low densities the ground state corresponds to a lattice of $^{56}_{26}Fe$; when the density increases, the Fermi energy increases too and electrons become relativistic. For density of about $10^7\ \mathrm{g/cm}^3$ electrons combine with protons, via inverse-decay, so the ground state shifts to nuclei richer in neutrons (see table of Fig 1.4). When the density reaches about the drip one, the chemical potential of neutrons reaches zero, thus neutrons *drip out* of nuclei, i.e. they begin to fill states in the continuous part of the energy spectrum. The lower energy state is therefore a two-phase system, in which we have nuclei, electrons and unbound neutrons. The neutron drip point announces the end of the outer crust and the beginning of the inner crust. The outer crust extends for some hundred meters;

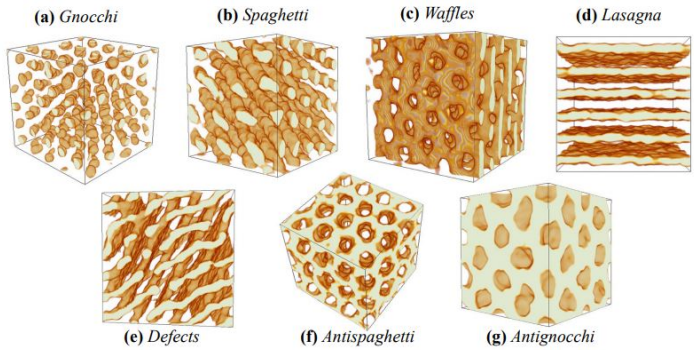

Figure 1.5: Nuclear pasta configurations produced in MD simulations with 51,200 nucleons. Credits to Caplan & Horowitz (2017).

- the *inner crust*, which ends at about half of the saturation density for terrestrial nuclei $\rho_0 = 2.4 \times 10^{14}\mathrm{g/cm^3}$. Here, it can be found a *lattice* of very neutron-rich nuclei together with a gas of neutrons and electrons. The bottom of the inner crust is reached when we have such a high density that nuclei dissolves in a sea of protons, neutrons and electrons. A very interesting feature is that neutrons are paired together making them a neutron superfluid. In fact, excluding new born NSs, the temperature inside this region is smaller than the Fermi temperature at ρ_0, and thus Cooper pairing is energetically favored.

  The inner crust is a unique system, the properties of which are not directly accessible in terrestrial laboratories because of the presence of free neutrons. Theoretical approaches based on many-body theory imply calculations that are out of reach at the present time due to spatial inhomogeneities; even in the simplified case of homogeneous matter, calculations are very difficult since nucleons are strongly interacting via two and three body forces. As a result, the inner crust of neutron stars has been studied with phenomenological models. We will not show here in details the theoretical model used to study this layer of the star, reminding only the main idea: when density grows, we have a sequence of heavy nuclei, surrounded by a sea of drip neutrons. In particular at the bottom of the crust, for densities of the order of $10^{13} \div 10^{14}\mathrm{g/cm^3}$, spherical nuclei are no longer energetically favored. This is due to the fact that in this case nuclei become large enough to fill about half of their Wigner-Seitz cell, where attractive strong interactions at short distance and Coulomb repulsion at long distance become comparable. This leads to a competition between these two interactions, called *frustration*, with the formation of complex nuclear structures with different shapes, as shown in Fig 1.5: spheres (gnocchi), cylinders (spaghetti), plates (lasagna), as well as spherical and cylindrical holes surrounded by nuclear matter. This layer has been called *pasta phase* and also *mantle*. Finally when the density reaches about $0.5\rho_0$, nuclei disappears, leaving place to the core.

- the *outer core*, extending from $0.5\rho_0$ to about $2\rho_0$, made of a sea of neutrons, and, in small percentage, of protons, electrons and muons. Also in this region neutrons forms a superfluid, but here even protons show pairing, creating a giant superconductor. It is still debated what kind of superconductor (type I or II) could be formed, but is believed that there could be a transition from type I to type II inside

the outer core, for sufficiently high density. The outer core occupies some km of the neutron star internal structure;

- the *inner core*, where matter exceed $2\rho_0$. Here we could find many exotic configurations, ranging from pions to hyperons, but also kaons or deconfined quarks.

1.4 Pulsars

Pulsars (i.e. pulsating stars) are rotating neutron stars, emitting electromagnetic waves in the form of periodic pulse. Although on timescale lower than 1 ms pulse shape is quite complex, showing microstructure, the average of many pulses is incredible stable: by averaging pulses we can verify that pulsars are excellent clock, with periods known to a part in 10^{13}! The typical pulsar period P lies in the range from millisecond to seconds and it is observed that periods are increasing in a steady way (excluding *glitches*, see below), with $\dot{P}$ value that are typically $\dot{P} = 10^{-15} ss^{-1}$, but can vary over 10 orders of magnitude between different classes (1.8). Rotating neutron stars are observed mainly in radio wavelengths but also in optical (Vela,Geminga) and X-ray ones (pulsars in a binary system accreting mass from a companion). Moreover some neutron stars are also γ- ray sources.

Modelling the star as a rotating magnetic dipole, forming an angle α with respect to the rotation axis, one can estimate the energy lost by the star using the non relativistic Larmor' s formula (Jackson 1991)

$$\dot{E}_{em} = \frac{2}{3c^3}|\ddot{\boldsymbol{m}}|^2, \tag{1.1}$$

where E_{em} is the electromagnetic energy of the source, c is the light speed and $\boldsymbol{m}$ is the stellar magnetic dipole. Assuming that the dipole rotates with angular velocity $\Omega = 2\pi/P$ but remains fixed in magnitude m, Eq (1.1) can be rearranged as

$$\dot{E}_{em} = \frac{2}{3c^2} m^2 \Omega^4 \sin^2 \alpha. \tag{1.2}$$

Now, if, for simplicity, we model the star as a uniformly magnetized sphere of radius R, rotating around the z-axis in vacuum, the magnetic dipole intensity can be written as $m = R^3 B_P/2$, where B_P is the magnetic field value near the poles and thus the power radiated is

$$\dot{E}_{em} = \frac{R^6 B_p^2 \sin^2 \alpha}{6c^2} \Omega^4. \tag{1.3}$$

Emission is interpreted as a beamed radiation generated in proximity of the magnetic poles, sweeping across the line of sight of the observer as the neutron star rotates 1.6.

This is the classic result of the vacuum-dipole-model. However, as discussed first by Goldreich & Julian (1969), due to the large values of the magnetic field of the NS, the vacuum configuration is unstable, and, in fact, the pulsar is surrounded by a magnetosphere, formed by electron-positron plasma. When the effects of the magnetosphere are taken into account, as in the force-free models, one can show (Spitkovsky 2006) that the spin down luminosity can be approximated as

$$\dot{E}_{em} = \frac{R^6 B_p^2}{4c^2} \left(1 + \sin^2 \alpha\right) \Omega^4. \tag{1.4}$$

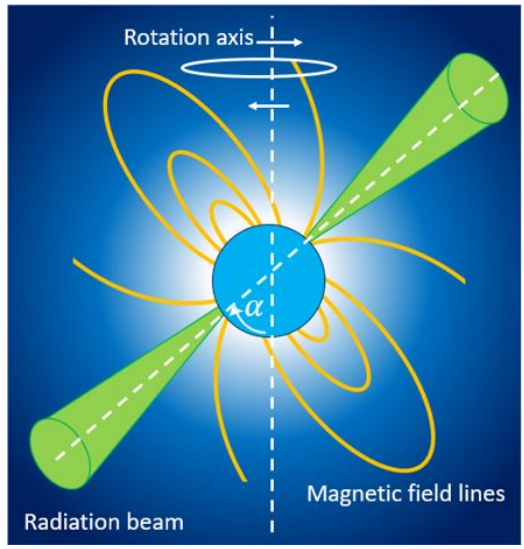

Figure 1.6: Schematic section of a rotating neutron star, modelled as a magnetic dipole forming an angle α with the rotation axis.

This equation tells us that even in the aligned case ($\alpha = 0$) one has a non-zero emission, and the power is ever larger than in the vacuum orthogonal rotator ($\alpha = \pi/2$). Since the luminosity $\dot{E}_{em}$ must be equal to the observed decrease of rotational kinetic energy $I\Omega|\dot{\Omega}|$ of the star (I is the moment of inertia) it is thus possible to infer from the observational data, P and $\dot{P}$, the intensity of the effective magnetic field, defined as $B_* = 1/2B_p(1 + sin^2\alpha)^{1/2}$, at the surface.

1.4.1 Breaking index

Since the star loses energy, it slows down ($\dot{P} > 0$) but this effects is so small that period can be assumed practically constant over the years. Equation (1.4) can be written explicitly as

$$\dot{\Omega} = -\frac{R^6 B_*^2}{4Ic^2}\Omega^3, \tag{1.5}$$

and easily generalized for a breaking torque proportional to Ω^n

$$\dot{\Omega} = -\beta\Omega^n. \tag{1.6}$$

The parameter n is called *braking index* and is clearly $n = 3$ for pure electromagnetic emission; in the case of pure gravitational wave emission, instead, one finds $n = 5$ (see chapter 6). If we assume the constancy of β, the above equation can be used to estimate the pulsar age τ_n: consider $\tilde{\tau} = -\Omega_o/\dot{\Omega}_o = \beta\Omega_o^{n-1}$, where the subscript o remind us that it is are the actual *observed* star's value. In this case

$$\dot{\Omega} = -\tilde{\tau}\frac{\Omega^{n-1}}{\Omega_o^{n-1}}. \tag{1.7}$$

Integrating this expression starting from the pulsar birth one obtains the general relation

$$\tau_n = \frac{\tilde{\tau}}{n-1}\left[1-\left(\frac{\Omega_o}{\Omega_i}\right)^{n-1}\right]. \tag{1.8}$$

Finally, assuming that the angular velocity at birth Ω_i was extremely larger than the actual angular velocity, i.e. $\Omega_i \gg \Omega_o$,

$$\tau_n \simeq -\frac{1}{n-1}\frac{\Omega_o}{\dot{\Omega}_o}. \tag{1.9}$$

This characteristic age is considered a less reliable estimate of what is called the true age, i.e. the age obtained from dynamical information, such as observed space velocities of the pulsar coupled with a known birthplace, or from the direct observation of the supernova explosion, as for the Crab pulsar. Typically they differ by factors of two or three, in the cases in which both kinds of age estimates are available. Furthermore it is also possible (though difficult) to estimate the braking index by measuring the second derivative of the angular velocity as

$$n = \frac{\Omega\ddot{\Omega}}{\dot{\Omega}^2}. \tag{1.10}$$

Actually, among all the radio pulsars, only some young ones have an accurate measure of n, with values all smaller than 3 (as example,$n = 2.509 \pm 0.001$ for Crab ((Lyne et al. 1993) and $n = 1.4 \pm 0.2$ for Vela (Lyne et al. 1996)). A possible explanation for these values is linked to the magnetic field evolution: $n = 3$ only for constant surface magnetic field, but $n < 3$ if the surface value is increasing in time. The emerging idea is, therefore, that soon after birth the magnetic field is buried by infalling material and then slowly diffuse to the NS surface. Some other pulsars show anomalous braking indices up to 100, while many pulsars show negative values of n (e.g. $n = -1.5$ for J0537-6910), which can be understood in terms of missed or unresolved glitches (Alpar & Baykal 2006).

1.5 Pulsar classification

Observations of NS in all the electromagnetic spectrum have shown a very rich family of objects, with very different properties. If for normal stars the main representative diagram is the Hertzsprung-Russell one, for pulsars we use the $P - \dot{P}$ diagram (see Fig 1.8), where we can distinguish between these main classes:

Rotation-Powered Pulsars (RPP), which are neutron stars spinning down as a consequence of their magnetic dipole and particles emission, covering a broad band of the electromagnetic spectrum, going from the radio to gamma-rays. Their inferred dipolar magnetic field is typically $10^{12} - 10^{14}$ G. The spin-down of this object is stable for most of the time, but many of them show *glitches* (see section 1.6), sudden increase of their spin-down frequency with typical jumps in the range $\Delta\nu/\nu \simeq 10^{-11} - 10^{-5}$. At the time of writing more than 2000 RPP are been discovered, allowing a sub-classification into *normal* and *MilliSecond* Pulsars (MSP), i.e. the ones with a period less than or equal to 1 ms. The latter are thought to be very old "recycled" neutron stars (see chapter 6), with a characteristic age above 100 Myr. There is also another subpopulation of RPP, the one of Rotating Radio TransientS (RRATS) (Keane & M.A. 2011), showing different transient radio behaviour, from no pulsations for long periods of time to stable modulated

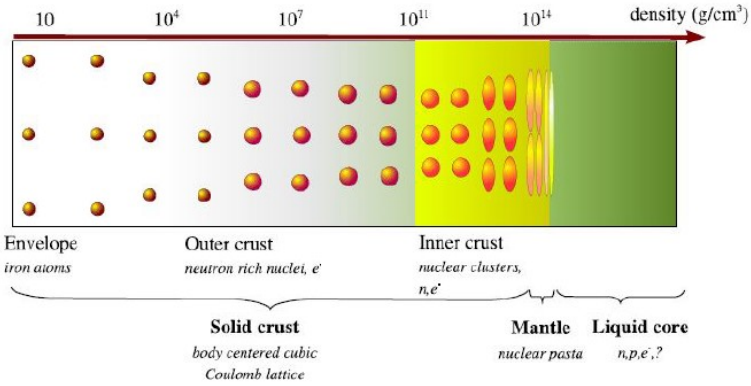

Figure 1.7: Schematic section of a neutron star, covering over 14 orders of magnitude in density. Credits to Chamel & Haensel (2008).

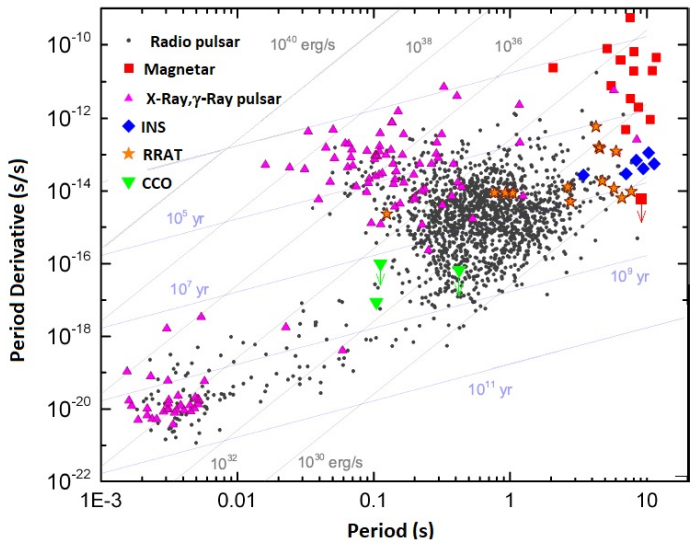

Figure 1.8: $P - \dot{P}$ diagram for known neutron stars, divided into Isolated Neutron Stars (INS), Compact Central Objects (CCO), Rotating Radio Transients (RRATs) and magnetars. Data are taken from http://www.atnf.csiro.au/people/pulsar/psrcat/. Gray lines of constant characteristic age, and dipole spin-down luminosity (see section 1.4), are superposed. Credits to Harding (2013).

pulsations. The cause of this transition is still unknown, but global changes in the density of charge distribution or currents in the pulsar magnetosphere have been proposed (Kalapotharakos et al. 2012).

Magnetars (Thompson & Duncan 1995) are NS with inferred magnetic field of the order of $10^{14} - 10^{15}$G. It is still debated how such a large B field can be achieved: on the one hand, it could be due to special conditions at birth as a highly magnetized progenitor, in the fossil field hypothesis (Woltjer 1964), and, on the other hand, Thompson & Duncan (1993) proposed that in a rapidly rotating proto-neutron star a shear-driven dynamo effect could be the main trigger for reaching large value of B.

This class of objects includes two distinct astronomical sources, the Anomalous X-ray Pulsars (AXPs) and the Soft Gamma-ray Repeaters (SGRs). The first where called anomalous because of the difficulties in the explanation of their high X-ray luminosity as accreting binary system. The latter, instead, undergo repeated bursts, with typical waiting times of years; in addition, three giant flares have been detected, with luminosities up to 10^{47}erg/s for about one second, showing also very interesting pulsations in their longer decay. The X-ray emission of magnetars during their quiescent period is due to ohmic decay of their enormous magnetic field; B is also thought to be responsible for the flare events, since magnetic stresses can eventually break the stellar crust, allowing the reconnection of twisted magnetic field lines frozen and releasing large amount of energy (Thompson & Duncan 1995, 1996).

Compact Central Objects (CCOs) are isolated stars, observed near the center of young ($10^3 - 10^4$ yr) SuperNova Remnants (SNRs), showing only X-ray emission. Measurements of P and $\dot{P}$ constrain the magnetic field to $10^{10} - 10^{11}$ G, and thus is probable that this objects are born with unusual low B. The X-ray spectrum is purely thermal, with multiple blackbody components, and can be used to extract many useful information on the physics of NSs. In this sense the CCO in Cas A has been extremely important. The decrease of the temperature of this object by 4% in 10 years (Papitto et al. 2010), in fact, has challenged the standard cooling models, requiring the presence of a superfluid component in the interior of the star (Shternin et al. 2011)[2]. Furthermore, the same emission has been used for a measurement of the stellar radius: H and He atmosphere models gave unrealistic $R < 1$ km values; using C atmosphere models, however, has been recently found the value of $10 - 12$ km (Ho & Heinke 2009), suggesting an accretion of heavy elements on the NS surface. Also *Isolated Neutron Stars* (INSs) emits essentially in the soft X-ray band, with the exception of faint contributions in the optical/UV wavelengths, but, differently from the CCOs, they are not associated with supernova remnant or nebula. At the time of writing (August 2019) seven confirmed INS are known (The Magnificent Seven), and they are thought to be nearby, cooling middle-ages NSs (Kaplan 2008).

Accretion-powered pulsars can be found in binary systems, when the NSs accrete matter from the companion, and globular clusters. In these stars it is the gravitational energy of the infalling matter that powers the main part of the observed emission. This class of objects, that are usually observed in X-Ray, are divided into two sub-groups, depending on the mass of the companion: the low mass X-Ray binaries (LMXB, where the donor is a low mass main sequence star, a red giant or a white dwarf, and the mass transfer occurs through an accretion disk) and the *High Mass X-Ray Binaries* (HMXB, where the companion is a massive main sequence star, and the NS interacts with its stellar wind). According to the actual NSs evolutionary scheme LMXB were thought to be the progenitors of rotation-powered millisecond pulsars (Papitto et al. 2014). This scenario has

[2]However, the interpretation of the cooling data of Cas A is rather controversial, see e.g. Posselt et al. (2013)

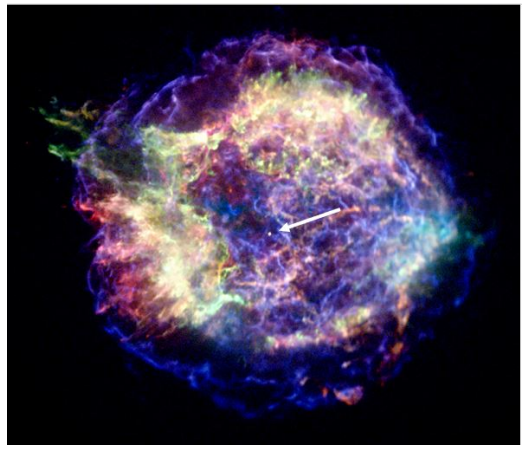

Figure 1.9: Chandra X-Ray Observatory satellite image of the Cassiopeia nebula, one of the most detailed image ever made of an exploded star. The CCO, known as Cassiopeia A, is the white dot in the center indicated by the arrow. The image is color coded for the photon energy: red for $0.5-1.5\mathrm{keV}$, green for $1.5-2.5\mathrm{keV}$ and blue for $4.0-6.0\mathrm{keV}$. The outer ring (blue) is ten light years in diameter and marks the location of a shock wave generated by the supernova. A jet-like structure that extends beyond the shock can be seen in the upper left. Adapted from `chandra.harvard.edu`.

been confirmed by obsbervations of millisecond pulsars in accreting systems, the most famous being SAX J1808.4-3658 discovered in 1998 (Wijnands & van der Klis 1998).

1.6 Glitches

Pulsar's periods, tracked with high accuracy over years, shows a very regular spin-down trend. However, many of these objects exhibit sudden jumps of their rotational frequency, called *glitches*, followed by a period of slow recovery (lasting from days to months) with typical values of the relative jumps that cover the range $\Delta\nu/\nu = 10^{-11} - 10^{-5}$. At the time of writing about 500 events have been detected in 168 stars in the Jodrell Bank Catalogue[3]. These detections have permitted to have some statistical study about glitches (Espinoza et al. 2011; Fuentes et al. 2017). In particular, it has been shown that the glitch size distribution is bimodal (Fig 1.10), with a broad distribution of small events and a narrower peaked around 20 μHz; furthermore, glitchers are spread in all pulsars types (see Fig 1.12), except for millisecond pulsars, for which we have only one glitching star.

It has to be underlined that most of the observed objects (more than 60%) have shown only one glitch, and this is why most of the studies concern the "very frequent glitchers", i.e. the star with a number of glitches larger than 12. Among the ones that glitch repeatedly, two (PSR J0537-6910 and Vela) are quasi-periodic (Haskell & Melatos 2015; Melatos et al. 2008b). In particular, Vela is the most studied NS and the first one to exhibit a glitch in 1969. It has quite a regular sequence of glitches (one every 2.8 years), with a similar size of $\Delta\nu/\nu = 10^{-6}$. However, even for Vela pulsar there are still no solid statistical studies of the glitching behavior, due to the paucity of data and to intrinsic difficulties.

[3] http://www.jb.man.ac.uk/ pulsar/glitches.html

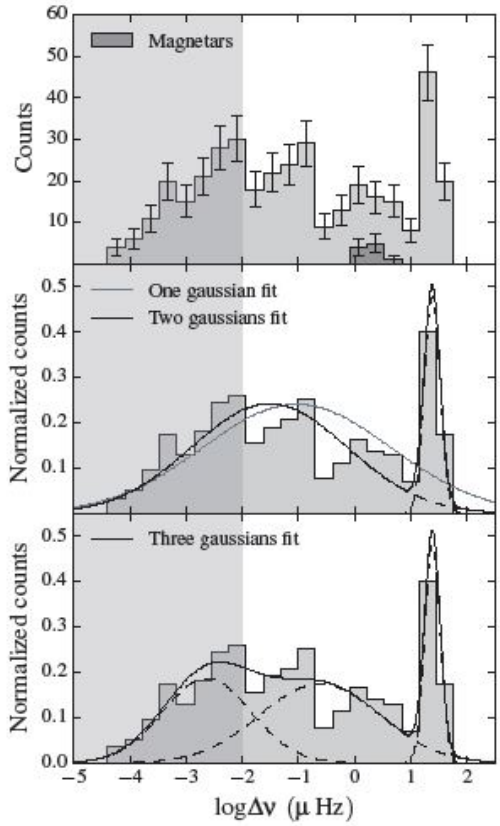

Figure 1.10: Histogram of the glitch size $\Delta\nu$ of all glitches in the database of Fuentes et al. (2017). *Upper panel*: Magnetar events are labelled with a darker gray, while the error bars are calculated as the square root of the number of events per bin. *Middle and lower panels*: best fits (solid lines) with one, two, and three Gaussians, without the inclusion of magnetar glitches. Dashed lines represent the best fits components. Since smaller glitches may be missing, due to detectability issues, the region below 0.01 μHz is shaded. Image courtesy of Fuentes et al. (2017).

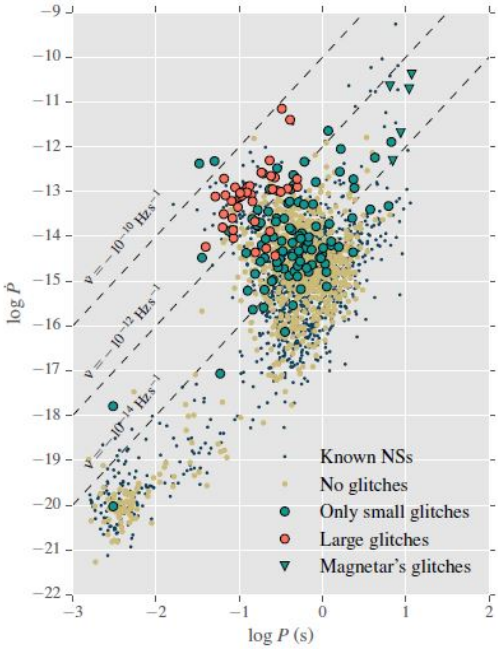

Figure 1.11: $P - \dot{P}$ diagram for known NS. Pulsars with a long term observation but no glitches are denoted with amber dots, while the others with blue dots. Pulsars showing glitches have been divided into two main groups, the one with large events (red circles) and the other with only small glitch (turquoise circles). Magnetars with observed glitch activity are labelled with turquoise triangles. Image courtesy of Fuentes et al. (2017).

With the exception of Vela-like stars, glitches size span several orders of magnitude both when comparing different object and when fixing the observation on a given star. Generally speaking, glitches seem not to have a preferred timescale for inter-glitch times nor a preferred amplitude. All these characteristics seem to suggest a close analogu between glitches and quakes. Melatos (Melatos et al. 2008b) shown that the glitches magnitude seems to be well described with fat tailed Probably Distribution Function (PDF), while Espinoza et al. (2014) studying the Crab glitches size distribution claimed that there is a lower limit for the glitches size of about 10^{-9}, well above the smallest resolvable event. Whether or not this implies a true limit in the small glitches of the Crab depends on the form of the extrapolated PDF, which is at present quite uncertain because of the relatively small number statistics. Furthermore, timing noise events of different origin (maybe magnetospheric) can contaminate the studied population; therefore further studies are required to rule out this possibility.

Glitches models

Glitches models dates back to Ruderman (Ruderman 1969), who proposed the *starquake* mechanism, later renewed by Baym & Pines (1971). The starquake mechanism is the following. The outer layer of a neutron star (the crust) is a crystalline solid, since it solidified in an early epoch, when the star was just born and was spinning relatively fast, is is rather oblate. As the star slows down, the centrifugal force decreases and some stress arises due to the gravitational force, that tries to drive the crust to a less oblate shape. This loading of the crust ceases when the stresses reach a critical value and the crust cracks. Some stress is relieved and the excess oblateness is reduced. In a simple one-component model this clearly decreases the star moment of inertia, increasing, by the conservation of the angular momentum, its rotation velocity. Following this model, the glitch observation is related only to the jump in the crust rotation velocity, that is due to the abruptly modified moment of inertia of the crust itself. However, soon after the introduction of this model it became clear that starquakes alone cannot explain the large Vela's glitches; therefore another model, called the "two component" model (Baym et al. 1969) was proposed. Pulsars are supposed to be made of two different parts: the "normal" one, composed by the crust lattice and the charges of the whole star, and the neutron superfluid. [4] Only the first component is strongly coupled with the magnetic field. This part rotates with angular velocity Ω_c and slows down under the action of the external torque. A glitch is modelled as a sudden jump in rotational velocity of the crust, which is rapidly communicated to the charged parts and only slowly to the neutral one.

We can thus write

$$\begin{cases} I_p\dot{\Omega}_p = -T_{em} - \frac{I_p(\Omega_p-\Omega_n)}{\tau_c} \\ I_n\dot{\Omega}_n = \frac{I_p(\Omega_p-\Omega_n)}{\tau_c} \end{cases} \tag{1.11}$$

where T_{em} is the external electromagnetic torque, I_c and I_n are respectively the "normal" and the superfluid moment of inertia and τ_c is the model parameter that describes the coupling timescale between components. Introducing the steady state value for the crust velocity Ω_0 and $I = I_p + I_n$, we can solve these equations. We obtain

$$\Omega_n(t) = \Omega_0(t) + \Delta\Omega\left(Qe^{-(t/\tau_c)} + 1 - Q\right) \tag{1.12}$$

[4] Glitches are considered one of the probes for the existence of a superfluid phase in NS interior: the interaction timescale between two normal fluids would be very short compared with the one that are observed in these events. Superfluids, on the contrary, can flow without friction; moreover they are theoretically expected in this environment (see for example Haskell & Sedrakian (2017)).

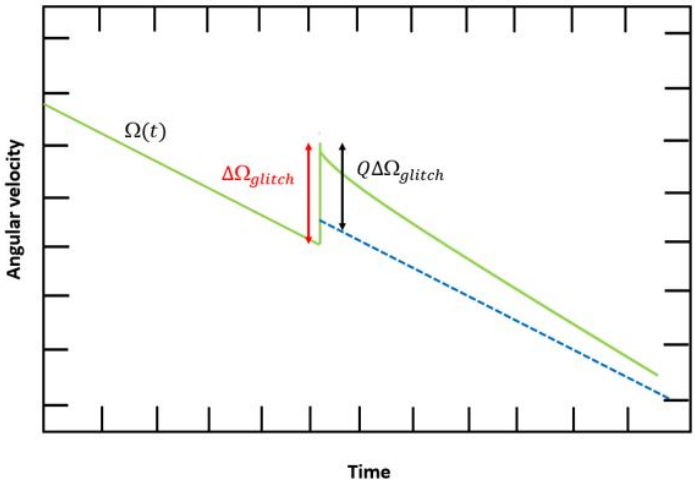

Figure 1.12: Schematic diagram of a glitch, following the notation introduced by (Baym et al. 1969): the spin up phase is instantaneous to the accuracy of data and thus the glitch amplitude is found by considering the jump between a pre-glitch model and the fitted relaxation. The three parameters $\Delta\Omega$,τ_c and Q in Eq (1.12) allow to fit the post glitch relaxation. In particular, the healing parameter Q estimates the fraction of the extrapolated jump that recovers before the next glitch. Models that do not allow for permanent changes in the properties of the star have $Q = 0$ at infinity. in general, at least another glitch is triggered before complete recovery is attained.

where Q is called the healing parameter and indicates the degree to which the angular velocity relaxes back to the steady state.

For Vela glitches $Q \simeq 1$, while for the Crab Q is typically small (Crawford & Demiansku 2003). The model here briefly described mainly focuses on the post-glitch relaxation, that can be easily followed, contrary to the rise time of the event, that has been resolved only very recently Palfreyman et al. (2018); Ashton et al. (2019).

An interesting parameter for studying NS glitches is the *glitch activity*, defined as the time average change of the rotation frequency due to glitches, i.e.

$$\mathcal{A} = \frac{P}{T_{obs}} \sum_i \Delta\nu_i. \tag{1.13}$$

In the above expression T_{obs} is the time over which the pulsar has been searched for glitches, while P is a typical value for the period of the pulsars ($\Delta\nu \ll \nu$, so the exact value of P doesn't affect much the result). It has been recently pointed out (Lyne et al. 2000; Espinoza et al. 2011; Fuentes et al. 2017; Ashton et al. 2017) an interesting correlation between the absolute activity $\nu\mathcal{A}$ and the spin down rate $|\dot{\nu}|$: in particular, for pulsars and magnetars with $-13.5 < log|\dot{\nu}| < -10.5$ one finds that $\nu\mathcal{A} = (0.010 \pm 0.001)|\dot{\nu}|$, where the relation is dominated by large glitches.

Part II
The model

CHAPTER 2

The model

2.1 Introduction

In this chapter we introduce a model for describing the deformations of a compressible and self-gravitating neutron star under the effect of specified forces in a Newtonian framework. As already underlined, despite the fact that NS are General Relativity objects, the Newtonian limit is a very useful tool that can be used as a first approach to understand the global response of the star and its dependence of the physical characteristic of the object. For example, as we will see in the next chapter, the Newtonian approach can be used to obtain simple analytical solutions.

This model, originally built for the Earth by (Sabadini et al. 1982), is here adapted and used in a totally new context for the description of a neutron star. This implied an astrophysically sounded choice of the stellar stratification, of its elastic parameters, of different interesting loadings and different realistic EoSs in Newtonian Gravity (with a brief excursus on GR). Moreover, I wrote a code in *Mathematica* for the numerical implementation of the model. It has been used to study possible causes of starquakes, related both to glitches and gravitational waves. Concerning this last point the prevision of the model could be tested in the near future by the one-year observational run (O3) by the LIGO-Virgo collaboration.

The generality of this approach allows to consider not only centrifugal forces, as other works in the literature (Cutler et al. 2003), but also tidal and non-conservative forces (like vortex pinning to impurities in the crust), or loads which account for inhomogeneities inside the star (the so-called *bulk* loads), as well as *surface* loads. In the framework of NS physics, these last particular loads can be used to study the effect of accretion of matter onto the crust, making the inclusion of these forces potentially interesting. However, it is known that these kind of loads need a specific technique to handle the boundary conditions (Sabadini et al. 2016), so that we will not include them here in order to maintain the discussion self-contained. Our model is, at the best of our knowledge, more general than the ones already present in the literature and it is moreover self-consistent. Its development should therefore be a clear improvement in our modelization of NSs structure and their features.

The structure of the chapter is the following. Before the discussion of the main equations of the model, we will rapidly review the elastic properties of a realistic neutron star, i.e. its bulk and shear moduli. Then we introduce the equations describing the deformation of a self-gravitating NS under the effect of a chosen perturbative force, and discuss the proper boundary conditions needed to obtain a defined solution.

2.2 Elasticity

As introduced in the previous section, in the cold-catalyzed matter hypothesis, the microscopic structure of the crust is a body-centered cubic (bcc) crystal lattice. However, at larger scales the crust is often treated as an isotropic bcc polycrystal, i.e., a crystal composed of different oriented microscopic domains (Chamel & Haensel 2008). The crust properties are found by angle averaging the ones of a bcc lattice properties. In this simple configuration the elastic properties of the crust are fixed by two moduli, the shear modulus μ and the bulk modulus κ, and the stress tensor τ is expressed as (we use the Einstein summation convention)

$$\tau_{ij} = \kappa \left(\partial^i u_i\right) \delta_{ij} + 2\mu \left(u_{ij} - \frac{1}{3} \left(\partial^i u_i\right) \delta_{ij} \right). \tag{2.1}$$

Here we have introduced the displacement field $\boldsymbol{u}$, describing the relative perturbations with respect to the reference position $\boldsymbol{x}$, namely

$$\boldsymbol{r} = \boldsymbol{x} + \boldsymbol{u}(\boldsymbol{x}). \tag{2.2}$$

The deformation energy in this case assumes the form

$$\epsilon_{def} = \frac{1}{2}\kappa \left(\partial^i u_i\right) \left(\partial_i u^i\right) + \mu \left[\frac{1}{2}(\partial^i u_j + \partial^j u_i) - \frac{1}{3} \left(\partial^i u_i\right) \delta_{ij} \right] \left[\frac{1}{2}(\partial_i u^j + \partial_j u^i) - \frac{1}{3} \left(\partial_i u^i\right) \delta^{ij} \right]. \tag{2.3}$$

The bulk modulus can be easily calculated, since it is linked to the adiabatic index value (see 2.3 for details) and the local pressure as

$$\kappa = \gamma P. \tag{2.4}$$

On the other side the exact calculation of the shear modulus is much more complicated; the first attempt to extract an exact value was done by Ogata & Ichimaru (1990) using Monte Carlo simulations. For an ideal cubic crystal lattice there are only three independent elastic moduli, called c_{11}, c_{12} and c_{44} (see Kittel (1996)); however, for a pure shear deformation the deformed energy depends only on c_{44} and on the difference $b_{11} = 1/2\,(c_{11} - c_{12})$. At $T = 0$[1] one has (Ogata & Ichimaru 1990), in agreement with the previous classical result of Fuchs (1936),

$$b_{11} = 0.0245 n_N \frac{(Ze)^2}{R_{cell}} \tag{2.5}$$

$$c_{44} = 0.1827 n_N \frac{(Ze)^2}{R_{cell}}, \tag{2.6}$$

where Z is the number of electrons and R_{cell} is the radius of the Wigner-Seitz cell. Furthermore, by averaging over rotations of the Cartesian axes, one finds an *effective* shear modulus (Fig 2.1)

$$\mu_{eff} = \frac{1}{5}\left(2b_{11} + 3c_{44}\right) = 0.1194 n_N \frac{(Ze)^2}{R_{cell}}. \tag{2.7}$$

[1]The $T = 0$ is a good approximation for the description of crust with temperature below the melting temperature, i.e. $T < 10^8$ K. The melting temperature varies by several orders of magnitude throughout the crust, reaching about 10^9 K in the deepest layers (Chamel & Haensel 2008).

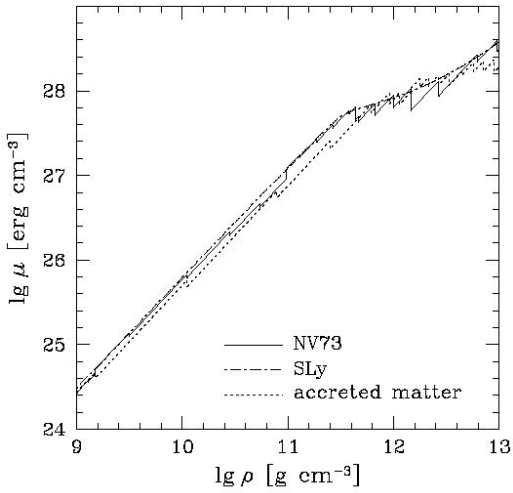

Figure 2.1: Effective shear modulus μ as a function of the crust density, for a bcc lattice configuration. The solid line is obtained for cold catalyzed matter Haensel & Pichon (1994) for the outer crust, and that of Negele & Vautherin (1973) for the inner crust). Also the dash-dotted line is obtained for cold catalyzed matter, but calculated by (Douchin & Haensel 2001). The dotted line indicates the accreted crust model of Haensel & Zdunik (1990). Figure made by A.Y. Potekhin. Credit to Chamel & Haensel (2008).

This approach was recently renewed by Molecular Dynamics (MD) simulations, suggesting that the polycristal domains lead to an effective angle-averaged shear modulus (Horowitz & Kadau 2009; Hoffman & Heyl 2012). The way to obtain the average modulus deserves a comment. Ogata & Ichimaru (1990) used an averaging method firstly proposed by Voigt, that, as shown by (Hill 1952) gives an *upper limit* to μ_{eff}: recently Kobyakov & Pethick (2015) claimed, using a method that gives very good results for terrestrial material, i.e. the self-consistent theory (for a review see (DeWit 2008)), that a more realistic value for the effective shear modulus is 28% smaller than the one obtained by Ogata & Ichimaru (1990). We observe that although all the above formulae are, strictly speaking, valid in the outer crust and therefore are reliable mainly in that region, nearly all the literature uses this approximation also in the the inner crust - mostly for the lack of knowledge of the pasta phase[2]-and we will do the same.

Strohmayer et al. (1991) studied the dependence of the effective shear modulus on temperature, finding that it decreases with increasing temperature, but only weakly.

We have already introduced the nuclear pasta in section 1.3. This layer has very peculiar elastic properties, that are intermediate between solids and liquid: for this reason these kinds of matter is called liquid crystal. Pethick & Pothekhin (1998) were the first to study the elastic properties of pasta, introducing an analytical approach. Recent MD simulation (Caplan et al. 2018) showed that this first model describes well the qualitative elastic response of idealized lasagna plates and, furthermore, showed that the shear modulus of nuclear pasta can be as large as $10^{31}\mathrm{erg/cm}^3$. Such a large value is comparable with the ones obtained by extrapolating the shear modulus behaviour of the outer crust to the high densities of the core-crust boundary. However, these are still very pre-

[2]The elastic properties of the inner crust may also differ from those of the outer crust due to the presence of the neutron superfluid (Kobyakov & Pethick 2014, 2016)

liminary results. In fact, these molecular dynamics simulations are purely classical and, moreover, the interactions between nucleons are very simplified.

2.2.1 Strain angle and breaking strain

The strain tensor is obtained from the displacement field via (Landau & Lifshitz 1970)

$$\sigma_{ij} = \frac{1}{2}\left(\frac{\partial u_i}{\partial x_j} + \frac{\partial u_j}{\partial x_i}\right) . \tag{2.8}$$

In order to study the breaking of the elastic crust a failure criterion is needed. We assume the widely used Tresca failure criterion; we thus introduce the *strain angle* $\alpha(r, \theta)$, the local quantity defined as the difference between the maximum and minimum eigenvalues of the strain tensor at a specific point. The Tresca criterion assumes that, locally, the elastic behavior of a material ceases when the strain angle approaches a particular threshold value σ^{Max}, known as the *breaking strain*

$$\alpha \approx \frac{1}{2}\sigma^{Max} . \tag{2.9}$$

Smoluchowski & Welch (1970) estimated that in the lower neutron star crust the breaking strain could be in the range $10^{-5} - 10^{-3}$, an idea confirmed by Ruderman (Ruderman 1969, 1976) who proposed that for the crust as a whole an effective σ^{Max} as small as 10^{-4} to 10^{-5} should be plausible. Thompson & Duncan (1995) argued that the soft gamma-ray events are triggered by the cracking of the crust and thus the maximum energy released implies (in a model-dependent way) that the maximum strain is in the $10^{-2} - 10^{-3}$ range.

On the other side, a simple estimation for a perfect one-component crystal gives the larger values of $10^{-2} - 10^{-1}$ Kittel (1996); however this value was thought to be only a theoretical upper limit, since an effective value of σ^{Max} depends on the weakest places over the entire crust. Interestingly, Baiko & Chugunov (2018) recently found that the maximum strain for the stretch deformation sustainable by a polycrystalline crust is ~ 0.04. The use of multimillion MD both for accreted (Horowitz & Kadau 2009) and non accreted (Hoffman & Heyl 2012) crusts, gives an estimate that agrees with this latter values. In particular, these works found that the crust rather than yielding continuously at low strain as metals do on Earth, fails suddenly in a collective manner at a large strain 10^{-1}. This failure mechanism also inhibits the formation of voids or fracture to appear: simulations starting out with a cylindrical hole into a crystal show that the void quickly heals under the influence of the enormous pressure of the system, confirming the theoretical prediction of Jones (2003) that voids would not form because of the high pressure.

Horowitz & Kadau (2009) found that the breaking strain is only moderately affected by the introduction of impurities, defects and grain boundaries. However, for non accreting neutron star crusts Hoffman & Heyl (2012) found a different result: the comparison between a "perfect" bcc lattice and another with some inhomogeneities showed different shear modulus and yield strain: this effect should be due to the number of defects or grain boundaries (Fig 2.2). Furthermore, the study of a second break after the first yield event show that the crystal behaviour is similar to the one of the imperfect crystal (Fig 2.3). On the other side, below the melting temperature the breaking strain is essentially not affected by the crustal temperature.

Finally, contrary to accreted crust case, where simulations show essentially no size effect for the single crystal deformation, Hoffman & Heyl (2012) found that larger samples yield at lower breaking strain with respect to the smaller ones.

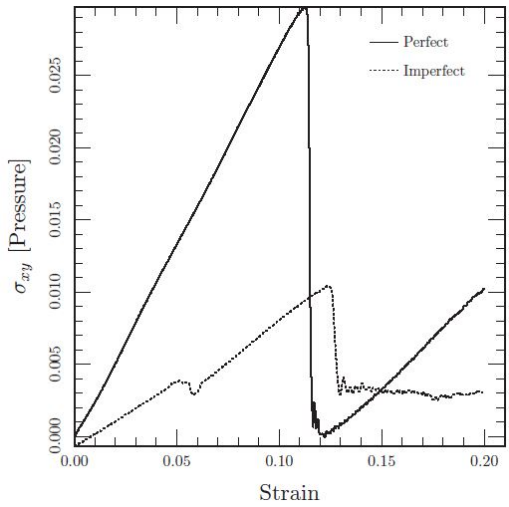

Figure 2.2: Comparison of the stress–strain relationships of a perfect and an imperfect crystal. For both simulation a strain rate was applied of 20×10^{-6} in the X direction. Pressure is normalized. Credit to Hoffman & Heyl (2012).

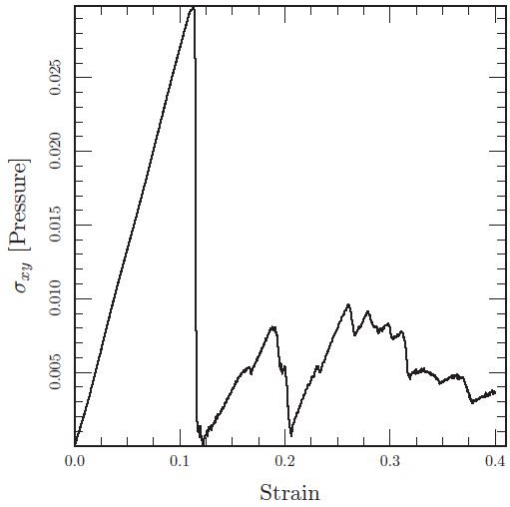

Figure 2.3: The stress–strain relationship for a pure iron bcc crystal of 31250 particles. A strain rate of 20×10^{-6} was applied in the X direction. The simulation box was deformed to a maximum strain of 0.4 in order to investigate the occurrence of a second material failure. The second yielding event occurs between a strain of 0.133 and 0.186. Credits to Hoffman & Heyl (2012).

Note that the strength of the crust is expected to be larger for higher density, since it is essentially linked to the Coulomb interactions between ions. However, the actual MD simulations ignored the contribution of the neutron superfluid above the neutron saturation density (see 1.3). The interaction between the ions and the superfluid can change the structure of the lattice (Kobyakov & Pethick 2015) but MD simulation have shown that the crust strength of a bcc and fcc lattice is almost the same. The situation becomes more intriguing when one tries to estimate the yield strain of the pasta phase, where the competition between the Coulomb repulsion and the strong nuclear interaction becomes important. The first study of the elasticity of nuclear pasta by Pethick & Pothekhin (1998), that considered the energy of deformation of parallel pasta plates, depends only on two elastic parameters. Unfortunately their analytic techniques are difficult to apply to asymmetric pasta or pasta lacking long range order. For this reason, MD simulations has been used to study the pasta behaviour, suggesting that the pasta, like the ion crust, does not have a uniform orientation across the star. Thus also the pasta layer is "polycrystalline" in the sense that is composed of many microscopic domains with distinct orientations. Using MD simulations Caplan et al. (2018) found that idealized nuclear pasta in the lasagna and waffle phase has a very large breaking strain of about 0.3.

Hence, to take into account the large uncertainties on the breaking strain, in this thesis work we will consider physically acceptable values of σ^{Max} in the whole range $10^{-5} \div 10^{-1}$. Furthermore, we assume a constant value for the breaking strain since, accordingly to our current understanding, it should have only a small dependence on impurities and defects, and on temperature, at least if we are well below the melting temperature, see (Horowitz & Kadau 2009).

2.3 The bulk modulus and the response of matter

Following the standard description for cold catalyzed matter in a NS interior, we consider here a barotropic EoS of the kind $P(n_b)$, $\rho(n_b)$, where P is the local pressure, ρ is the star density and n_b is the local baryon density.

The pressure can be obtained as

$$P\left(n_b\right) = n_b^2 \frac{d}{dn_b} \frac{E\left(n_b\right)}{n_b}\,, \tag{2.10}$$

where $E\left(n_b\right)$ the ground state energy density. The equation of state for matter in chemical equilibrium is characterized by the adiabatic index γ_{eq}, defined as

$$\gamma_{eq}(n_b) = \frac{n_b}{P} \frac{\partial P\left(n_b\right)}{\partial n_b}. \tag{2.11}$$

Hence, γ_{eq} can be used to describe pressure-density perturbations whose dynamics is very slow with respect to the typical timescales of the reactions[3] that carry the system towards the full thermodynamic equilibrium.

The opposite limit, in which all the chemical reactions are so slow that they can be considered frozen, is also interesting for astrophysical studies. However, in this case the relation Eq (2.11) cannot be used to define the proper adiabatic index which regulates the pressure-density perturbations. The corresponding adiabatic index γ_f, where the

[3] In other words, γ_{eq} is the index that correctly describes perturbations to the reference configuration when the typical timescale of the dynamical process considered is orders of magnitude larger than that of all the relevant nuclear and electroweak reactions.

subscript f stands for *frozen*, now depends also on the chemical fractions x_i for the i-species of particles (neutrons,electrons, protons...):

$$\gamma_f(n_b, x_i) = \frac{n_b}{P}\frac{\partial P\left(n_b, x_i\right)}{\partial n_b}\,, \tag{2.12}$$

where the derivative is carried out at fixed x_i values (Haensel et al. 2002). Clearly, in this case the elastic response of the star will be different from the previous case since matter does not have enough time to reach the complete thermodynamic equilibrium in the meanwhile stresses build-up. This is a well-known problem, already discussed in many papers involving stellar pulsations (Meltzer & Thorne 1966; Chanmugam 1977; Gourgoulhon et al. 1995; Haensel et al. 2002) and thermal fluctuation in accreting neutron stars (Ushomirsky et al. 2000)[4]. Furthermore, Yakovlev et al. (2006) estimate that the equilibration timescale involving modied URCA processes scales as $\sim (2\mathrm{months})/\mathrm{T}_9^6$, where T_9 is the internal temperature in units of 10^9K. Hence, due to the strong dependence on the temperature of the star, the rotation-induced stresses that can develop on the timescale of years in a mature spinning-down (or spinning-up) NSs should be calculated by taking into account that the adiabatic index for perturbations of matter may differ from γ_{eq}.

In addition to the equilibrium and frozen adiabatic indices, we introduce also the concept of *effective* adiabatic index; let us consider the initial density

$$\rho_0 = \rho_0\left(P_0, s_0, x_i\right), \tag{2.13}$$

as function of the initial pressure P_0, entropy s_0 and the set of chemical fractions x_i. In the previous expressions we assumed matter in its ground-state, i.e. in a state of zero entropy. The gradient of (2.13) is

$$\boldsymbol{\nabla}\rho_0 = \left[\left.\frac{\partial\rho_0}{\partial P_0}\right|_{s_0,x_i}\partial_r P_0 + \left.\frac{\partial\rho_0}{\partial s_0}\right|_{P_0,x_i}\partial_r s_0 + \left.\frac{\partial\rho_0}{\partial x_i}\right|_{P_0,s_0}\partial_r x_i\right]\boldsymbol{e}_r, \tag{2.14}$$

where we used the spherical symmetry of the unperturbed configuration. Using equations (2.19) and (2.11) we can recast Eq (2.14) as

$$\partial_r\rho_0 = -\frac{\rho_0^2 g}{P_0}\left(\frac{1}{\gamma_{eq}} - \frac{1}{\delta\gamma}\right) = -\frac{\rho_0^2 g}{\gamma P_0}. \tag{2.15}$$

where we have highlighted the presence of γ_{eq} plus a departure $\delta\gamma$. This equation is an implicit definition of the *effective* adiabatic index γ

$$\gamma = -\frac{\rho_0^2 g}{P\partial_r\rho_0}. \tag{2.16}$$

The first term in the brackets of Eq (2.15) shows how the initial density profile of the star is characterized by a given adiabatic index: a finite value of γ_{eq} yields a negative density gradient $\partial_r\rho_0$ so that the initial density increases with depth, accordingly to compression of the NS due to its own weight (self-compression). The second term, on the other hand,

[4] In this case we have different processes, with different timescales, competing against each other, such as accretion, local equilibrium reactions, thermal diffusion and buoyancy equilibrium. Thus, the crust stratification is continuously changed, with the probable formation of local inhomogeneities. This is reflected in a non-adiabatic response of matter.

represents the departure from the self-compression due to non-adiabatic and chemically heterogeneous stratifications. We call *compressional* a stratification that is adiabatic and chemically homogeneous (Cambiotti & Sabadini 2010; Cambiotti et al. 2013).

Once we have chosen a specific EoS, we calculate the initial unstressed configuration in a Newtonian framework, obtaining the radial profiles $P(r)$ and $\rho(r)$ via Eqs (2.19) and (2.20). In this state the pressure-density relation supporting the star is characterized by the equilibrium adiabatic-index of Eq (2.11). However, once the loads and rotation are turned on, the response of the star will depend on the dynamical timescale proper of each external force: only in the case of a very slow evolution of the stresses it is possible to use γ_{eq}. In this sense we characterize the initial unstressed configuration by the equilibrium adiabatic index, while the choice of γ_f or γ_{eq} will be be used to describe different astrophysical scenarios, depending only on the star's response to external forces.

In this work, in order to maintain consistence with our Newtonian analysis and to study rigorously the importance of possible deviations of the adiabatic index from the value γ_{eq}, we use a polytropic EoS with polytropic index $n = 1$[5],

$$P(\rho) = K\rho^2 = Km_n^2 n_b^2 , \tag{2.17}$$

so that the adiabatic index is not a function of the density n_b, but takes a constant value

$$\gamma_{eq} = \frac{\rho}{K\rho^2}\frac{\partial\left(K\rho^2\right)}{\partial\rho} = 2 . \tag{2.18}$$

On the other hand, we have little clues about the actual value of the frozen adiabatic index: typically γ_f is larger than γ_{eq} (Meltzer & Thorne 1966; Chanmugam 1977; Haensel et al. 2002; Ushomirsky et al. 2000), but the actual relation between them strongly depends on the microscopic model underlying the specific EoS.However, from the practical point of view, the uncertain value of γ_f is not a strong limitation: we will assume different values and study how the estimated stress and strain change, starting from values that differ by only some percent from γ_{eq}, up to the incompressible limit, namely $\gamma_f \gg \gamma_{eq}$. Since for most of the EoSs the main differences between the equilibrium and the frozen adiabatic index are expected to be in the crust (Ushomirsky et al. 2000), we choose to change the value of γ just there.

We stress that for any realistic EoS, γ_{eq} and γ_f have a complex dependence on the local properties of matter (see e.g. Douchin & Haensel 2001; Haensel et al. 2002). However, since equilibrium adiabatic index given by Eq (2.18) is constant, we will assume a constant γ_f in the elastic layer as well.

2.4 Main Equations

We assume that the star can be divided into an internal, fluid core, topped by a number N of stratified layers with different elastic properties.

We start by considering an unperturbed, non rotating NS, characterized by a density ρ_0, hydrostatic pressure P_0 and gravitational potential ϕ_0. In this configuration the crust is unstressed and the momentum and Poisson equations are

$$\boldsymbol{\nabla} P_0 + \rho_0 \boldsymbol{\nabla}\phi_0 = 0 \tag{2.19}$$

$$\nabla^2\phi_0 = 4\,\pi\,G\,\rho_0 . \tag{2.20}$$

[5]This is quite a common choice in the literature, see for example in Ushomirsky et al. (2000) and Haskell et al. (2006)

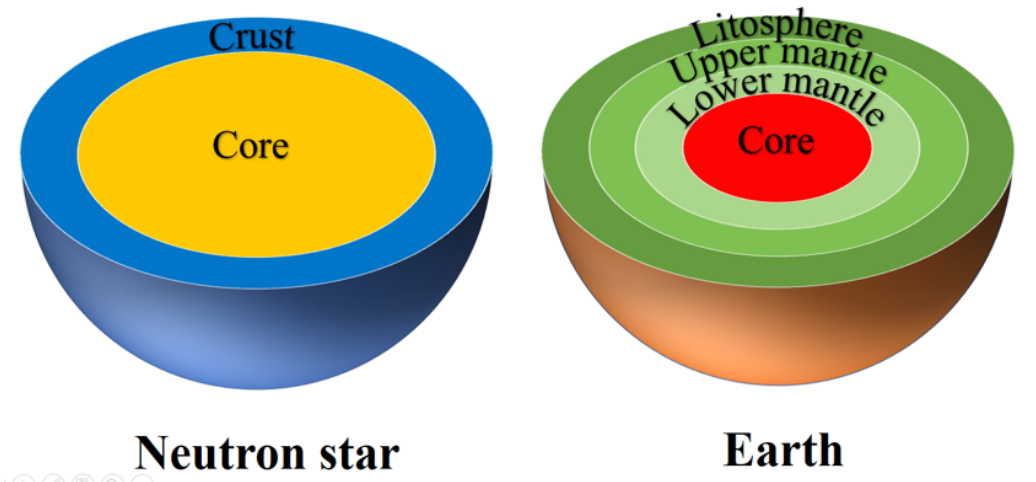

Figure 2.4: We model a NS as an object with only two layers: a fluid core and an elastic crust. However, the proposed equations allow to introduce an arbitrary large number N of elastic layers: better comprehension of the elastic properties of a NS crust will allow to introduce additional layers. Our model allows to treat continuous stratification of both density and elastic coefficients.

The previous equations defines the initial state of hydrostatic equilibrium for a non-rotating star: the functions P_0, ρ_0 and ϕ_0 are function only on the spherical radial distance r. Taking this hydrostatic configuration we can introduce a displacement field $\boldsymbol{u}$ which describes perturbations with respect to the reference position $\boldsymbol{x}$, namely

$$\boldsymbol{r} = \boldsymbol{x} + \boldsymbol{u}(\boldsymbol{x})\,, \tag{2.21}$$

where $\boldsymbol{x}$ and $\boldsymbol{r}$ are the initial and the perturbed positions of the infinitesimal matter elements respectively. Hence, the total Cauchy stress tensor, describing surface forces, can be expressed as

$$\boldsymbol{\tau}(\boldsymbol{r}) = -P_0(\boldsymbol{x})\,\mathbf{1} + \boldsymbol{\tau}^{\delta}(\boldsymbol{x})\,. \tag{2.22}$$

In this work, following the notation described in (Sabadini et al. 2016): for a generic quantity f, the "local increment" f^{Δ} coincides with what is usually called Eulerian change (see e.g. Shapiro & Teukolsky 1983). On the other hand, the Lagrangian changes of f are dubbed "material increments" and are indicated by f^{δ}. We indicate with $\mathbf{1}$ the identity tensor and with $\boldsymbol{\tau}^{\delta}$ the material stress given by Hooke's law (cf. Eq (2.1)) (Love 1934; Landau & Lifshitz 1970; Sabadini et al. 2016)

$$\boldsymbol{\tau}^{\delta} = (\kappa - 2/3\,\mu)\,(\boldsymbol{\nabla}\cdot\boldsymbol{u})\mathbf{1} + \mu\,\left(\boldsymbol{\nabla}\boldsymbol{u} + (\boldsymbol{\nabla}\boldsymbol{u})^{T}\right)\,, \tag{2.23}$$

κ and μ being the bulk and shear moduli respectively. The transpose operation is indicated as usual by the superscript T.

Many NS are in binary systems, therefore, in general, we are also interested in the tidal effect by the star's companion. If we include this contribution the equilibrium (2.19) and Poisson (2.20) equations become

$$\boldsymbol{\nabla}\cdot\boldsymbol{\tau}-\rho\,\boldsymbol{\nabla}\Phi+\boldsymbol{h}=0 \tag{2.24}$$
$$\nabla^2\Phi=4\,\pi\,G\,(\rho+\rho^t)+2\,\Omega^2 \tag{2.25}$$

where $\boldsymbol{h}$ are the non-conservative body forces, and ρ, ρ^t are the density of the NS and of the companion respectively. The potential Φ encodes all the conservative body forces and can be split as

$$\Phi=\phi+\phi^C+\phi^t \tag{2.26}$$

with ϕ being the gravitational potential due to the density distribution of the NS, ϕ^t the one due to the companion (also called *tidal* potential) and ϕ^C, the centrifugal potential.[6]

2.5 Perturbations and spherical harmonics expansion

Let us introduce the local incremental density ρ^Δ and the total potential Φ^Δ of the NS

$$\rho(\boldsymbol{r})=\rho_0(\boldsymbol{r})+\rho^\Delta(\boldsymbol{r}) \tag{2.27}$$
$$\Phi(\boldsymbol{r})=\Phi_0(\boldsymbol{r})+\Phi^\Delta(\boldsymbol{r}) \tag{2.28}$$

The first is related to the displacement $\boldsymbol{u}$ via mass conservation

$$\rho^\Delta=-\boldsymbol{\nabla}\cdot(\rho_0\,\boldsymbol{u}), \tag{2.29}$$

while the other is the local *incremental* potential

$$\Phi^\Delta=\phi^\Delta+\phi^c+\phi^t\,, \tag{2.30}$$

which includes the incremental gravitational potential of the NS. The centrifugal and tidal potential have only incremental contributions, since the star's unperturbed reference configuration is the one of an isolated, non rotating pulsar.

Using the definitions provided in Eqs (2.23), (2.27), (2.28) and performing a linear expansion in the displacement field (i.e. neglecting all the non-linear terms in the perturbed quantities), after substitution of Eqs (2.19) and (2.20) into Eqs (2.24) and (2.25) and making use of (2.29) we obtain the incremental momentum and Poisson equations

$$\boldsymbol{\nabla}\cdot\boldsymbol{\tau}^\delta-\boldsymbol{\nabla}\cdot(\rho_0\,\boldsymbol{u}\cdot\boldsymbol{\nabla}\phi_0)+\boldsymbol{\nabla}\cdot(\rho_0\,\boldsymbol{u})\,\boldsymbol{\nabla}\phi_0-\rho_0\,\boldsymbol{\nabla}\Phi^\Delta+\boldsymbol{h}=0 \tag{2.31}$$
$$\nabla^2\Phi^\Delta=4\,\pi\,G\,(-\boldsymbol{\nabla}\cdot(\rho_0\,\boldsymbol{u})+\rho^t)+2\,\Omega^2\,. \tag{2.32}$$

In our case of a nearly spherical body, the symmetry of the problem simplifies the treatment of the above equations: we introduce the usual spherical coordinate system $\{r,\theta,\varphi\}$, that are the radial distance from the center of the NS, the colatitude and the longitude of a point respectively. Hence, we expand the potential Φ^Δ and the displacement $\boldsymbol{u}$ in spherical harmonics (see Appendix A for the conventions used). We observe that due to the symmetry of the initial hydrostatic configuration the elastic parameters κ and μ are functions of the coordinate r only.

Thanks to the expansion in spherical harmonics $Y_{\ell m}$ and some amount of algebra, finally Eq (2.31) can be rearranged as

[6] For an uniform rotating star with angular velocity Ω, $\nabla^2\phi^C=2\,\Omega^2$.

$$-\rho_0\partial_r\Phi_{\ell m}-\rho_0\partial_r\left(gU_{\ell m}\right)+\rho_0 g\chi_{\ell m}+\partial_r\left[\left(\kappa-\frac{2}{3}\mu\right)\chi_{\ell m}+2\mu\partial_r U_{\ell m}\right]+$$
$$\frac{1}{r^2}\mu\left[4r\partial_r U_{\ell m}-4U_{\ell m}+\ell\left(\ell+1\right)\left(3V_{\ell m}-U_{\ell m}-r\partial_r V_{\ell m}\right)\right]+h^R_{\ell m}=0 \quad (2.33)$$

$$-\frac{\rho_0}{r}\Phi_{\ell m}-\frac{\rho_0}{r}gU_{\ell m}+\frac{\left(\kappa-\frac{2}{3}\mu\right)}{r}\chi_{\ell m}+\partial_r\left[\mu\left(\partial_r V_{\ell m}+\frac{1}{r}U_{\ell m}-\frac{1}{r}V_{\ell m}\right)\right]+$$
$$\frac{1}{r^2}\mu\left[5U_{\ell m}+3r\partial_r V_{\ell m}-V_{\ell m}-2\ell\left(\ell+1\right)V_{\ell m}\right]+h^S_{\ell m}=0, \quad (2.34)$$

$$\partial_r\left[\mu\,\partial_r W_{\ell m}-\frac{\mu\,W_{\ell m}}{r}\right]+\frac{3\mu}{r}\partial_r W_{\ell m}-\frac{1+\ell\left(\ell+1\right)}{r^2}\mu W_{\ell m}+h^T_{\ell m}=0\,. \quad (2.35)$$

In the above equations $U_{\ell m}$, $V_{\ell m}$ and $W_{\ell m}$ are the radial, tangential and toroidal displacements, $h^R_{\ell m}, h^S_{\ell m}, h^T_{\ell m}$, are the spherical expansion components of the non-conservative forces and the scalars $\chi_{\ell m}$ are linked to the volume change according to

$$\boldsymbol{\nabla}\cdot\boldsymbol{u}=\sum_{\ell=0}^{\infty}\sum_{m=-\ell}^{\ell}\chi_{\ell m}Y_{\ell m}\,, \quad (2.36)$$

where the scalar $\chi_{\ell m}$ is

$$\chi_{\ell m}=\partial_r U_{\ell m}+\frac{2}{r}U_{\ell m}-\frac{\ell\left(\ell+1\right)}{r}V_{\ell m}. \quad (2.37)$$

The radial (2.33) and tangential (2.34) components of the equilibrium equations are called *spheroidal equations* while the third component (2.35) is called *toroidal equation*. With a similar treatment the Poisson equation (2.32) becomes

$$\nabla^2_r\Phi_{\ell m}=-4\pi G\left(\rho_0\chi_{\ell m}+U_{\ell m}\partial_r\rho_0\right)+4\pi G\rho^t_{\ell m}\,, \quad (2.38)$$

where

$$\nabla^2_r=\partial_r+\frac{2}{r}\partial_r-\frac{\ell\left(\ell+1\right)}{r^2} \quad (2.39)$$

and $\rho^t_{\ell m}$ are the density spherical harmonics coefficients of the NS companion. The Eqs (2.33, 2.34, 2.35, 3.3) hold only for $\ell>0$; the case $\ell=0$ needs a specific treatment, as shown in detail in the following, see 2.9.

Furthermore, we stress that the toroidal equation (2.35) is decoupled from Eqs (2.33, 2.34, 3.3). This fact allows us to neglect, in all the situation studied in these work thesis, the toroidal equation. In fact only some kind of non-conservative forces, having non-axial symmetry, can have an impact on the toroidal equation (Sabadini et al. 2016).

2.6 Spheroidal deformations

The remaining three equations, i.e. the spheroidal equations (2.33, 2.34 and the Poisson equation 3.3) are second order differential equations in $U_{\ell m}$, $V_{\ell m}$ and $\Phi_{\ell m}$, respectively. For this reason it is very useful to recast them into six differential equations of the first order. For this purpose, we introduce the spheroidal 6-vector solution $\boldsymbol{y}_{\ell m}$

$$\boldsymbol{y}_{\ell m} = \left(U_{\ell m}, V_{\ell m}, R_{\ell m}, S_{\ell m}, \Phi_{\ell m}, Q_{\ell m}\right)^T . \tag{2.40}$$

As shown in Appendix A, the meaning of the six components is as follows: the first and the second components are the radial and tangential displacements, the third and the fourth the radial and tangential stresses. The fifth component is the total potential while the sixth, named *potential stress* $Q_{\ell m}$, is defined by

$$Q_{\ell m} = \partial_r \Phi_{\ell m} + \frac{\ell+1}{r}\Phi_{\ell m} + 4\pi G \rho_0 U_{\ell m} . \tag{2.41}$$

Thanks to the definition (2.40), the whole system of equations ((2.33), (2.34), 3.3) can be written in the elegant and compact form

$$\frac{d\boldsymbol{y}_{\ell m}}{dr} = \boldsymbol{A}_\ell\left(r\right)\boldsymbol{y}_{\ell m}\left(r\right) - \boldsymbol{h}_{\ell m}\left(r\right). \tag{2.42}$$

Here we introduced the 6×6 matrix $\boldsymbol{A}_\ell$, which contains the stellar characteristic elastic quantities (the bulk modulus and the shear modulus) and the initial configuration profiles for the density and the gravitational acceleration field, where $\beta = \kappa + \frac{4}{3}\mu$ and λ is the Lamè coefficient $\lambda = \kappa - \frac{2}{3}\mu$:

$$A_\ell\left(r\right) = \begin{pmatrix} -\frac{2\lambda}{r\beta} & \frac{\ell(\ell+1)\lambda}{r\beta} & \frac{1}{\beta} & 0 & 0 & 0 \\ -\frac{1}{r} & \frac{1}{r} & 0 & \frac{1}{\mu} & 0 & 0 \\ \frac{4}{r}\left(\frac{3\kappa\mu}{r\beta} - \rho_0 g\right) & \frac{\ell(\ell+1)}{r}\left(\rho_0 g - \frac{6\kappa\mu}{r\beta}\right) & -\frac{4}{r}\frac{\mu}{\beta} & \frac{\ell(\ell+1)}{r} & -\frac{\rho_0(\ell+1)}{r} & \rho_0 \\ \frac{1}{r}\left(\rho_0 g - \frac{6}{r}\frac{\mu\kappa}{\beta}\right) & \frac{2\mu}{r^2}\left[\ell\left(\ell+1\right)\left(1+\frac{\lambda}{\beta}\right) - 1\right] & -\frac{\lambda}{r\beta} & -\frac{3}{r} & \frac{\rho_0}{r} & 0 \\ -4\pi G\rho_0 & 0 & 0 & 0 & -\frac{\ell+1}{r} & 1 \\ -\frac{4\pi G\rho_0(\ell+1)}{r} & \frac{4\pi G\rho_0\ell(\ell+1)}{r} & 0 & 0 & 0 & \frac{\ell-1}{r} \end{pmatrix}. \tag{2.43}$$

Finally, the non-homogeneous term $\boldsymbol{h}_{\ell m}$ in equation (2.42), which contains the non-conservative forces radial and tangential contributions, is

$$\boldsymbol{h}_{\ell m} = \left(0, 0, h^R_{\ell m}, h^S_{\ell m}, 0, 0\right)^T . \tag{2.44}$$

2.7 Boundary conditions

In order to solve Eq (2.42) we have to impose some boundary conditions. First we assume that matter does not cross the interface between two elastic layers; and second

that all the spheroidal vector solutions are continuous across the boundaries between different layers, say at $r = r_j$, so that (Sabadini et al. 2016)

$$\boldsymbol{y}_{\ell m}\left(r_j^-\right) = \boldsymbol{y}_{\ell m}\left(r_j^+\right) \ . \tag{2.45}$$

This continuity requirement gives us a straightforward way to impose simply boundary conditions at the surface-vacuum and at the core-crust boundary.

2.7.1 Surface-vacuum boundary

Let a be the stellar radius. The behaviour of the spheroidal solution at the boundaries suggests us three simple conditions. The first is that the potential stress (2.41) must be continuous across the interface at $r = a$, i.e.

$$Q_{\ell m}\left(a^-\right) = Q_{\ell m}\left(a^+\right) \ . \tag{2.46}$$

To implement the condition (2.46) in our model, let us first expand the centrifugal potential as (Sabadini et al. 2016)

$$\phi^c\left(r,\theta,\varphi\right) = \phi^c_{00}\left(r\right) Y_{00}\left(\theta,\varphi\right) + \sum_{m=-2}^{2} \phi^c_{2m}\left(r\right) Y_{2m}\left(\theta,\varphi\right) \ , \tag{2.47}$$

where

$$\phi^c_{00}\left(r\right) = -\frac{\Omega^2 r^2}{3} \tag{2.48}$$

and

$$\phi^c_{2m}\left(r\right) = \frac{\Omega^2 r^2}{3}\frac{(2-m)!}{(2+m)!} Y_{2m}\left(\theta,\varphi\right) \ , \tag{2.49}$$

while the other harmonic coefficients of the expansion are zero:

$$\phi^c_{\ell m} = 0 \quad \text{for} \quad \ell = 1, 3 ... \infty. \tag{2.50}$$

Neglecting for the moment the $\ell = 0$ term, whose resolution is discussed in section 2.9, we can assume

$$\phi^c_{\ell m}\left(r\right) = \phi^c_{\ell m}\left(a\right)\left(\frac{r}{a}\right)^{\ell} . \tag{2.51}$$

The expansion of the gravitational and tidal potential is easy, since the Poisson equation (2.32) reduces to the Laplace equation in the region between the NS and the body exerting the tidal force, placed at radius a^{t}. By imposing the regularity conditions for $r \to \infty$ and $r \to 0$, we obtain

$$\phi^{\Delta}_{\ell m}\left(r\right) = \phi^{\Delta}_{\ell m}\left(a\right)\left(\frac{r}{a}\right)^{-\ell-1} \qquad r > a \tag{2.52}$$

$$\phi^{t}_{\ell m}\left(r\right) = \phi^{t}_{\ell m}\left(a\right)\left(\frac{r}{a}\right)^{\ell} \qquad r < a^{\mathrm{t}}. \tag{2.53}$$

Thanks to the expansions in Eqs (2.51, 2.52, 2.53), we obtain the general form of the expression in Eq (2.46) as

$$Q_{\ell m}\left(a^-\right) = \frac{2\ell+1}{a}\left[\phi^c_{\ell m}\left(a^+\right) + \phi^t_{\ell m}\left(a^+\right)\right] \ , \tag{2.54}$$

where we used the relation

$$\partial_r \Phi^G_{\ell m}\left(a^+\right) = -\frac{\ell+1}{a}\Phi^G_{\ell m}\left(a\right), \tag{2.55}$$

to cancel the gravitational potential terms.

Besides Eq (2.54), we impose that the tangential stress $S_{\ell m}$ must be zero in vacuum,

$$S_{\ell m}\left(a^-\right) = 0\,. \tag{2.56}$$

The same is valid for the radial stress $R_{\ell m}$ since the pressure outside the star is zero,

$$R_{\ell m}\left(a^-\right) = 0\,. \tag{2.57}$$

The three conditions (2.54, 2.56, 2.57) can be rearranged in the compact form

$$\boldsymbol{P}_1 \boldsymbol{y}\left(a^-\right) = \boldsymbol{b} \tag{2.58}$$

where $\boldsymbol{P}_1$ is the projector that selects only the third, fourth and sixth components of the spheroidal vector solution $\boldsymbol{y}$ and the vector $\boldsymbol{b}$ is defined as

$$\boldsymbol{b} = \begin{pmatrix} 0 \\ 0 \\ -\frac{(2\ell+1)}{a}\left(\phi^c_{\ell m} + \phi^t_{\ell m}\right) \end{pmatrix}. \tag{2.59}$$

2.7.2 Core-Crust boundary

In our model the core is fluid and inviscid, so that it cannot support deviatoric stresses. Also across the core-crust boundary we can use the continuity of the spheroidal vector but, differently with respect to the previous case, we have to allow for a free slip at the interface (i.e. the core can slip under the crust). This request implies that

$$\boldsymbol{y}(r_c^+) = \begin{pmatrix} U_{\ell m}\left(r_c^-\right) \\ 0 \\ R_{\ell m}\left(r_c^-\right) \\ 0 \\ \Phi_{\ell m}\left(r_c^-\right) \\ Q_{\ell m}\left(r_c^-\right) \end{pmatrix} + \begin{pmatrix} 0 \\ C_2 \\ 0 \\ 0 \\ 0 \\ 0 \end{pmatrix}, \tag{2.60}$$

where r_c is the core-crust radius and C_2 is a constant of integration describing the tangential displacement. The vector solution in the core can be easily found; let us see how.

By setting $\mu = 0$ and omitting the terms related to the loading of the crust, Eqs (2.33) and (2.34) can be rearranged as

$$\frac{\partial_r R_{\ell m}}{\rho_0} - \partial_r\left(g U_{\ell m}\right) + g\chi_{\ell m} - \partial_r \Phi_{\ell m} = 0 \tag{2.61}$$

$$\frac{R_{\ell m}}{\rho_0} - g U_{\ell m} - \Phi_{\ell m} = 0\,. \tag{2.62}$$

Inserting these two equations into the Poisson one (3.3), we obtain

$$\nabla^2_r \Phi_{\ell m} = 4\pi G \partial_r \rho_0 \frac{\Phi_{\ell m}}{g}\,. \tag{2.63}$$

Since $\partial_r \rho_0 = 0$ must hold at the center of the star, the regularity of the potential at $r = 0$ implies

$$\lim_{r\to 0} r^{-\ell}\psi_{\ell m}(r) = 1\,, \tag{2.64}$$

with $\Phi_{\ell m}(r) = C_1\psi_{\ell m}(r)$. This proportionality relation will be particularly convenient and useful in the following calculation.

Subtracting the radial derivative of Eq (2.62) from (2.61), and using the relation

$$R_{\ell m} = \kappa\chi_{\ell m}, \tag{2.65}$$

valid in the fluid limit, we obtain the so-called Adams-Williamson relation (Cambiotti & Sabadini 2010; Cambiotti et al. 2013),

$$\frac{\kappa}{\rho_0^2}\left(\partial_r\rho_0 + \frac{\rho_0^2 g}{\gamma P}\right)\chi_{\ell m} = 0\,, \tag{2.66}$$

that can be equivalently written using Eq (2.15), as

$$\frac{\kappa}{\rho_0^2}\frac{\partial_r\rho_0}{\gamma}\left(\gamma - \gamma_{eq}\right)\chi_{\ell m} = 0\,. \tag{2.67}$$

Clearly, when the stratification is compressional (i.e. $\gamma = \gamma_{eq}$, see section 3), the above equation is automatically satisfied. This case is of interest for the study of a neutron star that gradually changes its state of rotation: the dynamical timescales of both spin-up or spin-down are large enough to allow for an elastic response at chemical equilibrium. Therefore, the two Eqs (2.61) and (2.62) are not linearly independent, providing a way to constrain the radial stress at the core-crust interface. In fact, at $r = r_c$ Eq (2.62) can be written as

$$R_{\ell m}(r_c) = \rho_0(r_c)g(r_c)\left[U_{\ell m}(r_c) - \left(-\frac{\Phi_{\ell m}(r_c)}{g(r_c)}\right)\right] = \rho_0 g C_3\,, \tag{2.68}$$

where the constant of integration C_3 indicates the difference between the radial displacement $U_{\ell m}$ and the geoid displacement at $r = r_c$

$$U_{\ell m}^{geoid} = -\frac{\Phi_{\ell m}(r)}{g(r)}. \tag{2.69}$$

Note that in the case of compressional stratification the volume change within the core is undetermined: below the core-crust interface we cannot specify the displacement and radial stresses with the above assumptions. However, this does not constitute a problem because we are interested only in the deformation of the crust, which is uniquely determined by the boundary conditions. The constants C_1, C_2, C_3 define the solution in the fluid core, calculated at the core-crust boundary, that can be written as

$$y_{\ell m}^{Core}(r_c) = \begin{pmatrix} -C_1 + \frac{\psi_{\ell m}}{g} + C_3 \\ C_2 \\ \rho_0 g C_3 \\ 0 \\ C_1\psi_{\ell m} \\ C_1 q_{\ell m} + 4\pi G\rho_0 C_3 \end{pmatrix}, \tag{2.70}$$

where we have defined

$$q_{\ell m} = \partial_r \psi_{\ell m} + \frac{\ell+1}{r}\psi_{\ell m} - \frac{4\pi G}{g}\psi_{\ell m}\,. \tag{2.71}$$

The core-crust boundary condition (2.60) can thus be written in the compact form

$$\boldsymbol{y}_{\ell m}\left(r_c^+\right) = \boldsymbol{I_C}\boldsymbol{C}\,, \tag{2.72}$$

where $\boldsymbol{I}_C$ is the 6×3 matrix

$$\boldsymbol{I}_C = \begin{pmatrix} -\psi_\ell\left(r_c\right)/g\left(r_c\right) & 0 & 1 \\ 0 & 1 & 0 \\ 0 & 0 & g\left(r_c\right)\rho_0\left(r_c^-\right) \\ 0 & 0 & 0 \\ \psi_\ell\left(r_c\right) & 0 & 0 \\ q_\ell\left(r_c\right) & 0 & 4\pi G\rho_0\left(r_c^-\right) \end{pmatrix} \tag{2.73}$$

and $\boldsymbol{C}$ is the 3-vector

$$\boldsymbol{C} = \left(C_1, C_2, C_3\right). \tag{2.74}$$

2.8 Elastic solution

The general solution of the system of equations (2.42) reads

$$\boldsymbol{y}_{\ell m}\left(r\right) = \boldsymbol{\Pi}_\ell\left(r, r_0\right)\boldsymbol{y}_{\ell m}(r_0) - \int_{r_0}^{r}\boldsymbol{\Pi}_\ell\left(r, r'\right)\boldsymbol{h}_{\ell m}\left(r'\right)dr'. \tag{2.75}$$

The first terms on the right side of Eq (2.75) is the homogeneous solution, while the second term is a particular solution which accounts for the external non-conservative forces. The so-called *propagator* matrix $\boldsymbol{\Pi}_\ell$ solves the homogeneous equation in every layer

$$\frac{d\boldsymbol{\Pi}_\ell\left(r, r'\right)}{dr} = \boldsymbol{A}_\ell\left(r\right)\boldsymbol{\Pi}_\ell\left(r, r'\right)\,, \tag{2.76}$$

with the condition

$$\boldsymbol{\Pi}_\ell\left(r', r'\right) = \boldsymbol{1}\,. \tag{2.77}$$

The obvious condition of continuity of the solution imposes the continuity of the propagator at every boundary, that is:

$$\boldsymbol{\Pi}_\ell\left(r_j^+, r'\right) = \boldsymbol{\Pi}_\ell\left(r_j^-, r'\right)\,. \tag{2.78}$$

If we choose the core-crust radius as the starting point of the integration, namely $r_0 = r_c^+$, we have

$$\boldsymbol{y}_{\ell m}\left(r_c^+\right) = \boldsymbol{I}_C\boldsymbol{C}\,. \tag{2.79}$$

This gives us

$$\boldsymbol{y}_{\ell m}\left(r\right) = \boldsymbol{\Pi}_\ell\left(r, r_c^+\right)\boldsymbol{I}_C\boldsymbol{C} - \boldsymbol{w}\left(r\right)\,, \tag{2.80}$$

where $\boldsymbol{w}\left(r\right)$ is defined as

$$\boldsymbol{w}\left(r\right) = \int_{r_c^+}^{r}\boldsymbol{\Pi}_\ell\left(r, r'\right)\boldsymbol{h}_{\ell m}\left(r'\right)dr'\,. \tag{2.81}$$

The three constants of integration in the vector $\boldsymbol{C}$ can be estimated by imposing the conditions at the star surface given by Eq (2.58), so that Eq (2.80) now reads

$$\boldsymbol{y}_{\ell m}(r) \quad = \quad \boldsymbol{\Pi}_\ell(r, r_c)\, \boldsymbol{I}_C \left[\boldsymbol{P}_1 \boldsymbol{\Pi}_\ell\left(a^-, r_c^+\right) \boldsymbol{I}_C\right]^{-1} \left(\boldsymbol{P}_1 \boldsymbol{w}\left(a^-\right) + \boldsymbol{b}\right) \; - \; \boldsymbol{w}(r)\,. \tag{2.82}$$

This equation represents the most general response of the star to the internal (such as vortex pinning) and centrifugal, tidal or other conservative loads: it uniquely determines the spheroidal deformations and the potential within the crust, as well as the radial and tangential spheroidal stresses and the potential stress.

If the only external force is conservative (e.g. the centrifugal force) the solution in Eq (2.75) assumes the simpler form

$$\boldsymbol{y}_{\ell m}(r) = \boldsymbol{\Pi}_\ell(r, r_c)\, \boldsymbol{I}_C \left[\boldsymbol{P}_1 \boldsymbol{\Pi}_\ell\left(a^-, r_c^+\right) \boldsymbol{I}_C\right]^{-1} \boldsymbol{b}\,. \tag{2.83}$$

Moreover, when deformations with respect to the spherical reference configuration are induced only by rotation, the displacement field $\boldsymbol{u}$ is the sum of only two contributions, namely $\boldsymbol{u} = \boldsymbol{u}_{00} + \boldsymbol{u}_{20}$. This decomposition relies on the fact that we have assumed a constant rotation axis; taking into account also a possible nutation would in general require the contributions of other $m \neq 0$ harmonics.

2.9 The $\ell = 0$ harmonic

As said in the previous part, the $\ell = 0$ harmonic need a specific treatment since its contribution is purely radial, i.e. the tangential displacement and stress are zero. The matrix $A_\ell(r)$, for the harmonic $\ell = 0$ is

$$A_0(r) = \begin{pmatrix} -\frac{2\lambda}{r\beta} & \frac{1}{\beta} & 0 & 0 \\ \frac{4}{r}\left(\frac{3\kappa\mu}{r\beta} - \rho_0 g\right) & -\frac{4}{r}\frac{\mu}{\beta} & -\frac{\rho_0}{r} & \rho_0 \\ -4\pi G\rho_0 & 0 & -\frac{1}{r} & 1 \\ -\frac{4\pi G\rho_0}{r} & 0 & 0 & -\frac{1}{r} \end{pmatrix}. \tag{2.84}$$

This expression can be obtained from the general form for the matrix A (see Eq (2.43)) by putting $\ell = 0$ and neglecting the tangential displacement and stress. The equation that we have to solve is

$$\frac{d\boldsymbol{w}_{00}}{dr} = \boldsymbol{A}_0 \boldsymbol{w}_{00} + \boldsymbol{f}, \tag{2.85}$$

where $\boldsymbol{f}$ is the force vector

$$\boldsymbol{f}_{cen} = (0, f_r, 0, 0) \tag{2.86}$$

and the spherical solution $\boldsymbol{w}_{00}$ is the four-vector

$$\boldsymbol{w}_{00}(r) = \left(U(r), R(r), \Phi(r), Q(r)\right). \tag{2.87}$$

We observe that in this case the approach is different with respect to the one presented in Eq (2.30) for $\ell \geq 2$, since here the potential Φ^Δ coincides with the perturbed gravitational potential ϕ^Δ, i.e. also conservative forces are contained in the term $\boldsymbol{f}$. Equation (2.85) can be simplified and subdivided into two distinct problems. In fact, rows 3 and 4 of that equation are

$$\frac{\Phi(r)}{r} - Q(r) + 4G\pi U(r)\rho_0(r) + \Phi'(r) = 0, \tag{2.88}$$

and

$$\frac{Q\left(r\right)}{r}+\frac{4\pi GU\left(r\right)\rho_{0}\left(r\right)}{r}+Q'\left(r\right)=0. \tag{2.89}$$

By replacing

$$Q(r)=\overline{Q}\left(r\right)+\Phi/r. \tag{2.90}$$

Eq (2.88) becomes

$$\Phi'\left(r\right)=\overline{Q}\left(r\right)-4\pi GU\left(r\right)\rho_{0}\left(r\right). \tag{2.91}$$

Using this relation in Eq (2.89) one obtains a differential equation for $\overline{Q}\left(r\right)$

$$2\frac{\overline{Q}\left(r\right)}{r}+\overline{Q}'\left(r\right)=0, \tag{2.92}$$

whose solution is

$$\overline{Q}\left(r\right)=\frac{\overline{C_{2}}}{r^{2}}. \tag{2.93}$$

Using both Eq (2.91) and Eq (2.93) one can rewrite the system (2.85) as

$$\left(\begin{array}{c} -\frac{R(r)}{\beta(r)}+\frac{2U(r)\lambda(r)}{r\beta(r)}+U'(r)=0\\ -f_{r}\left(r\right)+\frac{4R(r)\mu(r)}{r\beta(r)}-\frac{12U(r)\kappa\mu(r)}{r^{2}\beta}-\frac{C_{Q}}{r^{2}}\rho\left(r\right)+\frac{4gU(r)\rho(r)}{r}+R'\left(r\right)=0\\ 0\\ 0 \end{array}\right), \tag{2.94}$$

i.e., starting from a 4×4 matrix we obtain two differential equations involving only $U(r)$ and $R(r)$.

In the innermost region of the star the density is roughly constant, like the bulk and shear modulus. For this reason we can set

$$\rho\left(r\right)=\overline{\rho},\ \kappa\left(r\right)=\overline{\kappa},\ \mu(r)=\overline{\mu}=0, \tag{2.95}$$

where we remember that the core is fluid, so that its shear modulus is zero. By imposing the regularity of the solution near the center one can write the general solution for $U(r)$ and $R(r)$ as the sum of a homogeneous solution (i.e. setting $f_r = 0$) and a particular solution

$$U_{00}\left(r\right)=U^{homo}\left(r\right)+C_{f}U^{f}\left(r\right), \tag{2.96}$$

$$R_{00}\left(r\right)=R^{homo}\left(r\right)+C_{f}R^{f}\left(r\right), \tag{2.97}$$

where C_f is a constant, that can be fixed by imposing the boundary condition for the radial stress, namely

$$R_{00}\left(a^{-}\right)=0. \tag{2.98}$$

Part III
Incompressible models

CHAPTER 3

Incompressible limit

The first, useful limit case to study is the *incompressible* one, i.e. when $\kappa \to \infty$ ($\gamma \to \infty$). In fact, in this limit all the equations presented in the previous chapter become simpler and one can get an analytic solution. The incompressible approximation (for the whole star) can be justified in view of the internal profile of the density: in most regions of the star, the density do not vary appreciably. Note however that the density varies by about 14 orders of magnitude throughout the crust. Clearly a scenario of fixed crust density is not totally realistic, but, as we can see in the following, some of the key aspect of the deformation are already shown, since they depends mainly on the global physical characteristics of the star. Furthermore the presence of an analytic solution allows a better and easier study of the deformation as a function of the main stellar parameters, such as radius and mass.

The incompressible approximation was previously adopted by Franco, Link and Epstein (Franco et al. 2000) (FLE from now on) for the study of a NSs deformation under rotation. However, in their papers the authors do not analyze the strain angle dependence of the strain angle on the stellar characteristics.

The chapter is organized as follows: (1) we derive, following Sabadini et al. (2016), the explicit form of the general elastic solution in the incompressible limit; (2) then we study in details the dependence of the star's response by varying both its mass and EoS for the FLE model. In this chapter we use the FLE notation, so the core-crust radius is indicated as $r = R'$ and the stellar radius as R; (3) we show that the FLE model can be found as a limit of our more general model, where both the core and the crust have the same density; (4)Finally we compare the results obtained with the FLE model analysis with the ones got from our more refined two-density model; in particular, we calculated the maximum strain angle developed on a realistic neutron star in the time between two glitches.

3.1 Elastic solution

We assume that the neutron star has two homogeneous components, a fluid core and a solid crust, with density ρ_f and ρ_c respectively. Therefore, we require that the shear modulus is constant in each layer of the star, $\partial_r \mu = 0$. With this assumptions Eqs (2.33), (2.34) and (2.32) can be rewritten as

$$\frac{\beta}{\rho_0}\partial_r \chi_\ell - \partial_r (gU) + g\chi_\ell - \partial_r \Phi_\ell + \frac{\mu}{\rho_0}\frac{\ell(\ell+1)}{r} H_\ell = 0 \tag{3.1}$$

$$\frac{\beta}{\rho_0}\chi_\ell - gU_\ell - \Phi_\ell + \frac{\mu}{\rho_0}\partial_r (rH_\ell) = 0\,, \tag{3.2}$$

and

$$\nabla_r^2 \Phi_\ell = -4\pi G \left(\rho_0 \chi_\ell + U_\ell \partial_r \rho_0\right) , \tag{3.3}$$

where we remind that

$$\nabla_r^2 = \partial_r^2 + \frac{2}{r}\partial_r - \frac{\ell\,(\ell+1)}{r^2} .$$

Since in this chapter we are interested only into the effect of centrifugal forces, we can ignore the toroidal part of the momentum equation (2.35). The scalar H_ℓ introduced in the previous expression is defined as

$$H_\ell = \partial_r V_\ell + \frac{V_\ell - U_\ell}{r}.$$

According to the incompressibility assumptions there are no volume changes Δ. However, during the deformations, also incompressible materials must be able to react to isotropic stresses. We thus require that the bulk modulus κ is infinitely large but in such a way that the material increment of the pressure, which can be expressed as $p^\delta = -\kappa\Delta$, remains finite (Sabadini et al. 2016). Therefore, the coefficients p_ℓ of the expansion in spherical harmonics of p^δ remain finite when the formal limit

$$p_\ell \;=\; -\lim_{\substack{\chi_\ell \to 0 \\ \kappa \to \infty}} \kappa\, \chi_\ell$$

is taken (Love 1959). Using the incompressibility assumption $\chi_\ell = 0$, Eq (2.37) gives a relation between the radial and the tangential displacements:

$$V_\ell = \frac{r\partial_r U_\ell + 2U_\ell}{\ell\,(\ell+1)} . \tag{3.4}$$

The quantity H_ℓ can thus be written as

$$H_\ell = \frac{\nabla_r^2\,(U_\ell r)}{\ell\,(\ell+1)} . \tag{3.5}$$

Since in our model the layers are homogeneous (i.e. $\partial_r \rho_0 = 0$) the Eq (3.3) *within* each layers becomes the Laplace equation ($\ell \geq 1$)

$$\nabla_r^2 \Phi_\ell = 0 . \tag{3.6}$$

The solution of Eq (3.6) can be expressed as

$$\Phi_\ell = c_3 r^\ell + c_3^* r^{-(\ell+1)} \tag{3.7}$$

where c_3 and c_3^* are constants of integration. We observe that the absence of density perturbations within the layers does not implies that the gravitational perturbation Φ^Δ is zero. Indeed, there are density jumps $\Delta\rho_v$ between different layers at interfaces defined at the radius v ,

$$\Delta\rho_v = \rho_0\left(v^+\right) - \rho_0\left(v^-\right) \tag{3.8}$$

which means that we can write the density gradient as

$$\partial_r \rho_0 = (\rho_c - \rho_f)\delta(r - R')$$

$$\partial_r \rho_0 = -\rho_c \delta(r - R),$$

at the interfaces $r = R'$ and $r = R$, respectively. The introduction of the auxiliary quantity

$$\Gamma_\ell = -\frac{p_\ell}{\rho_0} - gU_\ell - \Phi_\ell \,,$$

allows to reduce the Eqs (3.1) and (3.2) to

$$\partial_r \Gamma_\ell + \frac{\mu}{\rho_0} \frac{\ell\,(\ell+1)}{r} H_\ell = 0 \,, \tag{3.9}$$

$$\Gamma_\ell + \frac{\mu}{\rho_0} \partial_r \left(r H_\ell\right) = 0 \,. \tag{3.10}$$

These two equations can be combined into

$$\nabla_r^2 \, \Gamma_\ell = 0, \tag{3.11}$$

which has the solution

$$\Gamma_\ell = -\frac{\mu}{\rho_0} \, c_1 \, r^\ell - \frac{\mu}{\rho_0} \, c_1^* \, r^{-\ell-1} \,, \tag{3.12}$$

where the quantity μ/ρ_0 have been inserted for convenience and c_1, c_1^* are two constants. Inserting this solution in (3.9) and using the relation (3.5) we obtain a differential equation for U_ℓ:

$$\nabla_r^2 (U_\ell \, r) = c_1 \, \ell \, r^\ell - c_1^* \, (\ell+1) \, r^{-\ell-1}. \tag{3.13}$$

Solving this equation and using (3.4) we finally get the radial and tangential displacement

$$U_\ell = c_1 \frac{\ell \, r^{\ell+1}}{2\,(2\ell+3)} + c_2 r^{\ell-1} + c_1^* \frac{(\ell+1)\, r^{-\ell}}{2\,(2\ell-1)} + c_2^* r^{-(\ell+2)}, \tag{3.14}$$

$$V_\ell = c_1 \frac{(\ell+3)\, r^{\ell+1}}{2\,(2\ell+3)\,(\ell+1)} + c_2 \frac{r^{\ell-1}}{\ell} + c_1^* \frac{(2-\ell)\, r^{-\ell}}{2l\,(2\ell-1)} - c_2^* \frac{r^{-(\ell+2)}}{\ell+1} \,. \tag{3.15}$$

Note that, in the limiting case of Eq (3.1), both $\lambda\chi_l$ and $\beta\chi_\ell$ converge to p_ℓ (the $\mu\chi_\ell$ contribution goes to zero). Using this property we can express the radial stress (see Appendix A) as

$$R_\ell = -p_\ell + 2\mu \partial_r U_\ell, \tag{3.16}$$

that is

$$\begin{aligned} R_\ell = c_1 \frac{\ell\rho_0 g r + 2\left(\ell^2-\ell-3\right)\mu}{2\,(2\ell+3)} r^\ell + c_2 \left[\rho_0 g r + 2\,(\ell-1)\,\mu\right] r^{\ell-2} + c_3 \rho_0 r^\ell + \\ + c_1^* \frac{(\ell+1)\,\rho_0 g r - 2\left(\ell^2+3\ell-1\right)\mu}{2\,(2\ell-1)} r^{-(\ell+1)} + \\ + c_2^* \left[\rho_0 g r - 2\,(\ell+2)\,\mu\right] r^{-(\ell+3)} + c_3^* \rho_0 r^{-(\ell+1)} \end{aligned} \tag{3.17}$$

In the same way, using the definition of the tangential stress (see Appendix A, Eq (A.12)) and the one of the potential (2.41), we obtain

$$S_\ell = c_1 \frac{\ell\,(\ell+2)}{(2\ell+3)\,(\ell+1)} \mu r^\ell + c_2 \frac{2\,(\ell-1)}{\ell} \mu r^{(\ell-2)} + c_1^* \frac{\left(\ell^2-1\right)}{\ell\,(2\ell-1)} \mu r^{-(\ell+1)} + c_2^* \frac{2\,(\ell+2)}{\ell+1} \mu r^{-(\ell+3)} \tag{3.18}$$

$$Q_\ell = c_1 \frac{2\pi G\rho_0 \ell}{2\ell+3} r^{\ell+1} + c_2 4\pi G\rho_0 r^{\ell-1} + c_3 \left(2\ell+1\right) r^{\ell-1} + c_1^* \frac{2\pi G\rho_0 \left(\ell+1\right)}{2\ell-1} r^{-\ell} + c_2^* 4\pi G\rho_0 r^{-(\ell+2)} \tag{3.19}$$

We remind that all the harmonic coefficients of the centrifugal potential expansion with $\ell \neq 0, 2$ are zero. Moreover, the coefficient with $\ell = 0$ is suppressed by the request of incompressibility. Therefore, in the case of deformations induced by the centrifugal force alone we have only the harmonic contribution corresponding to $\ell = 2$.

In order to fix these constants we have to impose the opportune boundary conditions (see section 2.7) at the interface between layers. In particular, within each layer of the star the solution can be written as

$$\boldsymbol{y}_\ell = \boldsymbol{Y}_\ell(r)\boldsymbol{C}_\ell, \tag{3.20}$$

where $\boldsymbol{Y}_\ell(r)$ is

$$\boldsymbol{Y}_\ell\left(r\right) = \begin{pmatrix} \frac{\ell r^{\ell+1}}{2(2\ell+3)} & r^{\ell-1} & 0 \\ \frac{(\ell+3)r^{\ell+1}}{2(2\ell+3)(\ell+1)} & \frac{r^{\ell-1}}{\ell} & 0 \\ \frac{\ell(\ell+2)\mu r^{\ell}}{(2\ell+3)(\ell+1)} & \left(\rho_0 g r + 2\left(\ell-1\right)\mu\right) r^{\ell-2} & \rho_0 r^{\ell} \\ \frac{\ell(\ell+2)\mu r^{\ell}}{(2\ell+3)(\ell+1)} & \frac{2(\ell-1)\mu r^{\ell-2}}{\ell} & 0 \\ 0 & 0 & r^{\ell} \\ \frac{2\pi G\rho_0 \ell r^{\ell+1}}{2\ell+3} & 4\pi G\rho_0 r^{\ell-1} & \left(2\ell+1\right) r^{\ell-1} \end{pmatrix}$$

$$\begin{pmatrix} \frac{(\ell+1)r^{-\ell}}{2(2\ell-1)} & r^{-\ell-2} & 0 \\ \frac{(2-\ell)r^{-\ell}}{2\ell(2\ell-1)} & \frac{\rho_0 g r - 2(\ell+2)\mu}{r^{\ell+3}} & 0 \\ \frac{(\ell+1)\rho_0 g - 2\left(l^2+3\ell-1\right)\mu}{2(2\ell-1)r^{\ell+1}} & \frac{\rho_0 g r - 2(\ell+2)\mu}{r^{\ell+3}} & \frac{\rho_0}{r^{\ell+1}} \\ \frac{\left(\ell^2-1\right)\mu}{\ell(2\ell-1)r^{\ell+1}} & \frac{2(\ell+2)\mu}{(\ell+1)r^{\ell+3}} & 0 \\ 0 & 0 & \frac{1}{r^{\ell+1}} \\ \frac{2\pi G\rho_0(\ell+1)}{(2\ell-1)r^{\ell}} & \frac{4\pi G\rho_0}{r^{\ell+2}} & 0 \end{pmatrix}, \tag{3.21}$$

and $\boldsymbol{C}_\ell$ contains the constants

$$\boldsymbol{C}_\ell = \left(c_1, c_2, c_3, c_1^*, c_2^*, c_3^*\right)^{\mathrm{T}}. \tag{3.22}$$

The expression in Eq (3.20) can be used to recast the propagator $\boldsymbol{\Pi}_\ell\left(r, r'\right)$, where both r and r' are in a single layer, as

$$\boldsymbol{\Pi}_\ell\left(, r'r\right) = \boldsymbol{Y}_\ell(r)\boldsymbol{Y}_\ell^{-1}(r'). \tag{3.23}$$

Clearly the propagator satisfies the Cauchy datum $\boldsymbol{\Pi}_\ell(r', r') = \mathbf{1}$. When, on the contrary, r and r' are placed in different layers, say jth and ith, with $j > i$, by using the continuity of the solution at the surfaces' boundary

$$\boldsymbol{y}_\ell(r_k^+) = \boldsymbol{y}_\ell(r_k^-) \text{ for } k = i, \ldots j-1, \tag{3.24}$$

we find

$$\boldsymbol{\Pi}_\ell\left(r, r'\right) = \boldsymbol{\Pi}_\ell\left(r, r_j\right) \left[\prod_{k=i+1}^{j} \boldsymbol{\Pi}_\ell\left(r_k, r_{k-1}\right)\right] \boldsymbol{\Pi}_\ell\left(r_i, r'\right). \tag{3.25}$$

The general solution in the jth layer will be obtain by propagating the solution from the core-crust boundary, and thus we need also the expression for the core-crust matric I_C. Since the core is incompressible, the Poisson equation (3.3) becomes the Laplace equation

$$\nabla_r^2 \psi_\ell(r) = 0 \tag{3.26}$$

with solution

$$\psi_\ell(r) = c r^\ell + c^* r^{-(\ell+1)}. \tag{3.27}$$

In this case the quantity q_ℓ is

$$q_\ell = 2(\ell-1) r^{(\ell-1)}. \tag{3.28}$$

By calculating the gravitational acceleration we can finally write

$$\boldsymbol{I}_C = \begin{pmatrix} -r^\ell/g(r_c) & 0 & 1 \\ 0 & 1 & 0 \\ 0 & 0 & g\,(r_c)\,\rho_c \\ 0 & 0 & 0 \\ r^\ell & 0 & 0 \\ 2\,(\ell-1)\,r^{\ell-1} & 0 & 4\pi G \rho_c \end{pmatrix}. \tag{3.29}$$

The condition at the star surface, Eq (2.58), will fix the constants and thus the elastic solution throughout the layers.

3.2 FLE model analysis

One of the first model introduced in the literature accounting for the effect of rotation on a realistic NS was developed by Franco, Link and Epstein (Franco et al. 2000). In the FLE approach the star is described as a homogeneous body, with a fluid core and an elastic crust of the same density. The authors of this model were interested mainly on NS precession, and thus did not publish any analysis of the dependence of the star's response on its main physical parameters, considering only a "standard" NS of mass $1.4 M_\odot$ and radius $R = 10$ km[1]. For this reason we perform in this section a study of the FLE model, going beyond their analysis, by focusing in particular on the strain angle as a function of the stellar mass and EoS.

Before presenting a much more general model, we performed a deep study of all the main characteristics and features of the FLE model that is here reported.

We start here by presenting briefly only the main characteristic of the model; for the complete derivation we refer to the original paper by Franco et al. (2000).

We are interested in calculating the displacement field $\boldsymbol{u}$ between a configuration rotating with velocity Ω and one rotating at $\Omega - \delta\Omega$, where $\delta\Omega > 0$ for a spinning down pulsar. The non-rotating configuration is known for our elastic star, since it coincides with the one given by the usual hydrostatic equilibrium for a fluid. Thanks to the assumed linearity of the problem, we calculate the displacements $\boldsymbol{u}_\Omega$ due to the spin-up of a spherical configuration to a rotating one having centrifugal potential proportional to Ω^2; then, the desired displacement between the two rotating configurations is given by

$$\boldsymbol{u} = \boldsymbol{u}_\Omega - \boldsymbol{u}_{\Omega-\delta\Omega} \propto \delta\Omega\,\Omega\,. \tag{3.30}$$

[1] As said above, in this chapter we will use the symbol R for the stellar radius, instead of a, that is one of the constants that fix the displacement in the FLE approach.

Franco et al. (2000) found an equation, for an auxiliary quantiti h, that is equivalent to Eq (3.11). In this way the corresponding displacement field $\boldsymbol{u}$ up to the linear order in $\delta\Omega$ is

$$\begin{aligned} u_r(r,\theta) &= \left(ar - \frac{1}{7}Ar^3 - \frac{1}{2}\frac{B}{r^2} + \frac{b}{r^4}\right) P_2 \equiv f(r)P_2 \\ u_\theta(r,\theta) &= \left(\frac{1}{2}ar - \frac{5}{42}Ar^3 - \frac{1}{3}\frac{b}{r^4}\right)\frac{dP_2}{d\theta}, \end{aligned} \tag{3.31}$$

where $P_2 = \frac{1}{2}\left(3\cos^2\theta - 1\right)$ is the second Legendre polynomial of argument $\cos\theta$ and we have defined the function $f(r)$. The four coefficients a, b, A and B are fixed by four boundary conditions, two at the core-crust transition radius $r = R'$ and two at the star's surface $r = R$. At both these interfaces we have to require the continuity of radial stresses, $T_{rr} = -p + \mu u_{rr}$, and that $\sigma_{r\theta} = 0$, since both the fluid core and the vacuum outside the star cannot support shears. It is useful to introduce the sound speed in the crust of transverse waves, $c_t = \sqrt{\mu/\rho}$, and the usual Keplerian velocity, $v_K = \sqrt{GM/R}$, so that the four boundary conditions read

$$\begin{aligned} &a - \frac{8}{21}AR^2 - \frac{B}{2R^3} + \frac{8}{3}\frac{b}{R^5} = 0 \\ &a - \frac{8}{21}AR'^2 - \frac{B}{2R'^3} + \frac{8}{3}\frac{b}{R'^5} = 0 \\ &f'(R) + \frac{1}{5}\frac{v_K^2}{c_t^2}\frac{f(R)}{R} - \frac{1}{3}\frac{\Omega\delta\Omega}{c_t^2}R^2 = -\frac{AR^2}{2} + \frac{B}{R^3} \\ &f'(R') = -\frac{1}{2}\left(AR'^2 + \frac{B}{R'^3}\right). \end{aligned} \tag{3.32}$$

Using the definition (3.31) and the boundary conditions (3.32), the four coefficient a, b, A, B are obtained with straightforward algebra.

It seems more useful to rewrite the displacement (3.31) as

$$\begin{aligned} u_r &= \left[\frac{\Omega\delta\Omega\, R^2}{Q(c_t, v_K, L)}\right] R\left(\frac{\tilde{a}r}{R} - \frac{\tilde{A}r^3}{7R^3} - \frac{\tilde{B}R^2}{2r^2} + \frac{\tilde{b}R^4}{r^4}\right) P_2 \\ u_\theta &= \left[\frac{\Omega\delta\Omega\, R^2}{Q(c_t, v_K, L)}\right] R\left(\frac{\tilde{a}r}{2R} - \frac{5\tilde{A}r^3}{42R^3} - \frac{\tilde{b}R^4}{3r^4}\right)\frac{dP_2}{d\theta}, \end{aligned} \tag{3.33}$$

where the tilde superscript indicates that now the coefficients are dimensionless: all the dependence on physical parameters has been included into the pre-factors (Q is a squared velocity built with the typical scales of the problem). Therefore, $\tilde{a}$, $\tilde{A}$, $\tilde{b}$ and $\tilde{B}$ are functions of the parameter $L = R'/R$ only (the limits $L = 0$ and $L = 1$ describe a completely solid star and a completely fluid star respectively). Since, when "realistic" EoS are used, the parameter L spans from about 0.86 to 0.95, the parameter $q = 1 - L$ is sufficiently small to consider the expansion of the coefficients $\tilde{a}$, $\tilde{b}$, $\tilde{A}$, $\tilde{B}$ and Q *only* up to the second order in q. The explicit form of the displacement coefficients (3.33), fixed by

the boundary conditions (3.32), is then

$$\begin{aligned}
\tilde{a} &= 280\left(13q^2 - 7q + 2\right) \\
\tilde{b} &= -5\left(643q^2 - 232q + 37\right) \\
\tilde{A} &= 280\left(15q^2 - 13q + 5\right) \\
\tilde{B} &= -560\left(70q^2 - 27q + 5\right)/3 \\
Q/v_K^2 &= -35\,\left(q^2\left(240\chi^2 - 109\right) + q\left(48 - 60\chi^2\right) - 11\right)\,.
\end{aligned} \tag{3.34}$$

In the above equations the parameter χ is defined as the ratio between the sound speed in the crust c_t and the star's Keplerian velocity v_K

$$\chi \;=\; \frac{c_t}{v_K} \;\ll\; 1\,. \tag{3.35}$$

According to current estimates of $\mu \sim 10^{28}$ erg/cm^3, χ is expected to be much less than unity in the whole crust (see e.g. Fig 7 of Zdunik et al. 2008). Interestingly, as noted by several authors (see e.g. Haskell et al. 2006; Bastrukov et al. 2007), the speed of transverse elastic shear waves $c_t \sim 10^8$ cm/s is rather constant (within a factor of 2) throughout the crust, so that we expect $\chi \sim 10^{-2}$. We interpret the parameter χ as an indicator of the relative importance of the elastic forces with respect to the unperturbed gravitational one: in this sense, this ratio gives an estimation of the goodness of the linear perturbation theory.

3.2.1 Parametric study of the FLE model

In their original work, Franco et al. (2000) considered only a "standard" NS of mass $M = 1.4M_\odot$, $R = 10$ km and $R' = 0.95\,R$ (i.e. $L = 0.95$ according to the present notation), as benchmark stellar configuration. Here, we extend their analysis investigating the behavior of the FLE model as a function of the star's parameters: radius, mass and crust thickness.

Let us focus for a moment on the displacement (3.33). We can define a dimensionless weight factor W

$$W = \frac{\Omega\,\delta\Omega\,R^2}{Q(c_t, v_K, L)}\,, \tag{3.36}$$

the numerator of which is half of the angular velocity difference between the squared angular velocity of the initial and final configuration, while the denominator is a proper combination of v_K and c_t, with the dimension of a squared velocity. In particular, using the smallness of the χ and q parameters, we can write (see also Eq 3.34)

$$Q \propto v_K^2. \tag{3.37}$$

In order to remove the dependence of the numerator on a particular set of rotational parameters, we can fix Ω and $\delta\Omega$ to some constant value. In this way, all the remaining contributions depend on the structural properties of the star. For the FLE model we see that

$$W \propto \frac{R^2}{v_K^2} = \frac{R^3}{GM} \propto \frac{1}{\rho}\,, \tag{3.38}$$

therefore, the denser the star, the smaller the displacement (3.33).

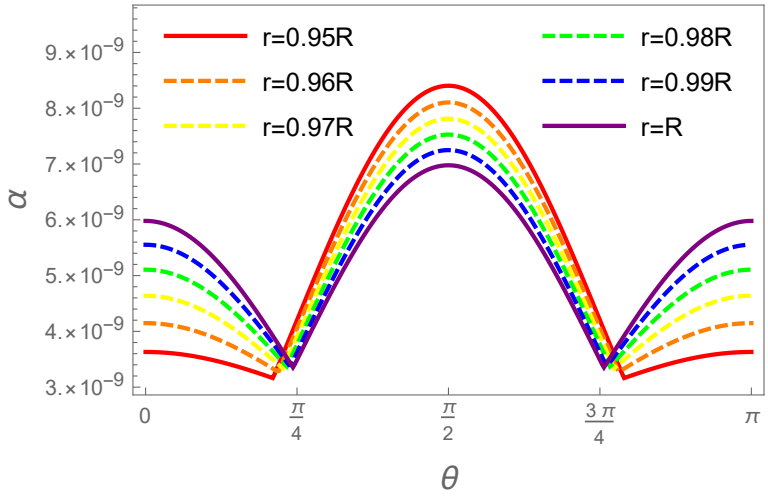

Figure 3.1: Strain angle as a function of the colatitude θ for the FLE model and fixed benchmark values $M = 1.4M_\odot$, $R = 10\,\text{km}$, $L = 0.95$. The strain angle is calculated for different values of the radius: $r = R$ (purple), $r = 0.99R$ (blue), $r = 0.98R$ (green), $r = 0.97R$ (yellow), $r = 0.96R$ (orange) and $r = 0.95R$ (red). In particular, we indicate with a solid line the innermost (red) and outermost (purple) value of α, and a dashed line for the others. We used $\Omega\delta\Omega = 1\,\text{rad}^2/\text{s}^2$.

For a better understanding of this behavior, the strain angle value α may be calculated[2] changing the parameters one by one, keeping fixed all the others. For comparison purposes, we set the relative extension of the core to be $L = 0.95$, the same used in the original FLE study.

Since the displacements, and thus the strain, are proportional to the actual spin down that occurred between the two configurations, we set the pre-factor $\Omega\delta\Omega$ equal to one[3] for simplicity. Therefore, to calculate the deformation for a certain star it is just sufficient to multiply the desired quantities for the actual parameter $\Omega\,\delta\Omega$. The strain angle, being a local quantity, depends on the position inside the crust; for given mass, radius and crust thickness of the star, it is shown in Fig. 3.1, where it is possible to observe that α is a decreasing function of r. Hence, we expect that, if the crust breaks, the failure threshold will be reached first at the crust-core interface, near the equatorial plane (i.e. $\theta \approx \pi/2$ in our coordinates). However, the value obtained with this test configuration is by far smaller than the smallest breaking strain theoretically expected of 10^{-5}. As we will see, this kind of behaviour is scarcely influenced by the model used.

Moreover,by looking at Eq (3.33) and (3.38), we see that deformations depends mainly on the radius and on the mean density of the star. In this sense, it is interesting to compare the strains of stars all having the same average density $\rho = 3M/(4\pi R^3)$, but different radii and masses. We find that, as long as the density is taken constant but the mass and the radius vary, the strain is nearly unchanged. An example of this is shown in Fig

[2]The procedure to calculate the the strain angle α is as follows. First, the relations (3.33) is used to obtain the strain tensor u_{ij} given by Eq (2.8); then, one locally calculates its eigenvalues and, finally, by making the difference between the maximum and minimum eigenvalues of the strain tensor at a specific point, obtains α.

[3]Incidentally, our choice to set $\Omega\delta\Omega = 1\,\text{rad}^2/\text{s}^2$ in all the calculations of the plotted strains is not so distant from the fiducial value $\Omega\delta\Omega \approx 0.6\,\text{rad}^2/\text{s}^2$ that we will use for the Vela pulsar (B0833-45) in the next section (see table 4.1).

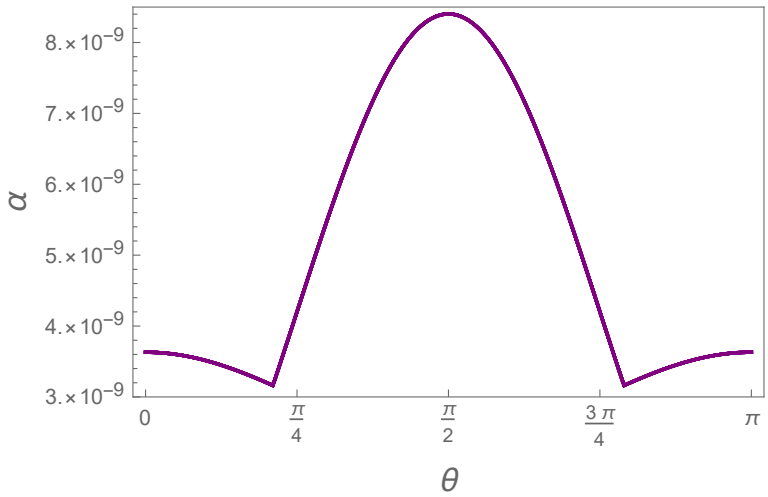

Figure 3.2: Strain angle α of the FLE model restricted to the spherical shell $r = R'$ as a function of the colatitude θ. The crust thickness parameter is fixed to $L = 0.95$ but we consider two extreme values of the stellar radius: $R = 10\,\text{km}$ and $R = 20\,\text{km}$. The corresponding two masses M are fixed by the constraint that the average density of both configurations is $\rho = 6.6 \times 10^{14}\,\text{g/cm}^3$. The two curves appear to be superimposed in the graph.

3.2, where we fixed ρ to be the average density of a star of $1.4\,M_\odot$ and $R = 10\,\text{km}$: different choices of the mass and of the radius that are consistent with the fixed density value do not move the estimated strains, providing a numerical check of the goodness of the approximation made in Eq (3.38). This result indicates that, in the original FLE model, the strain developed by a spinning-down pulsar (for a given value of $\Omega\delta\Omega$) depends essentially only on the average density of the star and on L: the independent choice of both M and R implies a degeneracy in the results.

From the $M - R$ relation of realistic equations of state we know that more massive stars typically have smaller radii, implying a larger average density and smaller W, as can be seen in Eq (3.38). In this sense, we can say that in the original FLE model heavier stars develop smaller strains during the spin-down, which is the expected behavior considering that the centrifugal force is less effective on more compact stellar configurations.

Finally we can study also how the changes of L affects α. We find that the strain angle is a weak increasing function of the crustal thickness, i.e. a decreasing function of L, in the range $0.85 \leq L \leq 0.95$, as can be seen in Fig. 3.3, where we computed the maximum value of $\alpha(L)$ over θ, for $r = R'$ and $M = 1.4M_\odot$ and $R = 10$ km (in particular $\alpha^{Max}(L = 0.85) \simeq 1.3\alpha^{Max}(L = 0.95)$). This figure shows clearly that a thick crust can support larger deformations with respect to a thinner one (as expected), but the dependence is not so strong. The reason is that the elastic restoring force is small compared to the gravitational one, see Eq (3.35).

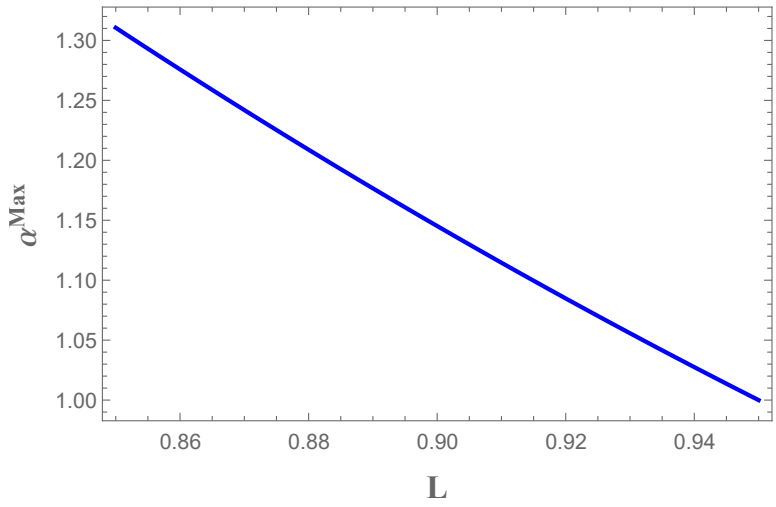

Figure 3.3: The maximum strain angle as a function of the thickness parameter $L = R'/R$ for the FLE model. The fixed benchmark values $M = 1.4M_{\odot}$, $R = 10\,\mathrm{km}$ have been used. The strain angle is normalized at the value reached for $L = 0.95$ and calculated at the core-crust interface $r = R'$. We used $\Omega\delta\Omega = 1\,\mathrm{rad}^2/\mathrm{s}^2$.

3.2.2 Cowling approximation

It is possible to exploit the FLE model as a tool to estimate the impact of the so-called Cowling approximation (Cowling 1941), according to which the perturbation of the star's gravitational potential is neglected.This kind of approach has been widely used in the literature, especially for the study of the oscillation modes of neutron stars (McDermott et al. 1988), but also for static deformations (Ushomirsky et al. 2000; Johnson-McDaniel & Owen 2013). This approximation, in fact, has both the advantage to considerably simplify the momentum equations and to avoid resolving the perturbed Poisson one. However it can have a very large impact on the estimation of elastic deformations, as we show in the following. The Cowling approximation can be achieved by setting $\delta\phi = 0$ in the perturbed equations of the original FLE model (Franco et al. (2000), see in particular Eq (12) and (31) therein).

Within the same original FLE scheme used in the previous section but assuming this further simplification, we can now rewrite the boundary conditions in Eq (3.32) as

$$\begin{aligned}
&a - \frac{8}{21}AR^2 - \frac{B}{2R^3} + \frac{8}{3}\frac{b}{R'^5} = 0\\
&a - \frac{8}{21}AR'^2 - \frac{B}{2R'^3} + \frac{8}{3}\frac{b}{R'^5} = 0\\
&-2f'(R) - \frac{v_K^2}{c_t^2}\frac{f(R)}{R} + \frac{2}{3}\frac{\Omega\delta\Omega}{c_t^2}R^2 = AR^2 + \frac{B}{R^3}\\
&-2f'(R') = AR'^2 + \frac{B}{R'^3}\,.
\end{aligned} \tag{3.39}$$

Using the definition (3.31), together with the solutions of the above equations, we obtain the corresponding displacement, that can be written in the dimensionless form introduced in Eq (3.33). The corresponding explicit form of the coefficients is given in

Appendix B. The simplest way to estimate the net effect of the perturbed gravitational potential is to neglect the terms containing the ratio χ and compare the displacement obtained with and without the Cowling approximation, indicated as $\boldsymbol{u}^C$ and $\boldsymbol{u}$ respectively. In the limit $\chi = 0$ we find that

$$\frac{u_r}{u_r^C} = \frac{u_\theta}{u_\theta^C} = \frac{5}{2} + O\left(\chi^2\left(1-L\right)\right). \tag{3.40}$$

Therefore, in the FLE scheme, the displacements calculated with the Cowling approximation are 40% of the ones calculated by considering also the gravitational potential perturbation (see also Appendix B).

3.2.3 FLE model with M-R relation from realistic equations of state

In the previous section, we analyzed the main physical properties of the FLE model by using only benchmark values for R, L and M. In this section, instead, we will study the strain developed in rotating NSs by using the mass-radius relation of two very different equations of state, the soft SLy (Douchin & Haensel 2001) which, contrary to other EoSs, describes consistently both the core and crust stratification, and the stiff GM1 (Glendenning & Moszkowski 1991).

This use of "realistic" EoSs, albeit still quite approximate in this case of uniform density, links all the parameters of the star (i.e. R, L and ρ) to its mass M. Given the EoS, by solving the hydrostatic equilibrium equations (namely, the Tolman-Oppenheimer-Volkoff (TOV) equations), we obtain the mass radius relation $R(M)$. At this point, the star is continuously stratified, but to use the FLE model, we choose the average uniform density $\rho(M)$ as

$$\rho(M) = \frac{3M}{4\pi R(M)^3}. \tag{3.41}$$

Furthermore, also the parameter L can be determined for a given EoS and total stellar mass: solving the TOV equations we find the radius $R'(M)$ corresponding to the crust-core density transition of the particular EoS under study, so that we can fix $L(M) = R'(M)/R(M)$[4]. This approach simplifies our parametric study, since the choice of the stellar mass fixes self-consistently all the other parameters, giving also a better estimate of what we might expect in an astrophysical scenario.

In Figs 3.4 and 3.5 we show, respectively, the strain angle $\alpha(r,\theta)$ calculated for a $1.4M_\odot$ NS at different radii and the one calculated at $r = R'$ for different stellar masses by using the relation given by the EoSs. As expected from the previous analysis, the strain is a decreasing function of the radius and of the mass.

On the other hand, it is interesting to compare the maximum strain angle α^{Max} calculated with different EoSs (Fig 3.6). A stiffer equation of state gives larger maximum values of α^{Max}. Again, this is has to be expected from Eq (3.38); for the same stellar

[4] L is a parameter that in Newtonian gravity is trivially related with the crust thickness. In GR the estimation of the crust thickness is slightly more complicated, since one has to calculate the proper radial distance z_{crust} as

$$z_{crust} = \int_{R'}^{R} e^{-\lambda(r)} dr, \tag{3.42}$$

where

$$e^{\lambda(r)} = \left(1 - \frac{2Gm\left(r\right)}{rc^2}\right)^{1/2} \tag{3.43}$$

and m is the mass-energy of the star contained in a radius r.

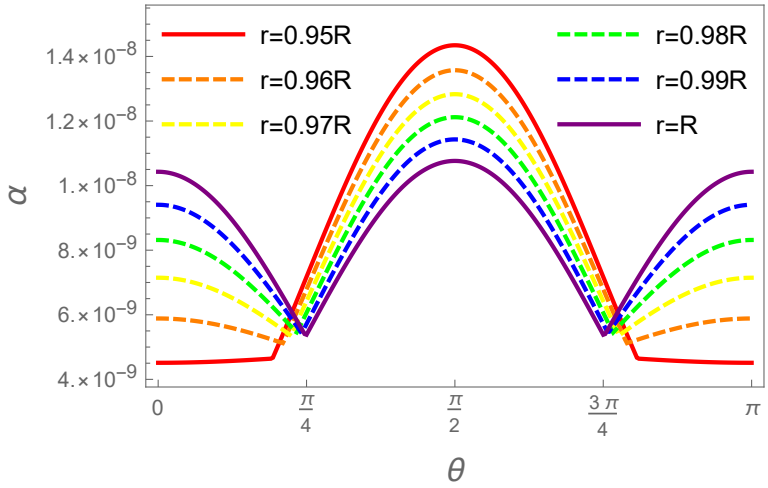

Figure 3.4: Strain angle α as a function of the colatitude for the original FLE model. The strain is calculated for $M = 1.4M_\odot$, with the SLy EoS, at different evenly spaced values of r, from $r = R'$ (red) to R (purple). In particular, we indicate with a solid line the innermost and outermost value of α, and a dashed line for the others. Again, the maximum strain occurs at the core-crust interface on the equatorial plane.

mass, a stiffer EoS gives a larger stellar radius, and thus a smaller compactness. Therefore, the numerical analysis confirms the qualitative picture that is expected from Eq (3.38); however, from the quantitative point of view, the use of more realistic combination of parameters, given by the use of the EoS, give larger strains with respect to the standard configuration ($M = 1.4M_\odot$, $R = 10$ km) chosen by Franco et al. (2000).

3.2.4 Glitches

The most important information that can be extracted from Fig 3.6 is that the maximum strain value (of the order of $\alpha^{Max} \sim 10^{-8}$) is three orders of magnitude smaller than the lowest theoretically expected breaking strain ($\sigma_{Max} \sim 10^{-5}$), when $\Omega\delta\Omega = 1\mathrm{rad}^2/\mathrm{s}^2$.[5]It is possible to give a rough estimate of the average spin-down $\delta\Omega$ that occurs between two glitches in a pulsar: given the spin down rate $\dot{\Omega} < 0$ and the average waiting time between glitches δt, we set $\delta\Omega = \omega = |\dot{\Omega}|\,\delta t$. In Table 3.1, the specific values of $\Omega\delta\Omega$ are reported for a selection of pulsars with at least 10 recorded events. Clearly, the most interesting pulsars for the present analysis are the ones with large values of the product $\Omega\,\omega$; the record holder is J0537-6910, followed by the Vela pulsar. As we can see, except for the Vela and J0537-6910, the actual rotational parameters can only decrease the values for the strain amplitude discussed above (that were all calculated for $\Omega\omega = 1\,\mathrm{rad}^2/\mathrm{s}^2$).

Therefore, according to the FLE model, it's unlikely that the spin down between two subsequent glitches could deform the crust enough to break it: the only viable possibility is that the crust is always in a stressed state, near the failure threshold.

The strain remains well below the critical threshold even in the limit of very light stars with stiff equation of state. Furthermore, if we consider the highest current estimate

[5]As already anticipated, all the values plotted in the figures have to be multiplied by $\Omega\delta\Omega$ in order to obtain the actual strain values of a specific pulsar.

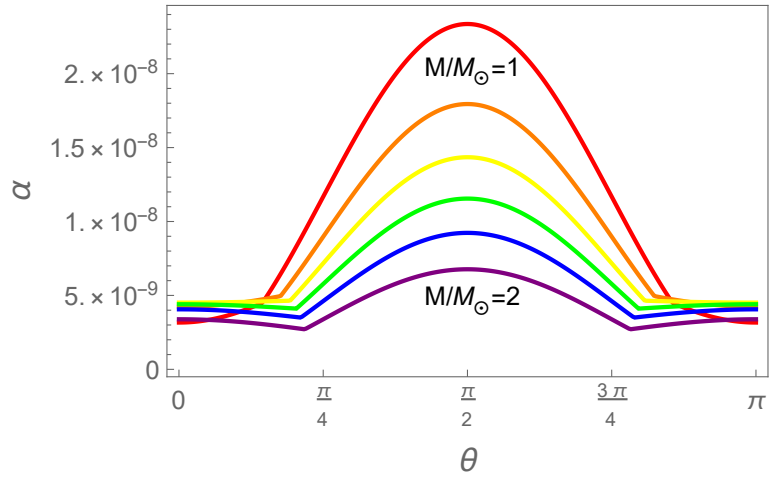

Figure 3.5: Strain angle α as a function of the colatitude for the original FLE model on a spherical shell of radius $r = R^{'}$, i.e. where the strain angle reaches its maximum value. The structural parameters have been fixed by considering the SLy EoS, for different stellar masses: $M = 1M_{\odot}$ (red), $M = 1.2M_{\odot}$ (orange), $M = 1.4M_{\odot}$ (yellow), $M = 1.6M_{\odot}$ (green), $M = 1.8M_{\odot}$ (blue), $M = 2M_{\odot}$ (purple).

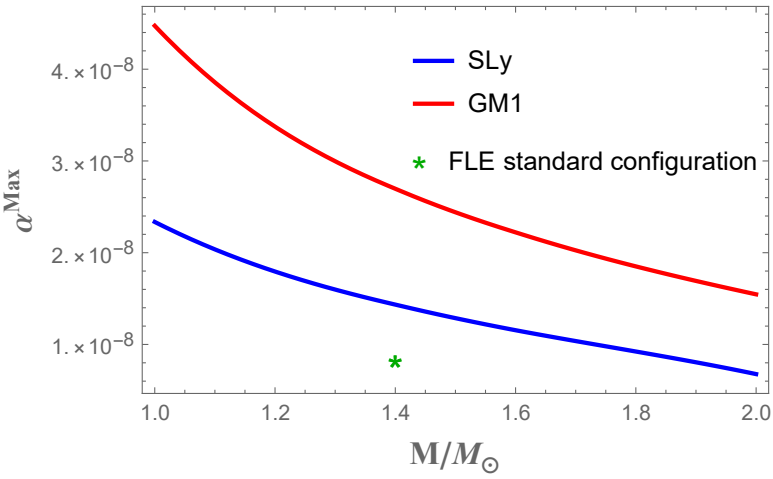

Figure 3.6: Comparison of the maximum values of the strain angle α^{Max} (which always occurs at $r = R^{'}$ and $\theta = \pi/2$), obtained with the original FLE model, as function of the stellar mass. A comparison between the SLy EoS (blue) and GM1 EoS (red) is made for our benchmark value $\Omega\delta\Omega = 1\,\mathrm{rad}^2/\mathrm{s}^2$. The green star indicates the maximum strain value obtained for the standard configuration used in (Franco et al. 2000) with $M = 1.4M_{\odot}$, $R = 10$ km, $L = 0.95$ (red curve of Fig 3.1). The curves approach for higher masses as the crust thickness decreases and R' gets closer to R; the GM1 line remains always well above SLy because a stiffer equation of state gives a thicker crust for the same mass.

Table 3.1: The rotational parameter $\Omega\delta\Omega$ that sets the actual value of the average stress developed in between two glitches is given for a selection of pulsars with at least 10 glitches. Data are taken from the Jodrell Bank Glitch Catalogue (www.jb.man.ac.uk/pulsar/glitches.html, see also Espinoza et al. 2011).

Pulsar Name	$\Omega\delta\Omega$ [rad^2/s^2]
J0537-6910	5±2
J0631+1036	0.006± 0.004
B0833-45 (Vela)	0.6± 0.3
B1338-62	0.04± 0.02
B1737-30	0.002± 0.002
B1758-23	0.005± 0.003
B1822-09	0.0002± 0.0001

of the breaking strain value $\sigma_{max} \sim 0.1$, we generally will not expect the crust to break via the spin down mechanism in the whole star life, as has been recently proposed by Fattoyev et al. (2018).

Finally, we can also compare the maximum strain angle using the original FLE approach (α_{FLE}) with the one obtained by using the homogeneous model of Baym and Pines (α_{BP}), where the star is described as an elastic, rotating, homogeneous spheroid: this is simply obtained by considering the limit $R' = 0$ of the FLE model. We choose $M = 1M_\odot$, and calculate all the other quantities according to the SLy equation of state, since the use of a light and soft star emphasizes differences (however, we observe that the same analysis can be done with the GM1 EoS or using some fiducial values for the stellar configuration, with analogous results). Both α_{FLE} and α_{BP} are the evaluated for the same radius r, that is the one at core-crust transition for a star obtained with the SLy EoS ($\rho_{core-crust} = 1.3 \times 10^{14}\mathrm{g/cm}^3$), and $\theta = \pi/2$, where the strain angle is maximum. In this case we obtain very similar values for the two models:

$$\alpha_{BP} = 2.33 \times 10^{-8}$$
$$\alpha_{FLE} = 2.55 \times 10^{-8}.$$

This result leads us towards another further step: the study of incompressible model in which the crust and the core can have different average densities.

3.3 Two-density model

The original FLE model provides a useful tool to estimate the deformation of a rotating NS in Newtonian gravity, but it is based on the strong assumption that the star must have the same constant density everywhere. In this section we show how to overcome this limitation, by using our self-consistent approach, where the neutron star is divided in two homogeneous layers representing the fluid core and the crust, with densities ρ_f and ρ_c respectively. As shown in section 3.1, the self-consistency of the model becomes manifest in two additional conditions for the gravitational potential. Note, in fact, that contrary to the FLE model, here one cannot use the knowledge of the gravitational potential of a perturbed homogeneous spheroid, but has to calculate it self-consistently by solving the perturbed Poisson equation.

In our two-density model, we find that the displacement $\boldsymbol{u}$ still has the same analytic form of the displacement given in Eq (3.31); this is not surprising as the main difference

with respect to the original FLE model lies in the treatment of the boundary conditions. In fact, at $r = R'$ we have a finite density discontinuity between the core and the crust, a detail which has to be carefully incorporated into the analysis of the crust-core interface. As a consequence, if we write down the displacement $\boldsymbol{u}$ in the form of Eq (3.33), the four coefficients $\tilde{a}, \tilde{b}, \tilde{A}, \tilde{B}$ will be functions not only of the thickness L and of χ, but also of the density ratio

$$d = \frac{\rho_c}{\rho_f} < 1. \tag{3.44}$$

As for the previous model, a simplified form for the coefficients $\tilde{a}$, $\tilde{A}$, $\tilde{b}$ and $\tilde{B}$ is given in Appendix B (the complete and exact form of the coefficients turns out to be much more complex with respect to the previous cases).

3.3.1 A first comparison with the original FLE model

We start by pointing out that the original FLE model can be obtained as a trivial limit $d = 1$ of our two-density model. In fact, imposing $d = 1$ in our model, we calculate the resulting displacement $\boldsymbol{u}$ and the analogous one (i.e. by using the same values of L, R, M and χ) with the FLE model, $\boldsymbol{u}^{FLE}$. The ratio between the two gives

$$\frac{u_r}{u_r^{FLE}} = \frac{u_\theta}{u_\theta^{FLE}} = 1 \text{ for } d = 1. \tag{3.45}$$

In other words, our model can be seen as a complete generalization of FLE approach, accounting in a self-consistent way for two different density in the NS core and crust.

We now follow the same analysis done for the FLE model in the previous section, varying in turn one parameter while keeping the others fixed. Since the parameter space is rather large, we will vary several parameters at the same time by using a realistic EoS in the next subsection. However, as a preliminary example, we make a comparison with the FLE model by studying a situation similar to the one described in Fig 3.1, which corresponds to a star with $R = 10$ km and mass $M = 1.4 M_\odot$: in Fig 3.7 we plot the strain at different radii for the two density model, using some fiducial values of the parameters involved, with $\rho_f \approx 7.8 \times 10^{14}\,\mathrm{g/cm^3}$ and $d = 0.1$, such that the total mass is still of $1.4\,M_\odot$. Firstly, we note that the strain angle in this case is larger with respect to the FLE one. Furthermore, as the radial dependence of $\alpha(r, \theta)$ shows, the strain angle reaches its maximum value α^{Max} at the crust-core interface. However, differently with respect to the FLE model, in this case the value of the strain is highest at the poles. Even more interestingly, the "bump" of the strain angle near the equator is due to the change of the failure plane at different colatitude. This deserves a little comment. Generally speaking, the strain tensor will be in the form

$$\sigma_{ij} = \begin{pmatrix} \sigma_{rr} & \sigma_{r\theta} & 0 \\ \sigma_{r\theta} & \sigma_{\theta\theta} & 0 \\ 0 & 0 & \sigma_{\varphi\varphi} \end{pmatrix}, \tag{3.46}$$

and thus will have an eigenvector along φ and other two in the r, θ directions. The strain angle is the difference between the local maximum and minimum eingevalues, that are related to two different eigenvectors. These two eigenvectors define a plane, that is perpendicular to the fault plane where the stress is maximum. Now, near the poles the largest and the smaller eigenvalues correspond to two eigenvectors, one in the r, θ plane and the other in the φ direction, which means that the star could break along the

meridians. On the contrary, near the equator the situation changes, since the maximum and the minimum eigenvalues are both in the r, θ plane, which means that the star will break along the φ direction, i.e. along the parallels.

As a first check, we set $\rho_f = \rho_c$ in the two-density model and we find, as expected, that the maximum strain is placed at the equator (cf Eq (3.45)). Therefore, the stratification (i.e. the presence of layers with different densities), introduces a new degree of freedom into the model. In this way, by changing the value of the d parameters the region of maximum stress moves away from the equator towards the poles.

Furthermore, we observe that, although the value of the strain angles obtained with the new model are larger than the one of the FLE approach, α is still well below the minimum breaking threshold of 10^{-5}.

As a final comparison, despite the fact that α is still a decreasing function of L, we note that the crust thickness has a larger impact on the strain value compared to the FLE model. In this case, in fact, we find, for a $1.4\,M_\odot$ NS, $d = 1/10$, $\alpha^{Max}(L = 0.85)/\alpha^{Max}(L = 0.95) \simeq 1.6$, (cf. with the factor 1.3 in Fig 3.3), as can be seen in Fig 3.8 where the strain angle, computed for a fixed stellar configuration, is shown as a function of the thickness parameter L.

3.3.2 Realistic equations of state

As already done for the FLE model in section 3.2.3, we investigate the behaviour of the two-density model by imposing that not all the parameters present in the equations are free: they have to satisfy the constrain which arises by the fact that an EoS for the internal matter is related to a particular mass-radius relation. In order to fix the fluid core density, here we use the simply prescription

$$\rho_f \simeq \frac{M}{4/3\pi\,(L \cdot R)^3}. \tag{3.47}$$

On the other hand, the exact value of d, whose definition is in Eq (3.44), is found by the appropriate relation due to the particular EoS that has been chosen and therefore is a known function of the stellar mass. The crust density can be assumed to be

$$\rho_c = d\rho_f \simeq d\frac{M}{4/3\pi\,(L \cdot R)^3}. \tag{3.48}$$

In Fig 3.9 the strain angle at the core-crust interface is shown for different stellar masses. As expected, also in this case we have that the strain decreases when the total mass is increased: again, heavier stars have smaller radii and higher density, and are thus more difficult to deform. However, we highlight the new interesting feature that never arises by using the original FLE model: the maximum strain α^{Max} is now, in most of the cases, at the poles. Interestingly, for the softer EoS and for heavier objects, there are also cases where the maximum is still at the equator. Here, in fact, the crust is extremely thin, and the strain tends to resembles the LFE behaviour. However, when the opposite is true, the crust gains a great importance in the strain shape, bringing the maximum at the poles, as can be seen also in Fig 3.11, where the strain angle color map for a standard NS of $M = 1.4M_\odot$ is shown.

Finally, in Fig 3.10 we compare the maximum strain angle α^{Max} as function of the stellar mass, calculated with the FLE and the two-density model, using both SLy and GM1 EoSs. Again, stiffer EoS gives larger strain, as discussed above. The use of our

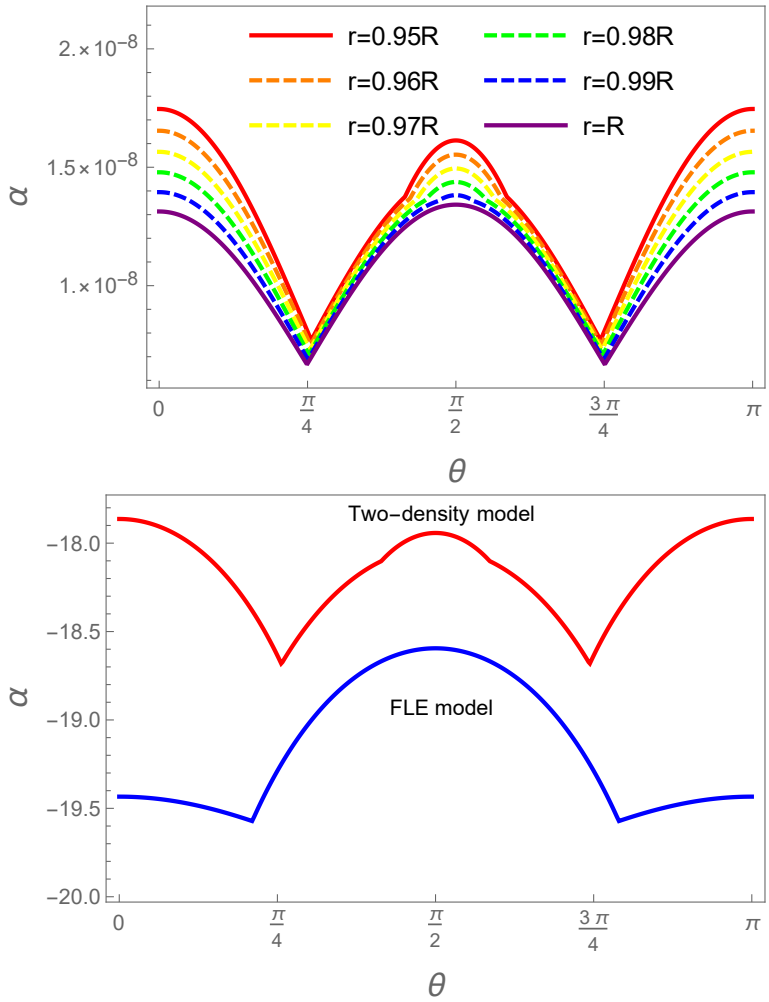

Figure 3.7: *(Top)* Strain angle as a function of the colatitude θ for the two-density model and fixed benchmark values $M = 1.4M_\odot$, $R = 10\,\text{km}$, $L = 0.95$, $\rho_f = 7.8 \times 10^{14}\text{g/cm}^3$, $\rho_c = \rho_f/10$. The strain angle is calculated for different values of the radius: $r = R$ (purple), $r = 0.99R$ (blue), $r = 0.98R$ (green), $r = 0.97R$ (yellow), $r = 0.96R$ (orange) and $r = 0.95R$ (red). In particular, we indicate with a solid line the innermost and outermost values of α, and with a dashed line the others. We used $\Omega\delta\Omega = 1\,\text{rad}^2/\text{s}^2$. *(Bottom)* Log-scale comparison of the strain angle calculated for the same configuration ($M = 1.4M_\odot$, $R = 10\,\text{km}$, $L = 0.95$, $r = R'$) using the FLE (blue, dashed) and the two-density (red) models.

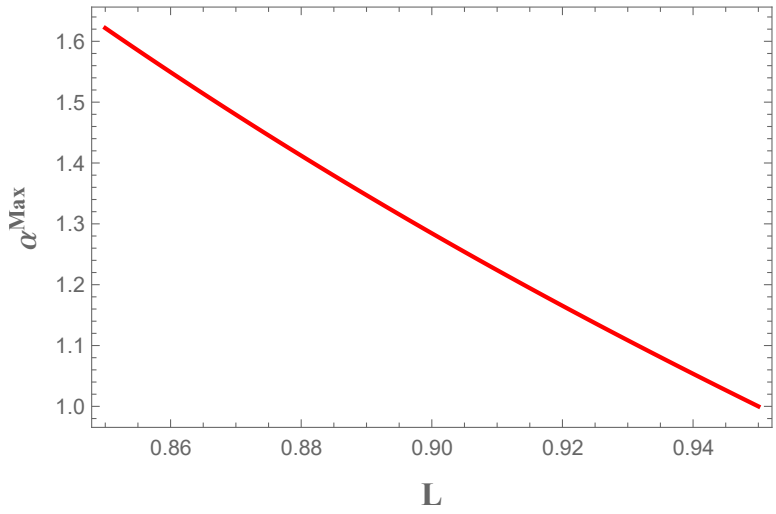

Figure 3.8: The maximum strain angle as a function of the thickness parameter $L = R'/R$ for the two-density model and fixed benchmark values $M = 1.4M_\odot$, $R = 10\,\text{km}$, $d = 1/10$ (cf. with Fig 3.3). The strain angle is normalized at the value reached for $L = 0.95$ and calculated at the core-crust interface $r = R'$. We used $\Omega\delta\Omega = 1\,\text{rad}^2/\text{s}^2$.

model allows to get larger strains, that are typically two times larger than the ones obtained with FLE model. As noted above, however, in both scenarios the maximum strain angle is still far even from the minimum breaking strain value of $\sim 10^{-5}$. Therefore, the analysis with this two-density model confirms that, starting from an unstressed configuration, the deformation due only to the inter-glitch spin down is not large enough to trigger a starquake.

3.4 Outlook

In this chapter we have studied what is the response of an incompressible neutron star under the effect of rotation. In particular, we have shown that the strain is scarcely influenced by the stellar mass, and by the crust thickness, while it depends mainly on the compactness parameter M/R. Furthermore, we have shown that a *stratification*, i.e. the presence of two layers with two different densities affects the strain, both in shape and amplitude. For this reason, in the next chapter we will study the behaviour of a compressible NS.

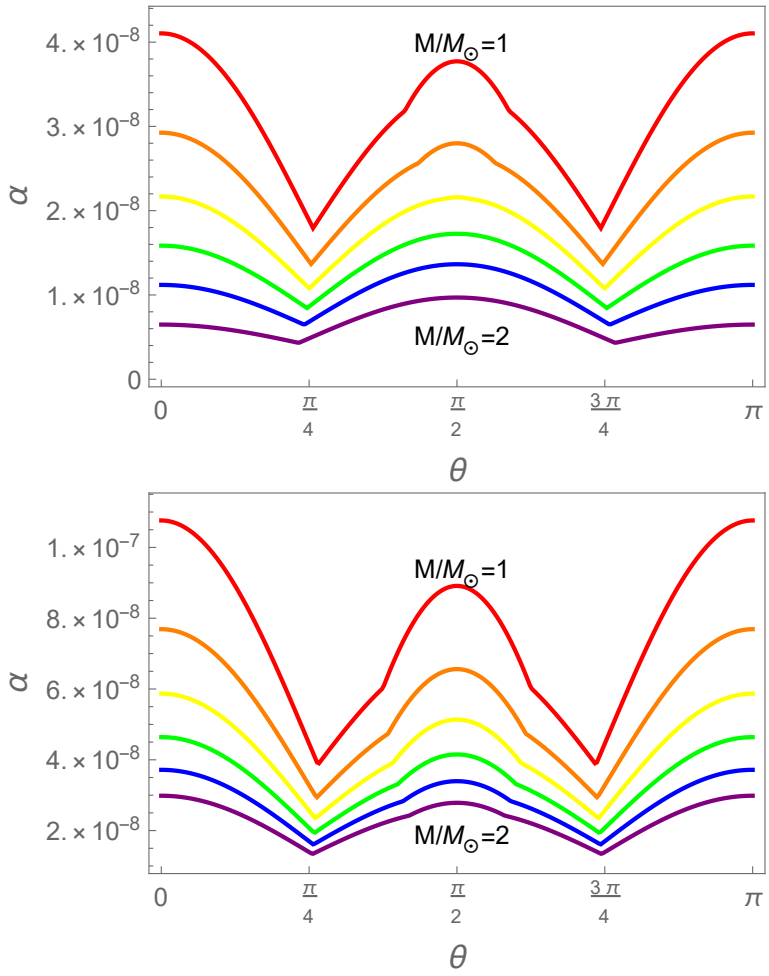

Figure 3.9: Strain angle at $r = R^{'}$ as a function of the colatitude θ for the two-density model and different masses: $M = 1M_{\odot}$ (red), $M = 1.2M_{\odot}$ (orange), $M = 1.4M_{\odot}$ (yellow), $M = 1.6M_{\odot}$ (green), $M = 1.8M_{\odot}$ (blue), $M = 2M_{\odot}$ (purple). The stellar structural parameter are fixed by using the SLy EoS in the upper panel, while GM1 was used for the lower one.

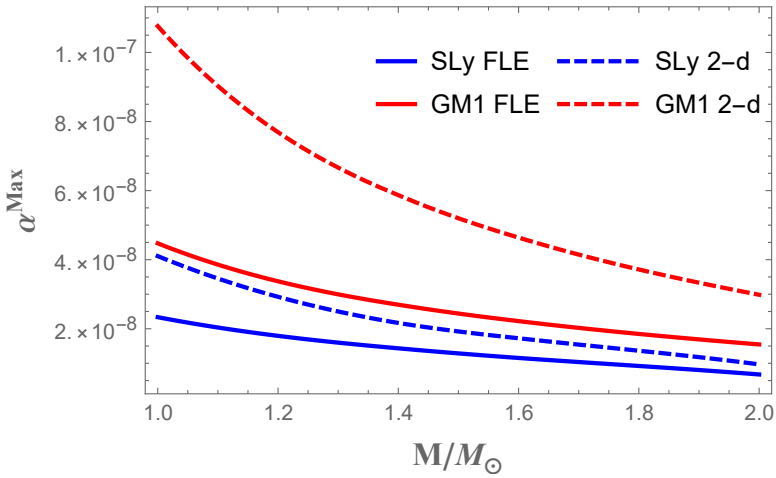

Figure 3.10: Maximum strain angle α^{Max} (which occurs at the core-crust interface) as a function of the stellar mass for the FLE (solid curves) and for the two-density model (dashed curves). The red curves refer to the GM1 equation of state, blue curves to SLy.

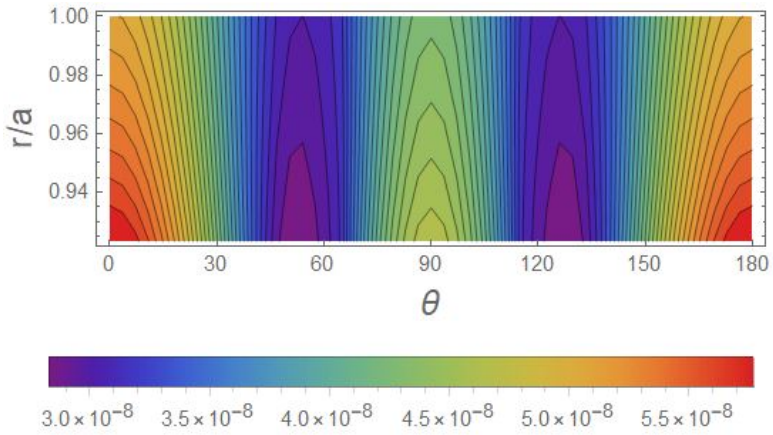

Figure 3.11: Color map of the strain angle α as a function of the colatitude and of the normalized radius r/R. The region shown here refers to the crustal layer, from $r = r_c$ to $r = R$ for a $M = 1.4M_\odot$ NS described by the SLy EoS. As can be seen, the maximum strain value is reached at the core-crust boundary.

Part IV
Compressible models

CHAPTER 4

Uniform rotating star

In this chapter we will study the effect of rotation on a self-gravitating, compressible star. We expect to see the influence of two main characteristics on the strain angle α: the star's stratification and its adiabatic index value. In fact, the analysis of models describing incompressible NSs in the previous chapter has shown that the stratification is a key characteristic that influences the shape of the strain angle in the crust. Furthermore, we know that the value of γ is crucial for the star's response since it is related to the bulk modulus by $\kappa = \gamma P$ (for instance, incompressibility is associated with infinitely large adiabatic index). Thus, the adiabatic index could have a large impact on the global star's rearrangement. As said previously in chapter 2, since for most of the EoSs the main differences between the equilibrium and the frozen adiabatic index are expected to be in the crust (Ushomirsky et al. 2000), we choose to change the value of γ just there.

4.1 Numerical solution for the polytrope $n = 1$

We will study the behaviour of a NS described by a polytrope with $n = 1$. In particular, we are interested in the comparison of displacements and strains of neutron stars with different masses. In fact, in this case we have a degenerate mass-radius relation, in the sense that the radius a and the mass M are independent of one another, allowing us to choose a suitable pair a, M from a realistic equation of state. Thus we consider the SLy equation of state (Douchin & Haensel 2001), solve the Tolman-Oppenheimer-Volkoff equations (TOV), see Fig 4.1, and fix the relation $a(M)$. In other words, despite the fact that the description of the star is made in a Newtonian framework, the mass-radius relation of the reference configuration is the one obtained in General Relativity, giving us realistic values of the radius and implying a reasonable estimates of the centrifugal force, as already done in the previous chapter.

For a given mass M in the range $1M_\odot \div 2M_\odot$ we can calculate the corresponding value of K in Eq (2.17) and of the central density $\rho_{ce} = \rho(r = 0)$ as

$$K = \frac{2}{\pi} a^2 G$$
$$\rho_{ce} = \frac{M}{4\pi^2} \left(\frac{K}{2\pi G} \right)^{-3/2} .$$

Following Ushomirsky et al. (2000), the crust-core transition is set at the fiducial density $1.5 \times 10^{14}\mathrm{g/cm}^3$, that implies a core-crust transition at $r_c \approx 0.90\, a$ for a standard neutron star with $M = 1.4M_\odot$.

The outer-crust boundary is placed at the density $1 \times 10^{11}\mathrm{g/cm}^3$ in order to guarantee the numerical stability of the solution against the computational problems due to the

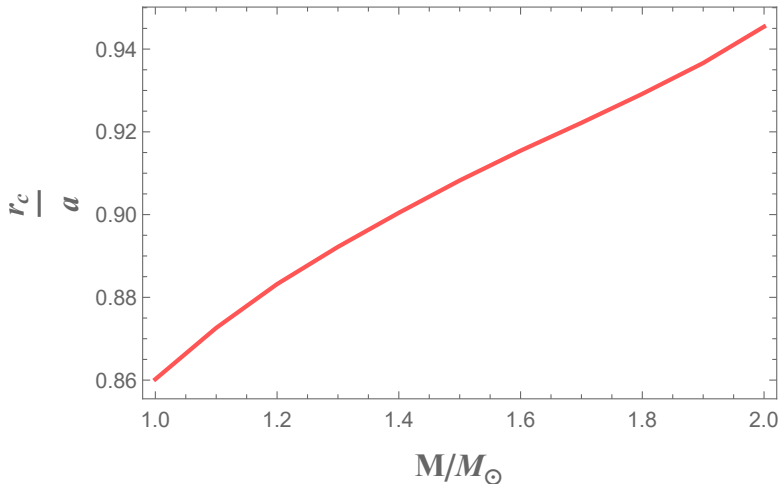

Figure 4.1: Normalized core-crust radius r_c/a as a function of the stellar mass, obtained for the SLy EoS.

Table 4.1: Parameters for a typical neutron star with $M = 1.4M_\odot$, as considered in this work. The angular velocity is set to the reference value 1 rad/s, so that the our numerical results can be easily rescaled to the case of different angular velocities by simply multiplying for the chosen squared angular velocity value Ω^2.

a (cm)	$\rho_{ce}(\mathrm{g/cm^3})$	$\mu_c(\mathrm{dyn/cm^2})$	$\Omega(\mathrm{rad/s})$
1.17×10^6	1.38×10^{15}	10^{30}	1

very rapid variation of the density in the outermost layers (Ushomirsky et al. 2000). Since the outer crust represents only a negligible fraction of the stellar mass, this truncation is not expected to have a severe impact on our numerical calculations.

All the physical quantities in our code are normalized by using the stellar radius a, the central density ρ_{ce}, the typical shear modulus μ_c at the core-crust interface r_c and the angular velocity Ω of the particular NS under consideration. The first two parameters vary with M, while the other two are fixed. In Tab 4.1 we report some values for a $M = 1.4M_\odot$ neutron star. In the following we show the results for a NS having the values reported in Tab 4.1, if not otherwise stated.

In order to get the dimensional quantities for a given angular velocity Ω, it is necessary to multiply these functions by the dimensionless factor

$$d\,(\Omega) = \frac{1}{3}\frac{\Omega^2 a^2}{v^2}\,, \tag{4.1}$$

where v is a velocity defined as $v = \sqrt{\mu_c/\rho_{ce}}$. To be more explicit, the results must be rescaled as

$$\boldsymbol{y} = d\,(\Omega) \times \begin{pmatrix} a \\ a \\ \mu_c \\ \mu_c \\ v^2 \\ v^2/a \end{pmatrix} \tilde{\boldsymbol{y}}\,, \tag{4.2}$$

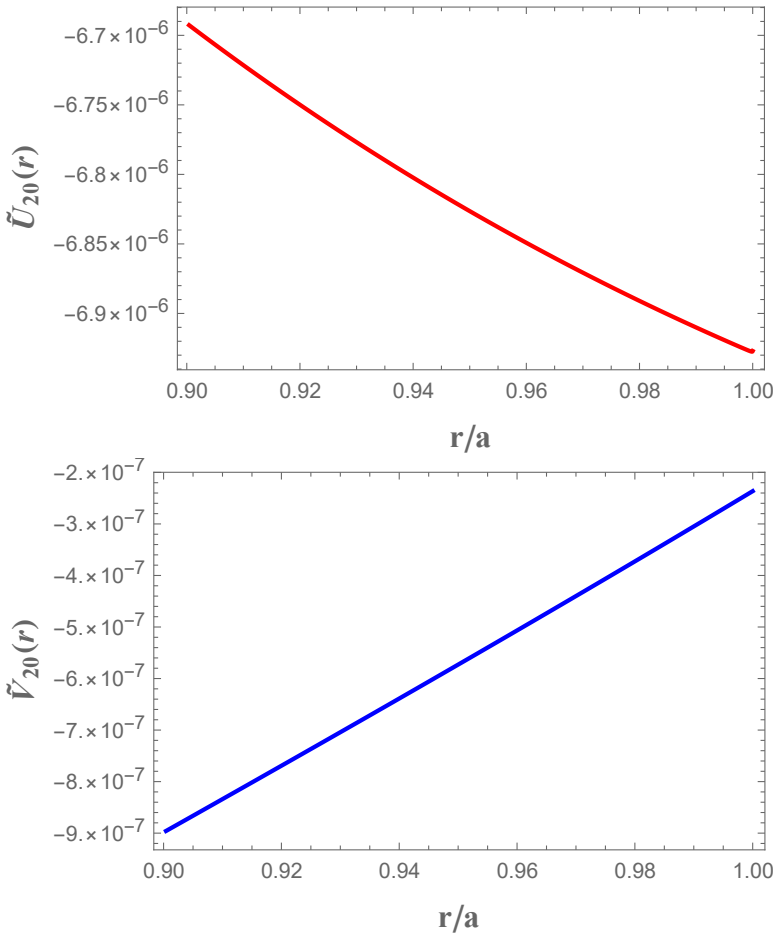

Figure 4.2: The $\tilde{U}_{20}(r)$ (top) and the $\tilde{V}_{20}(r)$ (bottom) normalized displacements as functions of the normalized radius, from $r = r_c$ to $r = a$.

where the tilde superscript indicates the dimensionless quantities. For practical purposes one can use the expression

$$d(\Omega) = 6.2 \times 10^{-4} \left(\frac{\Omega}{1\text{rad/s}}\right)^2 \left(\frac{\rho_{ce}}{1.38 \times 10^{15}\text{g/cm}^3}\right) \times \\ \times \left(\frac{\mu_c}{10^{30}\text{dyn/cm}^2}\right)^{-1} \left(\frac{a}{1.167 \times 10^6\text{cm}}\right)^2, \quad (4.3)$$

calculated by using a $M = 1.4 M_\odot$ neutron star as a reference. The elastic response of the star is fixed by the EoS and by the poorly known parameters κ and μ in the crust. We underline that the adiabatic index γ plays a fundamental role in the equilibrium configuration of the NS, since it is linked to the elastic modulus κ by the relation

$$\kappa = \gamma P\,. \quad (4.4)$$

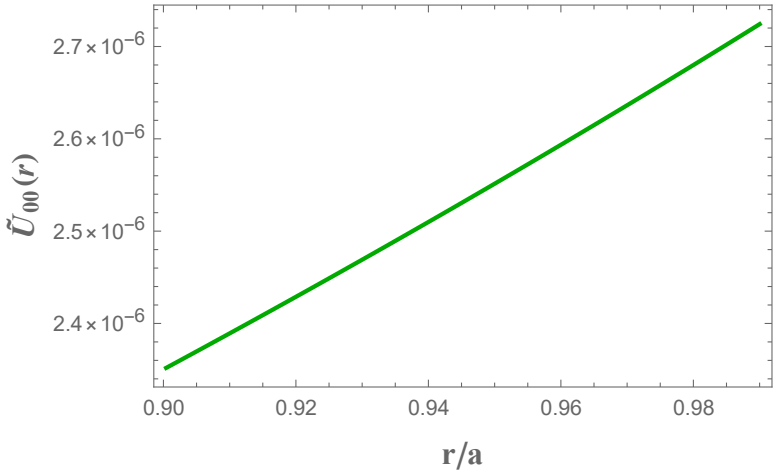

Figure 4.3: The $\tilde{U}_{00}\,(r)$ normalized displacement as a function of the normalized radius, from $r = r_c$ to $r = a$.

For the shear modulus we follow the same prescription as that of Cutler et al. (2003),

$$\mu(r) = 10^{-2} \times P(r)\,. \tag{4.5}$$

Clearly this relation holds only in the crustal layer, since in the *fluid* core the shear modulus is zero. The EoS, the adiabatic index governing perturbations, the shear modulus and the boundary densities which define the layers completely fix the elastic behaviour of the star: we can now study the effects of the centrifugal force, starting from a non-rotating and unstressed reference configuration.

4.1.1 Slow dynamics

We choose at first the equilibrium bulk modulus, given by Eq (4.4)

$$\kappa\,(r) = \gamma_{eq} P(r) = 2P(r)\,. \tag{4.6}$$

With this choice we are implicitly assuming that the stellar evolution has a much longer timescale compared to the one of the chemical reactions near equilibrium.

The centrifugal potential is particular as its expansion consists of only two spherical harmonics having $m = 0$, one with $\ell = 0$ and another one with $\ell = 2$. In the following, we will show the displacements and strains due to each of these contributions separately; the total effect of rotation is given by the sum of the two.

In Fig 4.2 the radial and tangential displacements are shown for the harmonic $\ell = 2$, while the harmonic term $\ell = 0$ is presented in Fig 4.3. According to our model and with the parameters given in Table 4.1, the displacement with respect to the non-rotating configuration is of the order of $|u_r(a)| \simeq 4.2 \times 10^{-3}$ cm at the equator. As we can see, the harmonic degree $\ell = 0$ gives a smaller contribution to the total displacement if compared to the $\ell = 2$ contribution as we find that $2.5 \leq |U_{20}/U_{00}| \leq 2.9$. Note that the $\ell = 0$ contribution corresponds to a global increase of volume of the star, since it is positive at every latitude.

Let's now explore the possibility of crust failure, by calculating the strain angle α and using the Tresca criterion in Eq (2.9). In Fig 4.4, the normalized strain angle $\tilde{\alpha} = \alpha/d(\Omega)$

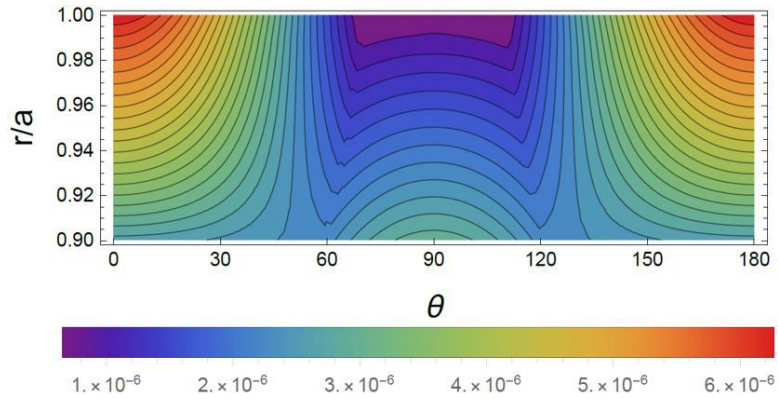

Figure 4.4: Color map of the normalized strain angle $\tilde{\alpha}$ as a function of the colatitude and of the normalized radius r/a. The region shown here refers to the crustal layer, from $r = r_c$ to $r = a$ for a neutron star with mass $M = 1.4 M_\odot$. As can be seen, the maximum strain value is reached at the stellar surface.

is shown as a function of the colatitude θ and of the normalized radius r/a. Our analysis shows that:

1. The strain angle is an increasing function of the radius, *contrary to the uniform, incompressible case* studied by Franco et al. (2000) and Giliberti et al. (2018). This was already noticed by Cutler et al. (2003): in the present model the shear modulus is not a constant but a decreasing function of the stellar radius, implying that the strain is expected to be larger near the surface.

2. Differently from the incompressible and uniform model of Franco et al. (2000), used also recently by Fattoyev et al. (2018), where the strain maximum is at the equator, in the case discussed here we find that the maximum value of the strain angle α^{Max} occurs at the *poles*.

3. For what concerns the dependence on mass, α is a decreasing function of M, as can be seen in Fig 4.5. Note that in this case we cannot simply study the normalized strain angle, since also the normalizing factor in Eq (4.1) depends on the stellar mass through a and v. Hence, in order to give a result that can be easily rescaled, we impose $\Omega = 1\,\mathrm{rad/s}$. The behaviour of α can be more easily understood by considering the incompressible limit of our model analyzed in the previous chapter, The key factor for the global behaviour of α is hidden into the factor W, which turns out to be proportional to

$$W \propto \frac{a^3}{GM} \propto \frac{1}{\rho}\,. \tag{4.7}$$

   Therefore, for more massive (i.e. denser) stars, smaller displacements are expected. This reasonable behaviour, which appears as a by-product of the simplified incompressible models remains a typical feature of more refined models, as can be seen in Fig 4.5.

4. The strain has a slightly larger slope as a function of M if we compare the homogeneous and the compressible models. In the first case, the ratio between the

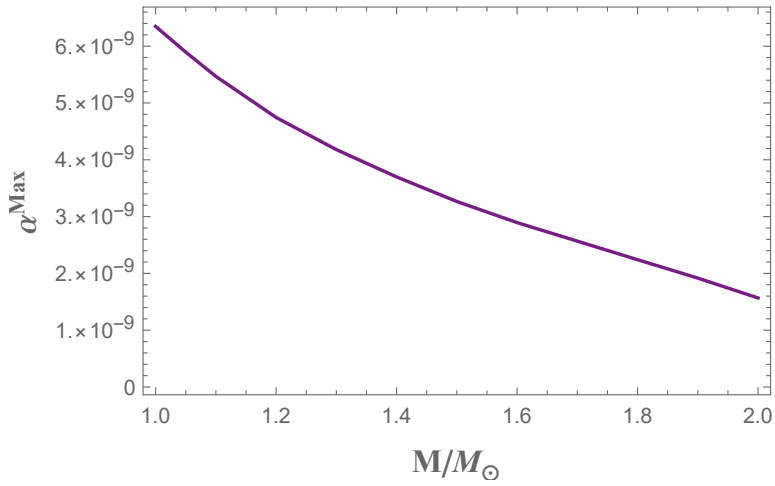

Figure 4.5: The maximum strain angle as a function of the mass, assuming $\gamma = \gamma_{eq}$ and $\Omega = 1$ rad/s.

maximum strain angle α calculated for a $M = 1\,M_\odot$ and for $M = 2\,M_\odot$ is about $2 \div 3$, depending on the EoSs used (see chapter 3), while in the compressible case we have

$$\frac{\alpha^{Max}\,(M = 1M_\odot)}{\alpha^{Max}\,(M = 2M_\odot)} \simeq 4\,. \tag{4.8}$$

In this sense, we expect the strain angle to have a stronger dependence on the stellar mass in refined and realistic models with respect to what is found by employing an homogeneous model.

4.1.2 Fast dynamics

We want now to explore a different scenario, assuming that the dynamical timescale of the perturbations is fast with respect to the reactions ones. This can be done by using the frozen adiabatic index instead of the equilibrium one, i.e.

$$\kappa\,(r) = \gamma_f P(r)\,. \tag{4.9}$$

Since the polytropic EoS that we employ does not have a typical value for the non-equilibrium adiabatic index, we make a comparison between different values of γ_f. This allows us to study how the adiabatic index value changes the star's response to the same external centrifugal force: we compare the displacements, stresses and strains in four different cases, characterized by the adiabatic indices $\gamma_1 = 2$, $\gamma_2 = 2.1$, $\gamma_3 = 200$ and $\gamma_4 = \infty$. The value of γ_2 is 5% larger than the equilibrium adiabatic index, while γ_3 mimics a very strong departure from the equilibrium, towards the incompressible limit $\gamma \to \infty$; actually, we expect the same stellar response for γ_3 and γ_4, since the first is just a numerical counterpart of the analytical incompressible limit.

It is extremely interesting to observe that even a small departure from the equilibrium value of the adiabatic index carries the system to a configuration similar to the incompressible one, as can be seen in Figs 4.6 and 4.7. Figure 4.6 shows the normalized values of $\tilde{U}_{20}$ and $\tilde{V}_{20}$ for a $M = 1.4M_\odot$ rotating neutron star, according to the values

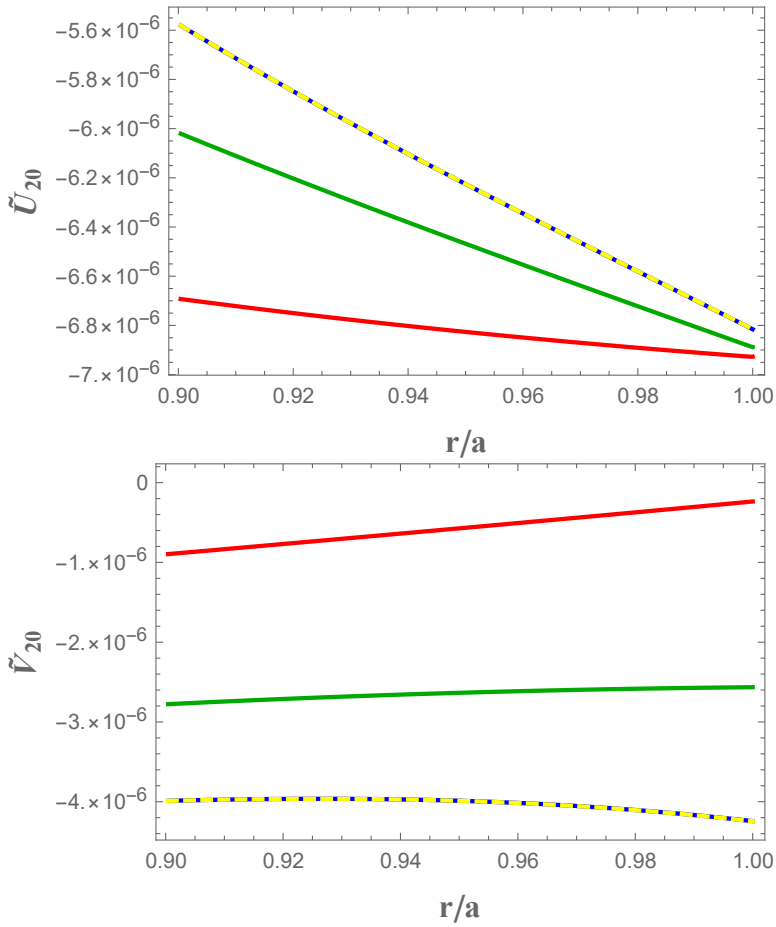

Figure 4.6: Normalized $\tilde{U}_{20}(r)$ (top) and $\tilde{V}_{20}(r)$ (bottom) displacements as function of the normalized radius. The plot refers to the crustal region, extending from $r = r_c$ to $r = a$. The same procedure is used with different adiabatic indices: $\gamma = 2$ (red), $\gamma = 2.1$ (green), $\gamma = 200$ (blue) and $\gamma = \infty$ (yellow dashed).

listed in Tab 4.1; the response of the star to the same change of the centrifugal force is very different in the equilibrium scenario with respect to the frozen ones. The same consideration is valid for the radial stress $\tilde{R}_{20}$ and the tangential stress $\tilde{S}_{20}$, as shown in Fig 4.7.

Figure 4.8 represents the radial displacement U_{00} for the same stellar mass $M = 1.4M_{\odot}$: again we note the difference between the equilibrium scenario and the frozen ones, with the change of the slope of the plotted curve for different γ.

This behaviour, that could seems strange, can be explained by focusing our attention on the particular physical elastic condition of NSs. Since in a neutron star it is expected that (Chamel & Haensel 2008)

$$\frac{\mu}{\kappa} \ll 1\,, \tag{4.10}$$

the key physical aspects of the problem are already present by studying the $\mu \to 0$ limit.

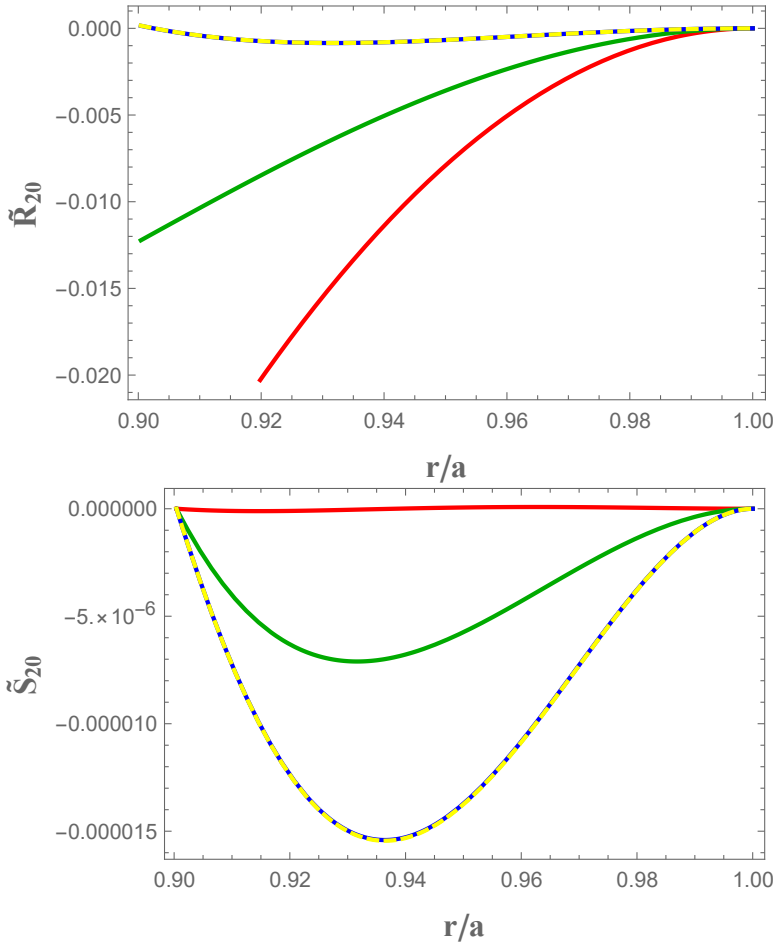

Figure 4.7: Normalized $\tilde{R}_{20}(r)$ (top) and $\tilde{S}_{20}(r)$ (bottom) stresses as function of the normalized radius. The plot refers to the crustal region, extending from $r = r_c$ to $r = a$. We used different adiabatic indices: $\gamma = 2$ (red), $\gamma = 2.1$ (green), $\gamma = 200$ (blue) and $\gamma = \infty$ (yellow dashed).

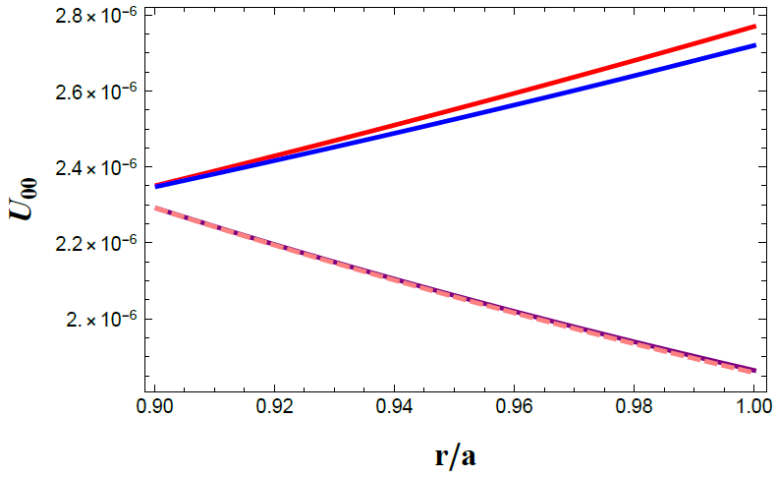

Figure 4.8: Normalized $\tilde{U}_{00}\,(r)$ displacement as function of the normalized radius, in the region between $r = r_c$ and $r = a$. As in the other figures, the curves refer to the results calculated by considering $\gamma = 2$ (red), $\gamma = 2.1$ (blue), $\gamma = 200$ (purple) and $\gamma = \infty$ (pink, dashed).

Therefore, we can consider the equilibrium equations (2.33) and (2.34) in the reduced form given for the fluid limit in Eqs (2.61) and (2.62), obtaining Eq (2.15). Now, if $\gamma \neq \gamma_{eq}$ the Adams-Williamson equation (2.15) requires $\chi_{\ell m}$ to be zero, implying that there can be no volume changes, see Eq (2.36) and thus

$$R_{\ell m} = \kappa \chi_{\ell m} = 0. \tag{4.11}$$

Via Eq (2.62) it is possible to show that the radial displacement must coincide with the geoid perturbation defined in Eq (2.69). Thus, for a realistic NS we expect that if $\gamma \neq \gamma_{eq}$

$$U_{\ell m} = -\frac{\Phi_{\ell m}}{g}. \tag{4.12}$$

As a check, let us focus on the $\ell = 2$ harmonic contribution by studying the radial displacement U_{20} and the geoid radial displacement. For the shear modulus provided in Eq (4.5), the difference between the radial and the geoid displacements decreases by increasing the adiabatic index, as can be seen in Fig 4.9: in the $\gamma_f = \gamma_{eq}$ case (panel-a) we have a clear departure from the geoid, but if $\gamma_f = 200$ (panel-d) the two radial displacements almost coincide. Furthermore, as expected, the cases $\gamma_f = 200$ and $\gamma_f = \infty$ give in practice the same results.

As a further step towards a better understanding of the response of the star, we calculate the radial and the geoid displacements for $\gamma_f = 2.1$ but with a shear modulus that is smaller than the one considered in Eq (4.5). When the elastic shear becomes smaller, the radial U_{20} displacement and the geoid one become similar, as shown in Fig 4.10. This expected behaviour has been also discussed in Cambiotti & Sabadini (2010) and Cambiotti et al. (2013) for a viscoelastic Earth model at large time scales (from million to billion years), when the shear stress goes to zero due to stress relaxation by viscous flow (as in the $\mu \to 0$ limit).

To properly understand the contribution of the $\ell = 0$ harmonic we need a further argument. As the out-of-equilibrium adiabatic index value increases, we approach the

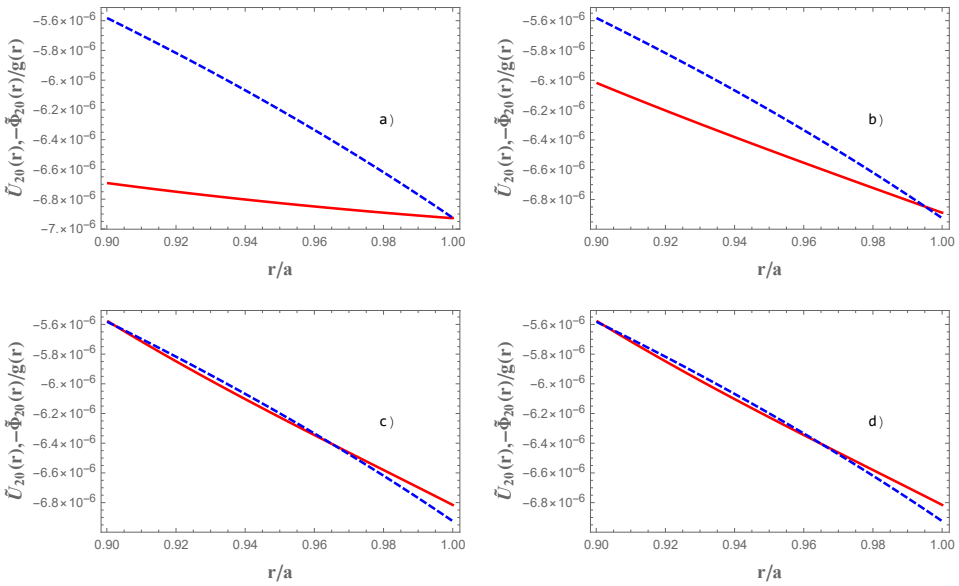

Figure 4.9: Radial $\tilde{U}_{20}$ (red, solid) and geoid (blue, dashed) normalized displacements as a function of the normalized radius, from $r = r_c$ to $r = a$, for fixed shear modulus μ and different values of the adiabatic index: $\gamma = 2$ (a), $\gamma = 2.1$ (b), $\gamma = 200$ (c) and $\gamma = \infty$ (d). As discussed in the text the incompressible limit $\gamma = \infty$ gives the same response as the case in which $\gamma = 200$. As can be seen, as the adiabatic index value increases to the incompressible limit, the radial displacement tends towards the geoid one (Eq (2.69)), as happens exactly in a pure fluid medium.

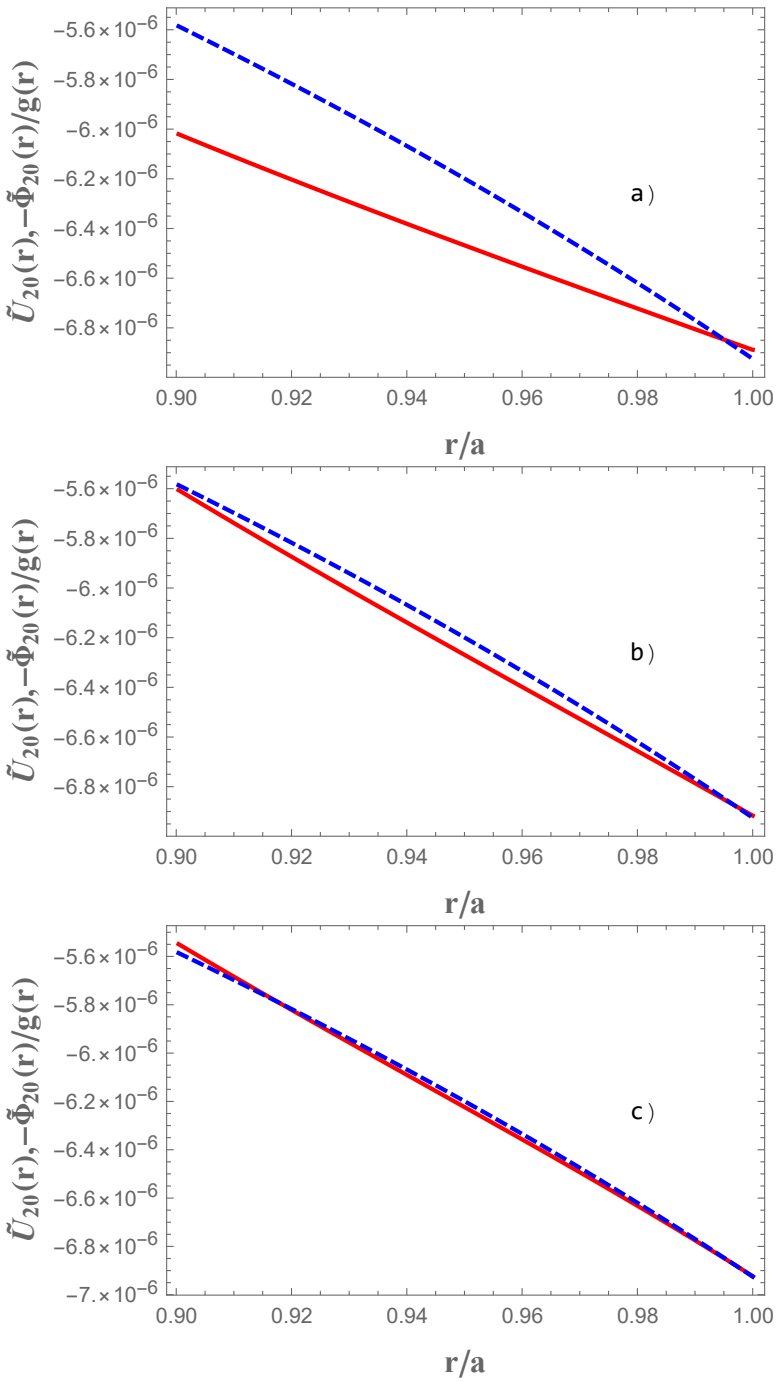

Figure 4.10: Radial $\tilde{U}_{20}$ (solid, red) and geoid (blue, dashed) normalized displacements as a function of the normalized radius, from $r = r_c$ to $r = a$, for fixed adiabatic index $\gamma = 2.1$ and $\mu = 10^{-2}P$ (a), $\mu = 10^{-3}P$ (b) and $\mu = 10^{-4}P$ (c).

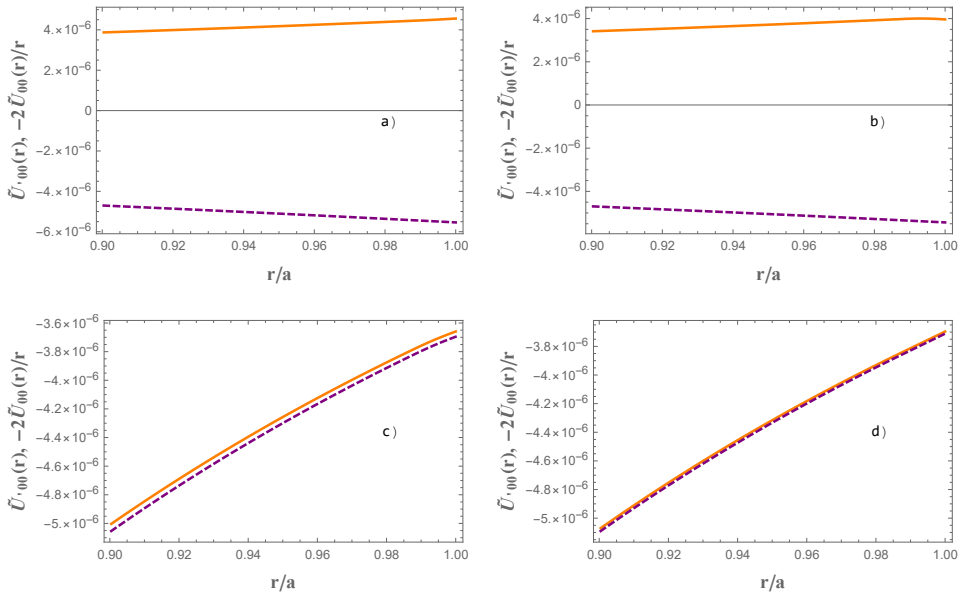

Figure 4.11: $\partial_r \tilde{U}_{00}$ (orange) and $-2\tilde{U}_{00}/r$ (purple) calculated for $\gamma = 2$ (a), $\gamma = 2.1$ (b), $\gamma = 200$ (c) and $\gamma = \infty$ (d). As explained in the main text, for growing value of the adiabatic index, we expect that for satisfying the equilibrium equations the difference between $\partial_r \tilde{U}_{00}$ and $-2\tilde{U}_{00}/r$ must go to zero.

incompressible limit, which provides a strong bond on the radial displacement. In fact, incompressibility requires $\chi_{\ell m} = 0$, and thus, reminding that

$$\chi_{\ell m} = \partial_r U_{\ell m} + \frac{2}{r} U_{\ell m} - \frac{\ell\,(\ell+1)}{r} V_{\ell m}\,, \tag{4.13}$$

we find (the $\ell = 0$ displacement is purely radial, i.e. $V_{\ell m} = 0$)

$$\partial_r U_{00} = -2\frac{U_{00}}{r}\,. \tag{4.14}$$

We remind that in our model we vary only the crust adiabatic index, and thus the core maintains its equilibrium compressibility also in the limiting case in which the crust is incompressible. Therefore, also for $\gamma_f = \infty$ the radial displacement is different from zero because the core modifies its shape during the spin-down, loading the crust. The balance between the core stress and the incompressible relation (4.14) determines the radial displacement of the $\ell = 0$ harmonic. In Fig 4.11 both $\partial_r \tilde{U}_{00}$ and $-2\tilde{U}_{00}/r$ are shown for the four different adiabatic indices considered.

In Fig 4.12 we plot the normalized strain angle $\tilde{\alpha}$ as a function of r and θ. The color maps representing the various values of $\tilde{\alpha}$ differ significantly when going from the equilibrium to the non-equilibrium configurations. The adiabatic index value influences the slope of the strain angle curve: if for $\gamma_f = 2$, α is an increasing function of r (see Fig 4.4), for $\gamma_f = 2.1, 200, \infty$ the opposite is true, and we recover the incompressible behaviour described in chapter 3. This is a very interesting result, since as noted above in section and as pointed out in the literature (Cutler et al. 2003), one could expect the strain to

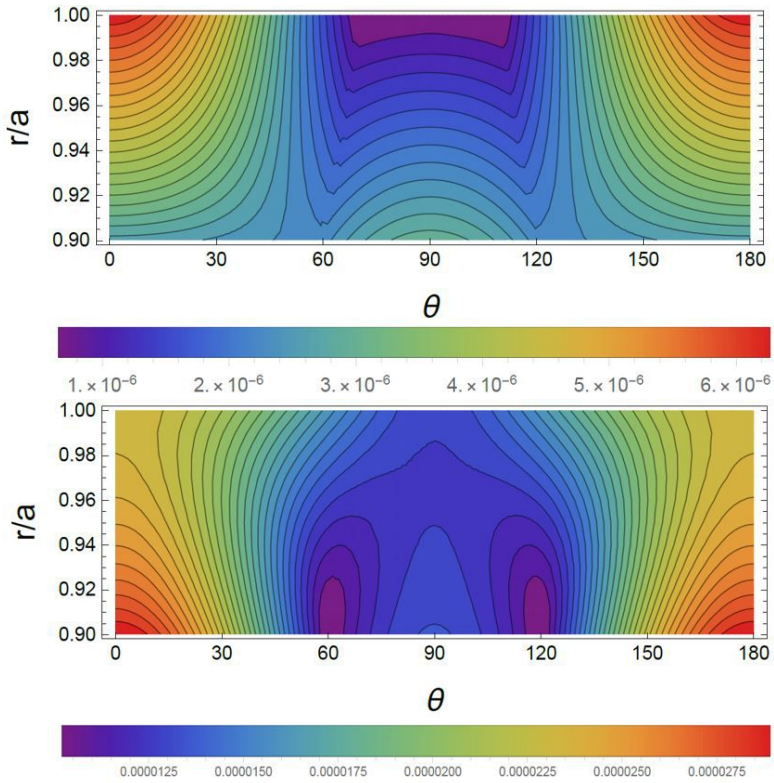

Figure 4.12: Color map of the normalized strain angle $\tilde{\alpha}$ as a function of the colatitude θ and of the normalized radius r/a. The region shown here refers to the crustal layer, from $r = r_c$ to $r = a$. Our reference star of $M = 1.4\,M_\odot$ has been used, with different adiabatic indices governing the perturbations: $\gamma = 2.1$ (top) and $\gamma = 200$ (bottom). Here α for $\gamma = \infty$ is not reported because it has the same shape and values of the case $\gamma = 200$. Cf the bottom panel with the color map for the incompressible model, Fig 3.11.

be maximum at the star's surface (where μ is smaller). However, the shear modulus is so small compared with the bulk modulus that the global crustal deformation is ruled essentially by the value of the adiabatic index, as explained.

Finally, we try to get a feeling of the impact of the stellar mass parameter M by studying the function $\alpha(M)$. Again, as in section 4.1.1 we have to evaluate the coefficient d, Eq (4.1), and we fix $\Omega = 1\,\mathrm{rad/s}$. We find that the strain dependence on mass is almost the same for every value of the frozen adiabatic index. We checked this behaviour by employing a larger set of values for γ_f, with values ranging from $\gamma_f = 2$ to $\gamma_f = 1000$, as reported in Fig 4.13.

The comparison between different adiabatic indices allows to calculate the ratio in Eq (4.8) for different scenarios, going from the equilibrium to the incompressible one. This is shown in Fig 4.14. As we can see that ratio has large values when values near γ_{eq} are employed, but it rapidly decreases towards the asymptote $\alpha(1M_\odot)/\alpha(2M_\odot) \simeq 2.6$ as the incompressible limit is approached. This latter value resembles the one obtained with the homogeneous two-density incompressible model where $\alpha(1M_\odot)/\alpha(2M_\odot) \simeq 2 \div 3$, see chapter 3.

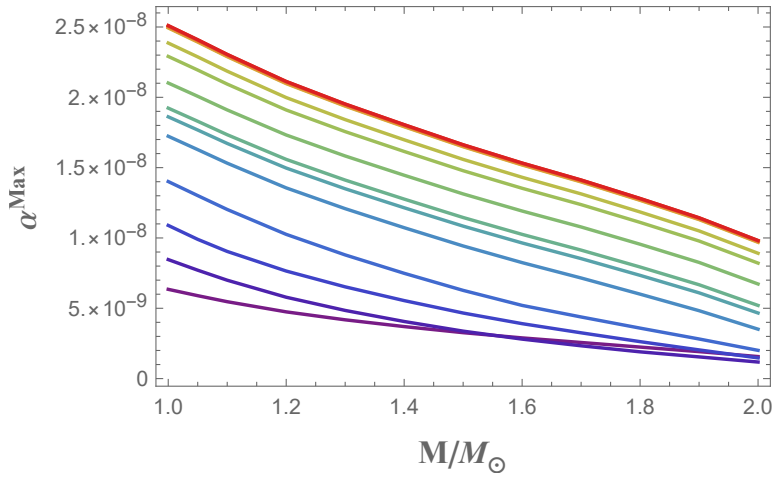

Figure 4.13: Maximum strain angle α^{Max} as a function of the stellar mass, calculated for $\Omega = 1\,\mathrm{rad/s}$ and different adiabatic indices (γ_f =2, 2.05, 2.1, 2.2, 2.5, 2.8, 3, 4, 7, 12, 100 and 1000) going monotonically from the lowest purple line ($\gamma_f = 2$) to the red one on top ($\gamma_f = 1000$). The curve for $\gamma_f \geq 100$ is superimposed to the one for $\gamma_f \geq 1000$, indicating that the star's behaviour is essentially indistinguishable with respect to the incompressible limit. The purple line coincides with the curve in Fig 4.5.

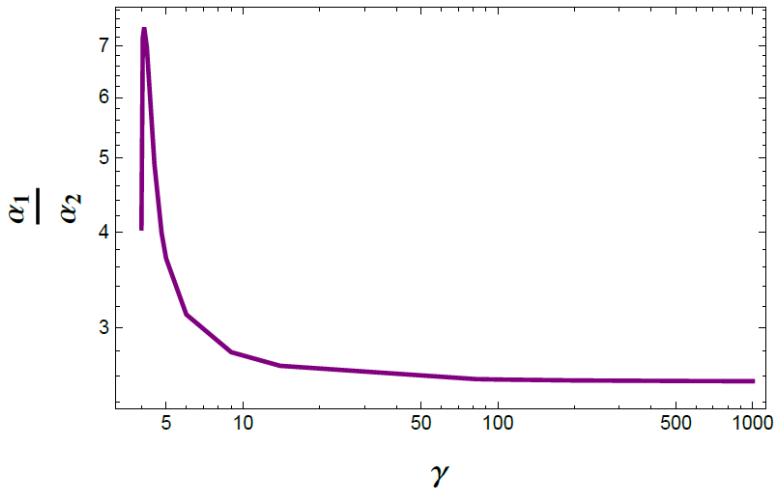

Figure 4.14: Ratio of maximum strain angle $\alpha^{Max}_{M=1M_\odot}/\alpha^{Max}_{M=2M_\odot}$, as function of the adiabatic index including both $\ell = 0$ and $\ell = 2$ harmonics contribution for $\Omega = 1$ rad/s.

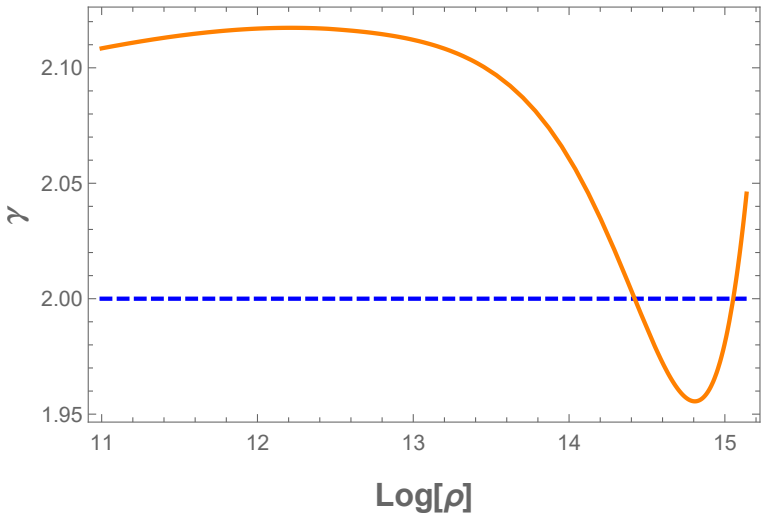

Figure 4.15: The effective adiabatic index calculated from the equilibrium configuration in General Relativity (orange) and in a Newtonian gravity (blue, dashed). Both the adiabatic indices are shown for a neutron star with a gravitational mass of $M = 1.4M_\odot$ which EoS is given by the polytrope $n = 1$.

4.1.3 Effective adiabatic index: the effect of General Relativity

We end this section with a technical note, expanding the motivation behind our basic working assumption of a non-relativistic framework.

The Adams-Williamson equation (2.66) tells us that the adiabatic index (both the equilibrium one as well as the more uncertain frozen one) depends strongly on the stratification: this can be envisaged by comparing the *effective* adiabatic index of Eq (2.16), calculated by using the equilibrium configuration of a star. As an explicit example we do this for the usual $M = 1.4\,M_\odot$ star described by a polytrope $n = 1$, for which stratification has been calculated both in the Newtonian and in General Relativistic frameworks (i.e. by using the TOV equations). The difference between the two effective adiabatic indices is shown in Fig 4.15.

In the Newtonian case the effective index is clearly given by $\gamma = 2$, as it should be. However, when the TOV equations are employed in order to find the stellar stratification, there is a radial departure of the effective adiabatic index γ from this value, exceeding the 5% in the crust. This means that one cannot use a general relativistic density profile in a Newtonian model , since in this way one introduces an artificial effective adiabatic index, that will not correspond to the physical response of the star.

4.2 Application to pulsar glitches

As done in the incompressible case of 3, in this section we focus our attention to the paradigmatic case of the Vela pulsar and we estimate the accumulated strain due to the spin-down of the pulsar in between two glitches, with parameters Ω and spin-down rate $\dot{\Omega}$ given in Tab 4.2. The same approach presented in the previous chapter is followed but employing the more refined model for crustal deformations: the absolute difference in angular velocity between two Vela glitches is estimated as $\omega \approx |\dot{\Omega}|\langle t_{gl}\rangle$, where $\langle t_{gl}\rangle \approx 3\,\mathrm{yr}$

Ω (rad/s)	$\dot{\Omega}$ (rad/s^2)	ω (rad/s)
70.338	-9.846$\times 10^{-11}$	80.44$\times 10^{-4}$

Table 4.2: Adopted parameters for the Vela pulsar.

is the typical observed inter-glitch time.

The strain developed during the inter-glitch time due to the variation of Ω is then roughly given by

$$\alpha = \tilde{\alpha}\left(d\left(\Omega\right) - d\left(\Omega - \omega\right)\right) \approx \tilde{\alpha}\,\frac{2\Omega\omega a^2}{3\,v^2}\,, \tag{4.15}$$

where $\tilde{\alpha}$ is the normalized strain angle, i.e. the strain angle calculated using the normalized displacements $\tilde{U}, \tilde{V}$, and $d(\Omega)$ is given in Eq (4.1). Using the parameters in Table 4.2, and assuming a typical mass of $M = 1.4 M_{\odot}$, we get

$$\alpha_{Vela}^{Max} = 3.5 \times 10^{-4}\tilde{\alpha}\,, \tag{4.16}$$

which means that the strain accumulated due only to the spin-down between two glitches is of the order of

$$\alpha_{Vela}^{Max} = 2.1 \times 10^{-9}\,. \tag{4.17}$$

This is an extremely small value if compared to the assumed breaking strain in the range $10^{-5} \div 10^{-1}$: therefore, the crust's failure may be a viable trigger for glitches (i.e. vortex unpinning) only in the eventuality that the crust is always stressed and very near to the breaking threshold. In other words, in order to trigger a sequence of glitches, the crust-quakes must release only an extremely small portion of the crustal stresses that have been accumulated up to that point.

4.3 Outlook

In this chapter we analyzed the deformation of a compressible NS caused by uniform rotation. As in the incompressible limit case, we showed that the strain angle is a weakly decreasing function of the stellar mass, depending mainly on the stellar compactness M/R: the crust of more compact stars is more difficult to deform and to break by changing the rotation rate with respect to the crust of a lighter star. This suggests that, *if* star-quakes are assumed as triggers of glitches, pulsars showing a dense sequence of timing irregularities should be lighter than pulsars showing sparse events.

Furthermore, we compared the α value obtained in different adiabatic index scenario, describing different astrophysical situations. The analysis of different adiabatic index values has confirmed our assumption that the strain angle is particularly sensitive on γ. The physical explanation of this behaviour is in the smallness of the shear modulus compared to the bulk modulus. The hypothesis of a uniform polytropic index is often used in the literature, but, since the equilibrium adiabatic index varies from the value of about 0.4 in the neutron drip point to the value of 2 near the crust-core boundary, for a more realistic treatment one should relax this hypothesis. Contrary to the behaviour of the equilibrium adiabatic index, the frozen index is, instead, constant throughout the star and we have shown that even a small difference between γ and γ_f is able to produce very different deformations. Thus we expect that the general response of the star will be of the same type also form more refined models accounting for an adiabatic index variations. In particular, the differences will be greater in the regions where the difference between γ and γ_f will be larger.

Despite the fact that the strain angle grows with larger γ, even the lowest theoretically expected breaking threshold of $\sigma^{Max} \simeq 10^{-5}$ is never attained. This clearly challenges the hypothesis according to which slow uniform rotation can induce a starquake on NSs. In the next section we will study two other different loads that could cause the crust failure.

CHAPTER 5

Differential rotation

In this chapter we will study two further forces that are thought to be effective during the spin-down of glitching pulsars: differential rotation and pinning. The analysis is thus divided into two different sections, where the two loadings are faced one by one. Since, contrary to the case of uniform rotation, this kind of forces are non-conservative, we will briefly show how to build explicitly the elastic solution, following the model described in chapter 2. As in the previous chapter we will study, for both cases, the strain dependence on the mass, the adiabatic index value and on the EoS. As we will see in the following, both forces are due to the presence of a neutron superfluid in the inner crust and in the core of NSs. For this reason, before analysing the deformation and the strain angle, in this case we will briefly introduce the superfluidity in the astrophysical scenario of interest.

5.1 Superfluidity

Baryons in neutron stars matter, except for a brief period soon after the star's birth, are expected to be in a superfluid state thanks to the attractive component of the baryon-baryon interaction. In fact, superfluidity is switched on when star thermal energy kT is less than the superfluid energy gap Δ, which corresponds to the binding energy per particle of Coopers pairs: since the pairing gap is roughly in the range 2 MeV$\div 10$ KeV[1] for both neutrons and protons, in the interior of neutron stars at temperature of 10^7K, corresponding to about 1 keV, they are thought to be superfluid (Shapiro & Teukolsky 1983). These Cooper pairs behave like bosons, i.e. they do not obey Pauli exclusion principle and thus can occupy a single-particle quantum state (Sauls 2019). In particular, theory predicts that in the inner crust there is a neutron superfluid in the singlet state ($^1S_0$) (protons are bound in nuclei and they cannot pair) while, in the core, both neutron ($^3P_2$) and proton superfluid are present (superconduction for the charged particles).

A superfluid is a fluid that can flow without internal dissipation (viscosity), which means that its motion can be described with the Euler equation, rather than the dissipative Navier-Stokes one[2]. This peculiar state of neutrons inside the NS has almost no effect on the EoS and on stars mass and radii, but, instead, it deeply affects neutron stars heat capacity and neutrino emission, and induce many macroscopic quantum phenomena. The most important for this work of thesis is that superfluid rotation is realized by

[1] For isotropic $^1S_0$ nuclear superfluids the critical temperature is thought to be about 1 MeV, while for the anisotropic $^3PF_2$ neutron superfluid can be much lower, see (Chamel 2017b).

[2] At finite temperature, the fluid dynamics is more complicated as it is described in terms of two fluid models; however, since the NS temperature is smaller than the critical temperature, we can always assume T=0.

quantized vortices parallel to the spin axis, pinned at the crust, the number of which is estimated to be around $2 \times 10^{16}/P$ where P is the stellar period in seconds.

Now, let us consider the ground state of a superfluid, that, as seen above, can be described as a single wave function (Sauls 2019)

$$\psi = n_0 e^{i\phi}, \tag{5.1}$$

where ϕ is the phase factor, while n_0 is proportional to the particle density. From quantum mechanics, we know that the current density can be expressed as

$$\boldsymbol{J} = -\frac{i\hbar}{m}\left(\psi^* \nabla\psi - \psi \nabla\psi^*\right) = |\psi|^2 \frac{\hbar\nabla\phi}{m} = |\psi|^2 \boldsymbol{v}, \tag{5.2}$$

where $\boldsymbol{v}$ is the superfluid velocity. Since the mass of the Cooper pair is $m = 2m_n$ we find

$$\boldsymbol{v} = \frac{\hbar\nabla\phi}{2m_n}. \tag{5.3}$$

This is a fundamental results, since it implies that the superfluid is irrotational

$$\boldsymbol{\nabla} \times \boldsymbol{v} = \frac{\hbar}{2m_n} \boldsymbol{\nabla} \times (\boldsymbol{\nabla}\phi) = 0. \tag{5.4}$$

Let us now consider a bucket rotating along its axis, filled with a fluid. In the case of a normal fluid the friction with the internal surface of the bucket will communicate the rotation to the fluid that ultimately will corotate with its container. Conversely, if we consider a superfluid, we can write its energy in the frame of reference of the rotating bucket E_{rot} as

$$E_{rot} = E - \boldsymbol{M} \cdot \boldsymbol{\Omega}, \tag{5.5}$$

where we indicated with E the total energy of the fluid in the laboratory frame, with $\boldsymbol{M}$ its angular momentum and $\boldsymbol{\Omega}$ the angular velocity of the bucket. This expression tells us that, in the case of a non-zero angular velocity the rotational energy will be minimum in a state where also the fluid is rotating, making thermodynamically favourable the configuration with $M \neq 0$. In particular, if $\Omega > E/\boldsymbol{M}$ the spinning state is favored. How can this statement be reconciled with the irrotationality? This contradiction can be solved by introducing singularities in the velocity field. In fact, consider the circulation

$$\oint_C \boldsymbol{v} \cdot d\,\boldsymbol{l} = \kappa, \tag{5.6}$$

where C is a closed loop that enclose a straight singularity and it is centered with it. Using Eq (5.3) we get

$$\kappa = \oint_C \boldsymbol{v} \cdot d\,\boldsymbol{l} = \oint_C \frac{\hbar\nabla\phi}{2m_n} \cdot d\boldsymbol{\ell}, \tag{5.7}$$

and thus, reminding that the variation of the phase on a closed loop must be an integer multiple of 2π, we finally have

$$\kappa = n\frac{h}{2m_n}, \tag{5.8}$$

where κ represents a quantum of vorticity. Since $n = 1$ is the most energetically favorable case (Haskell & Sedrakian 2018), in the following we assume $\kappa = h/2m_n$. Therefore we

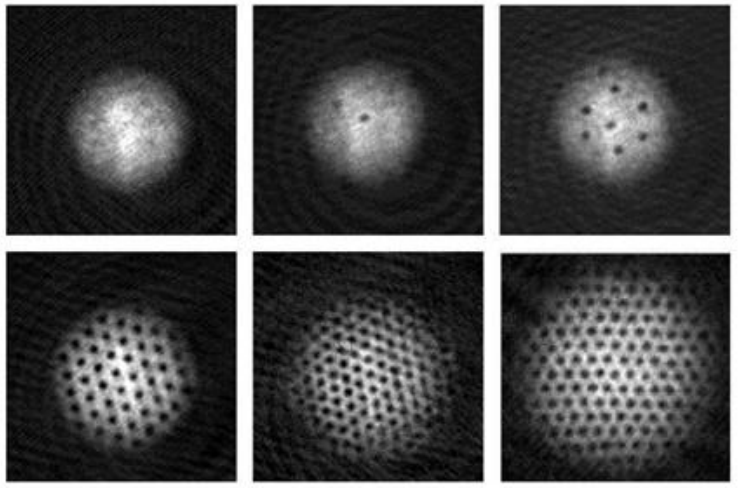

Figure 5.1: Vortex array in a Bose-Einstein condensate: the dark holes within the light areas are vortex cores. Credit: Lenz et al. (1993)

can modify the relation (5.4) by introducing vortex singularities of normal (i.e. non-superfluid) matter as

$$\nabla \times v = \kappa \delta^2 \left(r_v^i \right), \tag{5.9}$$

where r_v^i is the site of the ith vortex line. The system is in fact a lattice of *quantized vortex lines* that, from the macroscopic point of view, simulates a classical rotation.

Now, if we want to calculate the macroscopic velocity field of the fluid, we can consider a cylindrical region of superfluid, rotating on its axis. In the case of more than one vortex we can write

$$\oint_C \boldsymbol{v} \cdot d\boldsymbol{\ell} = \int_S (\nabla \times \boldsymbol{v}) \cdot \hat{\boldsymbol{n}} d\boldsymbol{S} = \kappa \sum_i \int_S \delta^2 \left(\boldsymbol{x} - \boldsymbol{x}_i \right) dS, \tag{5.10}$$

where x is the cylindrical radius and S is the surface with normal $\hat{n}$ enclosed in the path C. By introducing the vortex surface density $n(x)$, after some algebra we obtain the Feynman-Onsager relation

$$x \frac{d\Omega}{dx} + 2\Omega \left(x \right) = \kappa n \left(x \right). \tag{5.11}$$

If we assume for simplicity that the superfluid rotates as a rigid body ($\Omega = const$) we find a very simple expression for the number of vortices per unit area

$$n \left(x \right) = \frac{2\Omega}{\kappa}, \tag{5.12}$$

i.e. the $n(x)$ is proportional to the angular velocity of the superfluid.

5.1.1 Pinning

The complex interaction of vortices with the crystalline lattice can pin them in place, freezing the vortex array configuration. For this reason the superfluid can spin-down

only by expelling vortices, thus releasing the stored angular momentum during glitches (Anderson et al. (1982), see section 1.6). Pinning is not a peculiar characteristics of neutron superfluid, but is known also for terrestrial superfluids (Fig 5.1) as, for example, in helium experiments (for a review see Graber et al. (2017)). If a vortex filament terminates on a flat surface close enough to a local protusion, called *pinning site*, it is captured (Schwarz 1988). This happens because not all the configuration have the same energy and thus it could be favored the inhomogeneity confinement in the vortex core. Once the vortex is pinned, it is required a finite background flow velocity with respect to the pinning center to free it. In the NS context, typically *pinning* refers to the interaction of vortices with the crustal lattice and the pinning centers are the nuclei of the inner-crust.

While the microscopical pinning energy per pinning site is well defined as the difference between two benchmark configuration, one with one of the two nuclei confined into the vortex core and the symmetric one in which the vortex core lies onto the interface between the two Wigner-Seitz cells (Donati & Pizzochero 2004), the pinning force $\boldsymbol{f}_P$ is more difficult to estimate. At the present time there are not detailed methodologies to calculate this quantity in the literature. In the present work we supposed f_P to be a scalar quantity which represents the threshold for unpinning. We do not discuss here the details of calculation of the pinning force done by Seveso (2014), that we use as reference, but just report that it has maximum values of order $f_P \simeq 10^{15}\mathrm{erg/cm^2}$, that could be enough to explain large glitches (Antonelli 2017). Since vortex pinning freezes the angular velocity of the superfluid component, see e.g. Eq (5.12), it establishes a lag between the normal and superfluid component, that increases in time since the first is slowed down by the electromagnetic torque. This difference in the rate of rotation inside the star will be the argument of the next section.

5.2 Differential rotation

One of the possible consequence of the differential rotation is the so called *Ekman pumping*, a convective transport of angular momentum that is considerably shorter than the viscous diffusion: the Ekman timescale τ_E is roughly given by the geometric mean of rotation (P) and diffusion (τ_D) timescales

$$\tau_E \simeq \sqrt{P\tau_D}. \tag{5.13}$$

One of the fundamental assumptions of the two-component model by Baym & Pines (1971) is that the charged particles in the fluid core corotate with the solid crust, because of the large interior magnetic field. This is a basic assumption since it allows to treat the charged particles and the crust as a single, normal component (the other being the neutron superfluid). Soon after this work Easson (Easson 1979a,b) confirm this approach, finding that either Ekman pumping or magnetic coupling is very efficient to bring into corotation the crust with the core plasma. However, (see Abney & Epstein (1996)) Ekman pumping is expected to be inefficient for the uncharged neutron superfluid permeating the inner crust, that thus develops a significant differential rotation. Carter et al. (2000) were the first to suggest that centrifugal buoyancy could be a relevant cause of pulsar starquakes, studying the effect of differential rotation using a two fluids approach. Recently Chamel & Carter (2006) have renewed that first analysis by including the effect on entrainment[3], but this work of thesis is the first to include self-consistently the elasticity of the crust.

[3]The entrainment is a non-dissipative effect that couples the supefluid and the normal component in the inner crust (Andreev & Bashkin 1976; Chamel 2006, 2012, 2017a). From the practical point of view, entrainment

However, the most debated aspect is how large is the fraction of superfluid that maintains its angular rotation rate, being the angular momentum *reservoir* for the glitch. Many works considered only the superfluid present in the inner crust (Datta & Alpar 1993; Link et al. 1999): in this scenario, the core superfluid is strongly coupled to the normal component (Alpar et al. 1984), thus corotating with it. Recently this vision has changed, since it has been shown that the presence of entrainment reduces the effective moment of inertia associated to the superfluid component. Using the estimates of Chamel (2012) it has been shown that the glitching activity (see section 1.6) of some pulsars, and in particular of Vela, cannot be explained using as the only superfluid reservoir the one of the crust (Andersson et al. 2012; Chamel 2013; Delsate et al. 2016). This seems to favour other models that account for a reservoir extending into the core, where P-wave Cooper pairing should be more likely that singlet one. Following the idea of Ruderman & Sutherland (1975), Pizzochero (2011) in the so-called "Snowplow model" proposed that the core corotates with the superfluid in the crust: in fact, the actual theoretical calculation (Zuo et al. 2004), excluding a layer of normal matter at the crust core interface, cannot rule out the possibility that vortices fill the whole superfluid domain, extending throughout the core. Another possibility is that the superfluid involved in the glitch is only the one in the ${}^1S_0$, which, according to several theoretical calculations extends beyond the crust-core boundary. In order to estimate the exact boundary of the superfluid domain, in this latter case, one has to choose a specific model for the superfluid gap and also needs to estimate the internal temperature of the neutron star (that in turn depends on the pulsar age and cooling curve). For our analysis we will follow this latter hypothesis, as done by (Ho et al. 2015) and (Montoli et al. 2018), who chose different possible extension of the ${}^1S_0$ superfluid.

For studying the centrifugal buoyancy acting on NSs, we follow two main assumptions. The first is that we will not distinguish, in the inner core, between the superfluid and the normal component, i.e. we assume that this layer rotates as a whole. In this way we can simulate the differential rotation due to the presence of a superfluid component and calculate its stressing effect on the elastic lattice. We remind that in our model the outer-crust boundary is placed at the density $\rho = 10^{11}\mathrm{g/cm^3}$: this value is roughly equal to the neutron drip density, where the inner crust region starts. In other words, we can assume that in our calculation the solid layer corresponds to the inner part of a NS' crust.

The second assumption regards the shape of the loading that is assumed to be

$$\boldsymbol{f} = \boldsymbol{f}_{cen}\left[\frac{1}{2}\left(1 - \frac{2}{\pi}\arctan\left(\pm\frac{c/a - r/a}{\xi}\right)\right)\right], \tag{5.14}$$

where c is the radius of transition between the non-rotating and the rotating layer, ξ is a parameter that determines how sharp is the transition between these two layers and $\boldsymbol{f}_{cen}$ is the centrifugal force. Here, as a first step, we ignore the thickness of the transition and choose a very sharp jump by fixing $\xi = 10^{-6}$. In this way the step function $1/2\,(1 - 2/\pi\arctan[\pm(c/a - r/a)/(\xi)])$ can be used as a very good analytic approximation of the Heaviside $\Theta(r - c)$ function, which requires a more computational time of integration. The region in the middle between the non-rotating and rotating part will be called *jump region*, see Fig. 5.2. The $\pm$ in the argument of arctan is simply a tool to switch the rotation in the inner $(+)$ or in the outer $(-)$ part of the star. We will call for simplicity *internal* the force with "$-$" sign and *external* force the one with "$+$" sign.

is described in terms of an *effective mass*. The basic idea is that the dripped neutrons in the crust act like electrons in metals, so that they can be studied by using the band theory of solids (Chamel 2006, 2012). In fact, only neutrons in the upper conduction band can move throughout the crust, due to the Bragg scattering. The conclusion is that, even in the case of no dissipative effect, neutrons cannot be considered free.

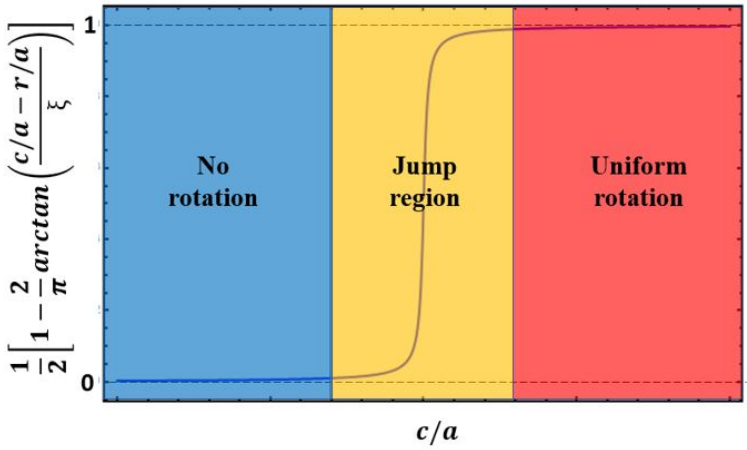

Figure 5.2: Schematic representation of the *external* jump function $\frac{1}{2}\left[1-\frac{2}{\pi}\arctan\left(\frac{c/a-r/a}{\xi}\right)\right]$. For a fixed transitional radius c we can divide the star into a inner non-rotating region, a middle jump region and an outer rotating region.

The complete solution of a differential rotating sphere with a fluid core and an elastic crust needs the knowledge of the inner solution, i.e. the effect of a loading as (5.14) on a fluid, self-gravitating object. This problem will be studied in the next section.

5.2.1 Equations

A self-gravitating, perturbed fluid is described by the two spheroidal equilibrium equations (2.33), (2.34) with $\mu = 0$, i.e.

$$\frac{\partial_r R_\ell}{\rho_0} - \partial_r\left(gU_\ell\right) + g\chi_\ell - \partial_r\Phi_\ell + \frac{h_\ell^r}{\rho_0} = 0, \tag{5.15}$$

$$\frac{R_\ell}{\rho_0} - gU_\ell - \Phi_\ell + \frac{rh_\ell^\theta}{\rho_0} = 0, \tag{5.16}$$

and the Poisson equation

$$\nabla_r^2\Phi_\ell = -4\pi G\left(\rho_0\chi_\ell + U_\ell\partial_r\rho_0\right). \tag{5.17}$$

The radial and tangential m_ℓ^r and m_ℓ^θ force terms, in the case of rotation Eq (5.14), are proportional to the star's density. Thus we can introduce the two auxiliary functions j_ℓ^r, j_ℓ^θ as

$$h_\ell^r\left(r\right) = j_\ell^r\left(r\right)\rho_0\left(r\right), \tag{5.18}$$

$$h_\ell^\theta\left(r\right) = j_\ell^\theta\left(r\right)\rho_0\left(r\right). \tag{5.19}$$

Note that, for the particular form of the centrifugal force

$$j_\ell^r = 2j_\ell^\theta. \tag{5.20}$$

The tangential equation (5.16) can be used to constraint the radial displacement

$$U_\ell = -\frac{\Phi_\ell}{g} + \frac{r\, j_\ell^\theta}{g} + \frac{\kappa\chi_\ell}{g\rho_0}. \tag{5.21}$$

Then, if we calculate the difference between the radial equation Eq (5.15) and the derivative of the tangential one Eq (5.16), by reminding Eq (5.20), we get

$$j_\ell^\theta + g\chi_\ell - r\partial_r j_\ell^\theta + \kappa\chi_\ell \frac{\partial_r \rho_0}{\rho_0} = 0. \tag{5.22}$$

This is the more general form of the Williamson-Adams equation (2.66) in the presence of a non-zero step centrifugal force given by Eqs (5.18), (5.19). The bulk modulus, as we have seen in chapter 4, can describe both adiabatic or non adiabatic stratification. Thus, in general we can write

$$\kappa = \delta\kappa - \frac{g\rho_0^2}{\partial_r \rho_0}, \tag{5.23}$$

where $\delta\kappa = \delta\gamma P = 0$ in the case of adiabatic stratification. Let us solve separately the adiabatic and the non adiabatic cases.

Adiabatic scenario

In the adiabatic case we substitute the radial displacement Eq (5.21) in the Poisson equation (5.25) and, using also the adiabatic relation

$$\kappa = -\frac{g\rho_0^2}{\partial_r \rho_0}, \tag{5.24}$$

we finally obtain

$$\nabla_r^2 \Phi_\ell = 4\pi G \left[\partial_r \rho_0 \left(\frac{\Phi_\ell}{g} - \frac{r\, j_\ell^\theta}{g}\right)\right]. \tag{5.25}$$

It is easy to see that this equation assumes the form (3.3) in the case of a conservative force, i.e. for $c \to 0$, since $r j_\ell^\theta = \Phi^C$.

Non adiabatic scenario

For the non adiabatic case we use a different approach. We introduce the auxiliary function Ξ_ℓ, defined as

$$\Xi_\ell = \delta\kappa \times \chi_\ell. \tag{5.26}$$

In this way we can write the above quantity using Eq (5.22)

$$\Xi_\ell = -\frac{\rho_0^2}{\partial_r \rho_0}\left(j_\ell^\theta - r\partial_r j_\ell^\theta\right). \tag{5.27}$$

Using the relations (5.21) and (5.27) in the Poisson equation (5.28) we find

$$\nabla_r^2 \Phi_\ell = 4\pi G \left[\partial_r \rho_0 \left(\frac{\Phi_\ell}{g} - \frac{r\, j_\ell^\theta}{g}\right) + \rho_0 \left(\frac{j_\ell^\theta}{g} - \frac{r\partial_r j_\ell^\theta}{g}\right)\right]. \tag{5.28}$$

For a pure uniform rotation, also the above equation assumes the same form of Eq (3.3).

5.2.2 Boundary conditions

For both the adiabatic and the non-adiabatic cases we obtained two differential equations for the gravitational potential, that need two initial conditions to be solved. In the innermost part of the star we can safely assume that the density is roughly constant, $\partial_r \rho_0 = 0$, and that the loading is zero (the force is proportional to the radial distance to the center r). In this case both Eqs (5.25), (5.28) become the Laplace equation

$$\nabla_r^2 \Phi_\ell = 0, \tag{5.29}$$

which has the regular solution

$$\Phi_\ell (r) = C_1 r^\ell. \tag{5.30}$$

This inner solution tells us that, for very small radii

$$\lim_{r\to 0} \Phi_\ell (r) = 0, \tag{5.31}$$

$$\lim_{r\to 0} \partial_r \Phi_\ell (r) = 0. \tag{5.32}$$

Using these two inner conditions we can solve the Poisson equations (5.25), (5.28) in the whole star. The general solution will be a linear combination of the homogeneous solution Φ_{homo} and the particular solution Φ_{part}, that is

$$\Phi_\ell (r) = C_1 \psi_{homo,\ell} (r) + \psi_{part,\ell} (r) . \tag{5.33}$$

From the previous analysis (see section 2.7.1) we know that for a pure gravitational potential

$$Q_\ell \left(a^-\right) = 0, \tag{5.34}$$

where Q_ℓ is the gravitational potential flux (2.41). This request fixes the C_1 constant, giving us the complete solution of the problem.

Fig 5.3 shows, for the $\ell = 2, m = 0$ harmonic, the perturbed potential solution for a $n = 1$ polytropic $\rho = \sin(\pi r/a)/(\pi r/a)$ stratification, for different values of the radius c, both in the adiabatic and the non-adiabatic scenario. As expected, in the limit $c \to 0$ the perturbed gravitational potential is the one found as the solution of a uniform rotating fluid sphere. However, when the transitional radius is large enough, the potential departs from this uniform solution: in particular, for fixed c, the non adiabatic solution shows a larger departure from the rigid rotating solution with respect to the adiabatic one, as expected for a "stiffer" equation of state (cf chapter (4)).

The knowledge of the solution for a self-gravitating, fluid core subject to a force in the form (5.14) can be used to find also the general solution in the case of a rotating star having an elastic layer over the fluid core.

5.2.3 General solution

The presence of a non conservative force in the core changes slightly the expression of the starting condition for the particular solution. Using Eq (5.16) and following the approach of section 2.7.2 we write

$$R_{\ell m} = \rho_0 g \left[U_{\ell m} - \left(-\frac{\Phi_{\ell m}}{g} \right) - \frac{r j_\ell^\theta}{g} \right] = \rho_0 g C_3. \tag{5.35}$$

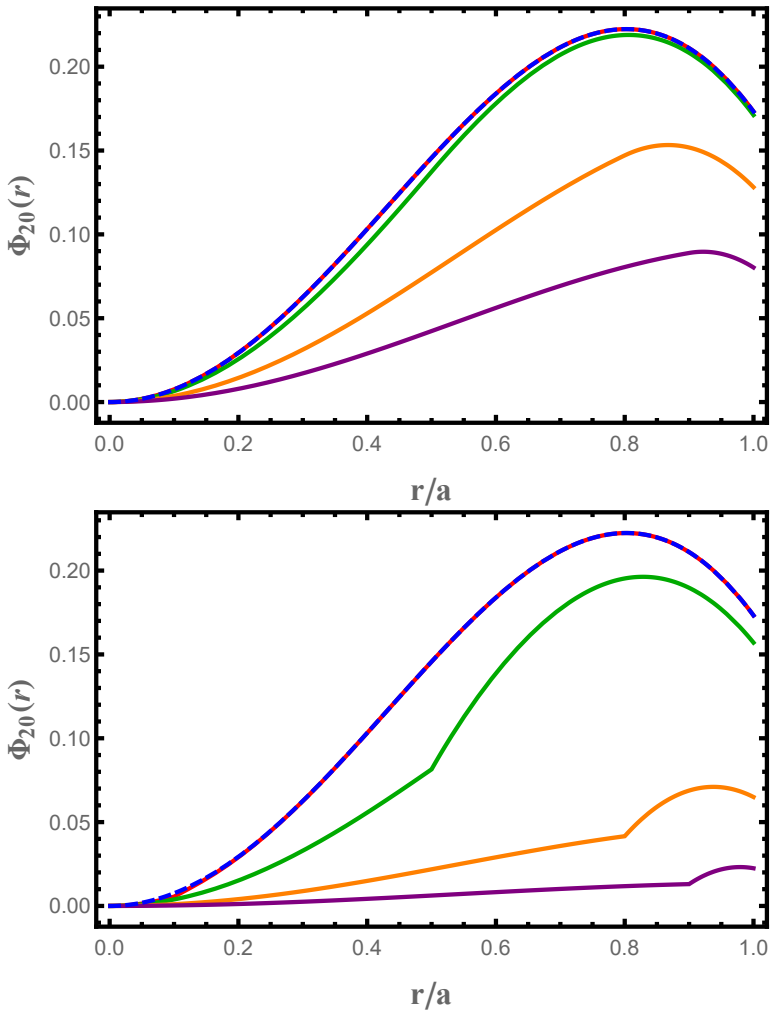

Figure 5.3: Normalized (i.e. in the case of stellar radius a=1) gravitational perturbed potential $\ell = 2, m = 0$ harmonic contribution for different transitional radii $c/a = 0.1$ (red), $c/a = 0.5$ (green), $c/a = 0.8$ (orange) and $c/a = 0.9$ (purple). In this case only the region $r > c$ is rotating. Blue dotted line refers to the normalized gravitational perturbed potential of a uniform rotating star. The upper panel is calculated in the adiabatic scenario, while the bottom panel is calculated in the non adiabatic one.

Finally we define, in analogy with Eq (5.36), the quantity $q_{\ell m}$ as

$$q_{\ell m} = \partial_r \psi_{\ell m} + \frac{\ell+1}{r}\psi_{\ell m} - 4\pi G U_{\ell m} \tag{5.36}$$

where $U_{\ell,m}$ is given by Eq (5.21). In this way our particular starting solution will be

$$y_{start,\ell m}(r_c) = \begin{pmatrix} -\psi_{\ell m,part}\left(r_c\right)/g\left(r_c\right) + r_c j^{\theta}_{\ell m}\left(r_c\right) g\left(r_c\right) \\ 0 \\ 0 \\ 0 \\ \psi_{part,\ell m}\left(r_c\right) \\ q_{part,\ell m}\left(r_c\right) + 4G\pi r j^{\theta}_{\ell m}\left(r_c\right)\rho_0\left(r_c\right)/g\left(r_c\right) \end{pmatrix}, \tag{5.37}$$

As above, the subscript *part* here indicates the *particular* solution both in the case of adiabatic and non-adiabatic scenario. The general solution in Eq (2.75) can be here expressed as (in this case $\boldsymbol{b} = \boldsymbol{0}$)

$$\boldsymbol{y}_{\ell m}\left(r\right) = \boldsymbol{\Pi}_{\ell}\left(r, r_c\right)\boldsymbol{I}_C\left[\boldsymbol{P}_1\boldsymbol{\Pi}_{\ell}\left(a^-, r_c^+\right)\boldsymbol{I}_C\right]^{-1}\left(-\boldsymbol{P}_1\boldsymbol{y}_{part,\ell m}\left(a\right)\right) + \boldsymbol{y}_{part,\ell m}\left(r\right). \tag{5.38}$$

The three homogeneous solutions are the propagated vectors of the core-crust matrix $\boldsymbol{I}_C$ (Eq (3.29)):

$$\begin{cases} \boldsymbol{y}^{\prime(j)}_{homo,\ell m} = \boldsymbol{A}_{\ell}\left(r\right)\boldsymbol{y}^{(j)}_{homo,\ell m} \\ \boldsymbol{y}^{(j)}_{homo,\ell m}(r_c^+) = \boldsymbol{I}^{(j)}_C(r_c^-) \qquad j = 1,2,3 \end{cases} \tag{5.39}$$

while the particular solution is defined as

$$\begin{cases} \boldsymbol{y}^{\prime}_{part,\ell m} = \boldsymbol{A}_{\ell}\left(r\right)\boldsymbol{y}_{part,\ell m} + \boldsymbol{h}_{\ell m} \\ \boldsymbol{y}_{part,\ell m}(r_c^+) = \boldsymbol{y}_{start,\ell m}(r_c^-) \\ \boldsymbol{h}_{\ell m} = \rho_0(0,0,j^r_{\ell m}, j^{\theta}_{\ell m}, 0, 0). \end{cases} \tag{5.40}$$

The knowledge of the inner fluid solution and the boundary conditions fix in an unique way the elastic solution Eq (5.38). We can now analyze the deformation of a NS subject to differential rotation.

5.2.4 Tests

Before any analysis of a realistic NS deformation, we performed two different tests on our solution. The corresponding figures are shown in the Appendix C.

The first test can be easily done in the case of *external* force, which means that only the region $r > c$ is rotating. In this configuration we expect that, in the limit of very small transitional radii $c \to 0$, the solution becomes equal to the uniform rotating one. This is exactly what happens as shown in the plots of Appendix C.

In the second test we required that the sum of the solutions for the *external* and *internal* force, with the same choice of the transitional radius c, is equal to the uniform solution. In fact, we expect that the total effect of a centrifugal force acting only in the inner part of the object plus the effect of a centrifugal force acting only in the outer layers is equal to the one due to a centrifugal force acting on the whole star. Also this request is fulfilled, as can be seen in Appendix C where the the displacements and stresses for the two configurations (external+internal and uniform) are shown.

Thus the solution confirms the physical expected behaviour in two different limits, and we are ready to explore the general case of differential rotation.

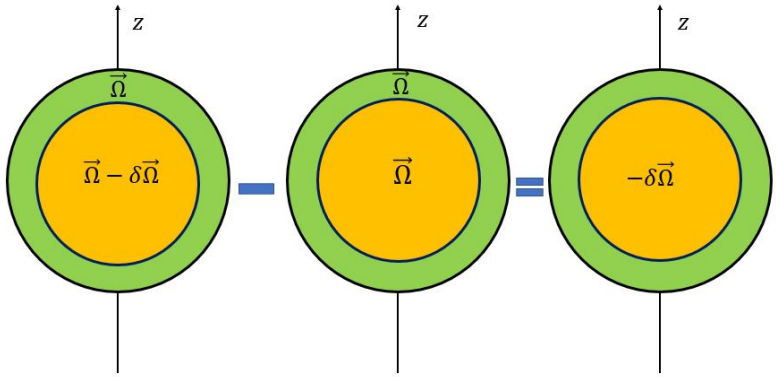

Figure 5.4: Schematic representation of the dynamical evolution of a NS between two glitches. As initial configuration (middle panel) we start from corotation between the superfluid (green) and the normal component (yellow). The final configuration, at the glitch time, is the one at the left: the normal component rotates slower than the supefluid one. The difference of these two configurations gives the net effect of the entire process (right panel): the inner region rotates with angular velocity $-\delta\Omega$, while the external part can be considered as non rotating.

5.2.5 Study of the model

In the above section we derived the solution in the case of a neutron star that develops a differential rotation, i.e. subjected to a force of the form of Eq (5.14). We are mainly interested into three main aspects regarding the strain angle: its dependence on the mass, its dependence on the EoS and its dependence on the adiabatic index.

In the previous analysis we focused our attention on the case of *external* forces, where is easier to check that the behaviour in the $c \to 0$ limit is about the same of the uniform rotation one. However, in the astrophysical scenario of glitches, the opposite case is more interesting. In fact, we can model a glitch using the following scheme. We start from an uniform rotating configurations, where both the normal and the superfluid component have the same angular velocity; then, the star is slowed down by the electromagnetic torque, that reduces the angular velocity of the normal component. The superfluid, on the other side, has a frozen vortex configuration and thus does not change its angular velocity, until something triggers the angular momentum exchange between the two components (glitch). The net effect due to this process can be estimated as the difference between the final and initial configuration, that is the one with a rotating core and a non rotating external layer, as represented in Fig. 5.4. For this reason, from now on we study the case of a differential rotating star where only the *inner* part of the star rotates, i.e. where the loading Eq (5.14) is in the form

$$\boldsymbol{f} = \boldsymbol{f}_{cen}\left[\frac{1}{2}\left(1 - \frac{2}{\pi}\arctan\left(-\frac{c/a - r/a}{\xi}\right)\right)\right]. \tag{5.41}$$

In the following all the quantities are normalized as described in section 4.1, in order to make easier the comparison of the results with the ones obtained with uniform rotation.

Different transitional radii

Let us analyze now the impact on the response of the star of a different choice of the transitional radius c. We fix the mass to the standard value $M = 1.4M_\odot$ as a reference. The NS is described in the adiabatic regime $\gamma = 2$ by the SLy EoS, which means that the mass-radius relation corresponding to this EoS is adopted.

As a first step, we select a very wide range of transitional radii, in order to explore very different scenarios, allowing to have a better understanding of the NS behaviour under differential rotation. The chosen values of c are $c = r_c/100, 1/2r_c, 2/3r_c, 0.995r_c$, with $r_c = 0.9a$, which means $c/a = 9 \times 10^{-3}, 0.45, 0.60, 0.896$. We decide not to place the transitional radius exactly at $c = r_c$ to avoid computational problems related to the extension of the differential rotation in the elastic layer: $c = 0.995r_c$ can be seen a numerical "safe" lower limit of the physical value $c = r_c$.

It easy to see that the size of the inner rotating region deeply affects the radial and tangential stresses near the crust-core boundary (see Fig 5.5): the larger the rotating region, the larger the pressure (radial stress) on the crust at $r = r_c$. This is not surprisingly, since the heavy inner core essentially tries to assumes a more oblate configuration, pushing the external non-rotating layer. In this case, contrary to the uniformly rotating scenario, the crust is not directly deformed by the centrifugal force, but it has to adapt its global shape to the rotating core. For this reason, the crust is subject to the maximum pressure at the core-crust interface, and the extension of the rotating region can dramatically change the value of $R_{\ell m}$: the radial stresses for $c = 0.995r_c$ is 9 times larger than the one reached for $c = 2/3r_c$. This is due to two effects: 1) for large c values we have a large fraction of the core that is rotating, and 2) the transition is closer to the non rotating crust. These conclusions are confirmed by the study of equally spaced transitional radii $c = 0.5a, 0.6a, 0.7a, 0.8a, 0.995r_c$,, as reported in Appendix D, where we explore also the behaviour near the crust-core boundary

Our parametric study thus shows that there is a strong dependence of the stellar deformation on c, with larger effects for transitional radii very close to the core-crust boundary. In the following, however, we will use a choice of the transitional radius based on the actual knowledge of the $^1S_0$ wave superfluid extension. Following Ho et al. (2015) and Montoli et al. (2018) we studied the effect of differential rotation between the core and the crust, assuming different extensions of the S-wave superfluid domain, i.e. different extension of the superfluid reservoir. In particular, recalling that we have already studied the limiting case of the superfluid reservoir extended to the whole star (uniform rotation), we consider the case of a superfluid which extends from the neutron drip density to $1\rho_0, 0.75\rho_0, 0.68\rho_0$ and $0.6\rho_0$, where $\rho_0 = 2.8 \times 10^{14}\mathrm{g/cm}^3$ is the nuclear saturation density. Finally, we study also the case of a superfluid domain limited to the crust, the most studied case in the literature.

Strain analysis

For every superfluid extension we can compute the strain angle α, while varying also the stellar masses and the EoSs. The normalized strain angle for a NS with $M = 1.4M_\odot$, $\gamma = 2$, calculated for $r = r_c$ and the various transitional radii corresponding to different S-wave domains is shown in Fig. 5.6. The most interesting feature is well peaked maximum at the equator; as expected, the strain grows for growing c values.

In Fig 5.7 we plot the colour map of $\tilde{\alpha}$, fixed $c = 0.995r_c$. Here the differences with the uniform rotating case (cf Fig 4.4) are even more clear, since for differential rotation the maximum strain is always at the equator, instead that at the poles, and the maximum value of $\tilde{\alpha}^{Max}$ is reached at the core-crust boundary, where the heavy core tries

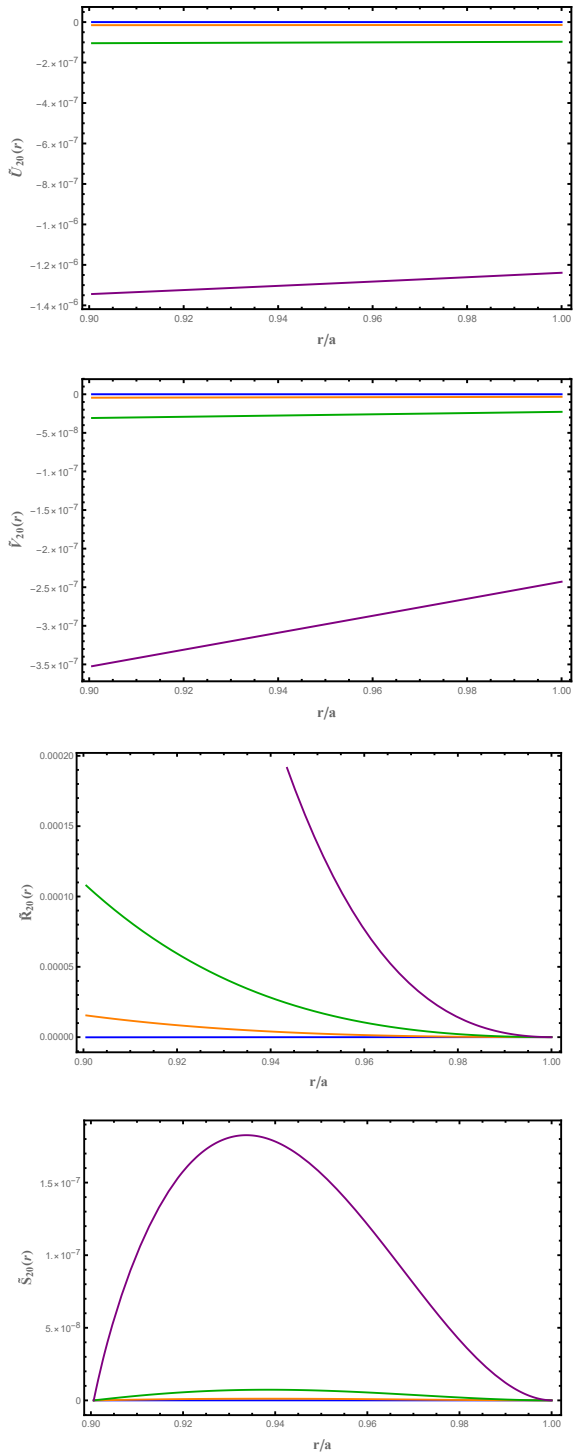

Figure 5.5: The $\tilde{U}_{20}(r)$ (first panel) and the $\tilde{V}_{20}(r)$ (second panel) normalized displacements and $\tilde{R}_{20}(r)$ (third panel) and the $\tilde{S}_{20}(r)$ (fourth panel) normalized stresses as functions of the normalized radius, from $r = r_c$ to $r = a$, for different choices of the transitional radius $c = r_c/100$ (blue), $c = 1/2r_c$ (orange), $c = 2/3r_c$ (green) and $c = 0.995r_c$ (purple). Only the region $r < c$ is rotating.

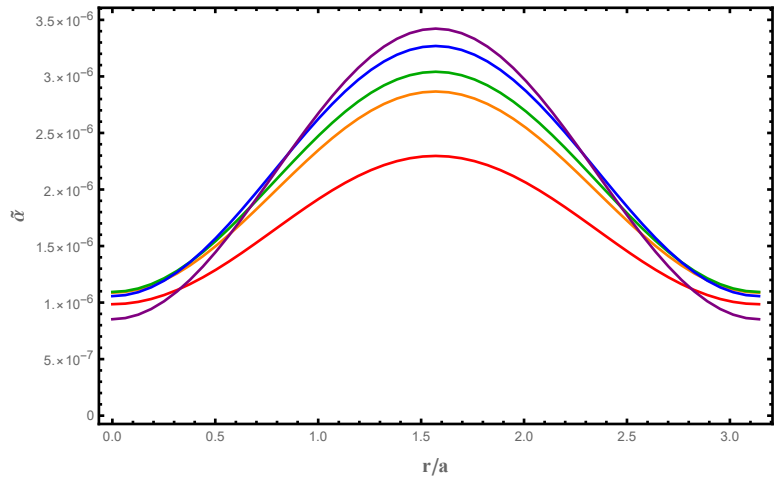

Figure 5.6: Normalized strain angle $\tilde{\alpha}$ for a NS with mass $M = 1.4M\odot$, described by the SLy EoS as a function of the colatitude for different choices of the transitional radius, corresponding at different superfluid extension: $1\rho_0$ (red), $0.75\rho_0$ (orange), $0.68\rho_0$ (green), $0.6\rho_0$ (blue) and $\rho \simeq \rho_{trans}$ (purple). Only the region with $r < c$ is rotating. The strain is calculated at the core-crust boundary $r = r_c$.

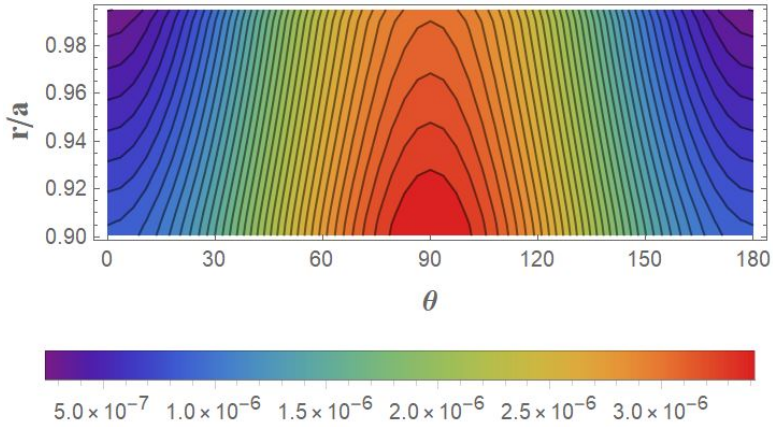

Figure 5.7: Color map of the normalized strain angle $\tilde{\alpha}$ as a function of the colatitude and of the normalized radius r/a, fixed $c \simeq r_c$. The deformation of the crust is due to the rotation of the inner stellar layers $r < c$. The region shown here refers to the crustal layer, from $r = r_c$ to $r = a$ for a NS with mass $M = 1.4M_\odot$. As can be seen, the maximum strain value is reached at the core-crust interface.

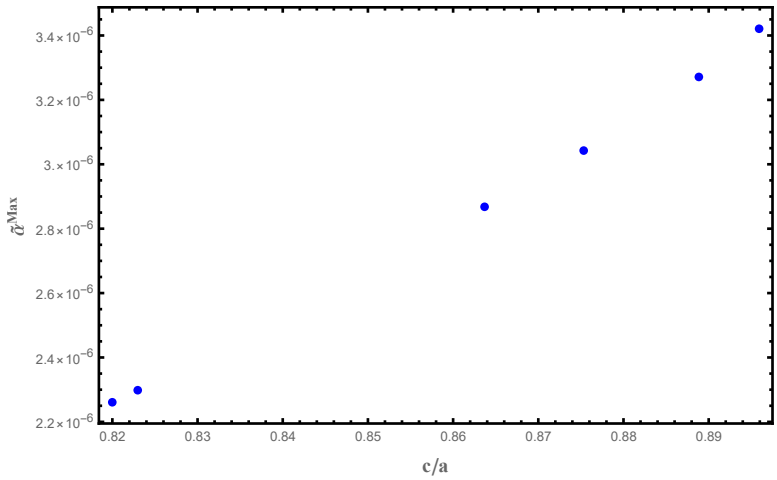

Figure 5.8: Maximum normalized strain angle $\tilde{\alpha}^{Max}$ as a function of the superfluid S-wave extension in terms of normalized stellar radius. The value are calculated for a $M = 1.4M_{\odot}$ NS described by the SLy EoS. The deformation of the crust is due to the rotation of the inner stellar layers $r < c$. The maximum strain obtained in the case of superfluid extending only in the inner crust ($c \simeq r_c$) is roughly 1.5 times the one of a superfluid reservoir reaching the nuclear saturation density ρ_0 ($c \simeq 0.82a$).

to impart its rotation to the crust, instead that at crust-vacuum interface. Furthermore, $\tilde{\alpha}^{Max}$ strongly depends on the superfluid extension, since its value varies of about 50% ranging from ρ_0 to $\simeq \rho_{trans}$ (see Fig 5.8).

The comparison of stars with different masses confirms that also in this case the strain depends on M only weakly. In fact, for differential rotation the ratio $\alpha_1^{Max}/\alpha_2^{Max}$ is smaller than in the uniform rotation scenario ($\alpha_1^{Max}/\alpha_2^{Max} \simeq 4$, cf Fig 4.14), since it is about 2 for $\gamma = 2$.

Pulsar glitches

As explain in the first part of this section, differential rotation can develop during the pulsar's slowdown between two glitches. Using the same approach as that of uniform rotation we calculate the maximum strain angle developed in the time between glitches as (cf. Eq (4.15))

$$\alpha = (d(\Omega - \omega) - d(\Omega))\tilde{\alpha}. \tag{5.42}$$

Also in this case we use the Vela parameters as reference (see Table 4.2), fixing $M = 1.4M_{\odot}$ and $\gamma = 2$. In Fig 5.9 we plot both the maximum strain angle for differential rotation (using different transitional radii) and the one for uniform rotation: the first is always smaller than the latter. Thus, using our simplified approach with only one rotating fluid, we conclude that starting from an unstressed configuration, even the development of a differential rotation cannot produce a strain that is large enough to break the crust.

Finally we explore also the case of a NS described by a different EoS, comparing the results obtained with SLy and BSk21 EoS. Our analysis shows that the general features described above for SLy EoS remains valid also for the BSk21 one; however, as for the uniform rotating case, a stiffer equation of state gives larger strains. In particular, if we

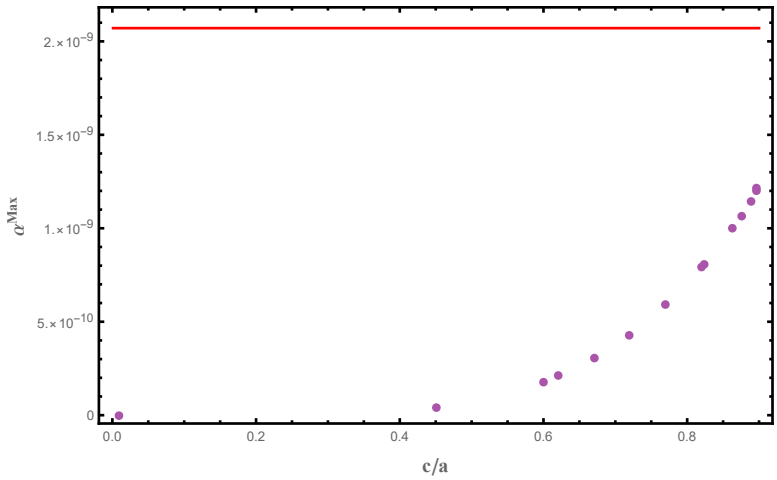

Figure 5.9: Maximum strain angle α as a function of the superfluid extension in terms of normalized stellar radius for a differential rotating star, where only the inner region ($r < c$) is rotating (purple dots). The red line is the maximum strain angle developed with an uniform rotation. The values are calculated for a $M = 1.4M_{\odot}$ NS described by the SLy EoS, using the Vela parameters as reference (see Table 4.2).

	$\rho = \rho_0$	$\rho = 0.75\rho_0$	$\rho = 0.68\rho_0$	$\rho = 0.6\rho_0$	$\rho \simeq \rho_{trans}$
$\alpha_{BSk21}/\alpha_{SLy}$	1.04	1.10	1.12	1.14	1.16

Table 5.1: Ratio of maximum strain angle due to an *internal* rotation, obtained for different choices of the superfluid extension inside the star and different EoS: the name of the equation of state used is in the strain angle's subscript. In this case we fix $M = 1.4M_{\odot}$.

compare the strain angle for a NS with a mass of $M = 1.4M_{\odot}$, we see that with the BSk21 EosS we obtain a value of α that is at most 16% larger than the one given by the softer SLy, as reported in Table 5.1.

Frozen index

In this section we want to explore the impact of different adiabatic index values on the star's behaviour. Following the analysis of the uniform rotating scenario in chapter 4 we focus on two values for the frozen adiabatic index: $\gamma_f = 2.1$ and $\gamma_f = 200$. As expected from the analysis of chapter 4, the NS's response depends strongly on the adiabatic index value, as shown by the comparison of the $\ell = 2, m = 0$ displacements and stresses in the adiabatic and non adiabatic scenarios, Figs 5.10 and 5.11. The reason of such a large discrepancy, as deeply discussed, depends on the smallness of the shear modulus μ with respect to the bulk modulus κ. On the other hand, the displacements (and thus the strains) for different γ show the same patterns for different choices of the transitional radius c, as shown in Fig. 5.12.

Since a stiffer EoS gives larger strain angle values, both the scenarios described by a frozen adiabatic index give values of α that exceed the one of the adiabatic case. However, the strain remains smaller than the corresponding uniform one also for the frozen cases. Differently from the uniform rotating case (cf Fig 4.12), the strain angle's peak

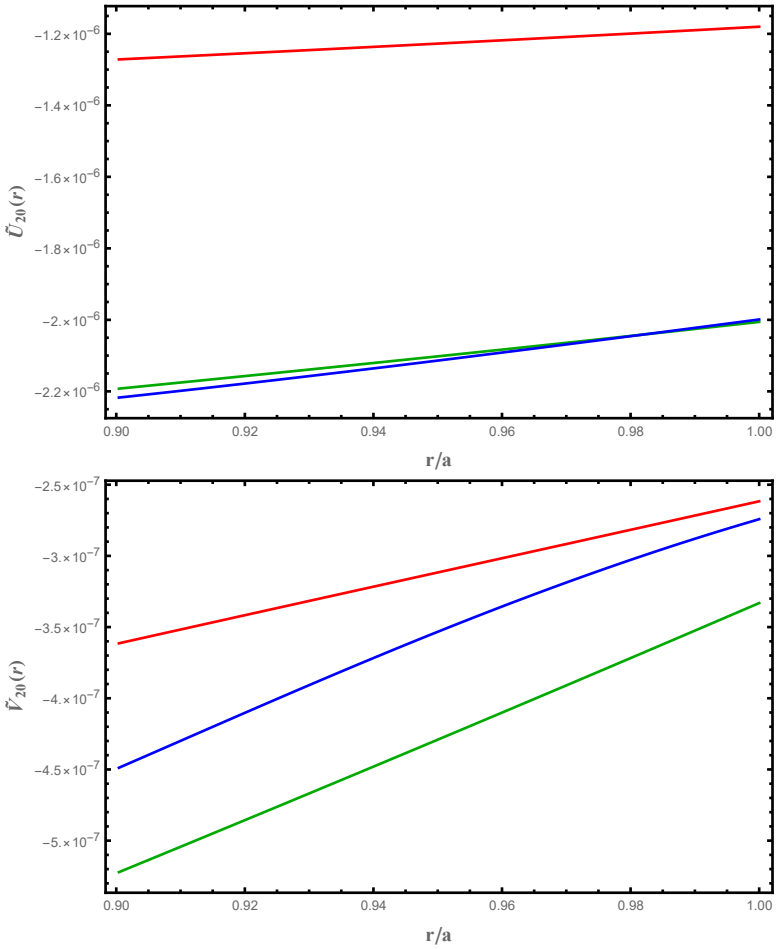

Figure 5.10: Radial $\tilde{U}_{20}$ and tangential $\tilde{V}_{20}$ normalized displacements caused by differential rotation (the region $r < c$ is rotating) as a function of the normalized radius for different values of the adiabatic index: $\gamma = 2$ (red), $\gamma = 2.1$ (green) and $\gamma = 200$ (blue). We choose a NS with a mass of $M = 1.4M_{\odot}$, described by the SLy EoS as a reference.

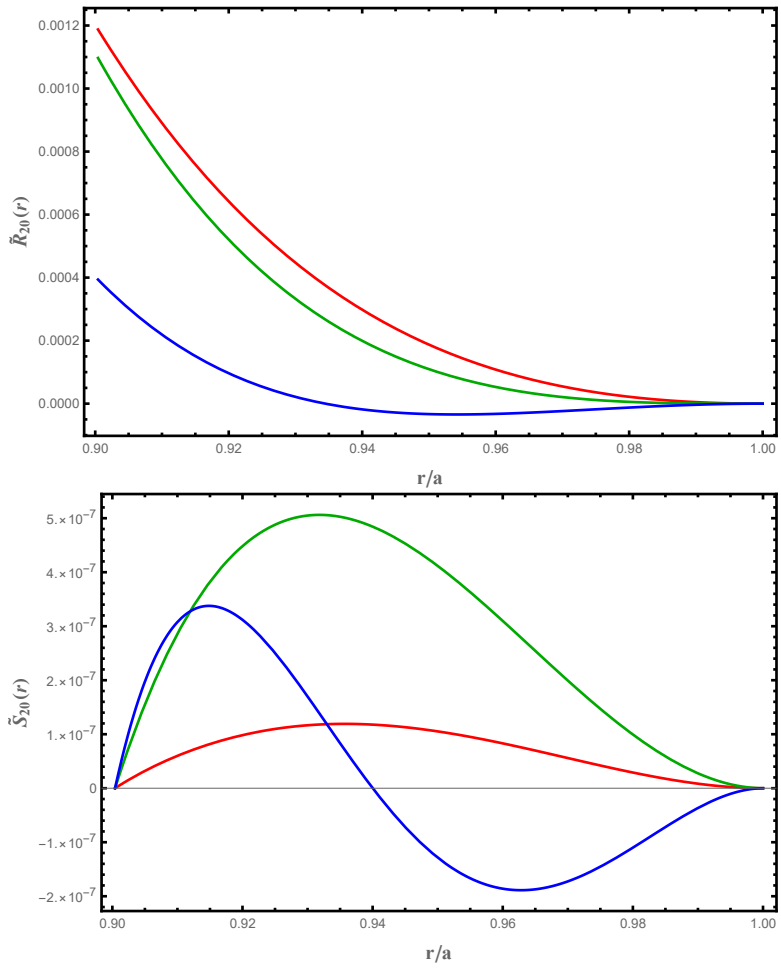

Figure 5.11: Radial $\tilde{R}_{20}$ and tangential $\tilde{S}_{20}$ normalized stresses caused by differential rotation (the region $r < c$ is rotating) as a function of the normalized radius for different values of the adiabatic index: $\gamma = 2$ (red), $\gamma = 2.1$ (green) and $\gamma = 200$ (blue). We choose a NS with a mass of $M = 1.4M_{\odot}$, described by the SLy EoS as a reference.

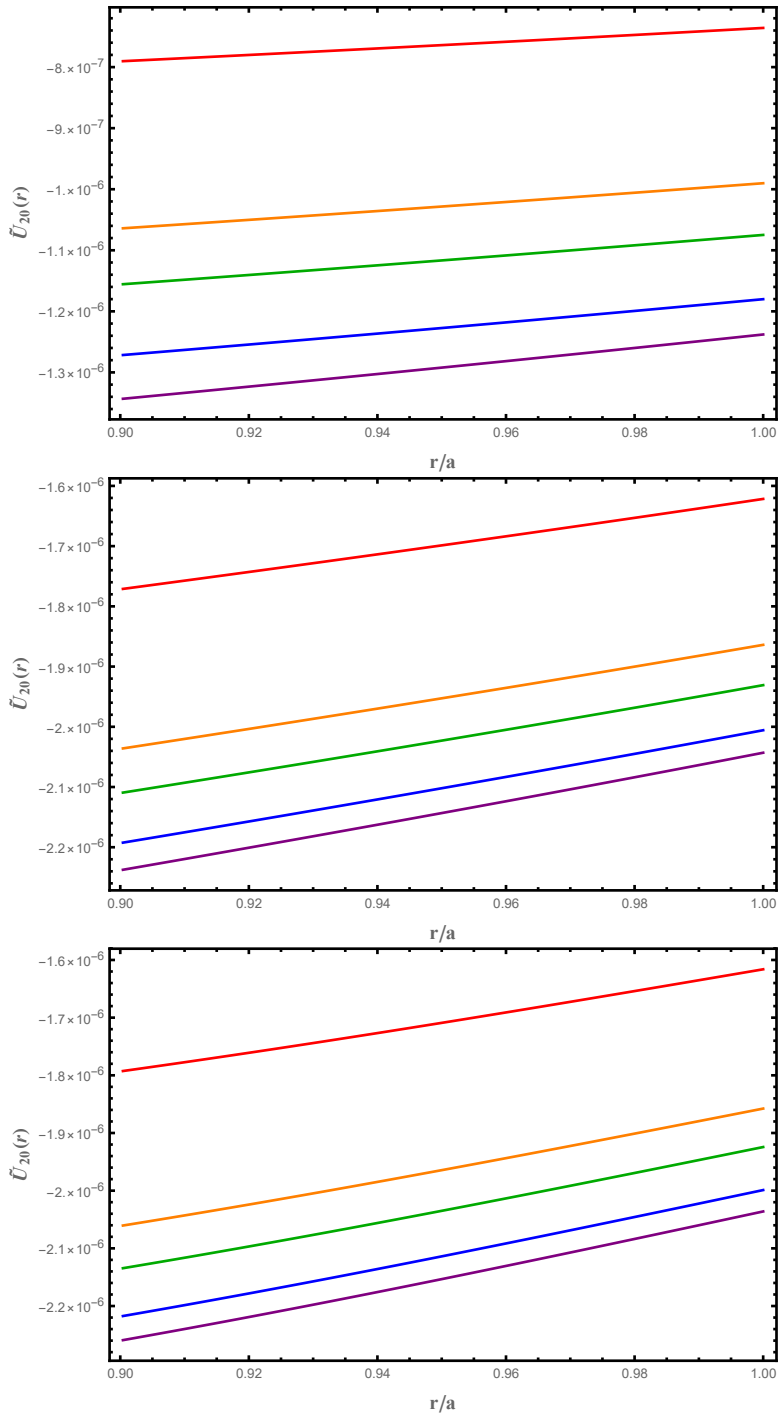

Figure 5.12: Radial $\tilde{U}_{20}$ normalized displacements for stars with different adiabatic index $\gamma_{eq} = 2$ (top panel), $\gamma = 2.1$ (middle panel) and $\gamma = 200$ (bottom panel), as a function of the normalized radius r/a, for different values of the transitional radius, corresponding to different superfluid cases: $1\rho_0$ (red), $0.75\rho_0$ (orange), $0.68\rho_0$ (green), $0.6\rho_0$ (blue) and $\rho \simeq \rho_{trans}$ (purple). In all cases the rotating region is the inner one ($r < c$).

is reached always at the equator, at the core-crust boundary, regardless of the adiabatic index value, see Fig. 5.13.

5.3 Magnus Force and slack pinning

The pinning interaction is not the only force that acts on a vortex line. Following the two component model, we can imagine to divide the whole star into a normal component composed of the crustal lattice and the charges of all the star, and the neutron superfluid part. Pinning forces force the vortex lines to have the same velocity as that of the normal component, so that they rotate as a rigid body with angular velocity Ω_p: this fact gives rise to the Magnus force, which can be written as (Langlois et al. 1998)

$$\boldsymbol{f}_m = \kappa \rho_n v_\ell \hat{\boldsymbol{x}}, \tag{5.43}$$

where $\hat{\boldsymbol{x}}$ is the cylindrical radius unit vector, ρ_n is the neutron superfluid density and $\boldsymbol{v}_\ell$ is the speed of a segment of vortex line as seen in the local frame comoving with the superfluid flow. In the case of pinning this is the relative speed of the normal component with respect to the superfluid one and thus we can write

$$|\boldsymbol{f}_m| = \kappa \rho_n r \sin\theta \left(\Omega_p - \Omega_n\right), \tag{5.44}$$

with Ω_n the angular velocity of the superfluid. Here f_m must be intended as a force per unit lenght. We call *slack pinning*[4] the case in which the vortices feel only the local pinning and the mesoscopic Magnus force. In this case, the local unpinning condition can be easily expressed as

$$|\boldsymbol{f}_m| = \overline{f}_p. \tag{5.45}$$

Here we indicate with the overline the pinning force per unit length, in order to distinguish it from the pinning body force. In the literature the above equation is usually rewritten in terms of a critical lag between the normal and the superfluid component as (Antonelli et al. 2018)

$$\Omega^{crit}(r,\theta) = \frac{\overline{f}_p(r)}{\kappa \rho_n(r)\, r \sin\theta}. \tag{5.46}$$

Thus, during the pulsar's slowdown we have both the stressing effect of the centrifugal force and the one of the pinning force on the crustal lattice. The conflict on each vortex between Magnus force and pinning one will cause the loads to build up to a critical point at which there will be a breakdown, bringing about a discontinuous readjustment (glitch). We expect that the breakdown can be reached in two main different manners:

- A sudden unpinning of many vortices, due to the breaking of the pinning bonds (Anderson & Itoh 1975; Link & Epstein 1991).

[4]The name "slack" is used to distinguish this situation from the "rigid vortex" one, where the infinite rigidity assumption is used as prescription that helps modelling the dynamical configuration of the vortex lines. In that case one has an axially symmetric and rigid configuration of vortices that cross the star as shown in Fig 5.14.

We underline however that here *slack* refers only to the behaviour of vortices at the macroscopic hydrodynamic scale: a completely slack vortex (that can stretch at the mesoscopic scale without any energy cost) would bend even over lengths comparable to the radius of the Wigner-Seitz cells in the crust, contrary to the "slack" vortices here defined, that are are not tensionless at the mesoscopic scale.

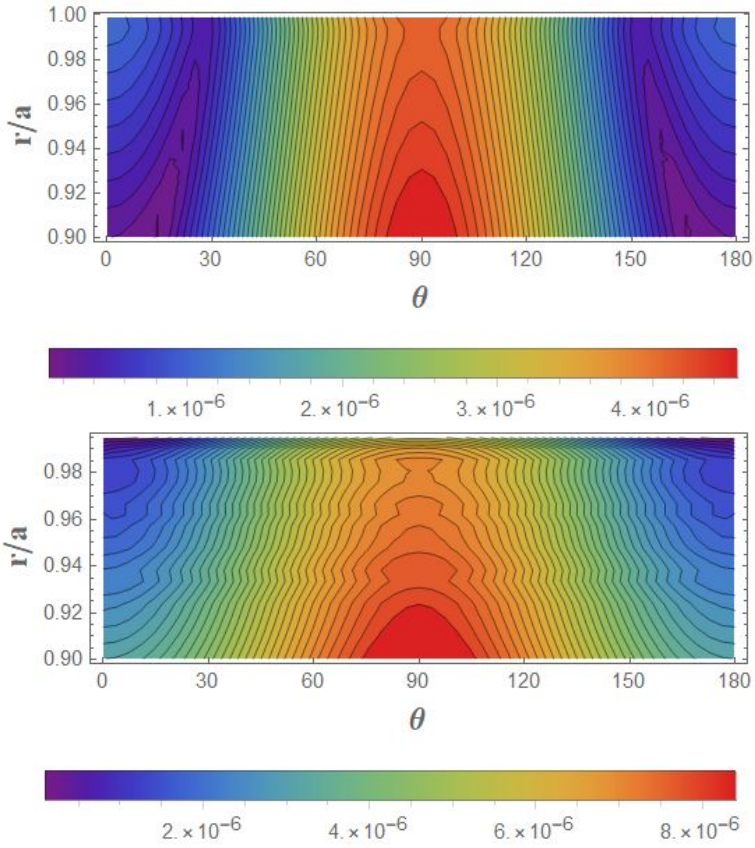

Figure 5.13: Color map of the normalized strain angle $\tilde{\alpha}$ due to differential rotation as a function of the colatitude and of the normalized radius r/a for two adiabatic index values: $\gamma_f = 2.1$ (top) and $\gamma_f = 200$ (bottom). In both cases the centrifugal force acts only in the inner layers, i.e. for $r < c$. The region shown here refers to the crustal layer, from $r = r_c$ to $r = a$ for a NS with a mass of $M = 1.4 M_\odot$. As can be seen, the maximum strain value is always reached at the equator at the core-crust interface, contrary to the uniform rotating case, cf Fig 4.12.

- The crust lattice breaks before vortex lines can unpin from it, as suggested in Anderson & Itoh (1975) and studied in detail by Ruderman (1976). This starquake, in turn, will trigger the vortex exchange between the core and the crust, that we can observe as a glitch. Link & Epstein (1996) proposed also a related model, the vortex creep model (Alpar et al. 1984), in which the coupling between the vortices and the crust is strongly temperature dependent. In this case the breaking of the crust causes a sudden local increase of the inner crust temperature that can then be shown to induce a glitch.

In order to discriminate between the above main scenarios, in this section we will study the deformation due to mesoscopic vortices pinning to the crust. As said above, entrainment provides a non-dissipative interaction between the normal and superfluid components, and thus affects also the vortex dynamics. Following the Newtonian two-fluids formalism presented in Prix (2004), we can write the momenta per baryon of each component $\boldsymbol{p}_p$ and $\boldsymbol{p}_n$ as linear combinations of the velocities of both fluids. In particular, the azimuthal component of the momenta can be put in the form

$$p_{p\varphi} = m_p x \left(\Omega_p + \varepsilon_p \Omega_{np}\right), \tag{5.47}$$

$$p_{n\varphi} = m_n x \left(\Omega_p + (1-\varepsilon_n)\,\Omega_{np}\right), \tag{5.48}$$

where m_p, m_n are the the mass per baryon of the two components and the entrainment parameters $\varepsilon_p, \varepsilon_n$ satisfy the condition $m_p n_p \varepsilon_p = m_n n_n \varepsilon_n$. It is useful to introduce an auxiliar angular velocity Ω_v such that $x\Omega_v = p_{n\varphi}/m_n$, i.e.

$$\Omega_v = \Omega_p + (1-\varepsilon_n)\,\Omega_{np}, \tag{5.49}$$

where

$$\Omega_{np} = \Omega_n - \Omega_p. \tag{5.50}$$

Ω_v is directly related to the Feynman-Onsager relation, Eq (5.11)

$$\kappa n_v = 2\Omega_v + x\partial_x \Omega_v. \tag{5.51}$$

The mesoscopic force due to pinning, Eq (5.55), is proportional to the number of vortex per unit area n_v, that in general is a function of the cylindrical radius x. Since we are interested in the maximum lag between the two components, following the model by Antonelli (2017) we impose (cf Eq (5.46))

$$\Omega_{np} = \omega^{crit}. \tag{5.52}$$

Thus we have

$$n_v = \frac{1}{\kappa}\left[2\Omega_p + (1-\varepsilon_n)\,2\omega^{crit}\right] + \frac{x}{\kappa}\frac{\partial\left[\Omega_p + (1-\varepsilon_n)\,\omega^{crit}\right]}{\partial x}.$$

Now, for simplicity, we assume that the angular velocity of the two fluids Ω_p, Ω_n are independent from the stellar radius. Interestingly, if we calculate the ratio between the first and the second term in the RHS of the above equation, using the Vela parameters of Table 4.2 and varying the stellar mass between 1 and 2 solar masses, we obtain

$$0 \leq \frac{x\partial_x\Omega_v}{2\Omega_v} \simeq \frac{x\partial_x\Omega_v}{2\Omega_p} \leq 0.10, \tag{5.53}$$

in the whole star. For this reason, to estimate the vortex density we use the approximate expression

$$n_v \simeq \frac{2\Omega_p}{\kappa}, \tag{5.54}$$

that does not depend on the distance from the rotation axis. Thus this loading has a spherical symmetry. Finally, we can express the body force due to slack vortex pinning as

$$|\mathbf{f}_P(r)| = \frac{2\Omega_p}{\kappa}\overline{f}_P(r). \tag{5.55}$$

Note that this force, having the same symmetry as the centrifugal one, can be decomposed using only the two harmonics terms $\ell = 0$ and $\ell = 2$.

5.3.1 Pinning force

As already said, the vector quantity $\boldsymbol{f}_P(x)$ is unfortunately not well defined, even if there are attempts to model it at the mesoscopic scale as the gradient of a spherical pinning potential (Warszawski & Melatos 2013; Haskell & Melatos 2016). However, in order to estimate the intensity of the force in Eq (5.55), we need the pinning threshold f_P resulting from the vortex-lattice interaction in the inner crust. Seveso et al. (2016) have proposed a numerical simulations, accounting for finite single vortex tension and random orientation to the lattice, to evaluate $f_P(n_b)$ at different densities n_b in the inner crust. We use the pinning profile corresponding to in-medium suppressed pairing gap[5], as shown in Fig 5.15. At the moment, this is the only detailed and density dependent estimate of the mesoscopic vortex-lattice interaction. We remark that the quantity f_P studied in Seveso et al. (2016) is not interpreted as the modulus of $\boldsymbol{f}_P$ but it represents the maximum value that the pinning force can sustain before letting the vortex free to move. We also force $\boldsymbol{f}_P$ to be zero outside the crust, i.e. we do not take into account core pinning. Theoretical estimates suggest that the protons in the core could form a type-II superconductor (Baym et al. 1969); thus the vortex motion could also be impeded by the interaction with magnetic fluxtubes. However, recent phenomenological study (Haskell & Pizzochero 2013) has shown that this pinning interaction should be small except for magnetars.

For the analysis of the model we use the equations described in section 5.2.3, changing only the force acting on the star. All the quantities are normalized using the reference values of Table 4.1 and the peak of the pinnig force f_{peak} inside the crust: for our $M = 1.4M_\odot$ standard NS we obtain $f_{peak} = 1.67 \times 10^{15}\mathrm{dyn/cm}$.

5.3.2 Adiabatic scenario

We start our study with a standard NS with a mass of $M = 1.4M_\odot$, described with the SLy EoS. In Fig 5.16 we plot the normalized displacements and stresses in the crust for $\ell = 2, m = 0$ harmonic, as an example. As in the other sections, we are mainly interested in the study of the strain dependence on the mass and on the localization of its peak inside the crust. For the case of slack pinning, the maximum strain angle is at the poles of the star, as can be seen from the color map in Fig 5.17. Furthermore, if we look only at the region near the maximum, we can see that the value of $\tilde{\alpha}$ depends very weakly on the crustal depth, i.e. we have essentially an uniform strained layer between $r_c \leq r \leq a$.

Mass does not affect much the α modulus, that, however, contrary to the previous studied scenarios, grows going from lighter to heavier stars. In this case, in fact, the force

[5]This is the case $\beta = 3$ and $L = 5000$ of Seveso et al. (2016), see Table 3 therein.

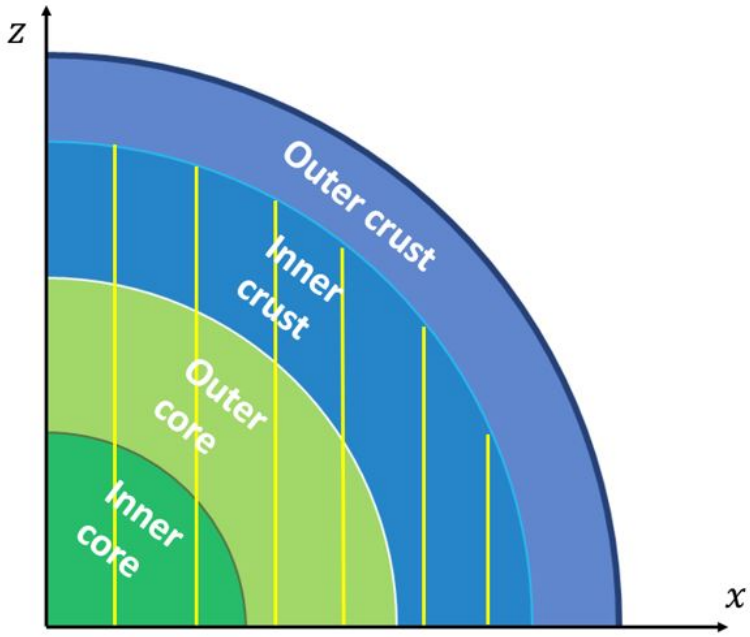

Figure 5.14: Sketch of the stellar configuration (out of scale) in the case of the "rigid vortex" extending throughout the whole star, i.e. in the case of the superfluid domain extends from the inner crust to the center of the star.

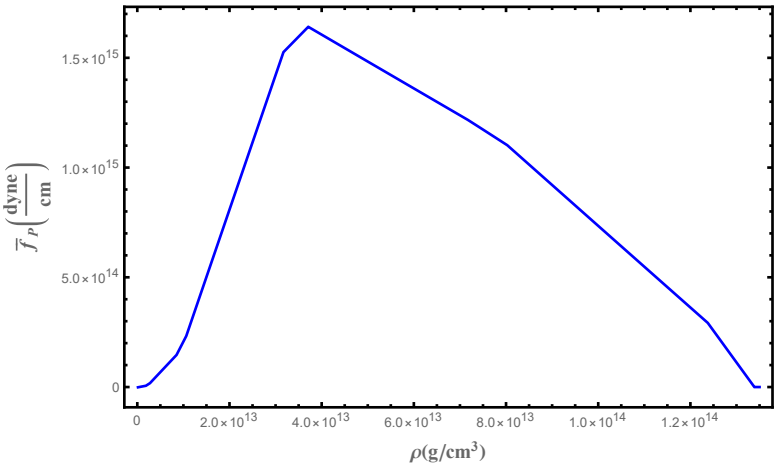

Figure 5.15: The pinning force profile per unit length f_P. We constrain the pinning force profile to be zero outside the density range $\rho_{drip} \leq \rho \leq \rho_{trans}$. The original profile (Seveso 2014) has been interpolated.

	$\gamma = 2$	$\gamma = 2.1$	$\gamma = 200$
$\tilde{\alpha}^{Max}$	0.0006	0.00025	0.00008

Table 5.2: Maximum normalized strain angle due to slack pinning for a $M = 1.4M_{\odot}$, described by the SLy EoS, obtained for different choices of the adiabatic index values $\gamma = 2, 2.1, 200$.

does not depend on the mass and the radius of the star: thus the same loading, acting on a thinner crust, cause a larger strain. In particular, for the slack pinning scenario we found the ratio $\alpha_1^{Max}/\alpha_2^{Max} \simeq 0.86$. For the uniform and the differential rotating cases, the maximum strain angle is a decreasing function of the stellar mass, since the deformation is essentially ruled by the compactness of the object. In the case of slack pinning, instead, the comparison between stars described with different EoSs shows an opposite result: stiffer EoSs (BSk21) give slighter smaller maximum strain angle than the softer ones (SLy). For example, for a $M = 1.4M_{\odot}$ NS the value of α^{Max} obtained with BSk21 is about 0.9 times the one obtained with SLy. This is probably again due to the fact that stiffer stars have also larger crusts, developing smaller strains when subject to the same stressing force.

5.3.3 Non adiabatic scenario

We move on by analysing the non adiabatic response for $\gamma_f = 2.1, 200$. As we have come to expect, even a small change in the adiabatic index gives a solution that is easily distinguishable from the adiabatic one, both in the displacements and in the stresses, as reported in Figs 5.18 and 5.19, respectively.

However, the strain angle pattern for $\gamma = 2.1$ is similar to the $\gamma = 2$ case, while the incompressible limit $\gamma = 200$ shows a completely different one, as the reader can check by comparing the normalized strain angle of Fig 5.20 with the one of the previous section, Fig 5.13. The maximum strain goes from the poles towards the equator, with a clear peak only near the more external part of the crust. Furthermore, the maximum value of the strain angle decreases for increasing adiabatic index value, contrary to the uniform and differential rotating cases, as reported in Table 5.2.

5.3.4 Pulsar glitches

As for uniform and differential rotation, we calculate the maximum strain angle developed during the slowdown between two glitches. As a reference we consider always the Vela pulsar, whose typical parameters are reported in Table 4.2. In the case of slack pinning the pre-factor that as to be used to obtain the strain is

$$d_{pinning} = f_{peak}\frac{a}{\mu_c}\omega = 1.91\times10^{-4}\left(\frac{f_{peak}}{1.67\times10^{15}\mathrm{dyn/cm}}\right)\left(\frac{a}{1.167\times10^{6}\mathrm{cm}}\right)\left(\frac{\mu}{10^{30}\mathrm{dyn/cm^2}}\right)^{-1}\left(\frac{\omega}{10^{-2}\mathrm{rad/s}}\right), \tag{5.56}$$

where we remind that $\omega = |\dot{\Omega}|\,\langle t_{gl}\rangle$. The strain angle reached for the typical Vela parameters, fixing $\gamma = 2$, is

$$\alpha_{pinning} \simeq 9\times10^{-10}, \tag{5.57}$$

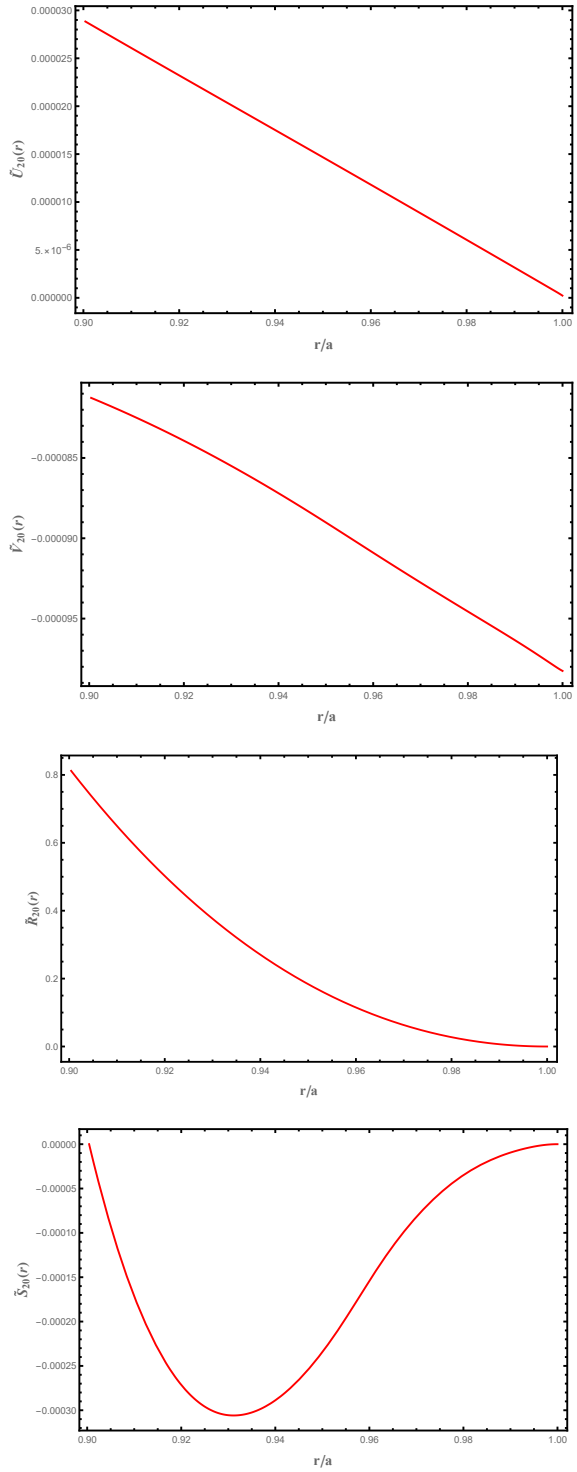

Figure 5.16: The $\tilde{U}_{20}(r)$ (first panel) and the $\tilde{V}_{20}(r)$ (second panel) normalized displacements and $\tilde{R}_{20}(r)$ (third panel) and the $\tilde{S}_{20}(r)$ (fourth panel) normalized stress as functions of the normalized radius, from $r = r_c$ to $r = a$, for slack pinning. This is the response of a NS with $M = 1.4M_{\odot}$ described with the SLy EoS.

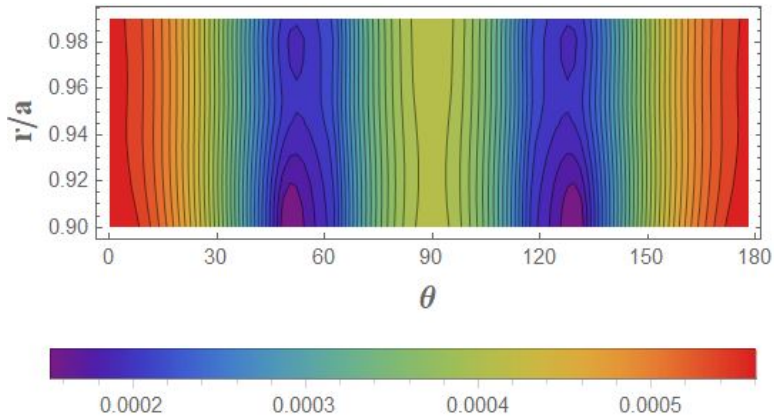

Figure 5.17: Color map of the normalized strain angle $\tilde{\alpha}$ as a function of the colatitude and of the normalized radius r/a for slack pinning acting on the crust, fixed $\gamma = 2$. The region shown here refers to the crustal layer, from $r = r_c$ to $r = a$ for a $M = 1.4M_\odot$ NS. As can be seen, the maximum strain value is reached near the poles and is essentially uniform through the crust.

i.e. a value even smaller than the one due to uniform rotation. Thus, also in this case we can conclude that, starting from a unstressed configuration, the strain developed between two glitch events is not large enough to cause a starquake. In this sense the first of the two possible scenarios depicted in the first part of section 5.3 has to be preferred: pinning has a very important role in the angular momentum exchange from the superfluid to the normal component, but seems to have a very weak stressing effect on the crust. In other words, our model suggests that it is hard to break the crust before the vortex unpinning, i.e. it is unlikely that starquakes are the triggers of glitches.

5.4 Outlook

In this chapter we investigated two loadings proposed in the NSs' literature as possible mechanism for breaking the crust: differential rotation and slack pinning. Both these forces are due to the presence of a neutron superfluid in the inner crust and in the NS core. This is a clear manifestation of peculiar characteristics of the NS's physics: the interior of this object can be modeled as an inviscid fluid, but also its macroscopic quantum features are to be taken into account.

Despite the fact that, following our Newtonian simple inter-glitch loading scenario, slack pinning and differential rotation cannot directly cause the breaking of the crust, the analysis of the deformation underlines the deep difference of the star's response in these cases with respect to the uniform slowdown studied in the previous chapter. In this sense, our approach can be seen as a complementary study of the dynamical fluid model for glitches (e.g. (Antonelli 2017)), since it gives information on the effect of pinning on the pulsar's elastic layer.

This chapter concludes our analysis of forces directly related to glitches. In fact, in the next section we will use our model to study a completely different group of stars, i.e. very fast rotating pulsars, and a completely different topic: gravitational waves emission.

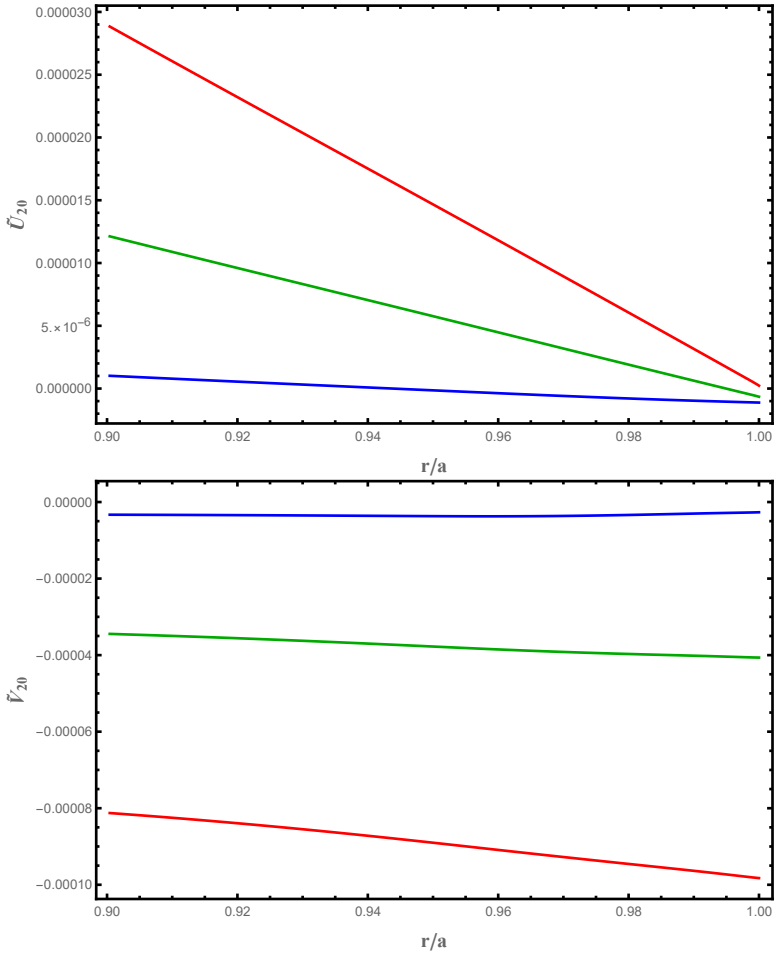

Figure 5.18: Radial $\tilde{U}_{20}$ and tangential $\tilde{V}_{20}$ normalized displacements a function of the normalized radius for slack pinning and different values of the adiabatic index: $\gamma = 2$ (red), $\gamma = 2.1$ (green) and $\gamma = 200$ (blue).

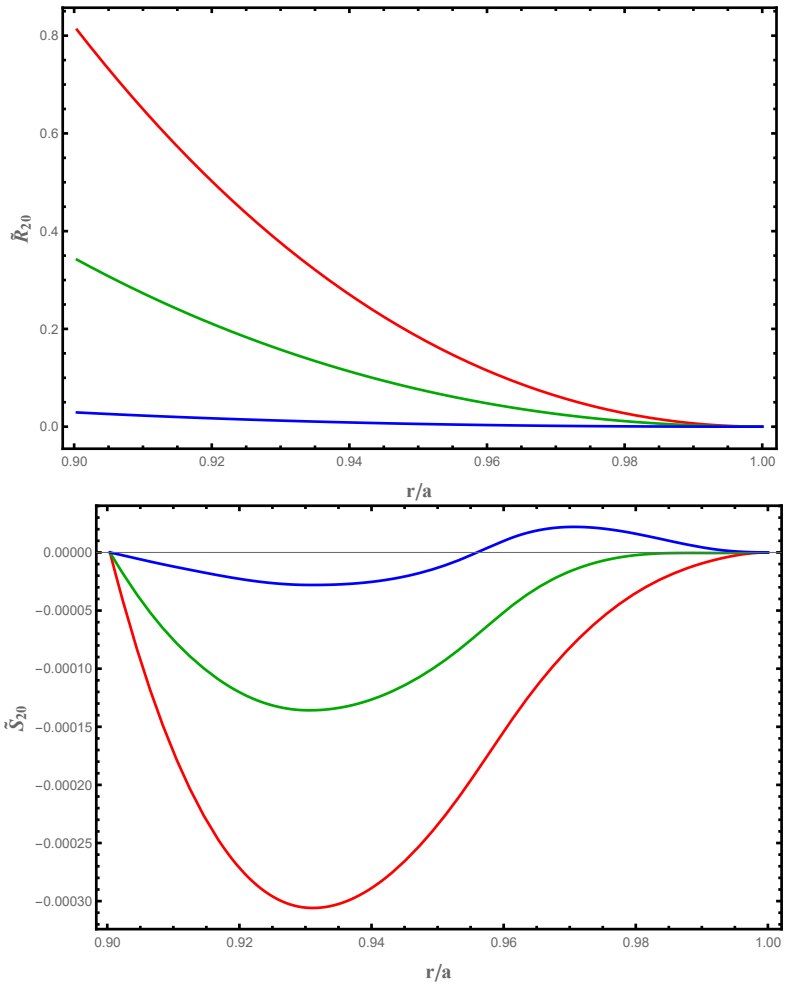

Figure 5.19: Radial $\tilde{R}_{20}$ and tangential $\tilde{S}_{20}$ normalized stresses a function of the normalized radius for slack pinning and different values of the adiabatic index: $\gamma = 2$ (red), $\gamma = 2.1$ (green) and $\gamma = 200$ (blue).

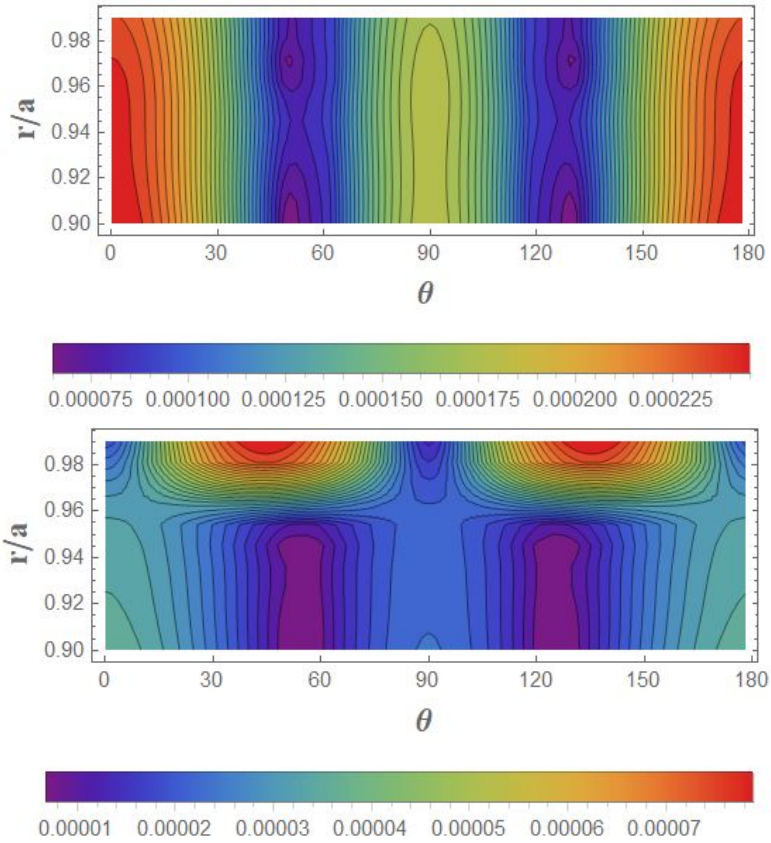

Figure 5.20: Color map of the normalized strain angle $\tilde{\alpha}$ as a function of the colatitude and of the normalized radius r/a for slack pinning in the crust, fixed $\gamma = 2.1$ (top) and $\gamma = 200$ (bottom). The region shown here refers to the crustal layer, from $r = r_c$ to $r = a$ for a $M = 1.4 M_\odot$ NS. As can be seen, the maximum strain value is reached near the poles and is essentially uniform throughout the crust for $\gamma = 2.1$, while for $\gamma = 200$ it is focused near the star's surface, at the intermediate colatitudes $\theta \simeq \pi/2, 3/4\pi$.

Part V
Gravitational waves

CHAPTER 6

Starquakes on fast rotating pulsar

6.1 Accreting pulsars

A pulsar is a sparking dynamo. The voltage produced by a neutron star depends on its rotation period P and its magnetic field B. During the NS's life, when this voltage drops below the critical value needed for copious pair production, the star will stop acting as a pulsar, i.e. a *pulsating* source (Ruderman & Sutherland 1975). In the $P - \dot{P}$ diagram the region to the right of this critical voltage line is called the graveyard of pulsars, see Fig 6.1.

In 1975 Hulse & Taylor (1975) (HT) discovered a peculiar pulsar, with an anomalous combination of short period and very low magnetic field (cf section 1.4). It was anomalous because, on the one side the high frequency of the NS suggests a very recent origin of the object, but on the other side the usually low magnetic field suggested on the contrary that the star might be very old. Furthermore, this was the first detected pulsar in a binary system. The combination of all these characteristics was then reconciled in the picture of a *recycled pulsar*, term coined by Radhakrishnan and his colleagues.

The idea is quite simple: a normal pulsars, after million years of life, died naturally, going in the $P - \dot{P}$ diagram graveyard region. Its magnetic field had decayed, maybe due to ohmic resistance or due to its binary history (accretion). Subsequently, the star is resurrected from its graveyard due to the spinning up of the accretion phase, i.e. thanks to the angular momentum gained from the material infalling from its companion.

Interestingly the first suggestions that accretion could be a mechanism to spin up a NS came earlier of the HT discovery by Pringle & Rees (1972) and Davidson & Ostriker (1973). Soon after the observation of that particular pulsar, Bisnovatyi-Kogan & Komberg (1976) and Smarr & Blandford (1976) argued that its characteristics might be understood in terms of its binary history. The next question to ask is then what would be the pulsar's frequency at the end of the spin up phase. To answer to this question we need some further ingredients.

One of the first idea regards the interaction between the accretion disks and the stellar magnetic field. Once the companion star overflows its Roche Lobe, matter can flow towards the NS, forming an accretion disk around it. By assuming that the gas pressure dominates, one finds that material flows in Keplerian orbits, with orbital frequency

$$\nu_K = \frac{1}{2\pi}\sqrt{\frac{GM}{r^3}} \simeq 767 \left(\frac{M}{1.4M_\odot}\right)^{1/2} \left(\frac{r}{20\,\mathrm{km}}\right)^{3/2}. \tag{6.1}$$

Then we can define the *corotation radius*

$$r_{co} = \left(\frac{GM}{\Omega^2}\right)^{1/3}, \tag{6.2}$$

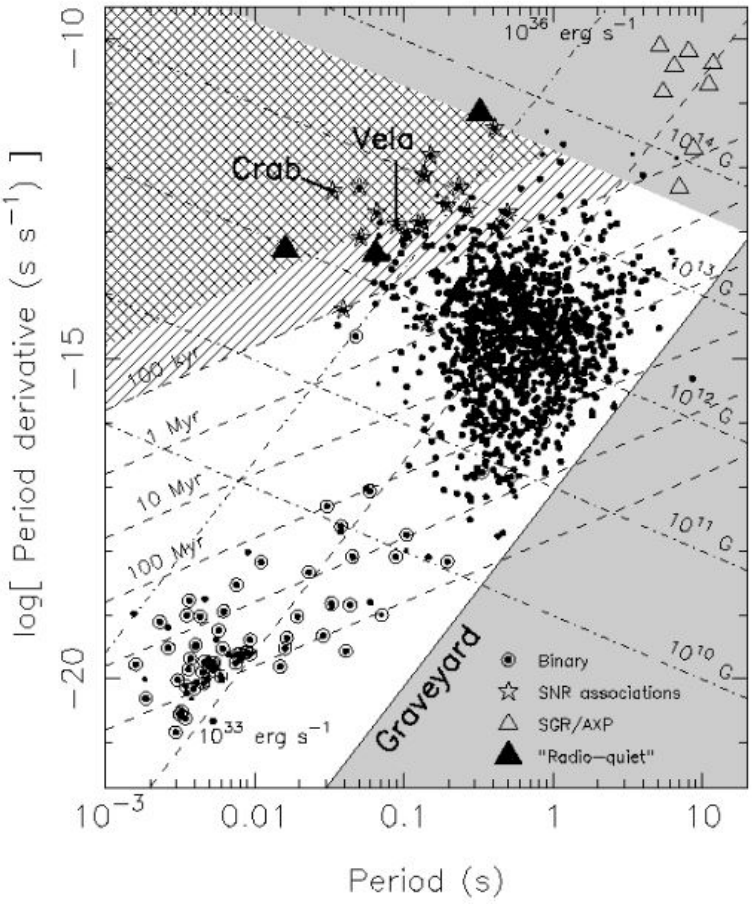

Figure 6.1: $P - \dot{P}$ diagram for the pulsars population. The region in the bottom right of the panel, beyond the *death line*, is the graveyard. Credit Lorimer & Kramer (2004).

which is the location where the gas rotates at the same angular velocity Ω as that of the NS. The gas can rotate in this way provided it is not close enough to be perturbed by the weak magnetic field of the NS: this happens at the *magnetospheric radius* r_m, defined as the radius where the energy of the free-falling gas becomes comparable to the magnetic energy of the pulsar magnetosphere. The gas accreting on the star is driven to the magnetic poles and, at the same time, the magnetic field is distorted by the infalling material. This coupling, between the field lines and the disc, results in a torque acting on the star that can spin it up or down, depending on the relative difference between the magnetospheric and the corotation radius: if $r_{co} > r_m$, matter will accrete, and spin up the star. As the star is spun up, r_{co} becomes smaller and smaller till, eventually, an equilibrium period is attained by the neutron star at which $r_m = r_{co}$. Conversely, if $r_m > r_{co}$, the NS spins faster than the disc, which spins the star down.

The main efforts we have to make is to estimate r_m, which is a poorly known quantity. In the simplified situation of spherical symmetric accretion, one can calculate the *Alfven radius*[1] (Pringle & Rees 1972)

$$r_A = \left(\frac{\mu^4}{2GM\dot{M}}\right)^{1/7}, \tag{6.3}$$

where $\mu = Ba^3$ is the magnetic moment of the pulsar and $\dot{M}$ is the mass accretion rate. The magnetospheric radius can then be written as

$$r_m = \xi r_A, \tag{6.4}$$

where ξ is a correction factor due to the non spherical-geometry of the problem, and it is known to typically fall in the range $0.5 - 1.4$ (Wang 1996).

This simple model has been examined in detail by White & Zhang (1997). They found that, at least for the data available at the time, this scenario implies an unexpected correlation between the infalling material accretion rate and the NS magnetic field strength (which would also need to be higher than expected).

Observation of Low-Mass X-ray Bynaries (LMXBs) has shown a paucity of stars rotating near the centrifugal breakup limit[2] (Lattimer & Prakash 2007; Chakrabarty 2008), opening the outstanding question of why these object seems to spin well under that limit. In fact, preliminary estimates by Cook et al. (1994) suggest that the spin-up timescale for NS in LMXBs should be large enough to allow them to reach at least 1 KHz. On the contrary, the actual fastest spinning accreting neutron star has $\nu = 599$ Hz (Galloway et al. 2005), and also millisecond pulsars, that are thought to be the ultimate fate of LMXBs, rotate slower than the breakup frequency. In particular, the actual distribution of the Accreting Millisecond X-ray Pulsars (AMXPs) gives an experimental maximum spin frequency of 730 Hz (Chakrabarty et al. 2003). One possible explanation for this behaviour is that this kind of pulsars emit gravitational waves, that make them slow down. In particular, many works (Bildsten 1998; Ushomirsky et al. 2000; Watts et al. 2008), suggest that accreting millisecond pulsars can reach an equilibrium configuration where the angular momentum gained from the infalling material is lost by gravitational waves emission. The perturbations that can trigger the quadrupolar deformation, and then this emission, can be divided roughly into two groups: static perturbations (in the frame of

[1] Consider the case of spherical symmetric fre-falling accretion, assuming also that the magnetic field of the NS is essentially dipolar $B = \mu/r^3$. In this configuration the magnetospheric radius is called Alfven radius.

[2] A very rough estimate of the frequency after which the centrifugal force tears apart the star can be obtained by comparing the rotation and Keplerian frequency, as defined in Eq (6.1): one finds $\nu_{limit} \approx 1$KHz.

the star), which are called *mountains*, and dynamic ones, i.e. modes of oscillation of NSs. In this chapter we will focus our attention only on the first scenario.

In the literature, two main mechanisms that are able to produce a static, strong ellipticity have been studied, namely: thermal mountains (Bildsten 1998; Ushomirsky et al. 2000; Haskell et al. 2015) and magnetically confined mountains (Cutler 2002; Melatos & Payne 2005; Haskell et al. 2008; Vigelius & Melatos 2009; Priymak et al. 2011). The first are due to electron captures and pycno-nuclear reactions that heat the accreted material deep into the crust. The latter, instead, is caused by a local enhancements of the magnetic field structure (due to perturbation related to accretion) that can sustain mountains. As said in section 2.2.1, multi-million molecular dynamics simulation have shown that the crustal breaking strain can be quite large (Horowitz & Kadau 2009), and therefore that the crust can, in principle, sustain a maximum ellipticity that is detectable, via gravitational waves emission, from Earth (Haskell et al. 2006; Johnson-McDaniel & Owen 2013). Using the high breaking threshold of the crust, and modeling a NS as a homogeneous, incompressible object, Fattoyev et al. (2018) claimed that starquakes can happen only on accreting, rapidly rotating star. In their paper they also introduced the hypothesis that the breaking of the crust might produce a quadrupolar deformation large enough to prevent the stellar spin up. However, in Fattoyev et al. (2018) the ellipticity caused by this effect was not self-consistently calculated as well as the evolutionary path-i.e. the reaching of the equilibrium angular velocity-of the NS.

In this chapter we will use our model to study the deformation of a rotating, compressible, non-magnetized, self-gravitating NS, due to a latter third mechanism that can act as a trigger: *starquakes*. In particular, we will explore the following physical picture. Imagine a NS that is accreting mass from a companion. The infalling material will create a disk that transfers angular momentum to the star, thus spinning-up the central object. The NS will rotate faster and faster, until a breaking threshold is reached: in that moment we'll have a starquake. This events alters the stellar axisymmetry by creating a non-zero ellipticity. From now on, the star can radiate GWs. The balance between the angular momentum gained from accretion and the one lost by emission will bring the star through a sequence of breaks and finally to a dynamical equilibrium frequency.

Our model can be used to calculate not only a possible breaking frequency, but also the ellipticity due to starquakes and the dynamical equilibrium frequency for stars with different masses, testing the above evolutionary picture.

6.2 Breaking frequency

As in the above chapters regarding compressible neutron stars, we choose a polytropic $n = 1$ stratification, with the normalization of variables and elastic parameters described in section 4.1. Moreover, in this chapter we will indicate with γ^* the equilibrium adiabatic index to prevent confusion with the dynamical equilibrium configuration subscript *eq* due to accretion.

We start from a non rotating reference configuration, that will be spun up from the accretion disc. As we already observed, rotation will deform the star, making it more oblate, and the stress in the crust will grow as the rotational velocity increases, till a breaking condition is reached. As in the previous chapters, to determine the breaking condition we use the Tresca failure criterion. The strain angle α due to rotation is proportional to the frequency squared

$$\alpha = \overline{\alpha}\nu^2, \tag{6.5}$$

where $\overline{\alpha}$ is a term depending only on the structure of the NS, i.e. its mass and EoS. From Eqs (2.9) and (6.5) we immediately get

$$\nu_b = \sqrt{\frac{\sigma^{Max}}{2\overline{\alpha}^{Max}}}, \tag{6.6}$$

where $\overline{\alpha}^{Max}$ is the maximum values of $\overline{\alpha}(r,\theta)$ on the whole NS crust, i.e. in the range $r_c \leq r \leq a$, $0 \leq \theta \leq \pi$. Therefore, the larger σ^{Max}, the larger the breaking frequency, as expected.

Unfortunately the value of σ^{Max} is very uncertain, as already explained in section 2.2.1. In order to give an upper limit for the breaking frequency ν_b and to make a comparison with the recent work of Fattoyev et al. (2018), in the present work we use the same larger value of 10^{-1}. In the case of the lowest estimation of $\sigma^{Max} = 10^{-5}$ we know from Eq (6.6) that the breaking frequency will decrease of about two orders of magnitude compared to the one calculated for our choice.

The results of this first analysis, coming from the model here briefly described, are shown in Fig 6.2, where the curves for ν_b are plotted for different EoSs and different values of the adiabatic index. We underline that the maximum strain angle is calculated with respect to an *unstressed* configuration, i.e. a non-rotating star. The main features of Fig 6.2 resembles the ones obtained for an uniform slowdown, that we will briefly summarise:

1. For a given NS mass, a softer EoS gives larger breaking frequency values. This is easy to understand, since a softer EoS produces larger stars, which means objects with a smaller compactness $W = M/a$. The compactness, as shown in chapters 3 and 4, is a key parameter for the description of stars deformation: a less compact object develops larger strains for a given angular velocity.

2. The larger the adiabatic index value, the lower the breaking frequency. This behaviour can be easily understood, using Eq (6.6), since we know that an incompressible star ($\gamma_f = \infty$) will develop larger strains with respect to a compressible one (cf chapter 4).

3. Furthermore, we underline that a small change in the adiabatic index value gives large changes in the breaking frequency curve. As an example, for the BSk21 EoS, we can see that the ν_b curve for $\gamma_f = 2.1$ lies exactly in the middle between the one for $\gamma^* = 2$ and the other for $\gamma = \infty$. This is a typical feature of compressible, self-gravitating star, that is due to the smallness of the shear modulus μ with respect to the bulk modulus κ in real NSs. In fact, if the ratio μ/κ is small, the object, despite its elastic crust, behaves essentially like a fluid. This means, in particular, that whenever the adiabatic index is different from its equilibrium value $\gamma^* = 2$, the star displacement is forced to be essentially the one of an incompressible medium, as discussed in detail in section 4.1.2.

4. Finally, for a typical $M = 1.4 M_\odot$ NS, we can say that the breaking frequency are all in the range $200 \div 600$ Hz, well below the maximum observed rotational frequency (Hessels et al. 2006)
$$\nu_o = 716.36\,\text{Hz}. \tag{6.7}$$
In this sense, our analysis, coming from a more refined modelization than the one made by Fattoyev et al. (2018), confirms their qualitative results: in fact, they found that for an incompressible star the crust could fail at frequency in the range $400 \div 1000$ Hz.

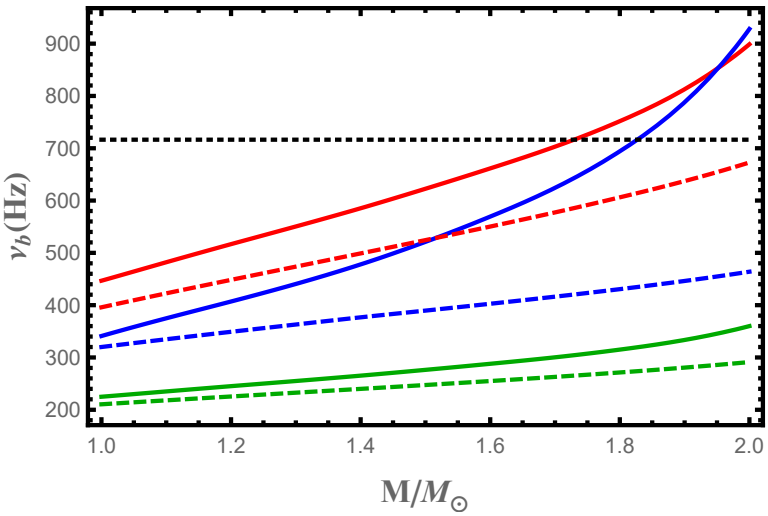

Figure 6.2: The breaking frequency ν_b as a function of the stellar mass for different EoS and adiabatic indices. The solid line are obtained with the SLy EoS, while the dashed ones for the BSk21 one. Different colours indicates different adiabatic indices values: red for $\gamma^* = 2$, blue for $\gamma_f = 2.1$ and green for $\gamma_f = \infty$. The black, dotted lines indicate the actual maximum observed rotational frequency $\nu_o = 716.36$ Hz (Hessels et al. 2006).

6.3 Starquakes induced ellipticity

When a NS reaches the breaking frequency i.e., for our model, when the Tresca failure criterion (2.9) is satisfied, the crust breaks. This event, as already said, is called *starquake* in the literature (Ruderman 1969; Baym et al. 1969). Now we want to explore the changes in ellipticity ϵ of a star caused by a starquake. We will show that this quantity can be estimated by calculating the difference between two axisymmetric, rotating configuration. The ellipticity, we remind, is defined as

$$\epsilon = \frac{A - B}{C}, \tag{6.8}$$

where A and B are the principal moments of inertia relative to the equatorial axes, while C is the one corresponding to the rotation axis. In the following, we adopt the notation used in Sabadini et al. (2016); for a brief summary of the main quantities see Appendix D.

6.3.1 Inertia tensor

Let's focus our attention on the deformation simply due to rotation. The centrifugal perturbation involves both the $\ell = 0$ and $\ell = 2$ harmonics; however, since we are interested into the calculation of the stellar ellipticity, we can focus only on the latter contribution. In fact, the $\ell = 0$ term would give the same contribution both to A and B, which is canceled exactly in the difference $A - B$. Furthermore, the term due to the perturbation in the denominator of Eq (6.8) impacts only at the second order, and thus can be neglected

in our first-order approximation. Therefore, Eq (6.8) becomes

$$\epsilon = \frac{\Delta A - \Delta B}{I_0}, \tag{6.9}$$

where with Δ we indicate the $\ell = 2$ harmonic contribution, while I_0 is the unstressed stellar moment of inertia. The perturbed inertia tensor ΔI_{ij} can be written in a very compact form. In fact, by definition we have

$$\Delta I_{ij} = \sum_{-\ell}^{\ell} Q_{ij}^{20} \frac{4\pi}{5} \int_0^a \rho_{2m}^{\Delta}(r)\, r^4 dr, \tag{6.10}$$

where ρ_{2m}^{Δ} are the $\ell = 2$ coefficient perturbations of order m and Q^{2m} is the conjugate spherical harmonics coefficient of degree $\ell = 2$ of the matrix Q_{ij}

$$Q_{ij} = \frac{1}{3}\delta_{ij} - \hat{r}_i \hat{r}_j. \tag{6.11}$$

The perturbation of the density profile can be linked to the total perturbed potential Φ^{Δ}, that, in this case, is the sum of the perturbed gravitational and centrifugal potentials. By expanding also the potential in spherical harmonics, we can write (Chao & Gross 1987)

$$\Phi_{2m}^{\Delta}(a) = -\frac{4\pi G}{5a^3} \int_0^a \rho_{2m}^{\Delta}(r)\, r^4 dr. \tag{6.12}$$

Therefore the perturbed tensor of inertia can be written as:

$$\Delta \boldsymbol{I}_{ij} = -\sum_{-\ell}^{\ell} Q_{ij}^{2m} \frac{a^3}{G} \phi_{2m}^{\Delta}(a)\,. \tag{6.13}$$

This expression is extremely useful for the calculation of the inertia changes, since it involves only the value of the total potential at the star's surface, that can be easily be obtain with the model presented in this work. From the above equation it is possible to deduce an upper limit for the ellipticity caused by starquakes, as it will be shown in the following subsection.

6.3.2 Estimation of ellipticity and GWs emission

In this section we want to explore the effect of starquakes as triggers for gravitational waves emission. Since an object can emit GWs only if has a non-zero ellipticity, our efforts will be spent mainly in the estimation of the maximumm value of ϵ due to crust failure.

In the simple case of an uniform rotation, the star has an axial symmetry, i.e. $A = B$ and thus (see Eq (6.8)), $\epsilon = 0$. Whatever the angular velocity, the crust of the star is stressed, since it cannot achieve the corresponding equilibrium configuration that it *would have if it was completely fluid*. The elastic crust, in fact, constrains the star to have a more prolate shape with respect to the fluid one. However, the completely axial symmetry caused by centrifugal deformation can be broken by starquakes, that can create *mountains* on the NS surface, leading the star to get an ellipticity different from zero, as shown in Fig. 6.3. From this moment on, the star can radiate gravitational waves.

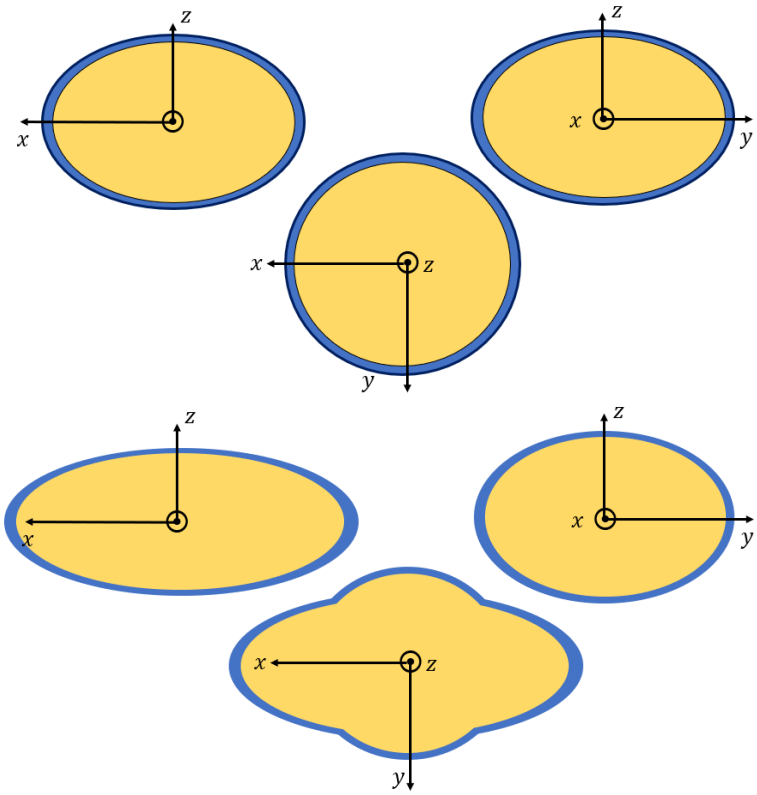

Figure 6.3: Sketch of the stellar deformation (not in scale). The star is divided into a fluid core (yellow) and an elastic crust (blue). *Top*: Vision of the star from the three axis x, y, z in the uniform rotation configuration. *Bottom*: Vision of the star from the three principal axis x, y, z after a starquake that has created a mountain in the x direction.

Starquakes can be seen as the attempts of a stressed star to achieve the equilibrium fluid shape (despite the constraining action of its elastic crust). Starting from an initial (pre-starquake) configuration, after a sufficient number of breaking events, the star will, therefore, reach its fluid configuration. In other words, the cumulative effect of a sequence of many crust failures is to give a more oblate shape to the star. Between the initial and the final configurations, that are axially symmetric, we expect long lasting intermediate states with non zero ellipticity. These are the configurations we are interested in to discuss the emission of GWs. The initial and final configuration inertia tensors can be both written in a diagonal form, namely

$$\boldsymbol{I} = \mathrm{Diag}[\Delta A, \Delta A, \Delta C] \tag{6.14}$$

Note that here $\Delta A = \Delta B$ since both the configurations are axisymmetric. Furthermore, note that we can restrict ourself only to the $\ell = 2$, $m = 0$ harmonic, by choosing a coordinate system in which the rotational axis z coincides with $\theta = 0$, and write

$$\boldsymbol{Q}^{20} = Diag[1/3, 1/3, 2/3]. \tag{6.15}$$

In this case $\Delta A, \Delta C$ satisfy the relation

$$\Delta C = -2\Delta A = -\frac{2}{3}\frac{a^3}{G}\phi^{\Delta}_{20}(a)\,. \tag{6.16}$$

In fact, the perturbation terms due to the $\ell = 2, m = 0$ spherical harmonic contribute only to the deviatoric part of the inertia tensor. The initial (stressed, elastic) and final (fluid) configuration will be characterized by two slightly different inertia tensors, $\boldsymbol{I}^E$ and $\boldsymbol{I}^F$, where E stands for *elastic* and F for *fluid*, respectively.

The explicit calculation of these two tensors is done by using Eq (6.13); reminding that the perturbed total potential is proportional to the stellar squared angular velocity Ω^2, we can write

$$\boldsymbol{I}^{E/F} = -\boldsymbol{Q}^{20} Z \Omega^2, \tag{6.17}$$

where

$$Z = \frac{1}{\Omega^2}\frac{a^3}{G}\phi^{\Delta}_{20}(a)\,. \tag{6.18}$$

If we assume, as said above, that a pure fluid star will be more oblate with respect to an elastic one, at the same rate of rotation, we can state that

$$\Delta C^E \leq \Delta C^F \tag{6.19}$$

$$\Delta A^F \leq \Delta A^E. \tag{6.20}$$

In between the initial and the final fluid-like configuration, the tensor of inertia, that is not necessarily symmetric, due to the intrinsic nature of the rupture process, can be given in the diagonal form (by considering again only the deviatoric $\ell = 2$ harmonic terms)

$$\boldsymbol{I}^Q = \mathrm{Diag}[\Delta A, \Delta B, \Delta C], \tag{6.21}$$

with $\Delta A \neq \Delta B$. With this sketch in mind, we require that

$$\begin{aligned} \Delta C^E \leq \Delta C \leq \Delta C^F \\ \Delta A^F \leq \Delta A, \Delta B \leq \Delta A^E. \end{aligned} \tag{6.22}$$

	$\gamma = 2$	$\gamma = 2.1$	$\gamma = \infty$
SLy	5.2×10^{-7}	1.5×10^{-5}	2.5×10^{-5}
BSk21	1.3×10^{-6}	3.3×10^{-5}	5.5×10^{-5}

Table 6.1: Maximum ellipticity (6.23) calculated with the SLy and the BSk21 EoSs for a $M = 1.4 M_\odot$ NS. In all the cases $\nu = \nu_o$ (Eq (6.7)).

In other words, we expect that the post-quakes configuration will be something between the elastic and the fluid ones. Using Eq (6.22) we see that the maximum difference $\Delta B - \Delta A$ can be expressed as $\Delta A^F - \Delta A^E$, and thus we obtain an upper limit for the ellipticity due to a series of starquakes:

$$\epsilon_{max} = \frac{a^3}{3 I_0 G} (\phi_{20}^{\Delta F}(a) - \phi_{20}^{\Delta E}(a)). \tag{6.23}$$

Therefore, to compute ϵ_{max}, we have to build two different rotating configurations for the same star: the first has an elastic crust, as sketched in Fig 2.4, while in the second the object is completely fluid. For each of this two configurations we can extract the perturbed total potential value at the stellar surface, calculate the corresponding change in the inertia tensor through Eq (6.13) and, finally, get the value of the maximum ellipticity (6.23). Note that, for the elastic configuration, we will use a typical shear modulus for cold catalyzed matter (Eq (4.5)). In fact, we are looking for the *maximum* difference between the elastic and fluid configuration: accreting neutron stars could reach very high temperature in the crust (10^8 K), but this does not affect much the shear modulus shape (Chamel & Haensel 2008). Temperature can lower the μ values, which means that the crust is more similar to a fluid with respect to the cold configuration (Hoffman & Heyl 2012). Furthermore, a high temperature lowers also the breaking strain σ^{Max}, and thus makes it easier to have a starquake.

In Table 6.1 are reported the values of ϵ_{max} for a NS with chosen mass $M = 1.4 M_\odot$, rotating at $\nu = \nu_o$ (Eq (6.7)) both with the SLy and the BSk21 EoSs. Typically, in the GWs literature it is the results of Johnson-McDaniel & Owen (2013) that are used as benchmark for the ellipticity value. We observe that our results are very different with respect to the ones given there. In fact, the ellipticity of Johnson-McDaniel & Owen (2013) is the maximum elastic deformation that the star can sustain *before* breaking, while the ellipticity given by our Eq (6.23) is the upper limit of the deformation that can be reached *due to* the breaking process. Note that if the star is in its equilibrium configuration (that is when the adiabatic index is $\gamma^* = 2$), the upper limit value that we find is lower than the maximum value of ellipticity ($\epsilon \approx 10^{-5}$) that a standard $1.4 M_\odot$ neutron star can sustain (Johnson-McDaniel & Owen 2013). But, as soon as we depart from this condition and $\gamma = 2.1$ or more, our model predicts upper limit values for ellipticity even exceeding 10^{-5}. We expect that starquakes can produce very large ellipticities, and in turn, gravitational waves detectable from Earth.

6.3.3 GWs emission

The estimation of the maximum ellipticity gives us also the possibility of calculating the corresponding maximum GWs amplitude. In fact, a triaxial neutron star, placed at distance d from Earth and rotating about its z principal axis at frequency ν_r with an

ellipticity done by Eq (6.8), will radiate gravitational waves with amplitude

$$h = \frac{4\pi^2 G}{c^4}\frac{I\,(2\nu_r)^2}{d}\epsilon, \tag{6.24}$$

where c is the speed of light and G the gravitational constant. We also assume that the NSs emit GWs at a frequency that is two times their rotating frequency ν_r (Ushomirsky et al. 2000). With the approximation $I = I_{zz}$, from Eqs (6.23) and (6.24) one finds:

$$h^{Max} = \frac{4\pi^2 G}{c^4}\frac{I_{zz}\,(2\nu_r)^2}{d}\left(\frac{a^3}{3I_0 G}(\phi_{20}^{\Delta F}\,(a) - \phi_{20}^{\Delta E}\,(a))\right). \tag{6.25}$$

This relation can be used to give an upper limit to the gravitational strain h of a selection of real pulsars, comparing their emission with the design sensitivity of LIGO/Virgo and ETB detectors[3]. Note that in this section we will not put any constraint on the ellipticity (like the ones that given by the spin-down modeling; on the contrary, we will use the realistic data coming from known pulsars in order to estimate the maximum strain that a population of NSs could produce. The discussion of the limit of this approach will be discussed in section 6.5.3.

Since (see section 6.2) the breaking frequency is essentially in the range $200 \div 700$ Hz, and we expect starquakes to be more "frequent" for high spin values (i.e. high crustal stresses), we collected only the "few" number of stars with $\nu_r > 100$ Hz in the ATNF database (http://www.atnf.csiro.au/research/pulsar/psrcat/). Here we assume also that all the stars that are rapidly rotating have a non-null ϵ, regarless of the fact that they are accreting or not. Finally, for an easiest comparison with the observational paper from the LIGO/Virgo collaboration, we used for the principal moment of inertia I_{zz} the reference value used therein (see for example Abbott et al. (2017))

$$I = 10^{45}\mathrm{g\,cm^2}. \tag{6.26}$$

Note, however, that the self-consistent calculation of I_{zz} in our model differs from the fiducial value of Eq (6.26) from a factors of a few, with larger discrepancies for heavier stars.

The GWs strain amplitude calculated for SLy and BSk21 EoSs, using Eq (6.25), is shown in Fig. 6.4 for a typical $M = 1.4M_\odot$ NS with $\gamma^* = 2$ (panel a), $\gamma = 2.1$ (panel b) and $\gamma = \infty$ (panel c). At the time of writing, we expect that no one of the sources can be directly detected by the LIGO interferometers if $\gamma^* = 2$. On the contrary, as soon as we depart from this value and enter the frozen regime, we expect that many sources could be seen. We remind that we are calculating upper limit values and, therefore, our expectations seem funded especially for the most favourable configurations. In this respect, the Eintein Telescope program should improve enough the sensibility to GWs to detect these sources in all the three scenarios depicted.

As already underlined above, however, these stars are continuous sources of GWs, and thus one can integrate the taken data over many months, in order to extract the signals deep buried into the noise. This is why in Fig 6.4 we show also the minimal detectable signal amplitude h_0 (Jaranowski et al. 1998)

$$h_0 \approx 11.4\sqrt{\frac{S_n}{DT_{obs}}}, \tag{6.27}$$

[3]The sensitivity curves are taken from https://dcc.ligo.org/LIGO-T1800044/public for LIGO and from http://www.et-gw.eu/index.php/etotherdocs/etsensitivities#references for the ET.

for a one-year-lasting observation run.[4] Here S_n is the Fourier power spectrum of the $h(t)$ detector's curve, T_{obs} is the time of observation and D is the number of detectors used. The pre-factor 11.4 reflects the uniform averaging over all the possible sky positions and orientation of the source, with a false alarm rate of 1% and a false dismissal rate of 10%.

In Fig 6.4 we indicated with dashed lines h_0, see Eq(6.27), calculated assuming an observation time of 1 year. We see that the integration of data for a long period should allow the detection of the brightest sources *in all the three scenarios*. Again, the description of stellar matter has a great impact on detection: a star described by a stiffer EoS would produce a larger signal, since it has a larger ellipticity. Furthermore, moving from the equilibrium towards the incompressible limit, our model expects a gain of about one order of magnitude in the GWs strain h. We observe that this transition is very *fast*: in fact, once the source is fixed, we find that a star with $\gamma_f = 2.1$ or $\gamma_f = \infty$ would emit a GW signal that is about 30 or 50 times, respectively, the one obtained with $\gamma^* = 2$ (SLy EoS). As already noted and deeply explained in chapter 4, this is a typical behaviour of compressible stars.

Another parameter that strongly impacts on the NS' ellipticity is the stellar mass. In Fig 6.5 we explore its effect on h, for the BSk21 EoS, in the case of $\gamma_f = 2.1$. Clearly, in this case we have to calculate the moment of inertia of each star in a self-consistent way, instead of using the canonical value given by Eq. (6.26). We can see that heavier stars are fainter, since they have a thinner crust and thus a smaller maximum value of ϵ. This behaviour is easy to understand, since our ellipticity (6.23) in some way is a measure of the difference between the elastic and the pure fluid configuration: the thinner the crust, the smaller the difference. The effect is very strong, since the strain due to a $1M_\odot$ NS is about 14 times the one due to a $2M_\odot$ object for the BSk21 EoS and 41 times for the SLy one. Softer equations are more sensitive to mass changes, since they produce thinner crusts with respect to the stiffer ones. Our results are in qualitative agreement with the ones found by Johnson-McDaniel & Owen (2013), where the ellipticity changes by about an order of magnitude going from 1 to 2 solar masses NSs.

6.4 Equilibrium frequency

In the previous sections we have shown that NSs rotating with frequencies in the range $200 \div 700$ Hz probably undergo a series of starquakes, and consequently emit GWs with a maximum amplitude given by Eq (6.25). Now we want to focus our attention on the consequences that this emission might have on the dynamical equilibrium of an accreting star.

Imagine a NS is tearing some material from its companion. The star gains angular momentum from the infalling material, with a rate N_{acc} that is roughly given by (Ushomirsky et al. 2000)

$$N_{acc} = \dot{M}\sqrt{GMa}. \tag{6.28}$$

At the same time the star, with a non-zero ellipticity, is losing angular momentum by emitting gravitational waves at a rate N_{GW}, that can be written as (Ushomirsky et al. 2000)

$$N_{GW} = \frac{128\pi^3}{5}\frac{GI_0^2\nu^5\epsilon^2}{c^5}, \tag{6.29}$$

[4] The first observing run of LIGO ("O1") lasted 3.5 months, while the second reached nearly 9 months. The third "O3" run hopefully will reach a 12 months of continuous observing (The LIGO Scientific Collaboration & authors 2019).

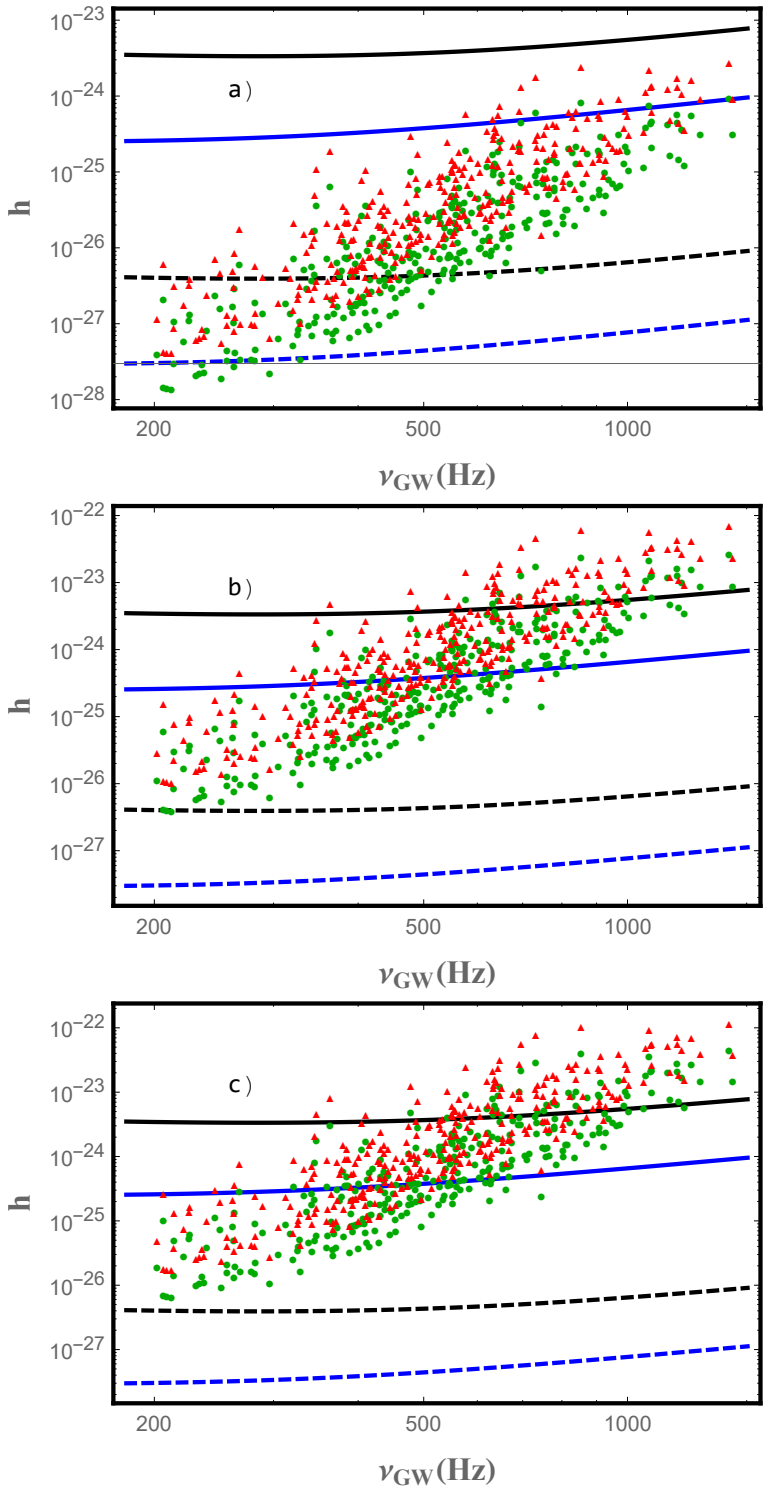

Figure 6.4: Comparison of the LIGO (solid, black) and ETB (solid, blue) sensitivity curves with the maximum gravitational waves emission (Eq (6.25)) of a group of millisecond pulsars, see Table E.1 in Appendix E, with $\gamma^* = 2$ (panel a), $\gamma = 2.1$ (panel b) and $\gamma = \infty$ (panel c). Stars are described with the BSk21 (red triangles) and the SLy (green circles) EoSs. The dashed lines represents the corresponding sensibility h_0 (6.27) reached after one year of integration.

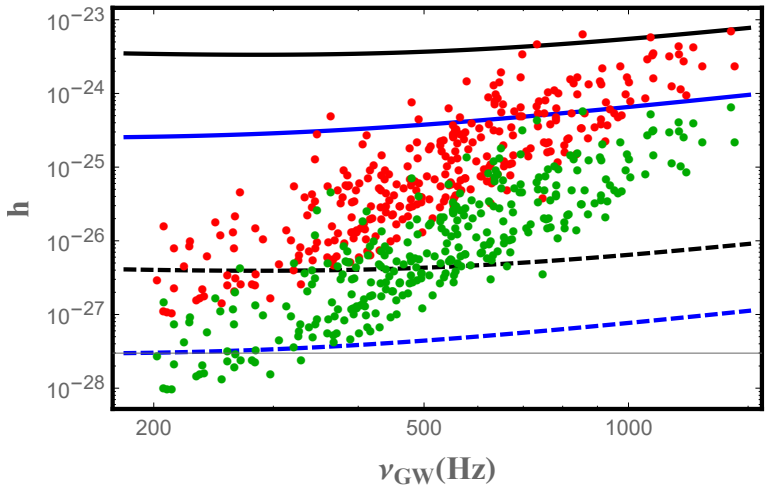

Figure 6.5: Comparison of the LIGO (solid, black) and ETB (solid, blue) sensitivity curves with the maximum gravitational waves emission of a group of millisecond pulsars, see Table E.1 in Appendix E, with $\gamma = 2.1$. Stars, described with the BSk21 EoS, have two different masses $M = 1M_\odot$ (red) and $M = 2M_\odot$ (green). The dashed lines represents the sensibility h_0 (6.27) reached after one year of integration.

where here c is the speed of light. As said in the first part of this chapter, Papaloizou & Pringle (1978) and Wagoner (1984) were the first to suggest that GWs emission could be a promising way to reach a dynamical equilibrium, but only more recently Bildsten (1998) studied the possibility of mountains on accreting object as a concrete mechanism for generating a non-zero ellipticity. We observe, however, that Bildsten explored a mechanism different from ours: the trigger was in that case a nonuniform electron capture, while in our work is a sequence of starquakes.

We now use our estimated maximum of ϵ, Eq (6.23), to get a *lower* limit for the equilibrium frequency value. In fact, generally speaking, we can express ϵ_{max} as

$$\epsilon_{max} = \bar{\epsilon}\nu^2, \tag{6.30}$$

where $\bar{\epsilon}$ is a function of the EoS and of the stellar mass. By equating (6.28) and (6.29), and using Eq (6.30) we get the *equilibrium frequency*

$$\nu_{eq} = C\frac{\dot{M}^{1/9}(Ma)^{1/18}}{I_0^{2/9}\bar{\epsilon}^{2/9}}, \tag{6.31}$$

where we have explicitly written all the terms depending on the EoS chosen and on the stellar mass, and here

$$C = \frac{\sqrt[9]{\frac{5}{2}}c^{5/9}}{2\pi^{5/9}\sqrt[18]{G}}. \tag{6.32}$$

From Eq (6.31) we can obtain ν_{eq}, both for the SLy and the BSk21 EoSs, as a function of the mass and of the adiabatic index value. Since the dynamical equilibrium depends on the rate $\dot{M}$ at which the star is accreting, in our calculation we use two different thresholds that roughly constraints the region where typically can be found the astrophysical values

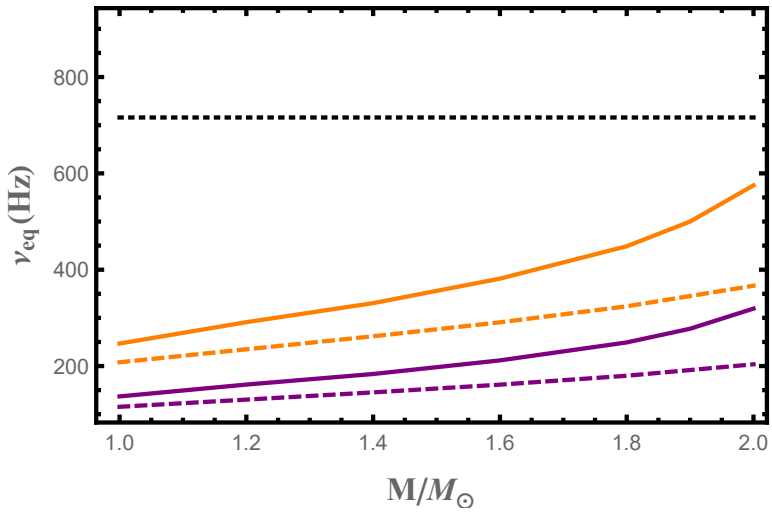

Figure 6.6: Equilibrium frequency ν_{eq} as function of the stellar mass for the SLy (solid) and the BSk21 (dashed) EoSs, fixed $\gamma^* = 2$. The curves are calculated for two different mass accretion rate: $\dot{M} = 2 \times 10^{-8} M_\odot/\mathrm{yr}$ (orange) and $\dot{M} = 10^{-10} M_\odot/\mathrm{yr}$ (purple). The black, dashed line represents the actual maximum observed rotational frequency $\nu_o = 716.36$ Hz.

for this kind of objects. In particular, we used the same values given by Ushomirsky et al. (2000): an upper limit of $\dot{M} = 2 \times 10^{-8} M_\odot/\mathrm{yr}$ and a lower one of $\dot{M} = 10^{-10} M_\odot/\mathrm{yr}$.

The results for $\gamma^* = 2$ are shown in Fig 6.6, while the study of the effect of different adiabatic index on the equilibrium frequency is exemplified for a $M = 1.4 M_\odot$ NS, in Tables 6.2 and 6.3. We expect that a more compressible star will have a smaller maximum ellipticity and thus a larger equilibrium frequency, if compared with an incompressible one, and this is exactly what happens. It is also interesting to plot the curves for $\gamma^* = 2$ in Fig 6.6, since they are the largest equilibrium frequency lines between the equilibrium and the frozen scenario. Note that the expected equilibrium frequency is smaller than ν_o. Furthermore, ν_{eq} (Tables 6.2 and 6.3) is always lower than the breaking frequency (cf. Fig 6.2 with Fig 6.6), i.e.

$$\nu_{eq} < \nu_b. \tag{6.33}$$

Despite the different values obtained for different adiabatic indices, the relation in Eq (6.33) remains valid, suggesting the following physical picture. An old star accreates some material from a companion, increasing its angular velocity. Stresses develop into the crust, till the breaking strain is reached: at that moment the crust fails, the star loses its axial symmetry and starts to emit gravitational waves. The rate of angular momentum lost by GWs is greater than the one gained from accretion, and the star spins-down, till the equilibrium is reached. However, we remind that the estimated values of ν_{eq} in this way calculated are the *lower* value, since in Eq (6.31) we have used our *upper* limit for the ellipticity. Since the breaking frequency is calculated for $\sigma^{Max} = 0.1$, in the general case when the breaking strain is smaller, we get a lower breaking frequency.

Thus our analysis shows that crust breaking seems to be certain for rapidly accreting pulsars, even in the case of very high (0.1) breaking strain; furthermore, through the development of a large ellipticity, it could explain why we don't observe any rotating NS above 700 Hz.

	$\gamma^* = 2$	$\gamma = 2.1$	$\gamma = \infty$
ν_b (Hz)	585	478	265
ν_{eq}^{Max} (Hz)	331	157	140
ν_{eq}^{Min} (Hz)	183	87	78

Table 6.2: Breaking frequency ν_b and equilibrium frequencies ν_{eq} calculated with the SLy EoS for a fixed NS mass $M = 1.4M_\odot$ and different mass accretion rate: $\dot{M} = 2 \times 10^{-8}\dot{M}_\odot/\mathrm{yr}$ (ν_{eq}^{Max}) and $\dot{M} = 10^{-10}\dot{M}_\odot/\mathrm{yr}$ (ν_{eq}^{Min}).

	$\gamma^* = 2$	$\gamma = 2.1$	$\gamma = \infty$
ν_b (Hz)	499	377	240
ν_{eq}^{Max} (Hz)	262	128	114
ν_{eq}^{Min} (Hz)	145	80	63

Table 6.3: Breaking frequency ν_b and equilibrium frequencies ν_{eq} calculated with the BSk21 EoS for a $M = 1.4M_\odot$ NS and different mass accretion rate: $\dot{M} = 2 \times 10^{-8}\dot{M}_\odot/\mathrm{yr}$ (ν_{eq}^{Max}) and $\dot{M} = \times 10^{-10}\dot{M}_\odot/\mathrm{yr}$ (ν_{eq}^{Min}).

6.5 Observational constraints on ϵ

In the previous sections, we used our upper limit value ϵ^{Max} as the largest possible value for the ellipticity developed by a rapidly rotating NS. Being it an upper value, we do not expect all the sources to reach this maximum possible deformation measured by ϵ. In this section we will estimate the maximum ellipticity of realistic stars starting from observational data, coming both from electromagnetic and GWs observations.

6.5.1 LMXB

Observation of LMXBs accreting NS can be used to extract a value of ϵ, giving an useful benchmark to compare with our upper limit, Eq (6.23). In fact, assuming that *the measured rotational frequency of an observed LMXB is its equilibrium frequency*, one can obtain the corresponding ellipticity

$$\epsilon_{acc} = \frac{C^{9/2}}{\nu_r^{9/2}} \frac{\left\langle \dot{M} \right\rangle^{1/2} (Ma)^{1/4}}{I_0}, \tag{6.34}$$

where the subscript *acc* stands for *accretion* and $\left\langle \dot{M} \right\rangle$ is the average mass accretion rate *during outburst*[5]. In the following, we use the data by Haskell et al. (2015) (see Table 1 therein), that gives, for each star, its rotational frequency, distance and average mass accretion rate. For simplicity we fix again the stellar mass at $M = 1.4M_\odot$, and the adiabatic index value at $\gamma^* = 2$ (the values of ϵ_{max} for $\gamma_f = 2.1, \infty$ are always larger than the one obtained with γ^*, giving a lower β_{acc}). We compare the two values of ellipticity by introducing the parameter β_{acc}, defined as

$$\beta_{acc} = \frac{\epsilon_{acc}}{\epsilon_{max}}. \tag{6.35}$$

[5]Typically accreting NS show short bursts, lasting from days to months, with a corresponding high accretion rate, and very long period of recovery, where the accretion is orders of magnitude smaller with respect to the active phase (Watts et al. 2008).

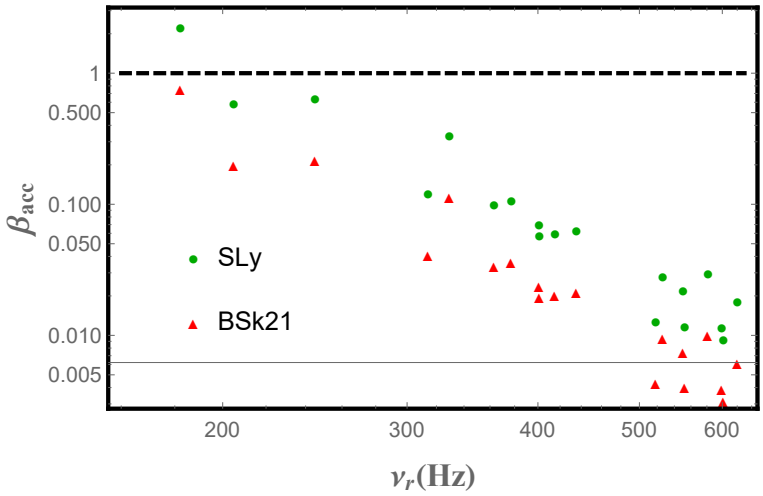

Figure 6.7: Ratio of the observational ellipticity assuming dynamical equilibrium in LMXB objects ϵ_{acc} (Eq (6.35)) and our upper limit ϵ_{max} (Eq (6.23)). The green circles are calculated with the SLy EoS while the red triangles with the BSk21 one. The dashed, black curve indicates $\beta_{acc} = 1$.

The meaning of β_{acc} is simple: every stars with $\beta_{acc} \leq 1$ has an equilibrium ellipticity that can be explained by the starquakes mechanism alone; on the contrary, for the ones with $\beta_{acc} > 1$ we need to invoke some other effect (a non-zero magnetic field, for example) to explain the equilibrium ellipticity. The results are shown in Fig 6.7. About 95% of the stars fall in the category $\beta_{acc} \leq 1$ both using BSk21 or SLy EoS. The smallest value of β_{acc} found with this method is 0.003 for BSk21 and 0.092 for SLy EoS. These results show that even a small fraction of our maximum value (6.23) is enough for LMXB stars to reach a dynamical equilibrium at frequency smaller than ν_o.

6.5.2 Alternative estimation of β

Generally speaking, we can expect that in real situation the actual value of ϵ is only a fraction β_o of ϵ_{max}, i.e.

$$\epsilon = \beta_o \epsilon_{max}; \quad \beta \leq 1. \tag{6.36}$$

The exact value of β_o will be linked to the crustal properties of the star and on its historic seismology. However, an estimation of the effect of a single starquake is extremely difficult. In fact, our knowledge of the NS crust physics is extremely poor, and a reasonable description of a quake involves a very large number of unknown parameters (dip and strike angles, displacement discontinuity, fault area etc.). For these reason it seems more reasonable to follow a different approach. Using the definition in Eq (6.36), one can express the equilibrium frequency as a function of β, as in Eq (6.31), namely

$$\nu_{eq}(\beta_o) = \nu_{eq} = C \frac{\dot{M}^{1/9} (Ma)^{1/18}}{I_0^{2/9} \beta_o^{2/9} \epsilon^{2/9}}, . \tag{6.37}$$

Then, given an EoS and fixed the stellar mass, we state that the minimum feasible values of β_o is the one that satisfies the condition

$$\nu_{eq}(\beta_o) = \nu_o, \tag{6.38}$$

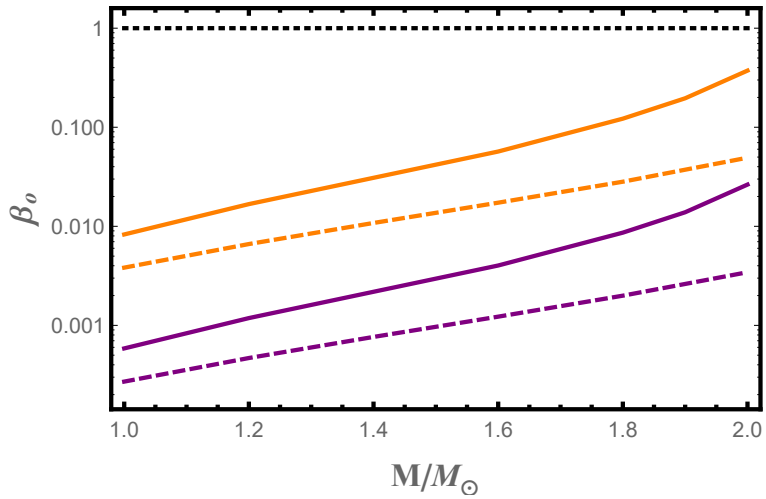

Figure 6.8: Minimum value of β, defined implicitly in (6.38), for the SLy (solid) and the BSk21 (dashed) EoSs. The curves are calculated for two different mass accretion rate: $\dot{M} = 2 \times 10^{-8} M_\odot/\mathrm{yr}$ (orange) and $\dot{M} = 10^{-10} M_\odot/\mathrm{yr}$ (purple). The black, dotted line represents $\beta = 1$.

where ν_o is the actual larger observed rotational frequency for a pulsar Eq (6.7). Using this selection criterion for different masses M and different mass accretion rate $\dot{M}$ we construct the curves shown in Fig. 6.8. In all the cases $\beta_o < 1$, and for the smaller mass accretion rate $\dot{M} = 10^{-10} M_\odot/\mathrm{yr}$, fixing as a typical value $M = 1.4 M_\odot$, we find, for the SLy EoS, $\beta_o = 0.002$, while $\beta_o = 0.0007$ for the stiffer BSk21.

6.5.3 Millisecond pulsars

In the previous sections we focused on accreting NSs, but now we try to extend our analysis also to spinning-down objects. If we assume that millisecond pulsars are the evolutionary descendants of accreting objects (Alpar et al. 1982; Bhattacharya & Van Den Heuvel 1991), i.e. old neutron stars that have been spun up to high rotational frequencies via accretion, we can also assume that LMXB objects can develop large ellipticity due to starquakes. Thus millisecond stars too could have a non-zero ϵ, i.e. a residual part of their initially larger quadrupolar deformation. In this case we can introduce a simple model to explain the millisecond actual decreasing period. These objects lose energy via electromagnetic and gravitational waves emission: following Woan et al. (2018), where it is assumed $I = 10^{45}\,\mathrm{gcm}^2$ and a vacuum dipole radiation, we thus write

$$\frac{\dot{P}}{10^{-20}} = 0.98 \left(\frac{1\mathrm{ms}}{P}\right) \left(\frac{I_0}{10^{45}\mathrm{g\,cm}^2}\right)^{-1} \left(\frac{B_s}{10^8 G}\right) + \\ +2.7 \left(\frac{1\mathrm{ms}}{P}\right)^3 \left(\frac{I_0}{10^{45}\mathrm{g\,cm}^2}\right) \left(\frac{\epsilon}{10^{-9}}\right)^2 . \tag{6.39}$$

However, here we will ignore the effect of the magnetic field, by fixing $B_s = 0$. Therefore the above equation can be used to calculate the ellipticity necessary to explain the observed stellar spin-down in the case of pure gravitational wave emission, i.e. in the

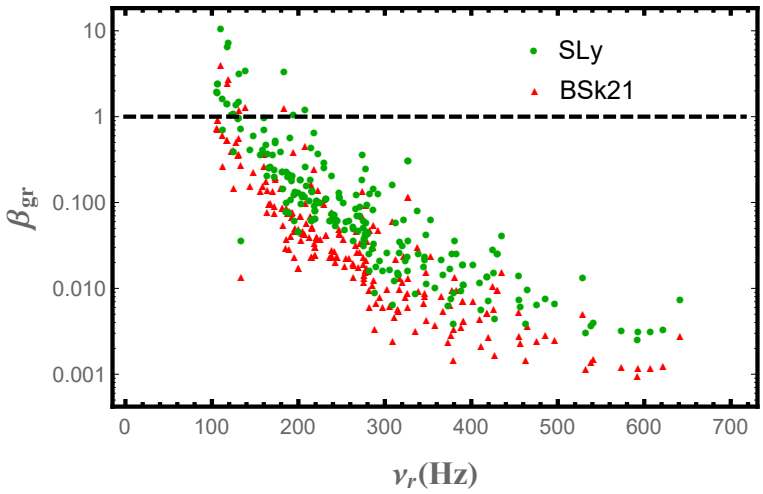

Figure 6.9: Ratio of the observational ellipticity in the gravitar limit ϵ_{gr} (Eq (6.40)) and our upper limit ϵ_{max}. The green dots are calculated with the SLy EoS while red triangles with the BSk21 one. The dashed, black curve indicates $\beta_{gr} = 1$.

case of a *gravitar* (Palomba 2005):

$$\epsilon_{gr} = 10^{-9}\sqrt{0.37\left(\frac{I_0}{10^{45}\,\mathrm{g\,cm^2}}\right)\left(\frac{\dot{P}}{10^{-20}}\right)\left(\frac{P}{1\mathrm{ms}}\right)^3}. \tag{6.40}$$

We can compare this value with our upper limit (6.23), assuming a standard star configuration with $M = 1.4M_\odot$ and an adiabatic index $\gamma^* = 2$. As representatives of millisecond pulsars we collected all the non-accreting stars with $\nu_r > 100$ Hz in the ATNF database (http://www.atnf.csiro.au/research/pulsar/psrcat/). In Fig. 6.9 we show the ratio

$$\beta_{gr} = \frac{\epsilon_{gr}}{\epsilon_{max}}. \tag{6.41}$$

The spin-down of all the stars with $\beta_{gr} \leq 1$ can be explained with pure gravitational wave emission due to starquakes, since the ellipticity necessary to produce the current stellar spin-down is smaller than the value of ϵ_{max} corresponding to that rotational frequency. In particular, when $\beta_{gr} < 1$ we are measuring the fraction of the maximum ellipticity that is needed to reach the gravitar limit. In the case of the stiff BSk21 EoS, roughly 97% of the selected star have $\beta_{gr} < 1$, while for SLy the percentage goes down to 90%. Finally, for all the objects with $\beta_{gr} > 1$ we need to invoke a non-null magnetic field to explain the current observed spin-down, i.e. to abandon the gravitar hypothesis, using the full expression of Eq (6.40). These results show that the starquakes mechanism can produce very large ellipticity, and thus that actual value of ϵ for millisecond pulsars can in principle be produced by crust rupture on their progenitors accreting stars. The minimum value of β_{gr} in our sample is

$$\beta_{gr} = 0.001. \tag{6.42}$$

Fig 6.9 shows also another interesting aspect. The slower neutron stars in our catalogue have a β_{gr} value that is larger than 1 which means that for this object, our upper limit

is smaller than the gravitar ellipticity value. In the debate whether to search for gravitational waves emitted by slowly rotating or fast rotating objects our model suggests the GWs search for high rotating pulsars, that have higher frequencies and expected larger ellipticities with respect to slowly rotating MSPs.

6.5.4 Constraints from GWs non-detection

The $O1$ and $O2$ runs of LIGO/Virgo detectors have been used to put constraints on the fiducial ellipticity for a selection of rapidly rotating ($\nu_r > 100$ Hz) pulsars (The LIGO Scientific Collaboration & authors 2019). These estimation can be very useful if compared with our maximum ellipticity value, Eq (6.23): in fact, we can assume that during their life real pulsars reach only a fraction $\beta < 1$ of our threshold, i.e.

$$\epsilon = \beta \epsilon_{max}. \tag{6.43}$$

If we state that the ellipticity of NSs is due *only* to the starquakes mechanism, we can extract the value of β simply as the ratio between LIGO/Virgo fiducial ellipticities and our upper limit

$$\beta_{GW} = \frac{\epsilon_{L/V}}{\epsilon_{max}}. \tag{6.44}$$

In this way, $\beta_{GW} > 1$ means that the observations are still not capable of give low enough limit on ϵ; if, on the contrary, $\beta_{GW} < 1$ we are measuring how large is the fraction of ϵ_{max} currently developed on the NS. In Fig 6.10 we show β_{GW}, obtained using the definition (6.44) and calculated for $1.4 M_\odot$, with both the EoSs. Using SLy we get a larger value of $\beta_{GW} = 0.047$, while for BSk21 $\beta_{GW} = 0.019$. These latter values are the largest estimation of β that we derived using different observational data. The actual LIGO-Virgo observational run (O3) is very important: we could have the first direct detection of continuous GWs (and thus a measurement of ϵ); if this were not the case, we could use the new data to lower the estimated value of ϵ (i.e., the estimation of β).

6.6 Outlook

In this chapter, it is presented for the first time (at least at the best of our knowledge) a realistic calculation of the effect of starquakes as trigger for NS ellipticity. In fact, this kind of mechanism has only been recently proposed by Fattoyev et al. (2018), who, however, didn't estimate the ellipticity in a consistent way. Our calculations shows that the crust failure can cause an ellipticity which, for $\gamma \neq \gamma^*$ and for highly spinning pulsars, is comparable with the maximum theoretically expected value (Johnson-McDaniel & Owen 2013). However, as explained above, the mechanism producing the quadrupolar deformation is completely different, since in this case the ellipticity is due to *crust breaking*, while in most of the work present in the literature ϵ is *sustained* by the elastic crust.

Furthermore, we tested in detail the picture of an accreting star presented at the beginning of this work: we found that for most of the scenarios (different EoSs and masses) the breaking frequency is lower than the actual maximum observed frequency, see Eq (6.7): in fact, assuming the maximum theoretically allowed value $\sigma_{max} = 0.1$, they are typically in the range $200 \div 700$ Hz. This supports the idea that NSs crusts fails during accretion.

The equilibrium frequency, in general, is found to be smaller than the breaking one, and thus again below the actual observable threshold. Thus we studied how large can be the ellipticity due to starquakes, giving an upper limit for ϵ between 10^{-9} and 10^{-5},

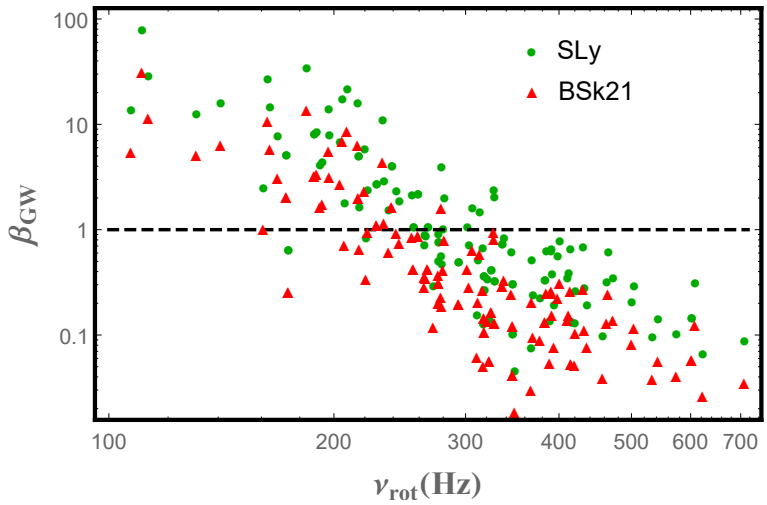

Figure 6.10: Ratio of the observational ellipticity given by *non-detections* of continuous GWs and our upper limit ϵ_{max}. β_{GW} (6.44) is calculated for $M = 1.4M_{\odot}$ with two different EoS: SLy (green circles) and BSk21 (red triangles). The dashed, black curve indicates $\beta_{GW} = 1$.

depending on the EoS and the mass of the object. Stiffer EoS produces larger ellipticies and thus brings the star towards lower equilibrium frequencies.

We studied also how the mass affect the star's response, finding that $2M_{\odot}$ objects can create ϵ about one order of magnitude smaller with respect to the lighter ($1M_{\odot}$) ones. Also different adiabatic values change the global value of ϵ, and even just a small discrepancy from the adiabatic equilibrium value leads to large differences on the ellipticity value.

Finally, we compared our upper limit estimation with data coming both from accreting objects and millisecond pulsars. We found that even a small fraction (down to $\sim 10^{-3}$) of ϵ_{max} could in principle explain an interesting fraction of the data available ($\sim 90\% \div 97\%$ depending on the EoS used). A first confirmation of this effect could be the detection of gravitational waves during the actual observational run by LIGO and Virgo.

Our model shows that the evolutionary scenario depicted in this chapter is robust, and that starquakes can produce ellipticities large enough to emit GWs detectable from Earth. Thus, collecting all the different clues presented in this work we can state that starquakes seems to be a competitive candidate for NSs dynamical equilibrium.

Part VI
Conclusions

Conclusions and future directions

At the present time, many different astrophysical events related to pulsars are taught to be due to starquakes, that could be caused by various possible loadings acting on the crust. However, there is still a lack of theoretical well based modeling for most of these loadings, and thus we have only a very rough knowledge of the physics of NSs' crusts response. This PhD work wants to be a first development of a more realistic calculation of the effects of chosen loadings, being due to rotation or pinning or magnetic field evolution. I adapted a model, already used in Geophysics for the study of the Earth and rocky planet's deformations (Sabadini et al. 2016), to the very different physical conditions of NS's crust. For this model, I also developed a code that allows the study of various chosen loadings that act on the crust of a self-gravitating pulsar, and used it in different scenarios: uniform rotation (both for incompressible and compressible stars), differential rotation, slack pinning and starquakes. Here below we summarize the main results obtained in all these different scenarios.

Incompressible two-density star, uniform rotation

I tested the model by comparing it with the incompressible approach by Franco et al. (2000), that has also recently been used in the literature (Fattoyev et al. 2018). I showed that the FLE model can be obtained as a limit case of our more general model, for a homogeneous object (core and crust with the same density). In the hypothesis of incompressibility the model can also be used to obtain an analytical, compact solution of the deformation of the crust: in chapter 3 I studied the case of a star with two layers (a fluid core and an elastic crust) strained by rotation, giving the explicit form of the solution, that can be used to make simple estimation of deformations. Furthermore, I showed that the peaks of the strain angle α are strongly affected by the presence of an homogeneous crust, with a different density with respect to the core. In fact, the maximum strain is reached at the poles, rather than at the equator as in the FLE model, and α is larger than in the case of a homogeneous star. Since α is used to estimate where the crust breaks, the differences between our results and those of FLE may be significant.

Compressible star, uniform rotation, differental rotation and slack pinning

I used our model to study the deformation of compressible NS in different physical scenarios. In particular, I studied the response of a *compressible* neutron stars to uniform rotation (chapter 4), differential rotation and slack pinning (chapter 5). All these different mechanisms have been introduced in the literature of glitches as possible trigger for

crust breaking. Our approach allowed to obtain an estimation of the stellar deformation, and to compare the response of a NS to such loadings.

Despite the strain angle showed very different pattern in the three situations studied, when starting from an unstressed configuration, I found that, in all the cases, the breaking condition for the crust cannot be reached in the time interval between two subsequent glitches. This is a very interesting result, since it challenges our understanding of the crust breaking, and of starquakes as glitches' trigger. Therefore, in our model the forces studied, although important for the development of the glitch, are not strong enough to cause starquakes (that thus should not be so frequent events).

The assumption that the star is initially in an unstressed configuration could be too restrictive. In fact, when a newly born NS solidifies, it does it with zero strain because the matter is in mechanical equilibrium. As the star spins down, stress develops that strains the crust. The characteristic time to do this is the spin-down time of the star and so, when the star is a few years old, it could develop a very large strain over several years as it rapidly spins down. In this case, one can think that a crust strain very close to its critical value could arise naturally and rapidly. An estimation of the average crustal spin-down strain angle has already been done by Cutler et al. (2003) that obtain the value of $\sim 5 \times 10^{-5}$. For this value to cause a starquake the crust should have a very small breaking threshold. Also in this case, our model can be useful to estimate where the crust is maximally strained, with the main physical results that, quite unexpectedly and differently from the FLE model where it is as the equator, it is at the poles.

Compressible star, starquakes

The versatility of our model permits also to study in a compact way the effect of starquakes on fast rotating NSs. The idea is that an old NS is spun-up by the infalling material of a companion; at a high rotational rate the centrifugal force is strong enough to cause starquakes, that break the axysymmetric configuration of the star. At this point, the NS emits GWs, thus reaching a dynamical equilibrium configuration between the emission and accretion. Using our model, I studied all the the passages of this evolution (breaking frequency, starquakes induced ellipticity and equilibrium frequency). I found that NSs crust can break in the frequency range $200 \div 700$ Hz, and estimated the ellipticity corresponding to this event, giving an upper limit for ϵ between 10^{-9} and 10^{-5}, depending on the EoS and the mass of the object. As deeply discussed in the main text, this mechanism could explain the observed LMXB distribution, since it can produce large ellipticities and thus, in turn, a loss of energy via gravitational waves emission that is large enough to guarantee a dyamical equilibrium frequency below about 700 Hz. The actual rapid development of gravitational waves astronomy could give us a lot of useful information. In fact, we expect continuous gravitational waves to be detected by the actual observational run (O3) of LIGO-Virgo: if this would be the case we could directly measure the ellipticity of very far objects; on the contrary, this lack of observations can be used to better constrain the values of β given by our model, where β is defined as the effective fraction of the maximum ellipticity due to starquakes (see chapter 6).

The approach used in this work can be also fruitfully used for the analysis of pulsars' deformation due to the action of other forces, such the magnetic field force, the effects on the star's surface under loading caused by accretion, or different pinning configurations. I would like to observe that, even if I focused my attention on standard neutron stars, the

model here developed is sufficiently general to allow also the introduction of different stratification and elastic properties in order to simulate the response of hybrid or quark stars.

Finally, there are three important questions that are still to be tackled, and I am planning to face them in the near future, in order to further develop the model:

- The original model introduced by Sabadini et al. (2016) is a *visco*-elastic model, i.e. it takes into accounts also the long time evolution of elastic layers due to a non-null viscosity. At the present time, the viscosity ν of NSs' crust is essentially unknown, but in the last years some first estimations have appeared (Kwang-Hua 2018; Lander & Gourgouliatos 2019). The inclusion also of this parameter in a consistent model can help the understanding of the global dynamics of a realistic NS, and is clearly a very interesting field of research.

- Another application worth mentioning in the conclusions concerns the study of Quasi-Periodic Oscillations (QPOs) found in the tails of giant flares from soft gamma-ray repeaters (Watts & Strohmayer 2006; Strohmayer & Watts 2006), which are thought to be global seismic vibrations (Duncan 1998), i.e. a clear signature of starquakes due to magnetic stresses. The idea is that the decay of the magnetic field in this stars can cause large stresses, and in turn the breaking of the crust. This magnetically-driven seismic activity is the core of the models widely used to explain burst and flares. Crustquakes induced by the magnetic field evolution has been recently studied (Lander et al. 2015; Lander & Gourgouliatos 2019): the model introduced in this work can be used to explore the dynamic of the crust, both for the reaching of the breaking condition and for the evolution of the seismic vibration through the star. This information could be very useful to constrain both the internal magnetic field geometry and the EoS (Samuelsson & Andersson 2007; Watts & Reddy 2007).

- One of the forces that I studied in this work is the centrifugal buoyancy; as explained in the main text, in the inner crust we probably have in the same place two different species, rotating with different angular velocity, that are the normal component (lattice) and the superfluid one. However, in our actual model I described the inner crust as composed only of an elastic layer. Thus, in order to better discuss the centrifugal buoyancy effect, one should include into this Newtonian model the approach used in the literature for the study of entrainment (Carter & Chachoua 2006). This is a two-components model, where one is fluid while the other is solid (elastic). This generalisation will be a bridge between the actual two-fluids mesoscopic approach present in the literature and our elastic Newtonian global model.

- Neutron Stars are General Relativity objects. As a first step, the use of a Newtonian model is fundamental to get a first physical insight about the response of these stars, but in order to obtain estimations more precise of the deformation of pulsars we need to upgrade the model to the General Relativity approach.

Appendices

APPENDIX A

Spherical harmonics

In this work spherical harmonics are defined as

$$Y_{\ell m}(\theta,\phi) = P_{\ell m}(\cos\theta)\, e^{im\phi}, \tag{A.1}$$

where $P_{\ell m}$ are the Legendre polynomials, given by

$$\begin{aligned} P_{\ell m}(x) &= \frac{(1-x^2)^{m/2}}{2^\ell \ell!}\frac{d^{\ell+m}\left(x^2-1\right)^\ell}{dx^{\ell+m}} && \text{if} \quad m \geq 0 \\ P_{\ell m}(x) &= (-1)^m \frac{(\ell-m)!}{(\ell+m)!} P_{\ell m}(x) && \text{if} \quad m < 0\,. \end{aligned}$$

Therefore, spherical harmonics are eigenvalues of the angular part of the Laplacian, i.e.

$$\nabla^2 Y_{\ell m} = -\frac{\ell(\ell+1)}{r^2} Y_{\ell m}, \tag{A.2}$$

and are normalized as

$$\int_\Omega Y_{\ell m} Y^*_{\ell m} d\Omega = \frac{4\pi}{2\ell+1}\frac{(\ell+m)!}{(\ell-m)!}\delta_{\ell\ell'}\delta_{mm'}\,, \tag{A.3}$$

where $d\Omega = \sin\theta d\theta d\phi$. Consistently with the previous definitions, it is possible to expand the total incremental potential Φ^Δ as

$$\Phi^\Delta(r,\theta,\phi) = \sum_{\ell=0}^{\infty}\sum_{m=-\ell}^{\ell} \Phi_{\ell m}(r)\, Y_{\ell m}(\theta,\phi)\,. \tag{A.4}$$

The expansion of vectorial quantities is more subtle: for example, the total displacement u is decomposed in terms of the spheroidal $\boldsymbol{u}_S$ and the toroidal $\boldsymbol{u}_T$ displacements as

$$\boldsymbol{u} = \boldsymbol{u}_S + \boldsymbol{u}_T\,, \tag{A.5}$$

where

$$\begin{aligned} \boldsymbol{u}_S(r) &= \sum_{\ell=0}^{\infty}\sum_{m=-\ell}^{\ell} \left[U_{\ell m}(r)\,\boldsymbol{R}_{\ell m}(\theta,\varphi) + V_{\ell m}(r)\,\boldsymbol{S}_{\ell m}(\theta,\varphi)\right] \\ \boldsymbol{u}_T(r) &= \sum_{\ell=0}^{\infty}\sum_{m=-\ell}^{\ell} \left[W_{\ell m}(r)\,\boldsymbol{T}_{\ell m}(\theta,\varphi)\right]. \end{aligned}$$

In the above expansions, the symbols $\boldsymbol{R}_{\ell m}, \boldsymbol{S}_{\ell m}, \boldsymbol{T}_{\ell m}$ are vectorial quantities defined by

$$\boldsymbol{R}_{\ell m} = Y_m \boldsymbol{e}_r \tag{A.6}$$

$$\boldsymbol{S}_{\ell m} = r\boldsymbol{\nabla} Y_{\ell m} = \partial_\theta Y_{\ell m} \boldsymbol{e}_\theta + \frac{1}{\sin\theta} \partial_\varphi Y_{\ell m} \boldsymbol{e}_\varphi \tag{A.7}$$

$$\boldsymbol{T}_{\ell m} = \boldsymbol{\nabla} \times (\boldsymbol{r} Y_{\ell m}) = \frac{1}{\sin\theta} \partial_\varphi Y_{\ell m} \boldsymbol{e}_\theta - \partial_\theta Y_{\ell m} \boldsymbol{e}_\varphi \,, \tag{A.8}$$

where $\boldsymbol{e}_r, \boldsymbol{e}_\theta$ and $\boldsymbol{e}_\varphi$ are the usual unit vectors of the spherical coordinate system.

The incremental stress acting on a spherical surface element with outward normal $\boldsymbol{e}_r$ can be computed as

$$\boldsymbol{\sigma}^\delta \cdot \boldsymbol{e}_r = \sum_{\ell m} \left(R_{\ell m} \boldsymbol{R}_{\ell m} + S_{\ell m} \boldsymbol{S}_{\ell m} + T_{\ell m} \boldsymbol{T}_{\ell m} \right) , \tag{A.9}$$

where

$$R_{\ell m} = \lambda \chi_{\ell m} + 2\mu \partial_r U_{\ell m} \,, \tag{A.10}$$

$$S_{\ell m} = \mu \left(\partial_r W_{\ell m} + \frac{U_{\ell m} - V_{\ell m}}{r} \right) , \tag{A.11}$$

$$T_{\ell m} = \mu \left(\partial_r W_{\ell m} - \frac{W_{\ell m}}{r} \right) . \tag{A.12}$$

We refer to $R_{\ell m}$ and $S_{\ell m}$ respectively as the *radial* and *tangential spheroidal* stresses. On the other hand, $T_{\ell m}$ is called *toroidal stress*.

Finally, a generic non-conservative force $\boldsymbol{h}$ can be expanded in terms of three real and independent sets of coefficients $h^R_{\ell m}$, $h^S_{\ell m}$ and $h^T_{\ell m}$ according to the formula

$$\boldsymbol{h} = \sum_{\ell=0}^{\infty} \sum_{m=-\ell}^{\ell} \left(h^R_{\ell m} \boldsymbol{R}_{\ell m} + h^S_{\ell m} \boldsymbol{S}_{\ell m} + h^T_{\ell m} \boldsymbol{T}_{\ell m} \right) . \tag{A.13}$$

APPENDIX B

Analytical incompressible solutions

In this Appendix we report the coefficients for the displacement obtained in chapter 3 with the FLE model, using the Cowling approximation, and for the two-density model.

Cowling approximation

The displacement in Eq. (3.31) can be rearranged in the form of Eq (3.33). If we use the Cowling approximation, discussed in Sec 3.2.2, we have different parameters with respect to the FLE case:

$$\begin{aligned}
\tilde{a}^C &= 560\left(13q^2 - 7q + 2\right)\\
\tilde{b}^C &= -10\left(643q^2 - 232q + 37\right)\\
\tilde{A}^C &= 560\left(15q^2 - 13q + 5\right)\\
\tilde{B}^C &= -1120\left(70q^2 - 27q + 5\right)/3\\
Q^C/v_K^2 &= -175\left(q^2(96\chi^2 - 109) + \right.\\
&\qquad \left. + q(48 - 24\chi^2) - 11\right).
\end{aligned} \tag{B.1}$$

It is now easy to check that Eq. (3.40) is valid when the (very small) terms proportional to $q^2\chi^2$ and $q\chi^2$ are neglected.

Two-density model

The displacements for the two-density model have the same analytic form given in Eq (3.33). In this case, the coefficients which appear into the explicit solution of the displacements are given by

$$\begin{aligned}
\tilde{a} =& q^2(-1680d^3v^2 + 8400d^2v^2 - 33600dv^2\chi^2 + \\
&- 6720dv^2 + 44520v^2\chi^2) + \\
&+ q(-840d^2v^2 + 6720dv^2\chi^2 + \\
&+ 840dv^2 - 12600v^2\chi^2) + \\
&+ 1680v^2\chi^2
\end{aligned}$$

$$
\begin{aligned}
\tilde{b} =& q^2\left(405d^3v^2 - 1575d^2v^2 + 14400dv^2\chi^2 + \right.\\
&+ 1170dv^2 - 24045v^2\chi^2 + \\
&\left.+ q\left(90d^2v^2 - 1920dv^2\chi^2 - 90dv^2 + 5400v^2\chi^2\right) + \right.\\
&- 555v^2\chi^2
\end{aligned}
\qquad units
$$

$$
\begin{aligned}
\tilde{A} =& q^2(-3780d^3v^2 + 15435d^2v^2 - 63840dv^2\chi^2 + \\
&- 11655dv^2 + 76440v^2\chi^2) + \\
&q(-1575d^2v^2 + 15960dv^2\chi^2 + \\
&+ 1575dv^2 - 26880v^2\chi^2) + \\
&4200v^2\chi^2
\end{aligned}
$$

$$
\begin{aligned}
\tilde{B} =& q^2\left(58240dv^2\chi^2 + 1680(d-1)^2dv^2 - 97440v^2\chi^2\right) + \\
&q\left(24080v^2\chi^2 - 8960dv^2\chi^2\right) + \\
&- 2800v^2\chi^2
\end{aligned}
$$

$$
\begin{aligned}
Q/v_K^2 =& q^2(1890d^3v^2 - 8820d^2v^2\chi^2 - 7560d^2v^2 + \\
&+ 35070dv^2\chi^2 + \\
&+ 5670dv^2 + 50400v^2\chi^4 - 49140v^2\chi^2) + \\
&q(630d^2v^2 - 5250dv^2\chi^2 - 630dv^2 - 12600v^2\chi^4 + \\
&+ 15330v^2\chi^2) + \\
&- 2310v^2\chi^2.
\end{aligned}
$$

The exact form of these coefficients is much more complex, here expressions have been truncated to the second order in q, which is the relative crust thickness.

APPENDIX C

Tests for differential rotation

In the main text (chapter 5) we introduced two tests for our differential rotating solution code:

- The first is that, for a perturbative force of the form

$$\boldsymbol{f} = \boldsymbol{f}_{cen}\left[\frac{1}{2}\left(1 - \frac{2}{\pi}\arctan\left(\frac{c/a - r/a}{\xi}\right)\right)\right], \tag{C.1}$$

  must coincide with the uniform rotating solution in the limit $c \to 0$. As numerical test we choose $c = r_c/1000$. In Fig C.1 are reported the radial and tangential displacements and radial and tangential stresses for $\ell = 2, m = 0$ harmonic for a $M = 1.4M_\odot$ described with the SLy EoS. The blue lines correspond to the differential rotating solution with $c = r_c/1000$, while the red, dashed lines are the uniform solution ones.

- As a second test we require that the sum of the solutions for the *external* and *internal* force with the same choice of the transitional radius c is equal to the uniform solution. In fact, we expect that the total effect of a centrifugal force acting only in r part of the object plus the effect of a centrifugal force acting only in the $r > c$ outer layers is equal to the one due to a centrifugal force acting on the whole star. In Fig C.2 we plot the radial and tangential displacements and stresses for the $\ell = 2, m = 0$ harmonic both for the sum of the differential rotating solution and the uniform one. As in the previous case we fix the mass of the star at the standard value of $M = 1.4M_\odot$ and we use the SLy EoS. As can be seen, the sum of the two solutions is superimposed to the one of uniform rotation.

Furthermore, we explore the impact of different transitional radii values c on the response of a NS subject to differential rotation. In particular, by choosing equally spaced radii $c = 0.5a, 0.6a, 0.7a, 0.8a, 0.995r_c$, it is evident that the solution has a rapid transition for very large value of c, i.e. $c \simeq r_c$, as shown in Fig. C.3, where we plot the radial and tangential displacements for the almost equally spaced values of c.

Finally, we report the study of the solution in the small region $0.81 \leq r \leq 0.896$, in order to show that the solution approaches smoothly the limit $r = 0.995r_c$. as shown in Fig C.4.

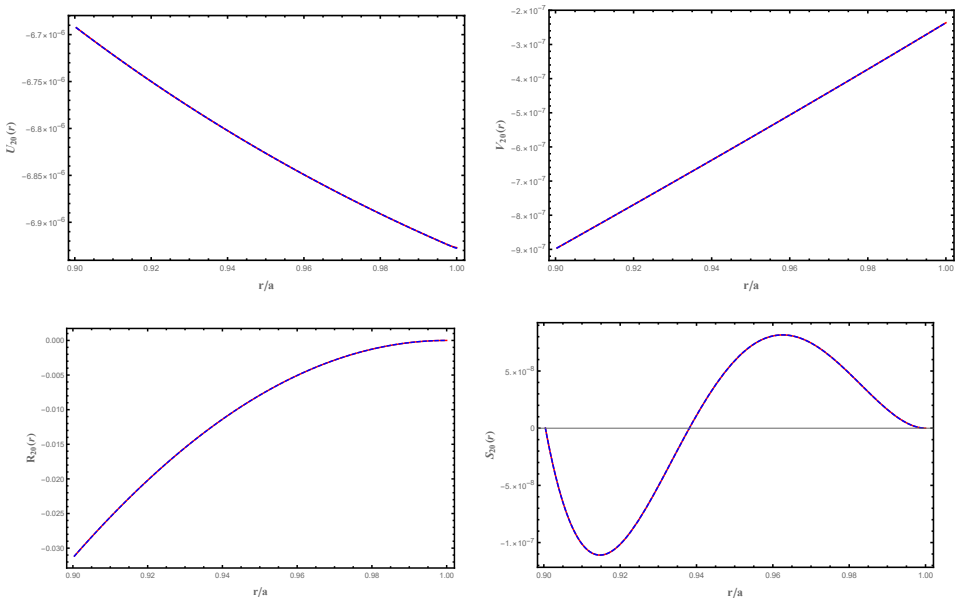

Figure C.1: The $\tilde{U}_{20}(r)$ (top,left) and the $\tilde{V}_{20}(r)$ (top, right) normalized displacements and $\tilde{R}_{20}(r)$ (bottom,left) and the $\tilde{S}_{20}(r)$ (bottom, right) normalized stresses as functions of the normalized radius, from $r = r_c$ to $r = a$, for a differential rotating star with $c = r_c/1000$ (blue lines) and for a uniform rotating NS (red, dashed lines). In this case the star has a standard mass of $M = 1.4M_\odot$ and is described by the SLy EoS.

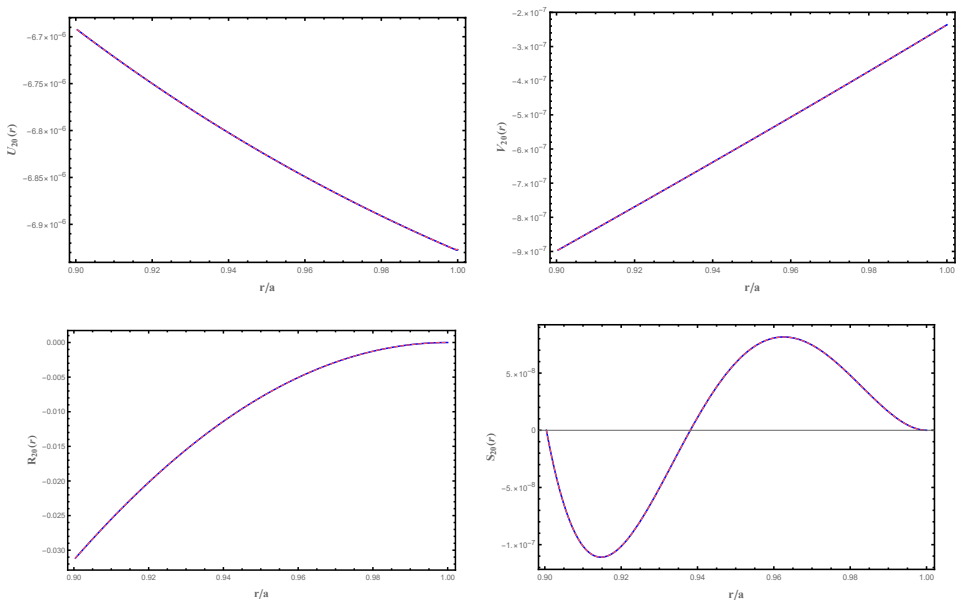

Figure C.2: The $\tilde{U}_{20}(r)$ (top,left) and the $\tilde{V}_{20}(r)$ (top, right) normalized displacements and $\tilde{R}_{20}(r)$ (bottom,left) and the $\tilde{S}_{20}(r)$ (bottom, right) normalized stresses as functions of the normalized radius, from $r = r_c$ to $r = a$, sum of the solutions for the *external* and *internal* force with $c = r_c/10$ (blue lines) and for a uniform rotating NS (red, dashed lines). In this case the star has a standard mass of $M = 1.4M_\odot$ and is described by the SLy EoS. The same results can obtained for any choice of the c values in the range $0 \leq c \leq r_c$.

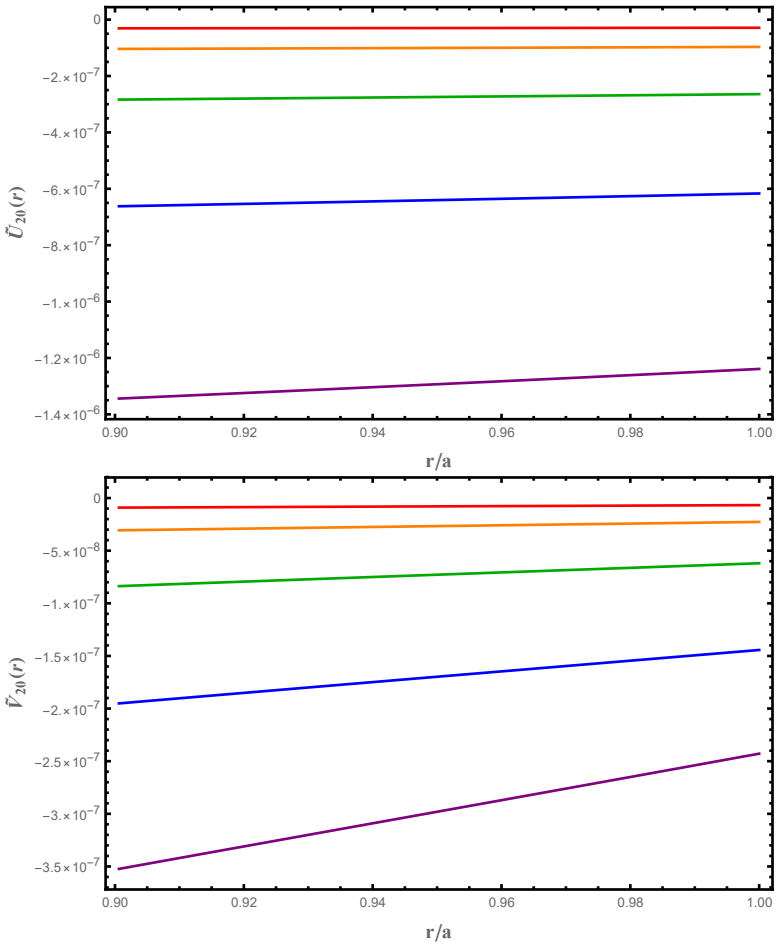

Figure C.3: The $\tilde{U}_{20}(r)$ (top) and the $\tilde{V}_{20}(r)$ (bottom) normalized displacements as functions of the normalized radius, from $r = r_c$ to $r = a$, for different choices of almost equally spaced transitional radii $c/a = 0.5$ (red), $c/a = 0.6$ (orange), $c/a = 0.7$ (green), $c/a = 0.8$ (blue) and $c = 0.995 r_c$ (purple). The rotating region is the one for $r < c$.

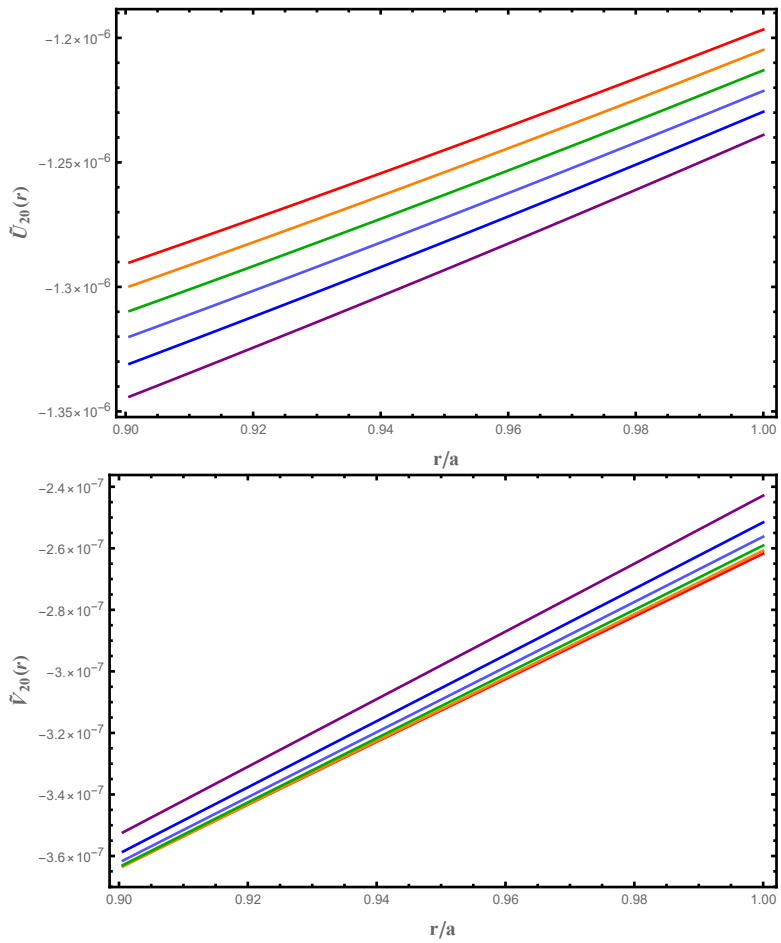

Figure C.4: The $\tilde{U}_{20}(r)$ (top) and the $\tilde{V}_{20}(r)$ (bottom) normalized displacements as functions of the normalized radius, from $r = r_c$ to $r = a$, for equally spaced transitional radii $c/a = 0.891$ (red), $c/a = 0.892$ (orange), $c/a = 0.893$ (green), $c/a = 0.894$ (blue) and $c = 0.995 r_c$ (purple). In this case the rotating region is the one for $r < c$.

APPENDIX D

The inertia tensor

The inertia tensor is defined as

$$I_{ij} = \int \rho\left(r\right)\left(r^2\delta_{ij} - r_i r_j\right) dV \tag{D.1}$$

where δ_{ij} is the Kronecker delta, r is the position spherical vector and $\rho\left(r\right)$ is the star's density. In this work we are interested in the perturbations due to rotation, and so we focus only on it. The initial, non-rotating stellar configuration will be deformed by centrifugal force, that gives rise to a change of its density profile, that can be written as

$$\rho\left(r\right) = \rho_0\left(r\right) + \rho^{\Delta}\left(r\right), \tag{D.2}$$

where we put in evidence the initial, unstressed profile ρ_0 and the local perturbation ρ^{Δ}. We can use the spherical symmetry of the problem to recast Eq (D.1). By using the spherical harmonics expansion (see Appendix A) we can write the star density perturbation as

$$\rho^{\Delta}\left(r,\theta,\varphi\right) = \sum_{\ell=0}^{\infty}\sum_{m=-\ell}^{m=\ell}\rho^{\Delta}_{\ell m}\left(r\right)Y_{\ell m}\left(\theta,\varphi\right) \tag{D.3}$$

and the total perturbed potential as

$$\Phi^{\Delta}\left(r,\theta,\varphi\right) = \sum_{\ell=0}^{\infty}\sum_{m=-\ell}^{\ell}\Phi^{\Delta}_{\ell m}\left(r\right)Y_{\ell m}\left(\theta,\varphi\right). \tag{D.4}$$

In this work, all the perturbed terms are the ones due to rotation, thus we can focus on the centrifugal potential ϕ^{C}. As seen in chapter 2, it can be expanded as a sum only of the $\ell = 0$ and $\ell = 2$ terms. If we substitute the density expansion in Eq (D.1), we can express the inertia tensor I as

$$I = I_0 + I^{\Delta}, \tag{D.5}$$

where we highlighted the unperturbed tensor of inertia I_0. Finally, with some straightforward algebra the perturbed inertia tensor can be divided into two terms

$$I^{\Delta} = I^{\Delta}_{00} + I^{\Delta}_{20}. \tag{D.6}$$

Note that by choosing a coordinate system in which the rotational axis z coincides with the one at $\theta = 0$, the centrifugal potential contains only the $m = 0$ order of the $\ell = 2$ harmonic term. The contributions of the perturbed inertia are

$$I^{\Delta}_{00} = \frac{8\pi}{3}\delta_{ij}\int_0^a \rho^{\Delta}_{00}\left(r\right)r^4 dr, \tag{D.7}$$

and

$$I_{20}^{\Delta} = \left(\frac{1}{3}\delta_{ij} - \hat{r}_i\hat{r}_j\right)\frac{4\pi}{5}\int_0^a \rho_{20}^{\Delta}(r)\, r^4 dr, \tag{D.8}$$

where a is the stellar radius and with the hat symbol we denote the unit vectors. For simplicity in the main text we use the notation

$$\Delta I = I_{20}^{\Delta}. \tag{D.9}$$

APPENDIX E

Fast rotating neutron stars

In chapter 6 we selected all the neutron stars with $\nu_r > 100$ Hz in the ATNF database (http://www.atnf.csiro.au/research/pulsar/psrcat/). Here we reported all the chosen stars, indicated with their J-name and characterized by the measure of their period P, period derivative $\dot{P}$ and distance. Where the value are unknown, a $*$ is present.

Name	P (s)	$\dot{P}(s/s)$	Distance (kpc)
J0023+0923	0.00305	1.14×10^{-20}	1.11
J0024-7201Z	0.004554	-4.54×10^{-21}	2.56
J0024-7204aa	0.00184	*	2.69
J0024-7204ab	0.003705	9.82×10^{-21}	2.54
J0024-7204C	0.005757	-4.99×10^{-20}	4.69
J0024-7204D	0.005358	-3.42×10^{-21}	4.69
J0024-7204E	0.003536	9.85×10^{-20}	4.69
J0024-7204F	0.002624	6.45×10^{-20}	4.69
J0024-7204G	0.00404	-4.22×10^{-20}	4.69
J0024-7204H	0.00321	-1.83×10^{-21}	4.69
J0024-7204I	0.003485	-4.59×10^{-20}	4.69
J0024-7204J	0.002101	-9.79×10^{-21}	4.69
J0024-7204L	0.004346	-1.22×10^{-19}	4.69
J0024-7204M	0.003677	-3.84×10^{-20}	4.69
J0024-7204N	0.003054	-2.19×10^{-20}	4.69
J0024-7204O	0.002643	3.03×10^{-20}	4.69
J0024-7204P	0.003643	6.64×10^{-19}	4.69
J0024-7204Q	0.004033	3.4×10^{-20}	4.69
J0024-7204R	0.00348	1.48×10^{-19}	4.69
J0024-7204S	0.00283	-1.21×10^{-19}	4.69
J0024-7204T	0.007588	2.94×10^{-19}	4.69
J0024-7204U	0.004343	9.52×10^{-20}	4.69
J0024-7204V	0.00481	*	4.69
J0024-7204W	0.002352	-8.66×10^{-20}	4.69
J0024-7204X	0.004772	1.84×10^{-20}	4.69
J0024-7204Y	0.002197	-3.52×10^{-20}	4.69
J0024-7204Z	0.004554	*	4.69
J0030+0451	0.004865	1.02×10^{-20}	0.32
J0034-0534	0.001877	4.97×10^{-21}	1.35
J0101-6422	0.002573	5.16×10^{-21}	1.
J0102+4839	0.00296	*	2.38

J0218+4232	0.002323	7.74×10^{-20}	3.15
J0251+26	0.00254	*	1.15
J0308+74	0.00316	*	0.38
J0337+1715	0.002733	1.77×10^{-20}	1.3
J0340+4130	0.003299	7.05×10^{-21}	1.6
J0437-4715	0.005757	5.73×10^{-20}	0.16
J0509+08	0.0041	*	0.8
J0514-4002A	0.004991	1.17×10^{-21}	13.2
J0533+67	0.00439	*	2.28
J0557+1550	0.002556	7.35×10^{-21}	1.83
J0605+37	0.00273	*	0.19
J0610-2100	0.003861	1.24×10^{-20}	3.26
J0613-0200	0.003062	9.59×10^{-21}	0.78
J0614-3329	0.003149	1.75×10^{-20}	0.63
J0621+25	0.00272	*	1.64
J0636+5129	0.002869	3.44×10^{-21}	0.21
J0645+5158	0.008853	4.92×10^{-21}	0.8
J0653+4706	0.00475	*	0.91
J0711-6830	0.005491	1.49×10^{-20}	0.11
J0740+41	0.003139	*	0.51
J0740+6620	0.002886	1.22×10^{-20}	0.43
J0751+1807	0.003479	7.79×10^{-21}	1.11
J0824+00	0.0099	*	1.72
J0922-52	0.00968	*	0.35
J0931-1902	0.004638	3.63×10^{-21}	3.72
J0952-0607	0.001414	*	1.74
J0955-61	0.001999	*	2.17
J1012-4235	0.003101	*	0.37
J1012+5307	0.005256	1.71×10^{-20}	0.7
J1017-7156	0.002339	2.22×10^{-21}	0.26
J1023+0038	0.001688	6.93×10^{-21}	1.37
J1024-0719	0.005162	1.86×10^{-20}	1.22
J1035-6720	0.002872	4.65×10^{-20}	1.46
J1036-8317	0.003408	*	0.93
J1045-4509	0.007474	1.77×10^{-20}	0.34
J1048+2339	0.004665	$3. \times 10^{-20}$	2.
J1101-6424	0.005109	1.8×10^{-21}	2.17
J1103-5403	0.003393	3.68×10^{-21}	1.68
J1120-3618	0.00555	*	0.95
J1124-3653	0.00241	*	1.05
J1125-5825	0.003102	6.09×10^{-20}	1.74
J1125-6014	0.00263	4.01×10^{-21}	0.99
J1125+7819	0.004202	6.96×10^{-21}	0.88
J1142+0119	0.00507	*	2.18
J1147-66	0.00372	*	1.79
J1207-5050	0.00484	*	1.27
J1216-6410	0.003539	1.62×10^{-21}	1.1
J1227-4853	0.001686	1.11×10^{-20}	1.8
J1231-1411	0.003684	2.28×10^{-20}	0.42
J1300+1240	0.006219	1.14×10^{-19}	0.6

J1301+0833	0.00184	*	1.23
J1302-32	0.00377	*	1.49
J1306-4035	0.002205	*	1.41
J1311-3430	0.00256	2.1×10^{-20}	2.43
J1312+0051	0.00423	*	1.47
J1327-0755	0.002678	1.77×10^{-21}	25.
J1337-6423	0.009423	2.47×10^{-20}	5.94
J1342+2822A	0.002545	*	9.9
J1342+2822B	0.002389	1.86×10^{-20}	9.9
J1342+2822C	0.002166	*	9.9
J1342+2822D	0.005443	*	9.9
J1400-1431	0.003084	7.23×10^{-21}	0.28
J1405-4656	0.007602	2.79×10^{-20}	0.67
J1417-4402	0.002664	*	4.4
J1421-4409	0.006386	1.27×10^{-20}	2.08
J1431-4715	0.002012	1.41×10^{-20}	1.82
J1431-5740	0.004111	6.42×10^{-21}	3.55
J1435-6100	0.009348	2.45×10^{-20}	2.81
J1446-4701	0.002195	9.81×10^{-21}	1.57
J1453+1902	0.005792	1.17×10^{-20}	1.27
J1455-3330	0.007987	2.43×10^{-20}	1.01
J1514-4946	0.003589	1.86×10^{-20}	0.91
J1518+0204A	0.005554	4.12×10^{-20}	8.5
J1518+0204B	0.007947	-3.33×10^{-21}	8.5
J1518+0204C	0.002484	2.61×10^{-20}	8.
J1518+0204D	0.002988	*	8.
J1518+0204E	0.003182	*	8.
J1529-3828	0.008486	2.7×10^{-20}	4.3
J1536-4948	0.00308	*	0.98
J1543-5149	0.002057	1.62×10^{-20}	1.15
J1544+4937	0.002159	2.93×10^{-21}	2.99
J1545-4550	0.003575	5.25×10^{-20}	2.25
J1546-3747A	0.002606	*	6.45
J1546-59	0.0078	*	3.89
J1551-0658	0.00709	*	1.32
J1552-4937	0.006284	1.9×10^{-20}	3.06
J1552+5437	0.002428	2.8×10^{-21}	2.64
J1600-3053	0.003598	9.5×10^{-21}	1.8
J1614-2230	0.003151	9.62×10^{-21}	0.7
J1628-3205	0.00321	*	1.22
J1629-6902	0.006001	$1. \times 10^{-20}$	0.96
J1630+37	0.00332	*	1.18
J1640+2224	0.003163	2.82×10^{-21}	1.52
J1641+3627B	0.003528	*	6.5
J1641+3627C	0.003722	*	6.5
J1641+3627D	0.003118	*	6.5
J1641+3627E	0.002487	*	6.5
J1643-1224	0.004622	1.85×10^{-20}	0.74
J1646-2142	0.00585	*	0.97
J1649+80	0.002021	*	3.01

J1652-48	0.003785	*	4.39
J1653-2054	0.004129	1.12×10^{-20}	2.63
J1658-5324	0.002439	1.12×10^{-20}	0.88
J1701-3006A	0.005242	-1.3×10^{-19}	7.05
J1701-3006B	0.003594	-3.48×10^{-19}	7.05
J1701-3006C	0.007613	-6.41×10^{-20}	7.05
J1701-3006D	0.003418	1.26×10^{-19}	7.05
J1701-3006E	0.003234	3.1×10^{-19}	7.05
J1701-3006F	0.002295	2.22×10^{-19}	7.05
J1708-3506	0.004505	1.14×10^{-20}	3.32
J1709+2313	0.004631	3.63×10^{-21}	2.18
J1710+49	0.00322	*	0.51
J1713+0747	0.00457	8.53×10^{-21}	1.22
J1719-1438	0.00579	8.04×10^{-21}	0.34
J1721-2457	0.003497	5.54×10^{-21}	1.37
J1723-2837	0.001856	7.54×10^{-21}	0.72
J1725-3853	0.004792	$5. \times 10^{-20}$	3.14
J1730-2304	0.008123	2.02×10^{-20}	0.62
J1731-1847	0.002345	2.54×10^{-20}	4.78
J1732-5049	0.005313	1.42×10^{-20}	1.87
J1737-0811	0.004175	7.93×10^{-21}	0.21
J1738+0333	0.00585	2.41×10^{-20}	1.47
J1740-5340A	0.00365	1.68×10^{-19}	2.2
J1741+1351	0.003747	3.02×10^{-20}	1.08
J1744-1134	0.004075	8.93×10^{-21}	0.4
J1744-7619	0.004688	9.68×10^{-21}	*
J1745+1017	0.002652	2.73×10^{-21}	1.21
J1747-4036	0.001646	1.31×10^{-20}	7.15
J1748-2021C	0.006227	-5.98×10^{-20}	8.24
J1748-2021F	0.003794	-1.05×10^{-20}	8.24
J1748-2446aa	0.005788	*	5.5
J1748-2446ab	0.00512	*	5.5
J1748-2446ac	0.005087	*	5.5
J1748-2446ad	0.001396	0.	5.5
J1748-2446ae	0.003659	*	4.4
J1748-2446af	0.003304	*	5.5
J1748-2446ag	0.004448	*	5.5
J1748-2446ah	0.004965	*	5.5
J1748-2446aj	0.002959	1.41×10^{-19}	4.4
J1748-2446ak	0.00189	8.85×10^{-20}	4.38
J1748-2446C	0.008436	-6.06×10^{-19}	5.5
J1748-2446D	0.004714	*	8.7
J1748-2446E	0.002198	*	5.5
J1748-2446F	0.00554	*	5.5
J1748-2446H	0.004926	*	5.5
J1748-2446I	0.00957	*	5.5
J1748-2446K	0.00297	*	5.5
J1748-2446L	0.002245	*	5.5
J1748-2446M	0.00357	*	5.5
J1748-2446N	0.008667	*	5.5

J1748-2446O	0.001677	*	5.5
J1748-2446P	0.001729	*	4.4
J1748-2446Q	0.002812	*	5.5
J1748-2446R	0.005029	*	5.5
J1748-2446S	0.006117	*	5.5
J1748-2446T	0.007085	*	5.5
J1748-2446U	0.003289	*	5.5
J1748-2446V	0.002073	*	5.5
J1748-2446W	0.004205	*	5.5
J1748-2446X	0.002999	*	5.5
J1748-2446Y	0.002048	*	5.5
J1748-2446Z	0.002463	*	5.5
J1748-3009	0.009684	*	5.07
J1750-3703B	0.006075	1.92×10^{-20}	13.8
J1750-3703D	0.00514	4.93×10^{-19}	13.8
J1751-2857	0.003915	1.12×10^{-20}	1.09
J1757-5322	0.00887	2.63×10^{-20}	0.94
J1801-0857A	0.007176	-5.13×10^{-19}	7.2
J1801-0857C	0.003739	-6.5×10^{-20}	7.2
J1801-0857D	0.004227	6.9×10^{-21}	7.2
J1801-1417	0.003625	5.3×10^{-21}	1.1
J1801-3210	0.007454	-4.44×10^{-23}	6.12
J1803-3002A	0.007101	*	7.8
J1803-3002B	0.004397	*	7.8
J1803-3002C	0.00584	*	7.8
J1804-2717	0.009343	4.09×10^{-20}	0.8
J1805+06	0.00213	*	3.88
J1807-2459A	0.003059	-4.34×10^{-21}	2.79
J1807-2459B	0.004186	8.23×10^{-20}	2.79
J1810+1744	0.00166	*	2.36
J1811-2405	0.002661	1.34×10^{-20}	1.83
J1813-2621	0.00443	1.25×10^{-20}	3.01
J1816+4510	0.003193	4.31×10^{-20}	4.36
J1823-3021A	0.00544	3.38×10^{-18}	12.1
J1823-3021D	0.00302	*	12.1
J1823-3021E	0.004394	*	12.1
J1823-3021F	0.00485	*	12.1
J1824+10	0.00407	*	2.93
J1824-2452A	0.003054	1.62×10^{-18}	5.5
J1824-2452B	0.006547	*	5.5
J1824-2452C	0.004159	*	5.5
J1824-2452E	0.00542	*	5.5
J1824-2452F	0.002451	*	5.5
J1824-2452G	0.005909	*	5.5
J1824-2452H	0.004629	*	5.5
J1824-2452I	0.003932	0.	5.5
J1824-2452J	0.004039	*	5.5
J1824-2452K	0.004461	*	5.5
J1824-2452L	0.0041	*	5.5
J1825-0319	0.004554	6.8×10^{-21}	3.86

J1828+0625	0.00363	*	1.
J1832-0836	0.002719	8.27×10^{-21}	2.5
J1835-0114	0.005116	$7. \times 10^{-21}$	3.45
J1835-3259A	0.003889	*	10.7
J1836-2354A	0.003354	2.32×10^{-21}	3.2
J1836-2354B	0.003232	-4.8×10^{-22}	3.2
J1843-1113	0.001846	9.55×10^{-21}	1.26
J1843-1448	0.005471	6.21×10^{-21}	3.47
J1844+0115	0.004186	1.07×10^{-20}	4.36
J1850+0124	0.00356	1.09×10^{-20}	3.39
J1850+0242	0.00448	1.63×10^{-19}	12.3
J1853+1303	0.004092	8.72×10^{-21}	1.32
J1857+0943	0.005362	1.78×10^{-20}	1.2
J1858-2216	0.00238	*	0.92
J1900+0308	0.004909	5.9×10^{-21}	4.8
J1901+0300	0.007797	4.57×10^{-20}	5.29
J1902-5105	0.001742	9.2×10^{-21}	1.65
J1902-70	0.0036	*	0.92
J1903+0327	0.00215	1.88×10^{-20}	6.11
J1903-7051	0.003598	1.04×10^{-20}	0.93
J1904+0451	0.006092	5.72×10^{-21}	4.4
J1905+0154A	0.003193	*	14.45
J1905+0400	0.003784	4.91×10^{-21}	1.06
J1906+0055	0.00279	3.32×10^{-21}	4.48
J1909+21	0.00256	*	2.59
J1909-3744	0.002947	1.4×10^{-20}	1.14
J1910+1256	0.004984	9.68×10^{-21}	1.32
J1910-5959A	0.003266	2.95×10^{-21}	4.55
J1910-5959B	0.008358	-7.9×10^{-19}	1.63
J1910-5959C	0.005277	2.16×10^{-21}	1.63
J1910-5959D	0.009035	9.64×10^{-19}	1.63
J1910-5959E	0.004572	-4.34×10^{-19}	1.63
J1911+0101A	0.003619	-6.58×10^{-21}	9.5
J1911+0101B	0.005384	$-2. \times 10^{-21}$	9.5
J1911-1114	0.003626	1.39×10^{-20}	1.07
J1911+1347	0.004626	1.69×10^{-20}	1.36
J1913+0617	0.00503	*	5.76
J1918-0642	0.007646	2.57×10^{-20}	1.11
J1923+2515	0.003788	9.56×10^{-21}	1.2
J1933-6211	0.003543	3.87×10^{-21}	0.65
J1935+1726	0.0042	*	2.31
J1938+2012	0.002634	7.5×10^{-22}	6.29
J1939+2134	0.001558	1.05×10^{-19}	3.5
J1943+2210	0.005084	8.79×10^{-21}	6.78
J1944+0907	0.005185	1.73×10^{-20}	1.22
J1944+2236	0.003618	7.46×10^{-21}	7.6
J1946+3417	0.00317	3.12×10^{-21}	6.97
J1946-5403	0.00271	*	1.15
J1950+2414	0.004305	1.89×10^{-20}	7.27
J1953+1846A	0.004888	*	6.

J1953+67	0.008565	*	5.44
J1955+2527	0.004873	9.12×10^{-21}	8.18
J1955+2908	0.006133	2.97×10^{-20}	6.3
J1957+2516	0.003962	2.74×10^{-20}	2.66
J1959+2048	0.001607	1.69×10^{-20}	1.73
J2010-1323	0.005223	4.82×10^{-21}	1.16
J2017+0603	0.002896	7.99×10^{-21}	1.4
J2019+2425	0.003935	7.02×10^{-21}	1.16
J2033+1734	0.005949	1.11×10^{-20}	1.74
J2043+1711	0.00238	5.24×10^{-21}	1.56
J2047+1053	0.00429	*	2.79
J2051-0827	0.004509	1.27×10^{-20}	1.47
J2052+1218	0.00199	*	3.92
J2124-3358	0.004931	2.06×10^{-20}	0.41
J2129-0429	0.00762	*	1.83
J2129+1210D	0.004803	-1.08×10^{-18}	14.2
J2129+1210E	0.004651	1.78×10^{-19}	14.2
J2129+1210F	0.004027	3.2×10^{-20}	14.2
J2129+1210H	0.006743	2.4×10^{-20}	14.2
J2129-5721	0.003726	2.09×10^{-20}	3.2
J2144-5237	0.00504	*	1.58
J2214+3000	0.003119	1.47×10^{-20}	0.6
J2215+5135	0.00261	3.34×10^{-20}	2.77
J2229+2643	0.002978	1.52×10^{-21}	1.8
J2234+0611	0.003577	1.2×10^{-20}	1.43
J2234+0944	0.003627	2.01×10^{-20}	0.77
J2236-5527	0.006908	9.6×10^{-21}	2.05
J2241-5236	0.002187	6.64×10^{-21}	0.96
J2256-1024	0.00229	*	1.33
J2302+4442	0.005192	1.38×10^{-20}	0.86
J2317+1439	0.003445	2.43×10^{-21}	2.
J2322+2057	0.004808	9.66×10^{-21}	1.01
J2322-2650	0.003463	5.83×10^{-22}	0.23
J2339-0533	0.002884	1.41×10^{-20}	1.1

Bibliography

Abbott, B. P., Abbott, R., Abbott, T. D., et al. 2017, *Astrophys. J.*, 839, 12

Abney, M. & Epstein, R. I. 1996, *Journal of Fluid Mechanics*, 312, 327–340

Alpar, M. A. & Baykal, A. 2006, *Mon. Not. R. Astron. Soc.*, 372, 489–496

Alpar, M. A., Cheng, A. F., Ruderman, M. A., & Shaham, J. 1982, *Nature*, 300, 728

Alpar, M. A., Langer, S. A., & Sauls, J. A. 1984, *Astrophys. J.*, 282, 533

Anderson, P. W., Alpar, M. A., Pines, D., & Shaham, J. 1982, *Philosophical Magazine, Part A*, 45, 227

Anderson, P. W. & Itoh, N. 1975, *Nature*, 256, 25

Andersson, N., Glampedakis, K., Ho, W. C. G., & Espinoza, C. M. 2012, *Phys. Rev. Lett.*, 109, 241103

Andreev, A. F. & Bashkin, E. P. 1976, *Soviet Journal of Experimental and Theoretical Physics*, 42, 164

Antonelli, M. 2017, Modelling Superfluid Neutron Stars Applications to Pulsar Glitches (Phd Thesis, Università degli Studi di Milano)

Antonelli, M., Montoli, A., & Pizzochero, P. 2018, *Mon. Not. R. Astron. Soc.*, 475, 5403–5416

Ashton, G., Lasky, P. D., Graber, V., & Palfreyman, J. 2019, *Nature Astronomy*, 417

Ashton, G., Prix, R., & Jones, D. I. 2017, *Phys. Rev. D*, 96, 063004

Baade, W. & Zwicky, F. 1934a, *Proc. National Acad. Sci.*, 20, 254

Baade, W. & Zwicky, F. 1934b, *Phys. Rev.*, 46, 76

Baiko, D. A. & Chugunov, A. I. 2018, *Mon. Not. R. Astron. Soc.*, 480, 5511

Bastrukov, S. I., Chang, H.-K., Takata, J., Chen, G.-T., & Molodtsova, I. V. 2007, *Mon. Not. R. Astron. Soc.*, 382, 849

Baym, G., Pethick, C., & Pines, D. 1969, *Nature*, 224, 673

Baym, G. & Pines, D. 1971, *Annals of Physics*, 66, 816

Bhattacharya, D. & Van Den Heuvel, E. P. J. 1991, *Physics Reports*, 203, 1

Bildsten, L. 1998, *Astrophys. J. Lett.*, 501, 89

Bisnovatyi-Kogan, G. S. & Komberg, B. V. 1976, *Soviet Astronomy Letters*, 2, 130

Cambiotti, G., Klemann, V., & Sabadini, R. 2013, *Geophys. J. Int.*, 193, 1071

Cambiotti, G. & Sabadini, R. 2010, *Geophys. J. Int.*, 180, 475

Caplan, M. E. & Horowitz, C. J. 2017, *Reviews of Modern Physics*, 89, 041002

Caplan, M. E., Schneider, A. S., & Horowitz, C. J. 2018, *Phys. Rev. Lett.*, 121, 132701

Carter, B. & Chachoua, E. 2006, *International Journal of Modern Physics D*, 15, 1329

Carter, B., Langlois, D., & Sedrakian, D. M. 2000, *Astron. Astrophys.*, 361, 795

Chakrabarty, D. 2008, *AIP Conference Proceedings*
Chakrabarty, D., Morgan, E., Muno, M., et al. 2003, *Nature*, 424, 42
Chamel, N. 2006, *Nuclear Physics A*, 773, 263
Chamel, N. 2012, *Phys. Rev. C*, 85, 035801
Chamel, N. 2012, *Phys. Rev. C*, 85, 035801
Chamel, N. 2013, *Phys. Rev. Lett.*, 110, 011101
Chamel, N. 2017a, *Journal of Low Temperature Physics*, 189, 328
Chamel, N. 2017b, *Journal of Astrophysics and Astronomy*, 38, 43
Chamel, N. & Carter, B. 2006, *Mon. Not. R. Astron. Soc.*, 368, 796
Chamel, N. & Haensel, P. 2008, *Living Reviews in Relativity*, 11, 10
Chanmugam, G. 1977, *Astrophys. J.*, 217, 799
Chao, B. F. & Gross, R. 1987, *Geophysic R. Astro. Soc.*, 91, 569
Cheng, B., Epstein, R., Guyer, R., & Young, A. 1996, *Nature*, 382, 518
Comella, J., H.D., C., Lovelace, R., Sutton, J., & Tyler, G. 1969, *Nature*, 221, 453
Cook, G. B., Shapiro, S. L., & Teukolsky, S. A. 1994, *Astrophys. J. Lett.*, 423, 117
Cowling, T. 1941, *Mon. Not. R. Astron. Soc.*, 367
Crawford, F. & Demiansku, M. 2003, *Astrophys. J.*, 595, 1052–1057
Cutler, C. 2002, *Phys. Rev. D*, 66, 084025
Cutler, C., Ushomirsky, G., & Link, B. 2003, *Astrophys. J.*, 588, 975
Datta, B. & Alpar, M. A. 1993, *Astron. Astrophys.*, 275, 210
Davidson, K. & Ostriker, J. P. 1973, *Astrophys. J.*, 179, 585
Delsate, T., Chamel, N., Gürlebeck, N., et al. 2016, *Phys. Rev. D*, 94, 023008
DeWit, R. 2008, *J. Mech. Mater. Struct*, 3, 195
Diehl, R., Halloin, H., Kretschmer, K., et al. 2006, *Nature*, 439, 45
Donati, P. & Pizzochero, P. M. 2004, *Nuclear Physics A*, 742, 363
Douchin, F. & Haensel, P. 2001, *Astron. Astrophys.*, 380, 151
Duncan, R. C. 1998, *Astrophys. J. Lett.*, 498, L45
Easson, I. 1979a, *Astrophys. J.*, 233, 711
Easson, I. 1979b, *Astrophys. J.*, 228, 257
Espinoza, C., Antonopoulou, D., Stappers, B., Watts, A., & Lyne, A. 2014, *Mon. Not. R. Astron. Soc.*, 440, 2755–2762
Espinoza, C., Lyne, C., Stappers, B., & Kramer, M. 2011, *Mon. Not. R. Astron. Soc.*, 414, 1679–1704
Fattoyev, F. J., Horowitz, C. J., & Lu, H. 2018, ArXiv e-prints
Franco, L. M., Link, B., & Epstein, R. I. 2000, *Astrophys. J.*, 543, 987
Fuchs, K. 1936, Proc. R. Soc. London, Ser. A, 153, 622–639
Fuentes, J., Espinoza, C., Reisenegger, A., et al. 2017, *Astron. Astrophys.*, 608, 1131
Galloway, D. K., Markwardt, C. B., Morgan, E. H., Chakrabarty, D., & Strohmayer, T. E. 2005, *Astrophys. J.*, 622, L45
Giacconi, R., Gursky, H., Paolini, F., & Rossi, B. 1962, *Physical Review Letter*, 9, 439
Giliberti, E., Antonelli, M., Cambiotti, G., & Pizzochero, P. M. 2019, *Publications of the Astronomical Society of Australia*, 36, e036
Giliberti, E., Cambiotti, G., Antonelli, M., & Pizzochero, P. 2018, arXiv e-prints, arXiv:1809.08542
Giliberti, E., Cambiotti, G., Antonelli, M., & Pizzochero, P. 2019, Submitted to *MNRAS*
Glendenning, N. 2000, Compact Stars: Nuclear Physics, Particle Physics and General

Relativity. (Springer)
Glendenning, N. K. & Moszkowski, S. A. 1991, *Phys. Rev. Lett.*, 67, 2414
Gold, T. 1968, *Nature*, 218, 731
Goldreich, P. & Julian, W. H. 1969, *Astrophys. J.*, 157, 869
Goriely, S., Chamel, N., & Pearson, J. M. 2013, *Phys. Rev. C*, 88, 024308
Gourgoulhon, E., Haensel, P., & Gondek, D. 1995, *Astron. Astrophys.*, 294, 747
Göğüş, E., Woods, P. M., Kouveliotou, C., et al. 2000, *Astrophys. J. Lett.*, 532, L121
Graber, V., Andersson, N., & Hogg, M. 2017, *International Journal of Modern Physics D*, 26, 1730015
Haensel, P., Levenfish, K. P., & Yakovlev, D. G. 2002, *Astron. Astrophys.*, 394, 213
Haensel, P. & Pichon, B. 1994, *Astron. Astrophys.*, 283, 313
Haensel, P. & Zdunik, J. L. 1990, *Astron. Astrophys.*, 229, 117
Harding, A. K. 2013, *Frontiers of Physics*, 8, 679
Haskell, B., Jones, D. I., & Andersson, N. 2006, *Mon. Not. R. Astron. Soc.*, 373, 1423
Haskell, B. & Melatos, A. 2015, *International Journal of Modern Physics D*, 24, 1530008
Haskell, B. & Melatos, A. 2016, *Mon. Not. R. Astron. Soc.*, 461, 2200
Haskell, B. & Pizzochero, P.M. Seveso, S. 2013, *Astrophys. J. Lett.*, 764, L25
Haskell, B., Priymak, M., Patruno, A., et al. 2015, *Mon. Not. R. Astron. Soc.*, 450, 2393–2403
Haskell, B., Samuelsson, L., Glampedakis, K., & Andersson, N. 2008, *Mon. Not. R. Astron. Soc.*, 385, 531
Haskell, B. & Sedrakian, A. 2017, ArXiv e-prints
Haskell, B. & Sedrakian, A. 2018, Astrophysics and Space Science Library, Vol. 457, Superfluidity and Superconductivity in Neutron Stars, ed. L. Rezzolla, P. Pizzochero, D. I. Jones, N. Rea, & I. Vidaña, 401
Hessels, J., Ransom, S., Ransom, S., et al. 2006, *Science*, 311, 1901
Hewish, A., Bell, S., Pilkington, J. H., Scott, P., & Collins, R. 1968, *Nature*, 217, 709
Hill, R. 1952, *Proc. Phys. Soc. A*, 65, 349
Ho, W. & Heinke, C. 2009, *Nature*, 462, 71
Ho, W. C. G., Espinoza, C. M., Antonopoulou, D., & Andersson, N. 2015, *Science Advances*, 1, e1500578
Hoffman, K. & Heyl, J. 2012, *Mon. Not. R. Astron. Soc.*, 426, 2404
Horowitz, C. J. & Kadau, K. 2009, *Physical Review Letter*, 102, 191102
Howitt, G., Melatos, A., & Delaigle, A. 2018, *Astrophys. J.*, 867, 60
Hulse, R. A. & Taylor, J. H. 1975, *Astrophys. J. Lett.*, 195, L51
Jackson, J. 1991, Classical Electrodynamics (John Wiley Sons, Inc., New Jersey)
Jaranowski, P., Królak, A., & Schutz, B. F. 1998, *Phys. Rev. D*, 58, 063001
Johnson-McDaniel, N. K. & Owen, B. J. 2013, *Phys. Rev. D*, 88, 044004
Jones, P. 2003, *Astrophys. J.*, 595, 342–345
Kalapotharakos, C., Kazanas, D., Harding, A., & Contopoulos, I. 2012, *Astrophys. J.*, 749, 2
Kaplan, D. L. 2008, *AIP Conference Proceedings*, 983, 331
Keane, E. & M.A., M. 2011, *Bull. Astr. Soc. India*, 39, 333
Keer, L. & Jones, D. I. 2015, *Mon. Not. R. Astron. Soc.*, 446, 865
Kittel, C. 1996, Introduction to Solid State Physics, Vol. 21
Kobyakov, D. & Pethick, C. 2015, *Mon. Not. R. Astron. Soc.*, 449, L110–L112
Kobyakov, D. & Pethick, C. J. 2014, *Phys. Rev. Lett.*, 112, 112504

Kobyakov, D. & Pethick, C. J. 2016, *Phys. Rev. C*, 94, 055806
Kohanoff, J. & J.P., H. 1996, Phys. Rev. E, 54, 768
Kwang-Hua, C. W. 2018, *Astrophys. Space Sci.*, 363, 184
Landau, L. 1932, *D. Phys. Z. Sowjetunion*, 1, 285
Landau, L. & Lifshitz, E. 1970, Theory of Elasticity (Pergamon Press)
Lander, S. K., Andersson, N., Antonopoulou, D., & Watts, A. L. 2015, *Mon. Not. R. Astron. Soc.*, 449, 2047
Lander, S. K. & Gourgouliatos, K. N. 2019, *Mon. Not. R. Astron. Soc.*, 486, 4130
Langlois, D., Sedrakian, D. m., & Carter, B. 1998, *Mon. Not. R. Astron. Soc.*, 297, 1189–1201
Lattimer, J. M. & Prakash, M. 2007, *Phys. Reports*, 442, 109
Lenz, G., Meystre, P., & Wright, E. M. 1993, *Phys. Rev. Lett.*, 71, 3271
Link, B. & Epstein, R. I. 1996, *Astrophys. J.*, 457, 844
Link, B., Epstein, R. I., & Lattimer, J. M. 1999, *Phys. Rev. Lett.*, 83, 3362
Link, B., Franco, L. M., & Epstein, R. I. 1998, *Astrophys. J.*, 508, 838
Link, B. K. & Epstein, R. I. 1991, *Astrophys. J.*, 373, 592
Lorimer, D. R. & Kramer, M. 2004, Handbook of Pulsar Astronomy
Love, A. 1934, A Treatise on the Mathematical Theory of Elasticity (University Press)
Love, A. 1959, A Treatise On the Mathematical Theory of Elasticity, Dover books on engineering and engineering physics (University Press)
Lyne, A., Shemar, S., & Graham Smith, F. 2000, *Mon. Not. R. Astron. Soc.*, 315, 534
Lyne, A. G., Pritchard, R. S., & Graham Smith, F. 1993, *Mon. Not. R. Astron. Soc.*, 265, 1003
Lyne, A. G., Pritchard, R. S., Graham Smith, F., & Camilo, F. 1996, *Nature*, 381, 497
Matsakis, D. N., Taylor, J. H., & Eubanks, T. M. 1997, *Astron. Astrophys.*, 326, 924
McDermott, P. N., Van Horn, H. M., & Hansen, C. J. 1988, *Astrophys. J.*, 325, 725
Melatos, A. & Payne, D. J. B. 2005, *Astrophys. J.*, 623, 1044
Melatos, A., Peralta, C., & Wyithe, J. S. B. 2008a, *Astrophys. J.*, 672, 1103
Melatos, A., Peralta, C., & Wythe, J. 2008b, *Astrophys. J.*, 672, 1103
Meltzer, D. W. & Thorne, K. S. 1966, *Astrophys. J.*, 145, 514
Montoli, A., Antonelli, M., & Pizzochero, P. 2018, arXiv e-prints, arXiv:1809.07834
Negele, J. W. & Vautherin, D. 1973, *Nuclear Physics A*, 207, 298
O'Connor, E. & Ott, C. D. 2011, in APS April Meeting Abstracts, Vol. 2011, L11.005
Ogata, S. & Ichimaru, S. 1990, Phys. Rev. A, 42, 4867–4870
Oppenheimer, J. R. & Volkoff, G. 1939, *Phys. Rev. D*, 55, 374
Pacini, F. 1967, *Nature*, 216, 567
Palfreyman, J., Dickey, J. M., Hotan, A., Ellingsen, S., & van Straten, W. 2018, *Nature*, 556, 219
Palomba, C. 2005, *Mon. Not. R. Astron. Soc.*, 359, 1150
Papaloizou, J. & Pringle, J. E. 1978, *Mon. Not. R. Astron. Soc.*, 184, 501
Papitto, A., Torres, D., & Rea, N.and Tauris, T. 2010, *Astrophys. J.*, 719, L167
Papitto, A., Torres, D., & Rea, N.and Tauris, T. 2014, *AstronomyAstrophysics*, 566, A64
Pearson, J. M., Chamel, N., Potekhin, A. Y., et al. 2018, *Mon. Not. R. Astron. Soc.*, 481, 2994
Pethick, C. & Pothekhin, A. 1998, *Physics Letters B*, 427, 7
Pizzochero, P. M. 2011, *Astrophys. J. Lett.*, 743, L20
Posselt, B., Pavlov, G. G., Suleimanov, V., & Kargaltsev, O. 2013, *Astrophys. J.*, 779, 186
Pringle, J. E. & Rees, M. J. 1972, *Astron. Astrophys.*, 21, 1
Prix, R. 2004, *Phys. Rev. D*, 69, 043001

Priymak, M., Melatos, A., & B., P. D. J. 2011, *Mon. Not. R. Astron. Soc.*, 417, 2696–2713
Ruderman, M. 1969, *Nature*, 223, 597
Ruderman, M. 1976, *Astrophys. J.*, 203, 213
Ruderman, M. A. & Sutherland, P. G. 1975, *Astrophys. J.*, 196, 51
Ruderman, R. 1991, *Astrophys. J.*, 382, 576
Sabadini, R., Vermeersen, B., & Cambiotti, G. 2016, Global Dynamics of the Earth: Applications of Viscoelastic Relaxation Theory to Solid-Earth and Planetary Geophysics (Springer Netherlands)
Sabadini, R., Yuen, D. A., & Boschi, E. 1982, *Journal of Geophysical Research*, 87, 2885
Samuelsson, L. & Andersson, N. 2007, *Mon. Not. R. Astron. Soc.*, 374, 256
Sauls, J. A. 2019, arXiv e-prints, arXiv:1906.09641
Sazhin, M. V. 1978, *Soviet. Astron.*, 22, 36
Schwarz, K. W. 1988, *Phys. Rev. B*, 38, 2398
Seveso, S. 2014, Advances in models of Pulsar Glitches (Phd Thesis, Università degli Studi di Milano)
Seveso, S., Pizzochero, P. M., Grill, F., & Haskell, B. 2016, *Mon. Not. R. Astron. Soc.*, 455, 3952
Shapiro, S. & Teukolsky, S. 1983, Black holes, white dwarfs, and neutron stars: the physics of compact objects, A Wiley-interscience publication (Wiley)
Shklovsky, I. S. 1967, *Astrophys. J. Lett.*, 148, L1
Shternin, P., Yakovlev, D., Heinke, C., Ho, W., & J.P., D. 2011, *Mon. Not. R. Astron. Soc.*, 412, L108
Smarr, L. L. & Blandford, R. 1976, *Astrophys. J.*, 207, 574
Smoluchowski, R. & Welch, D. O. 1970, *Phys. Rev. Lett.*, 24, 1191
Spitkovsky, A. 2006, *Astrophys. J.*, 648, L51
Strohmayer, T., Van Horn, H., Ogata, S., Iyetomi, H., & Ichimaru, S. 1991, *Astrophys. J.*, 375, 679–686
Strohmayer, T. E. & Watts, A. L. 2006, *Astrophys. J.*, 653, 593
Sukhbold, T., Ertl, T., Woosley, S. E., Brown, J. M., & Janka, H. T. 2016, *Astrophys. J.*, 821, 38
The LIGO Scientific Collaboration, t. V. C. & authors, A. 2019, ArXiv e-prints
Thompson, C. & Duncan, R. 1996, *Astrophys. J.*, 473, 322
Thompson, C. & Duncan, R. C. 1993, *Astrophys. J.*, 408, 194
Thompson, C. & Duncan, R. C. 1995, *Mon. Not. R. Astron. Soc.*, 275, 255
Tolman, R. 1939, *Phys. Rev.*, 55, 364
Ushomirsky, G., Cutler, C., & Bildsten, L. 2000, *Mon. Not. R. Astron. Soc.*, 319, 902
Vigelius, M. & Melatos, A. 2009, *Mon. Not. R. Astron. Soc.*, 395, 1972
Wagoner, R. V. 1984, *Annals of Physics*, 278, 345
Wang, M., Audi, G., Kondev, F. G., et al. 2017, *Chinese Physics C*, 41, 030003
Wang, Y.-M. 1996, *Astrophys. J. Lett.*, 465, L111
Warszawski, L. & Melatos, A. 2013, *Mon. Not. R. Astron. Soc.*, 428, 1911
Watts, A., Krishnan, B., Bildsten, L., & Schutz, B. F. 2008, *Mon. Not. R. Astron. Soc.*, 389, 839–868
Watts, A. L. & Reddy, S. 2007, *Mon. Not. R. Astron. Soc.*, 379, L63
Watts, A. L. & Strohmayer, T. E. 2006, *Astrophys. J. Lett.*, 637, L117
White, N. & Zhang, W. 1997, *Astrophys. J.*, 490, L87
Wijnands, R. & van der Klis, M. 1998, *Nature*, 394, 344

Woan, G., Pitkin, M. D., Haskell, B., Jones, D. I., & Lasky, P. D. 2018, ArXiv e-prints
Woltjer, L. 1964, *Astrophys. J.*, 140, 1309
Yakovlev, D. G., Gusakov, M. E., Kaminker, A. D., & Potekhin, A. Y. 2006, in Exotic Nuclei and Nuclear/Particle Astrophysics, 205–212
Zdunik, J. L., Bejger, M., & Haensel, P. 2008, *Astron. Astrophys.*, 491, 489
Zuo, W., Li, Z. H., Lu, G. C., et al. 2004, *Physics Letters B*, 595, 44

List of Publications

Refereed publications

Giliberti E., Antonelli M., Cambiotti G., Pizzochero P.M., *Incompressible analytical models for spinning-down pulsars*, PASA, 2019

Giliberti E., Cambiotti G., Antonelli M., Pizzochero P.M., *Modelling strains and stresses in continuously stratified rotating neutron stars*, MNRAS, 2019

Publications in preparation

Giliberti E., Cambiotti G., Antonelli M.,Haskell B., Pizzochero P.M., *Starquakes on millisecond pulsars and gravitational waves emission*, MNRAS

Acknowledgments

The acknowledgments will be present in the printed version of this work of thesis.